Ayman S. Mosallam
Brahim El Bhiri
Vistasp M. Karbhari
Shadi Saadeh *Editors*

Advances in Smart Materials and Innovative Buildings Construction Systems

Proceedings of the 4th International Conference on Advanced Technologies for Humanity (ICATH'2022)

Springer

Sustainable Civil Infrastructures

Editor-in-Chief

Hany Farouk Shehata, SSIGE, Soil-Interaction Group in Egypt SSIGE, Cairo, Egypt

Advisory Editors

Khalid M. ElZahaby, Housing and Building National Research Center, Giza, Egypt

Dar Hao Chen, Austin, TX, USA

Series Editor

Mourad Amer, IEREK—International Experts for Research Enrichment and Knowledge Exchange, Cairo, Egypt

Sustainable Civil Infrastructures (SUCI) is a series of peer-reviewed books and proceedings based on the best studies on emerging research from all fields related to sustainable infrastructures and aiming at improving our well-being and day-to-day lives. The infrastructures we are building today will shape our lives tomorrow. The complex and diverse nature of the impacts due to weather extremes on transportation and civil infrastructures can be seen in our roadways, bridges, and buildings. Extreme summer temperatures, droughts, flash floods, and rising numbers of freeze-thaw cycles pose challenges for civil infrastructure and can endanger public safety. We constantly hear how civil infrastructures need constant attention, preservation, and upgrading. Such improvements and developments would obviously benefit from our desired book series that provide sustainable engineering materials and designs. The economic impact is huge and much research has been conducted worldwide. The future holds many opportunities, not only for researchers in a given country, but also for the worldwide field engineers who apply and implement these technologies. We believe that no approach can succeed if it does not unite the efforts of various engineering disciplines from all over the world under one umbrella to offer a beacon of modern solutions to the global infrastructure. Experts from the various engineering disciplines around the globe will participate in this series, including: Geotechnical, Geological, Geoscience, Petroleum, Structural, Transportation, Bridge, Infrastructure, Energy, Architectural, Chemical and Materials, and other related Engineering disciplines.

SUCI series is now indexed in SCOPUS and EI Compendex.

Ayman S. Mosallam · Brahim El Bhiri ·
Vistasp M. Karbhari · Shadi Saadeh
Editors

Advances in Smart Materials and Innovative Buildings Construction Systems

Proceedings of the 4th International Conference on Advanced Technologies for Humanity (ICATH'2022)

Springer

Editors
Ayman S. Mosallam
Department of Civil and Environmental
Engineering
University of California, Irvine (UCI)
Irvine, CA, USA

Vistasp M. Karbhari
University of Texas at Arlington
Arlington, TX, USA

Brahim El Bhiri
EMSI
Rabat, Morocco

Shadi Saadeh
California State University
Long Beach, CA, USA

Contents

Part I
Reinforced Concrete and Masonry Structures

Chapter 1
Assessment and Calibration of the ACI Punching Shear Resistance of LW Slabs Using Reliability Methods

Soliman Alkhatib and Ahmed F. Deifalla

Abstract Failures due to shear are brittle and required reliable strength models. The challenge of refining those methods has been brought to question recently. This research study aims at applying recent reliability approaches for the case lightweight concrete (LW) slabs under shear. The American Concrete Institute (ACI) was selected. An experimental data base gathered from existing literature was implemented. A brief review of both the Second-Order Methods (SORM) and First-Order Method (FORM), which are commonly used for the computation of reliability are outlined. The FORM was selected to calculate the sensitivity index and reliability index were calculated for the ACI. A comparative analysis between those indices and the internationally set target ones was conducted. The ACI was found to be lacking the adequate reliability. Thus, ACI provision was optimized to achieve target reliability indices.

Keywords Lightweight concrete · Reliability index · Punching shear · ACI

1.1 Introduction

One of the most complicated problems is the reinforced concrete (RC) structures construction, which is governed at various stages with many ambiguities. Such variability has to be considered in the design stage, which could significantly affect the design. That uncertainty is related to the following factors: (1) load distribution, geometric configurations, and material mechanical properties; (2) size of element; (3) resistance modeling; (4) construction, and design errors; and (5) dilemma of the

S. Alkhatib · A. F. Deifalla (✉)
FUE, New Cairo, Egypt
e-mail: Ahmed.deifalla@fue.edu.eg

S. Alkhatib
e-mail: Soliman.alkhatib@fue.edu.eg

true behavior. Figure 1.1 shows the various mechanisms, which is affect the compli-
cated punching shear behavior of RC slabs. These include but not limited to: (1) at
the crossing of the shear diagonal crack and the flexure reinforcements, dowel action
mechanism; (2) across the compression zone, direct shear mechanism; and (3) across
the critical crack, both the interlocking of the aggregate crossing the crack and the
friction mechanism along crack sides. Worldwide, the RC elements under shear are
being examined by researchers (Ricker et al. 2021; Ju et al. 2021; Deifalla 2020a,
2021, 2020c). Especially, the lightweight concrete design (LW), which is still further
behind (Deifalla et al. 2020a, 2020b; Deifalla 2020b).

LW behavior differ in several features compared to normal weight concrete, which
includes the following: (1) lower aggregate interlock due to smooth crack across
weaker aggregates; (2) wider cracks due to lower modulus of elasticity; and (3)
different behavior due to lightweight aggregate having different types (Deifalla et al.
2020, 2020b; Deifalla 2020b; ACI-213 2014). ACI included new provisions for
the shear design of LW by using the density of the concrete mix (Deifalla et al.
2020, 2020b; Deifalla 2020b; ACI-213 2014). The reliability of the punching shear
provisions of the ACI need to be examined has been a finding of previous research
investigations (Deifalla 2020b; ACI-213 2014; Greene and Graybeal 2015).

Accurate assessment for structural systems safety level, require modern relia-
bility analysis techniques. The reliability analysis involves the load and resistance
uncertainties. The statistical analysis includes outliers' detection, which includes (1)
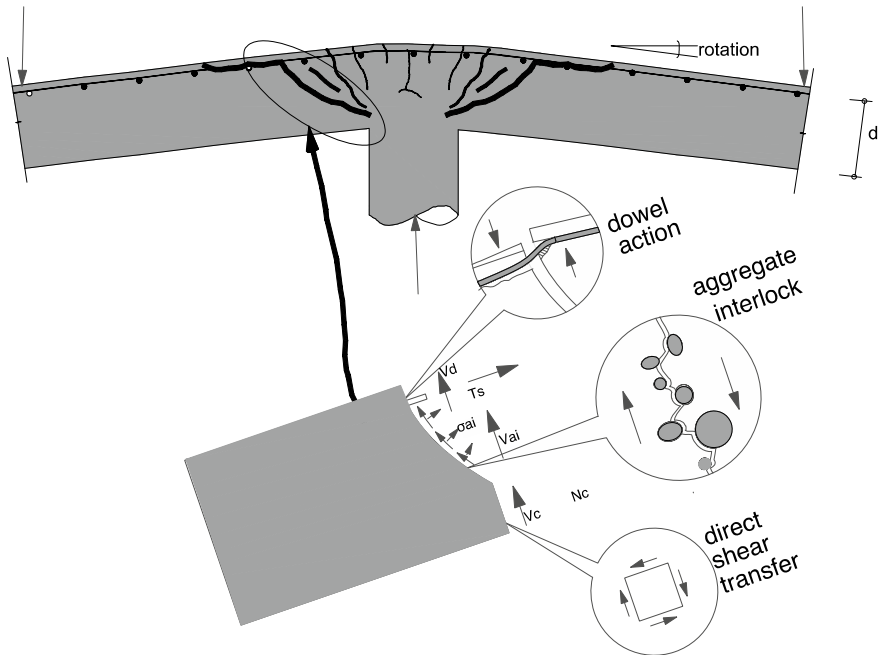
Fig. 1.1 The mechanisms of the concrete slabs under punching shear (Deifalla 2020a, 2021, 2020c)

histograms representation; (2) erroneous values correction; followed by computing the statistical measures (i.e., mean, skewness, kurtosis, and standard deviations) using the corrected data. In addition, it requires the random parameter uncertainty distribution, where lognormal distribution is the most appropriate. In existing literature, various methods to assess the design model reliability, which are the First and second order approach (known here in and after as FORM and SORM) (Ricker et al. 2021; Mallor et al. 2020; Sousa et al. 2010; Dithinde 2007; Ditlevsen and Bjeragger 1986). Moreover, several key investigations have investigated the calibration and assessment of the ACI using structural reliability methods for various scenarios including and not limited to behavior of RC under compression, and shear (Alkhatib and Deifalla 2002, 2022). However, none of these previous studies examined the ACI shear design of LW RC slabs (LWRCS). In this study, various reliability methods are outlined, discussed and implemented. The punching shear LWRCS design using the ACI was evaluated with respect to its reliability using (FORM). Sometimes when the performance function has a higher nonlinearity, we must study the curvature of the hypersurface which present the performance function, so the Second order Reliability have to calculate to precise the accuracy of the FORM. So, the reliability indices are also calculated by the SORM and compared with the FORM.

The sensitivity and reliability indices were evaluated using the (FORM) techniques. In addition, the reduction factors of the design provisions of the ACI were calibrated (EC2 1990; ACI-318-19 2019). Concluding remarks were discussed.

1.2 The ACI

In the study, we consider shear strength, which is calculated as: (V)

$$\mathbf{V} = 0.17\left(1 + \frac{2}{\boldsymbol{\beta_0}}\right)\lambda\lambda_s\sqrt{f_c}(4[c+\mathrm{d}])d \le 0.33\lambda\lambda_s\sqrt{f_c}d(\pi[\mathrm{c}+d]) \qquad (1.1)$$

where, $\lambda_s = \sqrt{\frac{2}{1+0.004d}} \le 1$, $\lambda = 3\frac{\gamma_c}{6400}$, $\boldsymbol{\beta_0}$ is the ratio between loading area dimensions.

1.3 Previously Tested LWRCS

Researchers have started testing LWRCS under punching shear since the 60's. A database of 129 LWRCS tested under punching shear, which was collected from thirteen different research study as shown in Table 1.1 (Deifalla 2020a, 2021, 2020c). The database covered a comprehensive range of many of the effective factors including loading area dimensions, concrete compressive strength, concrete density, coarse

Table 1.1 Uncertainty basic factors (Joint Committee on Structural Safety 2001)

Parameter	Distribution	Nominal	Mean	Standard deviation
f_{c}'	Log-normal	25	38.8[a]	4.67[a]
		35	47.2[a]	4.26[a]
		45	53.6[a]	3.76[a]
d	Normal	d_n	$d_n + 10$	10
c	Normal	c_n	$c_n + 0.003 c_n$	$4 + 0.006\, c_n$
γ	Normal	γ_n	γ_n	0.05

[a] Log-normal distribution corrected

aggregate type, loading pattern, aggregate maximum nominal size, slab dimensions, opening along column sides, percentage of main reinforcements, yield stress of the main reinforcement and eccentricity.

1.4 Reliability Analysis

Load, material, and geometry factors are subject to uncertainties, which can be classified. According to their nature. They can, thus, be represented by random parameter. In theory of probability, a system probability to complete its intended function during a certain period is called reliability. In addition, examining the system capability to fulfill its purpose, requirements and function (Ditlevsen and Bjeragger 1986). Moreover, the basic problem of reliability is how a building will achieve its purposes, according to well-defined environments and on a specific time (Joint Committee on Structural Safety 2001). Thus, it is feasible to express a failure probability (P_f), as the reliability complementary probability, which represent the safety of structure. Where the performance of the building is described using the following factors: (1) cross-section dimensions, (2) concrete density, (3) values of strength; (4) loads applied on structure. When selecting those needed factor for the description of the investigated dilemma, independent factors must identify, which is not always achievable. Depending on the available information about these factors, it is possible through probabilistic distributions to model them; however, their statistical measures must be selected cautiously. For a structural model, it can be improved or revised based on existing information. In the case of lack of adequate information to define the probabilistic function, a characteristic value point can be used, which is termed as the design. For a structural element, when the load resultant (E) of a determined loading Q is larger than the resistance value (R), failure is expected on that specific element. The performance function is designed in such a way that:

$$G\left(\overrightarrow{X}\right) = G\left(\overrightarrow{X}_1, \overrightarrow{X}_2, \ldots, \overrightarrow{X}_n\right) = R - E \qquad (1.2)$$

where G is the safety margin, and $\left(\vec{X}_1, \vec{X}_2, \ldots, \vec{X}_n \right)$ is the random factors vector of the performance function. When $R = E$, then the performance function is defined as the following:

$$G\left(\vec{x} \right) = G\left(\vec{x}_1, \vec{x}_2, \ldots, \vec{x}_n \right) = 0 \tag{1.3}$$

where the vectors $\left(\vec{x}_1, \vec{x}_2, \ldots, \vec{x}_n \right)$ are at the reliability index achieves the safety nominal extent. The calculation will be done by the FOMS. According to EN (2002), the reliability index β minimum values for ultimate limit states is value of 3.8. Furthermore, in structural analysis, the performance function G is defined as the difference between total resistance (R) and total load (E). For the purpose of design, the best choice is having R bigger than E. Thus, the limit state is when $G = R$, such that:

$$G\left(\vec{X} \right) = \theta_R v_c\left(d, c, \gamma_c, f_c \right).u_1(d, c).d - V_{Rd,c} = 0 \tag{1.4}$$

where θ_R is model uncertainty, d is the slab depth, c is dimensions of loaded area, u_1 is the control perimeter, v_c is punching shear stress at the control perimeter, γ_c is the concrete unit volume, f_c' is the concrete strength under compression, $V_{Rd,c}$ is the design value of the punching shear. Using the ACI provisions for the V, the performance function can be written as:

$$G\left(\vec{X} \right) = \theta_R \left[\min . \left(\sqrt{\frac{2}{1 + 0.004d}}, 1 \right) \left(3 \frac{\gamma_c}{6400} \right) \right]$$
$$\left[0.17\left(1 + \frac{2}{\beta_0} \right)\sqrt{f_c} \leq 0.33\sqrt{f_c} \right]\left(2\pi \left[\frac{c}{2} + \frac{d}{2} \right] \right)d - V_{Rd,c} = 0 \tag{1.5}$$

1.5 Variability of the ACI Resistance Model

For the failure mode under consideration, uncertainty modeling needs to be undertaken with regard to those factors in corresponding limit state function whose variability is judged to important (basic random factors). The ACI variability measures are indicated in Table 1.2. We consider the data lognormal distribution.

SORM and FORM are generally used for the calculation of reliability, defined as the probability of fulfilling a planned purpose, while uncertainties are expected. A second-order approximation of the limit-state function around the Point of high probability of failure; thus, can achieve highly accurate predictions for the reliability index β. Consider all random factors are independent and distributed in a normal

Table 1.2 Reliability index for loading area dimension

c (mm)	β FORM	β SORM
150	3.18	3.19
200	3.18	3.19
250	3.18	3.19
300	3.17	3.19
350	3.17	3.19
400	3.17	3.19

pattern, therefore, the relationship between the probability of the failure of the hyper-surface $G(\vec{X}) = 0$ and, the reliability index β can be expressed as $P_f = 1 - \Phi(\beta)$, where Φ is the standard cumulative distribution normal. In the following we illustrate FORM and SORM with detail and calculate the reliability index with respect to random factors considered in the performance function and the results and we arrange the result in several tables. Maple was used to do such calculation.

The main idea in this method is that for each non-normal random factor, corresponding mean and standard deviation is computed. The equivalent standard deviation σ_X^e and mean μ_X^e is calculated such that:

$$\mu_X^e = X^* - \sigma_X^e[\Phi^{-1}F_X(X^*)] \tag{1.6}$$

$$\sigma_X^e = \frac{1}{f_X(X^*)}\phi\left(\frac{X^* - \mu_X^e}{\sigma_X^e}\right) = \frac{1}{f_X(X^*)}\phi[\Phi^{-1}F_X(X^*)] \tag{1.7}$$

where ϕ and Φ are PDF and CDF for the normal distribution. $F_X(X)$ is the cumulative distribution function and $f_X(X)$ is the probability density, σ_X is the standard deviation and μ_X is the mean. Thus, for each of the design point values X^* corresponding to a non-normal distribution, the equivalent normal mean and standard deviation are calculated. If one or more X^* values correspond to a normal distribution, the equivalent normal factors are simply the actual factors. In this study, the θ_R and t$f_{c'}$ are regarded as lognormal distributions. To find the equivalent normal parameter for a lognormal random parameter X can be calculated such that:

$$\sigma_X^e = X^*\sigma_{lnX}, \ \mu_X^e = X^*[1 - \ln(X^*) + \mu_{lnX}] \tag{1.8}$$

Where, X^* is the design point value and σ_{lnX} and μ_{lnX} are the distribution parameter for the lognormal distribution.

The SORM was introduced as an improvement for the FORM where additional information about the curvature of the performance function is included (El-Gamal et al. 2005). SORM relies mainly on three factors: the curvature radius at the design point, the number of random factors and the first order β, more detail for this method cans be found in Alkhatib and Deifalla (2022). The Taylor expansion is given to

approximate the performance function at the design point:

$$G(X) = G(X^*) + \nabla G(X^*)(X - X^*)^T + \frac{1}{2}(X - X^*)\left[\nabla^2 G(X^*)(X - X^*)^T\right]$$

(1.9)

where $\left[\nabla^2 G(X^*)\right] = \left[\frac{\partial 2\mathbf{G}}{\partial X_i \partial X_j}\right]\Big|_{X^*} i = 1..n, j = 1..n$ is the Hessian matrix of $G(X)$ at X^*. The SORM is determined initially by the (FORM) results for the reliability index, the final design point, and the directional cosine vector at that final design point. The primary goal of the (SORM) is to improve the accuracy of the value of β calculated by the first order reliability method (FORM). The principal curvature of the hypersurface is determined first in this methodology. The calculation of curvature can produce positive, negative, or complex values depending on the nonlinearity of the performance function and the number of factors. The present paper uses Breitung's (SORM) method, which employs a parabolic approximation rather than a general second-order approximation. The probability estimate is derived using the theory of asymptotic approximation. Only for large values of β is the asymptotic formula accurate.. However, if the value of $\boldsymbol{\beta}$ is low, the (SORM) estimate may be inaccurate. If the number of factors is not large enough, or if the curvature radius is very large, the values of the reliability index between (FORM) and (SORM) are nearly identical.

We begin this method's procedure by computing the Reliability index and the directional cosine vector α=[α_i] as well as the final design point in the initial factors U* using the (FORM) -based method (FORM). Convert all factors from their original to standard form, depending on the type of distribution (when the random parameter is non-normal, we use the equivalent normal mean and equivalent standard deviation). Breitung's formula can be used to calculate the second order estimate of the probability of failure:

$$P_{f_2} = \Phi(-\beta) \prod_{i=1}^{n-1} [1 + \beta\kappa_i]^{-\frac{1}{2}}$$

(1.10)

where κ_i is the principal curvature at the design point of the failure surface. Finally, the SORM reliability index β_{SORM} is computed in such a way that:

$$\beta_{SORM} = -\Phi^{-1}(P_{f_2})$$

(1.11)

To calculate the curvature $\boldsymbol{\kappa_i}$ of the failure of a hypersurface, follow these steps: Construct the rotation matrix

$$R_0 = \begin{bmatrix} 1 & \cdots & 0 \\ \vdots & \ddots & \vdots \\ \alpha_1 & \cdots & \alpha_n \end{bmatrix}; [\alpha_i] = \frac{[\nabla G(Z^*)]^T}{\|\nabla G(Z^*)\|} \, and \, \nabla G(Z^*) = -\left.\frac{\partial G}{\partial Z_i}\right|_{(Z_i^*)} \quad i = 1..n$$

Convert the matrix R_0 to the orthonormal matrix R using the Gram-Schmidt orthogonalization procedure. Using the relationship $Y_i = RZ_i^*$ transform the vector (Z_i^*) to anther vector denoted by (Y_i). Construct a Hessian Matrix (D) containing the second derivative of limit stat at the design point in standard normal Space, where:

$$D = \left[[\nabla^2 G(Z^*)] = \left[\frac{\partial 2\mathbf{G}(.)}{\partial \mathbf{Z_i} \partial \mathbf{Z_j}} \right]\Big|_{\mathbf{Z}^*} \quad i = 1..n, j = 1..n \right]$$

Compute the matrix A whose elements a_{ij} are calculated as $A = [a_{ij}]_n = \left[\frac{RDR^T}{\sqrt{\|\nabla G(Z^*)\|}} \right]$. The last row and last column in the A matrix and the last row in the vector U_i are dropped because they present $\nabla G(Z^*)$ the first derivative of the Taylor Series found in the calculation of β by (FORM). Finally, the κ_i are calculated as the eigenvalues of the ((n-1) * (n-1)) matrix A. After calculating the κ_i we use Breitung's formula Eq. (1.12) to compute the failure probability.

1.6   Analysis

The reliability index determined for ACI using both the FOSM and SORM is compared to each other, and the target level β of value between 3.6-3.8. Tables 1.2, 1.3, 1.4, and 1.4 show the reliability index computed against the values of the effective factors f'_c, c, d, and γ_c, respectively. It is clear, for this case, the FORM yields result comparable with the SORM. Table 1.2 shows the influence of loaded area dimensions on the β, which is found for loaded area dimensions varying from 150 to 400 mm. Initial design point, is ($f_c\prime$ = 25MPa, d = 280mm, γ = 1900kg/m3). For a loaded area dimension of 400 mm, the lowest reliability index β was obtained with a β value of 3.17. For the other values of loaded area dimensions, the β values increased gradually, with a β value equal to 3.18 at a loaded area dimension of 150 mm. For all the loaded area dimensions, the reliability indices β is lower than the target level β.

Table 1.3 shows the influence of effective depth on the β, which is calculated for d varying from 400 to 100 mm. Initial design point is (c = 300mm, f'_c = 25MPa, γ = 1900kg/m3). For a d value of 400 mm, the lowest β was found to be value of 3.15. For the other values of d, the β values was increased progressively, with a β value equal to 3.23 at an d of 100 mm. For all the d values, the β is lower than the target level β.

Table 1.4 shows the influence of f'_c on the β, which is obtained for f'_c class C25, C35, and C45. Initial design point is (γ = 1900kg/m3, c = 300mm, d = 280mm).

Table 1.3 Reliability index for size

d (mm)	β FOSM	β SORM
100	3.23	3.26
200	3.20	3.21
250	3.18	3.19
280	3.17	3.19
300	3.17	3.19
400	3.15	3.17

Table 1.4 Reliability index for concrete compressive strength

$f_c{}'$ (MPa)	β FORM	β SORM
25	3.17	3.19
35	3.01	3.03
45	2.85	2.85

Table 1.5 Reliability index for density

γ (kg/m2)	β FORM	β SORM
1700	3.17	3.19
1900	3.17	3.19
2000	3.17	3.19
2200	3.17	3.19
2400	3.17	3.19

For $f_c{}'$ value of 45 MPa, the lowest β was obtained a value of 2.85. For the other values of $f_c{}'$, the β values increased gradually, with a β value equal to 3.18 at a $f_c{}'$ of 25 MPa. For all the values of $f_c{}'$, the β is lower than the target level β.

Table 1.5 shows the influence of γ on the β, which is obtained for γ varying from 2400 kg/m3 to 1700 kg/m3. Initial design point is ($d = 280\mathbf{mm}, c = 300\mathbf{mm}, f_c{}' = 25\mathbf{MPa}$). For γ value of 2400 kg/m3, the lowest β was achieved with a value of 3.18. For the other values of γ, the β increased gradually, with a β value equal to 3.18 at a γ value of 1700 kg/m3. For different values of γ, the β determined is lower than the target level β.

From Tables 1.2, 1.3, 1.4, and 1.5, the β is beneath the target limit. In addition, the fc' highly affected the design reliability, where the decrease in the fc'. Increased the reliability. On the other hand, no significant effect on the reliability due to the d and c. The β were calculated, while using a reduction coefficient with a value ranging from 0.5 to 0.9 as shown in Table 1.6, which were determined for based on the initial design point is ($d = 280\text{mm}, c = 300\text{mm}, f_c{}' = 45\text{MPa}, \gamma = 1900\text{kg/m3}$). To improve the reliability a reduction coefficient can be used. Thus, for the reliability index to reach the target value of 3.8, a reduction coefficient value of 0.7.

Table 1.6 ACI calibration

Reduction factor ($\varnothing$)	β FORM	β SORM
0.90	3.14	3.16
0.85	3.30	3.32
0.80	3.46	3.48
0.75	3.64	3.64
0.70	3.83	3.83
0.65	4.03	4.4
0.60	4.25	4.25
0.55	4.49	4.49
0.50	4.76	4.76

1.7   Conclusions

The reliability of the ACI for the punching shear provisions of LWRCS without shear reinforcement was examined with respect to standard reliability targets (Sykora et al. 2014, EN 2002). The following conclusions were reached at:

- The ACI reliability is below the target value.
- The ACI is significantly influenced by model uncertainty, which emphasis the important of improving model uncertainty.
- For the ACI, the model uncertainty is followed by the uncertainty of both the concrete compressive strength and the effective depth in influencing the reliability. Thus, both factors need further investigation with care. While the other factors have less influence on the reliability.
- For the ACI, using a reduction coefficient of 0.7 will increase the reliability to the target levels.

References

ACI-213 (2014) Guide for Structural Lightweight-Aggregate Concrete", ACI Committee 213, American Concrete Institute, Farmington Hills, Michigan, USA: ISBN: 978-0- 87031-897-9

ACI-318-19 (2019) ACI Committee 318. Building Code Requirements for Structural Concrete (ACI 318- 19) and Commentary on Building Code Requirements (ACI 318-19). Farmington Hills (MI): American Concrete Institute; 2019.

Alkhatib S, Deifalla A (2002) Reliability-based assessment and optimization for the two-way shear design of lightweight reinforced concrete slabs using the ACI and EC2. Case Stud Constr Mater 17(2022):e01209.

Alkhatib S, Deifalla A (2022) Punching shear strength of FRP-reinforced concrete slabs without shear reinforcements: a reliability assessment. Polymers 14:1743. https://doi.org/10.3390/pol ym14091743

Deifalla A (2020a) Design of lightweight concrete slabs under two-way shear without shear reinforcements: A comparative study and a new formula. Eng Struct 222(2020):111076

Deifalla A (2020b) Torsion Design of Lightweight Concrete Beams without or with Fibers: a comparative study and a refined cracking torque formula. Structures 28(2020):786–802. https://doi.org/10.1016/j.istruc.2020.09.004

Deifalla A (2020c) Strength and Ductility of Lightweight Reinforced Concrete Slabs under Punching Shear. Structures 27 (2020) 2329–2345; https://doi.org/10.1016/j.istruc.2020.08.002

Deifalla A (2021) A strength and deformation model for prestressed lightweight concrete slabs under two-way shear. Advances in Structural Engineering. 1–12. https://doi.org/10.1177/13694332211020408

Deifalla A, Awad A, AbdElrahman AA, Seleem H (2020a) Investigating the Behavior of Lightweight Foamed Concrete T-Beams under Torsion, shear, and Flexure. Eng Struct 219(2020):110741. https://doi.org/10.1016/j.engstruct.2020.110741

Deifalla A, Awad A, Seleem H, AbdElrahman A (2020b) Experimental and numerical investigation of the behavior of LWFC L-girders under combined torsion. Structures 2020; 26 (2020): 362–77, https://doi.org/10.1016/j.istruc.2020.03.070

Ditlevsen O, Bjeragger P (1986) Methods of structural system reliability. Struct Saf 3(3–4):195–229

El-Gamal S, El-Salakawy E, Benmokrane B (2005) Behavior of concrete bridge deck slabs reinforced with fiber-reinforced polymer bars under concentrated loads. ACI Struct J 102:727–735

EC2 (1990) Eurocode 2: Design of concrete structures – Part 1–1: General rules and rules for buildings. Incl. Corrigendum 1: EN 1992-1-1:2004/AC:2008, incl. Corrigendum 2: EN 1992-1-1:2004/AC:2010, incl. Amendment 1: EN 1992- 1:2004/A1

EN (1990:2002 + A1:2005 + A1:2005/AC:2010) (2002) Eurocode: Basis of Structural Design. CEN European Committee for Standardization

Greene G, Graybeal B (2015) Lightweight Concrete: Shear Performance. Report No. FHWA-HRT-15-022. Washington, DC: Federal Highway Administration, p 20

Joint Committee on Structural Safety (2001) JCSS Probabilistic Model Code. https://www.jcss-lc.org

Ju M, Ju J-W, Sim J (2021) A new formula of punching shear strength for fiber reinforced polymer (FRP) or steel reinforced two-way concrete slabs. Compos Struct 259 (2021) 113471

Mahongo Dithinde (2007) Characterization of Model Variability for Reliability-Based Design of Pile Foundations. Stellenbosch University http://scholar.sun.ac.za

Mallor C, Calvo S, Nunez J L, Rodriguez R (2020). A. Full second order approach for expected value and variance prediction of probabilistic fatigue crack growth life. Int J Fatigue 133:105454

Ricker M, Feiri T, Nille-Hauf K, Adam V, Hegger J (2021) Enhanced reliability assessment of punching shear resistance models for flat slabs without shear reinforcement. Eng Struct 226(2021):111319

Sousa H, Sørensen JD, Kirkegaard PH (2010) Reliability Analysis of Timber Structures through NDT Data Upgrading: Short Term Scientific Mission, COST E55 Action. Department of Civil Engineering, Aalborg University, DCE Technical reports No, p 96

Sykora M, Holicky M, Prieto M, Tanner P (2014) Variabilities in resistance models for sound and corrosion-damaged RC structures according to EN 1992-1-1. Mater Struct. https://doi.org/10.1617/s11527-014-0409-1

Chapter 2
Evaluation of Damage Caused by Soil Settlements in a Historical Masonry Building

Ali Fuat Genç, Ahmet Can Altunışık, and Esin Ertürk

Abstract Masonry structures, characterized by their brittle behavior, are susceptible to easy damage when subjected to external forces. Especially, soil-structure interaction problems are important factors which may cause deterioration or complete loss of structural integrity in the masonry structures. For this reason, different settlements and deformations occurred in the soil domain should be considered in numerical analyses of this type structures for a correct structural assessment. The objective of this paper is to ascertain the modal response and assess the damage condition of an authentic historical masonry building, the deterioration of which can be attributed to underlying soil issues. The structure is a historical masonry school building which is constructed in the 1870s in Samsun, Turkey. The numerical evaluation encompasses the creation of a numerical model that takes into account the soil-structure interaction. This model is then utilized to gauge the impact of soil settlements on dynamic properties, and to scrutinize the state of damage through nonlinear explicit analyses.

2.1 Introduction

Concrete, steel, and other modern materials have become commonplace in construction today; however, in the past, structures predominantly arose from raw or minimally treated elements such as stone, brick, adobe, and wood. These edifices, now referred to as historical buildings, were erected using the masonry construction method. Despite their simplicity in composition, grasping the authentic behaviors

A. F. Genç · A. C. Altunışık (✉)
Department of Civil Engineering, Karadeniz Technical University, Trabzon, Turkey
e-mail: ahmetcan8284@hotmail.com

E. Ertürk
Department of Civil Engineering, Yalova University, Yalova, Turkey

of these historical masonry structures often proves intricate due to the non-uniform and anisotropic characteristics of the materials (Altunisik et al. 2017). Consequently, safeguarding these structures presents an intricate endeavor demanding expertise and profound knowledge.

Numerous historical masonry structures have withstood the test of time, with some still standing strong today. Nevertheless, a multitude of these historical marvels have succumbed to demolition or deterioration across the years, owing to both natural elements and human interventions (Parisi and Augenti 2013). Such structures are susceptible to various forces including earthquakes, floods, fires, conflicts, and vandalism, leading to damages, as well as gradual material degradation, soil settling, time-induced wear and tear, and excessive, irregular loads due to unsuitable application (Toker and Ünay 2004). Characterized by meager tensile strength, historical masonry structures were engineered primarily to counter compressive stresses (Angelillo et al. 2014; Lourenço 1998).

Therefore, they are very vulnerable to actions that lead tensile stresses on the masonry walls such as seismic and soil settlement conditions. A wall subjected to tensile stress is easily damaged by mortar joints which have low tensile strength (Bui 2013; Fathyi et al. 2009; Nasser et al. 2014). Therefore, protection measures should be taken for historical structures against such effects.

Errors of foundation design, liquefaction, soil bearing capacity problems and horizontal displacements may cause soil settlement. Furthermore, the primary factors contributing to settlement encompass fluctuations in groundwater levels, alterations in the structural loading system, excavations conducted in the vicinity of the structure, dynamic forces, and vibrations. Settlement problem leads cracks, rotations, and different damage in the structure. Masonry walls are very sensitive to the smallest foundation settlement as they exhibit a brittle behavior.

In the literature, there are different approach for the damage assessment of historical structures. Rigid base approach does not consider the soil domain in the damage assessment of historical structures (Milani and Valente 2015; Llopis-Pulido et al. 2019; Valente and Milani 2016; Lazizi and Tahghighi 2019; Altıok and Demir 2021). On the other hand, soil domain is considered in the substructure approach, but structure and soil are modeled separately and structure work independently of the soil model (Mylonakis et al. 2006; Wolf 1985; NEHRP 2012; Gazetas 1991). This approach with a flexible support enables the differential soil settlement condition could be applied. Springs are modelled as not to resist tension. In this condition, the settlement is allowed in the structure and damage due to settlement can be achieved (Longo et al. 2021; Brunelli et al. 2021; Anastasios et al. 2020). On the other hand, studies on the detection of damages caused by soil settlements in historical masonry structures using the soil-structure interaction (direct approach) are rare in the literature (Kujawa et al. 2020).

The objective of this study is to assess the modal response and analyze the damage condition of an actual historical masonry building, the deterioration of which can be attributed to underlying soil-related issues. The structure is a historical masonry school building which is constructed in the 1870s in Samsun, Turkey. The numerical evaluation encompasses the creation of a finite element model that takes into account

direct soil-structure interaction. This model is then utilized to gauge the impact of soil settlements on dynamic properties, and to scrutinize the state of damage through nonlinear explicit analyses.

2.2 Description of the Historical Building

The subject of inquiry in this study is a historic edifice situated in Samsun, Turkey, which was erected during the 1870s. Originally functioning as both an infirmary and a dormitory, the building underwent a transformation in its history and was repurposed into a school. Notably, the passage of time took its toll on the structure, resulting in substantial damage and the deterioration of key structural components such as doors, windows, floors, and the roof. In the 1970s, a partial fire incident prompted restorative efforts to mend the impaired sections.

Comprising a rectangular layout, the building encompasses three levels: a basement, a ground floor, and a standard floor. Its total vertical extent measures 14.3 m, with the first floor at 2.64 m, the second at 4.26 m, and the third at 4.59 m. The structural support system of the building is characterized by a load-bearing masonry framework, fashioned using brick materials. Within the standard storey, interior walls were introduced as timber frames. Wall thickness is approximately 0.7 m at the basement level, while higher sections exhibit varying thicknesses ranging from 0.45 to 0.60 m. Timber elements were used for the construction of the slabs and roof system. Visual representations and façade depictions of the building can be observed in Fig. 2.1.

2.3 Numerical Model of the Building

The construction of the Finite Element (FE) models for the building was carried out using the Abaqus software (Abaqus 2016). These models took into consideration the soil domain to account for diverse settlements, shifts, and distortions in the foundation arising from alterations in soil properties. Employing the macro modeling technique, the FE models were developed using linear tetrahedral finite elements, specifically the C3D4 element with four nodes, across the entirety of the soil-structure system. The dimensions of the encompassing soil domain were established as 24 by 36 m. To ensure stability, fixed boundary conditions were enforced upon the soil domain. The FE representation of the integrated soil-structure system is illustrated in Fig. 2.2.

Extracting material samples from the walls for material testing to ascertain material properties is not allowed due to regulatory measures protecting historical structures. Consequently, the material characteristics of the brick masonry walls were determined by consulting a specialized guideline titled "Earthquake Risk Management Guide for Historical Buildings" (General Directorate for Foundations 2017), designed for evaluating historical structures. Furthermore, the Concrete Damage

(a)

South view   West view

North view   East view
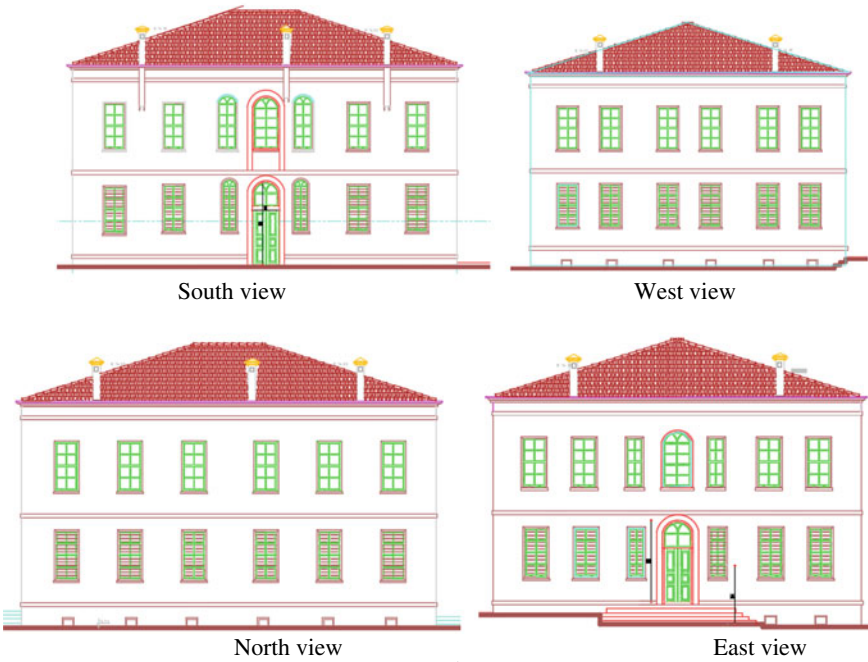
(b)

Fig. 2.1 Views of the building
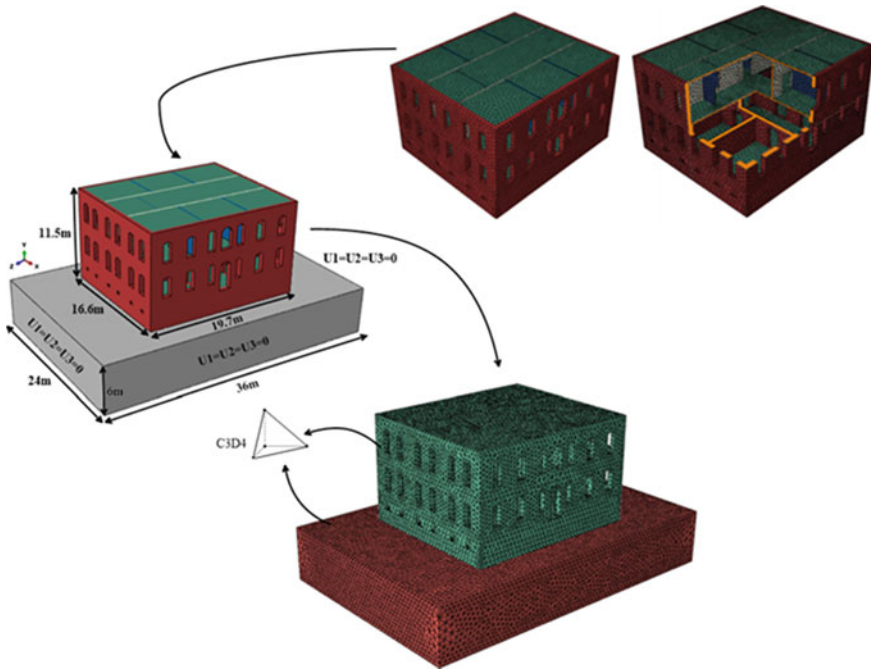
Fig. 2.2 Views of the numerical model with soil-structure system

Plasticity (CDP) model, adept at accommodating masonry structures, was employed to characterize the nonlinear material behavior of the masonry units (Lubliner et al. 1989; Lee and Fenves 1998). The tables containing the chosen linear and nonlinear material properties for the analysis can be found in Tables 2.1, 2.2, and 2.3 (General Directorate for Foundations 2017; Tiberti et al. 2016).

In the literature, soil-structure interaction (direct approach) is rare considered in damage assessment studies caused by soil settlements in historical structures. Generally, substructure approach is preferred over soil-structure interaction (direct approach). In this paper, rare approach in the literature was used to detection of

Table 2.1 The linear elastic parameters used in the numerical model (General Directorate for Foundations 2017)

Elements	Young's modulus (N/m^2)	Poisson ratio (–)	Material density (kg/m^3)
Masonry	1.8E9	0.2	1800

Table 2.2 CDP model parameters (Tiberti et al. 2016)

Material	Dilation angle	Eccentricity	f_{b0}/f_{c0}	K_c	Viscosity parameter
Stone	10	0.1	1.16	0.666	0.002

Table 2.3 Stress–strain values and damage parameters of the masonry (Tiberti et al. 2016)

Compression		Tension		Tensile damage parameters	
σ (MPa)	ε^{pl}	σ (MPa)	ε^{pl}	d_t	ε_t^{pl}
1.22	0	0.04	0	0	0
0.95	0.005	0.0005	0.003	0.95	0.003
0.95	0.001	0.0005	0.1		
0.8	0.1	–	–		

numerical damages of historical masonry school building caused by soil settlement. Therefore, the FE model of the soil domain was considered, and the elasticity module and density of the soil domain were changed to represent the damage to building due to the soil settlement. To achieve this aim, soil domain was tried to represent with a softer soil condition. The soil medium were progressively weakened. The soil domain conditions is shown in Fig. 2.3.

Soil	Modulus of Elasticity (N/m²)	Poisson Ratio (-)	Density (kg/m³)
	5.68E+9	0.30	2064
	3.45E+7	0.40	1667
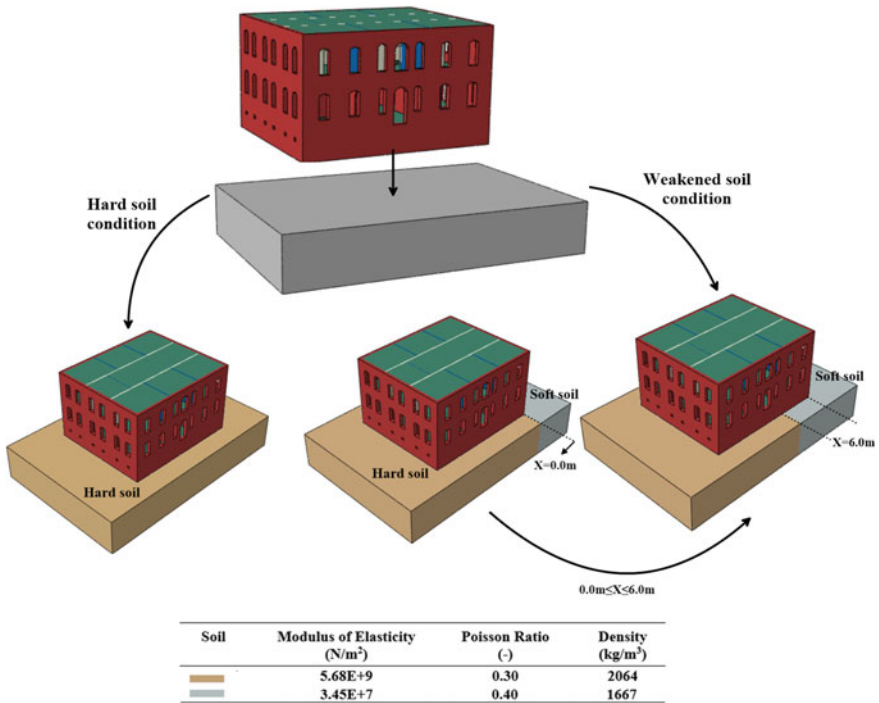
Fig. 2.3 Views of numerical models for the soil-structure system and soil properties

Table 2.4 Comparison of natural frequencies

		Frequency (Hz)		
		f_1	f_2	f_3
Hard soil condition		7.596	8.528	9.154
SSI system	Z = 0 m	7.579	8.478	9.141
	Diff. (%)	*8.63*	*8.37*	*5.40*
	Z = 2 m	6.925	7.768	8.647
	Diff. (%)	*4.27*	*9.71*	*3.55*
	Z = 4 m	6.629	7.014	8.340
	Diff. (%)	*5.08*	*7.86*	*0.04*
	Z = 6 m	6.292	6.463	8.337

2.4 Numerical Analyses

2.4.1 Modal Response

This section pertains to the vibration response of the building, focusing on scrutinizing the influence of varied settlements, shifts, and deformations at the foundation due to the deterioration of soil properties on both mode shapes and frequencies—integral dynamic attributes of the structure. Through modal analysis, the mode shapes and natural frequencies were extracted. A comparative overview of the natural frequencies is presented in Table 2.4. Furthermore, mode shapes of the building are given in Fig. 2.4. Across all scenarios, the mode shapes were identified as transverse, longitudinal, and torsional modes. Both Table 2.4 and Fig. 2.4 highlight the discernible trend of frequency reduction with increasing distances of soil weakening.

2.4.2 Damage Condition

Geometrically nonlinear analyses were conducted to discern the impact of soil settlement and the resulting structural damage to the building. During the analyses only the self-weight of the building was considered. As a result of the analysis, the displacement values in the Z direction were examined to determine the out-of-plane behavior in the part of the structure where the ground weakening is made. Deformed and undeformed shapes of the building in the Z direction for hard soil and weakened soil conditions are given in Fig. 2.5. Also, the maximum values of these contour diagrams are given in Table 2.5. As seen in Fig. 2.5 and Table 2.5, the higher displacement values obtained in weakened soil condition according to hard soil. In addition, an increase in displacement values was observed as the weakened soil distance increased. From this point of view, it can be concluded that the deformations occurred in the soil and structure will also increase as the distance of the weakened soil increases.

Hard soil condition		
f_1=7.596Hz	f_2=8.528Hz	f_3=9.154Hz

Weakened soil condition		
f_1=7.579Hz	f_2=8.478Hz	f_3=9.141Hz

H=0.0m

f_1=6.925Hz	f_2=7.768Hz	f_3=8.647Hz

H=2.0m

f_1=6.629Hz	f_2=7.014Hz	f_3=8.340Hz

H=4.0m

f_1=6.292Hz	f_2=6.463z	f_3=8.337Hz

H=6.0m
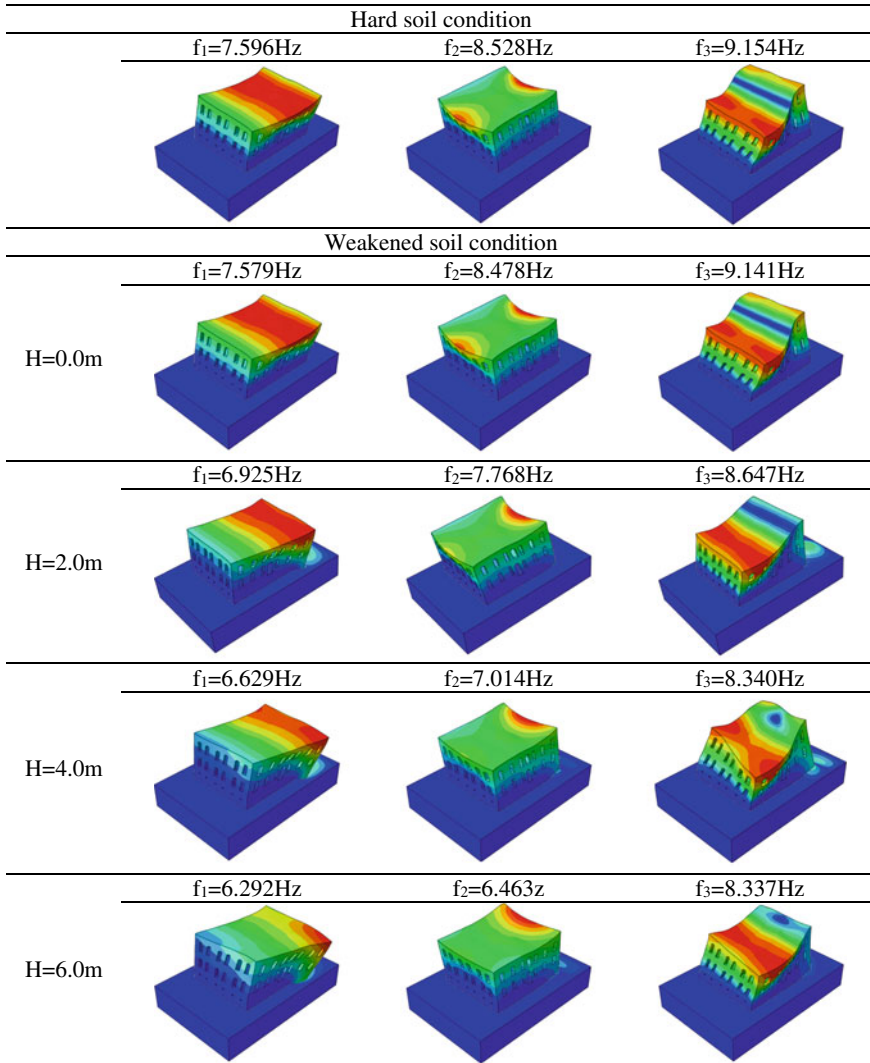
Fig. 2.4 Mode shapes of the building

The damages, which can be occurred based on different settlements, slips and deformations at the foundation due to the weakening of soil properties, were explained with tensile damage. Tension damage results for SSI systems are given in Fig. 2.6. The number of damaged elements obtained numerical analyses are given in Table 2.6. It should be noted from the Table 2.6 and Fig. 2.6 that the building is almost undamaged in hard soil condition and 0 m of weakened soil condition. On the other hand, cracks occurred, and the number of damaged elements increased as

(a) Hard soil condition

Z=0m

Z=2m

Z=4m

Z=6m

(b) Weakened soil condition
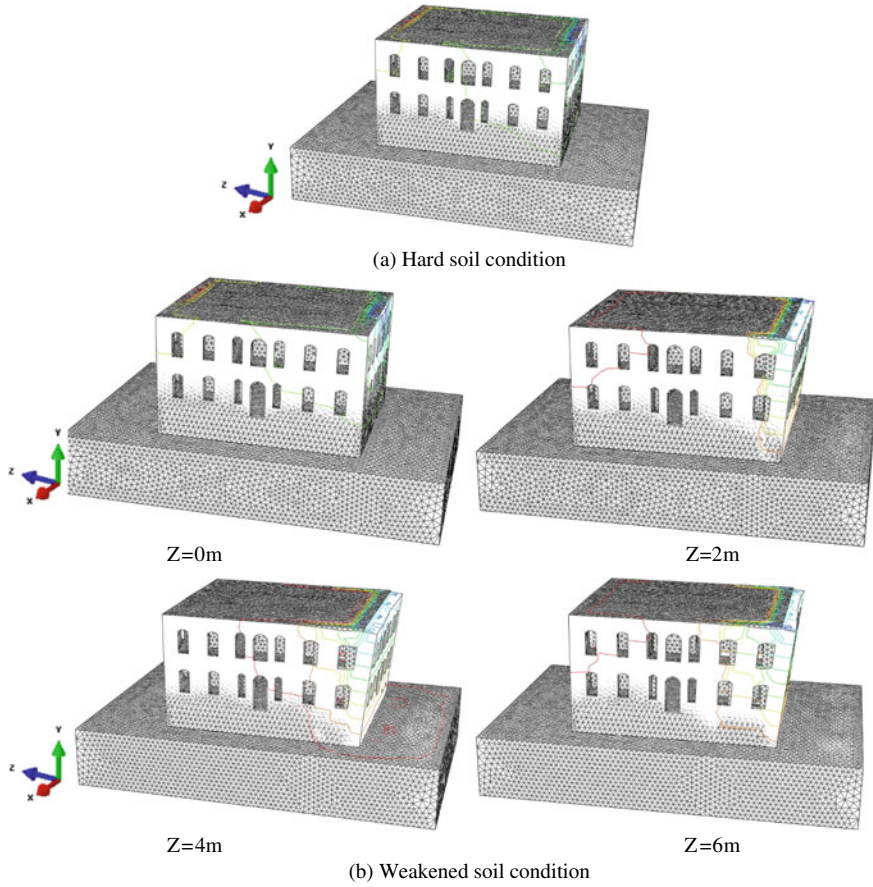
Fig. 2.5 Deformed and undeformed shape of the building in the Z direction for **a** hard soil and **b** weakened soil condition

Table 2.5 The comparison of the maximum displacements

		Max. displacement (m)
		Z Direction
Hard soil condition		0.0057
Weakened soil condition	X = 0.0 m	0.0064
	Diff. (%)	*80*
	X = 2.0 m	0.032
	Diff. (%)	*3.03*
	X = 4.0 m	0.033
	Diff. (%)	*5.71*
	X = 6.0 m	0.035

weakened soil distance increased. The structural damages occurred window openings and roof joints. The number of damaged elements constitutes 0.53% of the total number of elements in the hard soil condition. On the other hand, percentage of damaged elements are 0.54%, 1.20%, 1.70% and 2.23% for 0.0 m, 2.0 m, 4.0 m and 6.0 m of weakened soil condition, respectively.

(a) Hard soil condition

Z=0m   Z=2m

Z=4m   Z=6m

(b) Weakened soil condition
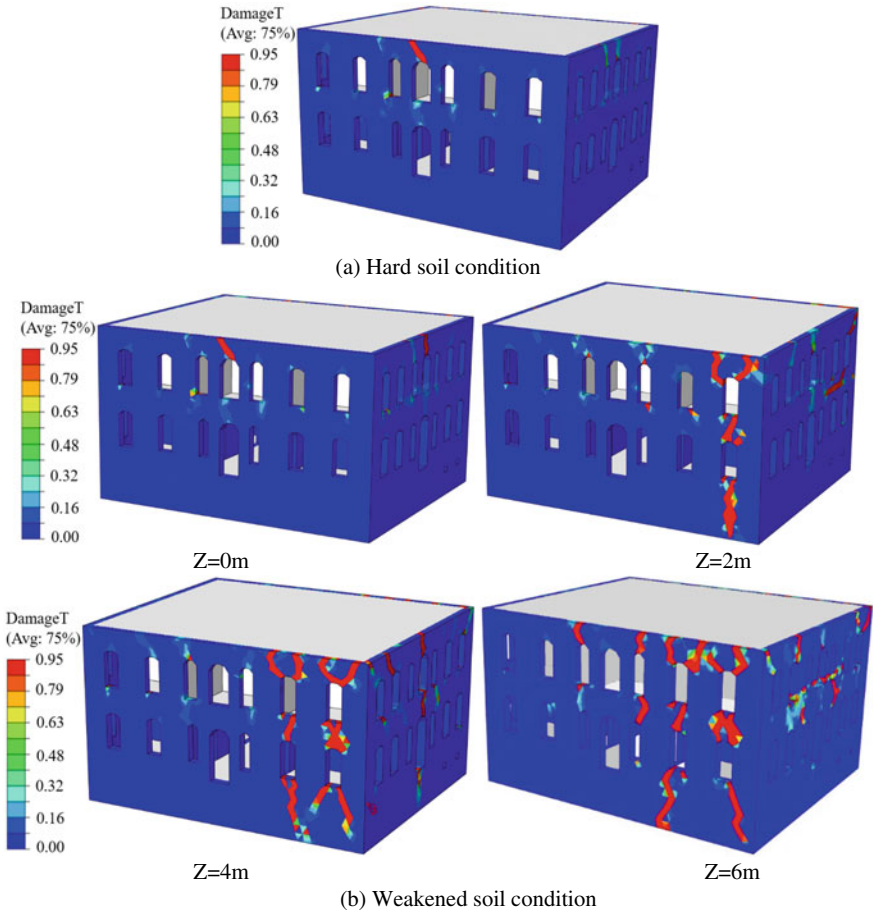
Fig. 2.6 Tension damage level for **a** hard soil and **b** weakened soil condition

Table 2.6 The amount of damaged elements and differences

SSI		Damaged elements	Diff.[a] (%)
Hard soil condition		429	0.53
Weakened soil condition	Z = 0 m	437	0.54
	Z = 2 m	964	1.20
	Z = 4 m	1366	1.70
	Z = 6 m	1788	2.23

[a] Diff. were calculated based on total number of elements (80,338)

2.5 Conclusion

In this paper, modal response and damage condition of a real historical masonry building which was damaged due to soil problems were investigated. The conclusion of this study is given the below;

- The initial three natural frequencies were identified as transverse, longitudinal, and torsional modes across all Soil-Structure Interaction (SSI) configurations. Notably, higher frequency values were recorded in scenarios with robust soil conditions compared to those with compromised soil conditions. Furthermore, it was observed that frequency values exhibited a decrease as the distance of soil weakening expanded.
- The higher displacement values obtained for weakened soil condition according to hard soil in Z direction. Also, an increase in displacement values were observed as the weakened soil distance increased. Differences between maximum displacement values changes from 3.03% to 80%
- The building is almost undamaged in hard soil condition and 0 m of weakened soil condition. The number of elements, which reaches damage parameter, 0.53% and 0.54% for these conditions. So, the building can be considered almost undamaged. On the other hand, percentage of damaged elements are 1.20%, 1.70% and 2.23% for 2.0 m, 4.0 m and 6.0 m of weakened soil condition, respectively. It was observed that cracks occurred and the number of damaged elements increased as weakened soil distance increased.
- The main structural damages occurred near the window openings.

In this paper, proposed approach is a rare approach specified in the literature. However, it makes it possible to consider different soil settlements by modeling the soil domain in finite element models. Especially, considering soil settlements is important in the evaluation of the structural behavior of the historical masonry structures. Because, historical masonry structures are very sensitive to the a smallest soil settlement as they exhibit a brittle behavior.

References

Abaqus (2016) Dassault syst'emes simulia corp. Providence: Rhode Island, USA

Altıok TY, Demir A (2021) Collapse mechanism estimation of a historical masonry minaret considered soil-structure interaction. Earthq Struct 21(2):161–172

Altunisik AC, Adanur S, Genc AF, Gunaydin M, Okur FY (2017) An investigation of the seismic behaviour of an ancient masonry bastion using non-destructive and numerical methods. Exp Mech 57(2):245–259

Anastasios D, Verstrynge E, Szekér P, Heirman G, Bejarano-Urrego E, Giardina G, Van Balen K (2020) Numerical modeling of a church nave wall subjected to differential settlements: soil-structure interaction, time-dependence and sensitivity analysis. Int J Arch Herit 14(8):1221–1238

Angelillo M, Lourenço PB, Milani G (2014) Mechanics of masonry structures masonry behavior and modeling. CISM Int Cent Mech Sci 551:1–26

Brunelli A, De Silva F, Piro A, Parisi F, Sica S, Silvestri F, Cattari S (2021) Numerical simulation of the seismic response and soil–structure interaction for a monitored masonry school building damaged by the 2016 Central Italy earthquake. Bull Earthq Eng 19:181–1211

Bui TT (2013) Étude expérimentale et numérique du comportement des voiles en maçonnerie soumis à un chargement hors plan. PhD INSA Lyon France

Fathyi AM, Planas J, Sancho MA (2009) Numerical study of masonry cracks. Eng Fail Anal 16:675–689

Gazetas G (1991) Formulas and charts for impedances of surface and embedded foundations. J Geotech Eng 117:9

General Directorate for Foundations (2017) Guide to the management of earthquake risks of historical structures. Ankara, Turkey

Kujawa M, Lubowiecka I, Szymczak C (2020) Finite element modelling of a historic church structure in the context of a masonry damage analysis. Eng Fail Anal 107:104233

Lazizi A, Tahghighi H (2019) Seismic Response Evaluation of Kashan Historical Bazaar Structure Including Soil-Structure Interaction. J Seism Earthq Eng 21(3):77–93

Lee J, Fenves GL (1998) A plastic-damage concrete model for earthquake analysis of dams. Earthq Eng Struct Dyn 27(9):937–956

Llopis-Pulido V, Durá AA, Fenollosa E, Martínez A (2019) Analysis of the structural behavior of the historical constructions: Seismic evaluation of the Cathedral of Valencia (Spain). Int J Arch Herit 13(1):205–214

Longo M, Sousamli M, Korswagen PA, Van Staalduinen P, Rots JG (2021) Sub-structure-based 'three-tiered' finite element approach to soil-masonry-wall interaction for light seismic motion. Eng Struct 245:112847

Lourenço PB (1998) Experimental and numerical issues of the mechanical behaviour of masonry. In: Roca P, González JL, Oñate E, Lourenço PB (eds) Structure analysis of historical constructions II CIMNE, Barcelona

Lubliner J, Oliver J, Oller S, Oñate E (1989) A plastic-damage model for concrete. Int J Solids Struct 25(3):299–326

Milani G, Valente M (2015) Failure analysis of seven masonry churches severely damaged during the 2012 Emilia-Romagna (Italy) earthquake: non-linear dynamic analyses vs conventional static approaches. Eng Fail Anal 54:13–56

Mylonakis G, Nikolaou S, Gazetas G (2006) Footings under seismic loading: analysis and design issues with emphasis on bridge foundations. Soil Dyn Earthq Eng 26(9):824–853

Nasser H, Al Heib M, Deck O (2014) Influence of differential settlements on masonry structures. In :Conferance; computational modelling of concrete and concrete structures, pp 819–825

NEHRP (2012). Soil-structure interaction for building structures. NIST GCR 12-917-21 U. S. Department of Commerce National Institute of Standards and Technology

Parisi F, Augenti N (2013) Earthquake damages to cultural heritage constructions and simplified assessment of artworks. Eng Fail Anal 34:735–760. https://doi.org/10.1016/j.engfailanal.2013.01.005

Tiberti S, Acito M, Milani G (2016) Comprehensive FE numerical insight into Finale Emilia Castle behavior under 2012 Emilia Romagna seismic sequence: damage causes and seismic vulnerability mitigation hypothesis. Eng Struct 117:397–421

Toker S, Ünay A (2004) Mathematıcal modeling and finite element analysis of masonry arch bridges. Gazi Univ J Sci 17(2):24–25

Valente M, Milani G (2016) Non-linear dynamic and static analyses on eight historical masonry towers in the North east of Italy. Eng Struct 114:241–270

Wolf J (1985) Dynamic soil–structure interaction. Prentice Hall, Englewood Clif

Chapter 3
Critical Shear Crack Theory for Shear Strength of Elements Subjected to Tension or Reinforced with FRP

Faisal Mukhtar, Ahmed Awad, Amr El-Said, Mohamed Ahmed Salama, Taha Elsayed, Ahmed F. Deifalla⬤, and Maged Tawfik

Abstract Many factors have led to revisiting the old problem of shear, including the following: (1) the brittle and catastrophic failure of concrete elements under shear strength, which is a complex phenomenon; (2) the new material advancement, including and not limited to FRP reinforcements; (3) the limited number of rigorous models that exist for such a problem. In this communication, A series of research investigations are briefly described. These works attempted to provide an extended critical shear crack theory model (ECSCT) for a variety of shear situations, such as reinforced concrete using fiber-reinforced polymers (FRP). The critical shear crack theory (CSCT) was selected because it is the base for the new Euro-code. The CSCT is a pioneering mechanical model for both one-way and two-way shear of concrete elements. More than 1000 specimens evaluated under one-way shear were used to verify the ECSCT. Comparisons were made between the model strength predictions and current design codes. In comparison to previous design standards, the model is more accurate and consistent while still making physical sense.

F. Mukhtar
King Fahd University of Petroleum & Minerals, Dhahran 31261, Saudi Arabia

A. Awad
MSA, 6th of October, Egypt
e-mail: a.elsayed@sha.edu.eg

A. El-Said · M. A. Salama · M. Tawfik
HTE, El Shrouk, Cairo, Egypt
e-mail: m.nashaat@sha.edu.eg

M. A. Salama
e-mail: amosad@msa.edu.eg

T. Elsayed
Benha University in Egypt, Banha, Egypt
e-mail: taha.ibrahim@feng.bu.edu.eg

A. F. Deifalla (✉)
Future University in Egypt, New Cairo, Egypt
e-mail: Ahmed.deifalla@fue.edu.eg

Keywords Shear · FRP reinforced concrete · Tensile force · FRP · CSCT

3.1   Introduction

Design codes require logical models to solve this difficult shear problem. Concrete elements without stirrups have numerous mechanisms that contribute to their shear resistance, including the following: (1) Dowel shear through flexure reinforcements; (2) interface shear over the sidewalls of the fractured concrete; and (3) direct shear through the uncracked concrete. (Deifalla and Mukhtar 2022; Ebid and Deifalla 2021; El-Meligy et al. 2017; Deifalla 2021a; Muttoni 2008; Muttoni et al. 2018). Shear failure of concrete elements is sudden and could be catastrophic. The shear strength and deformation are influenced by several factors. The shear resistance is constrained by the size effect, although the flexure resistance is first increased by the effective depth. Second, the longitudinal reinforcement's geometrical ratio, which boosts strength as it grows, may cause a more brittle failure. Thirdly, the concrete's compressive strength prevents cracks by directly influencing the shear contribution or indirectly raising the concrete's tensile strength (Deifalla 2021b, 2020, 2022, 2021c, 2021d; Ali et al. 2021a).

Axial tension forces occur combined with shear in many situations. The effect of axial tensile forces on the shear strength of concrete elements lacks a physical base and does not cover all parameters or mechanisms (Deifalla and Mukhtar 2022). In a still-unexplored area of research, fiber-reinforced polymer (FRP)-reinforced concrete is becoming more and more popular as a viable solution. This is because it has superior benefits over traditional RC, such as being electrically neutral and non-corrosive, among others. However, compared to the steel reinforcements, which have an impact on other shear processes, the FRP mechanical characteristics are noticeably different (Deifalla and Mukhtar 2022).

As a result, there is a need to extend these mechanical models to special problems such as FRP-reinforced concrete and those subjected to combined shear and axial tension forces. Three mechanical models developed by Deifalla and colleagues (Deifalla and Mukhtar 2022; Deifalla and Mukhtar xxxxa, b) are briefly outlined in this current study, where the Critical Shear Crack Theory (CSCT) was adapted and further extended to shear of various problems. The (ECSCT) was validated using over 700 tested elements under shear and validated by comparison with existing design codes.

3.2   (CSCT) The Critical Shear Crack Theory

The CSCT is based on correlating the crack width of the critical diagonal crack (w) and the shear strength. The shear strength of the RC element is governed by the development of a critical diagonal shear crack, which is the main theory assumption.

This critical crack governs the all parameters in terms of location, kinematics, and shape as shown in Table 3.1 include the details and test results for the experimental concrete beams, Moreover, the critical shear crack's opening must be proportionate to the effective depth in a control section multiplied by the longitudinal strain. Based on this, the shear forces can be carried by various shear-transfer actions, namely, the residual tensile strength of the cracked concrete V_{Res}, the role of aggregate interlock brought on by crack sliding V_{Agg}, the dowelling action of the longitudinal reinforcement crossing the crack V_{Dowel}, and the contribution of the inclination of the compression chord V_{Compr} shown in Fig. 3.1. To achieve this, the integration of appropriate constitutive material laws is required. The capacity of the section is given by Eq. (3.1) as the summation of all these actions.

$$V_R = \sum_{i=1}^{4} V_i = \frac{V_{Res} + V_{Agg} + V_{Dowel}}{1 - \cdot h_F / r_F} \tag{3.1}$$

This work is inspired by the CSCT (Muttoni 2008; Muttoni et al. 2018), where the shear strength (v_u) is calculated such that:

$$\frac{v_u}{\sqrt{f_c'}} = f(\omega, d_{dg}) \tag{3.2}$$
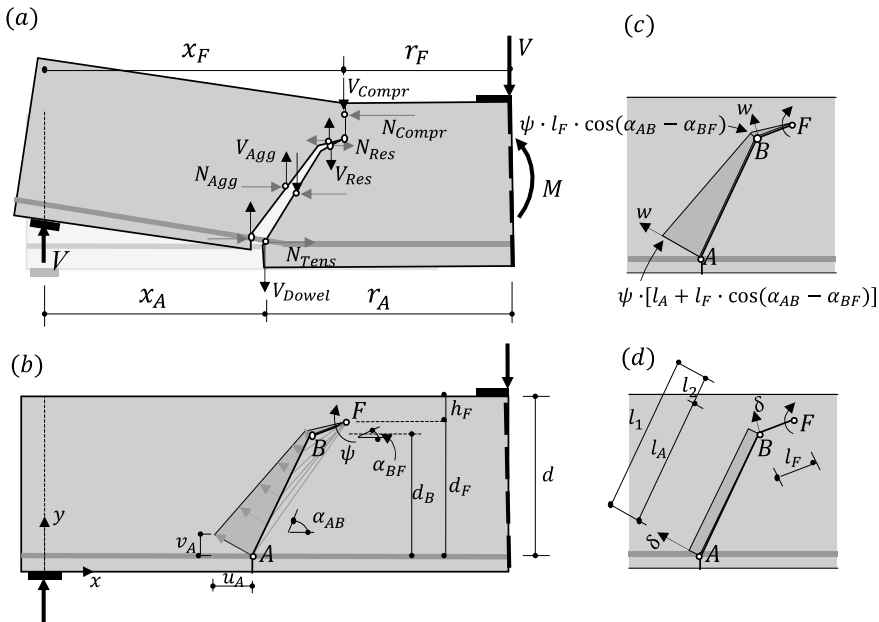
Fig. 3.1 The CSCT (Muttoni et al. 2018)

While d_{dg} is the maximum nominal aggregate size, $f_c^{'}$ is the compressive strength of cylinder, and ω is the Crack width.

$$\omega \propto \varepsilon d \tag{3.3}$$

where V is the shear strength, where ε longitudinal strain, which is determined from severe compression fibers at 60% of the effective depth (d) (Muttoni 2008; Muttoni et al. 2018).

$$\frac{v_u}{\sqrt{f_c}} = \frac{\alpha_1}{1 + \alpha_2 \frac{\varepsilon d}{d_{dg}}} \tag{3.4}$$

$$\varepsilon = \frac{M}{bd\rho_f E_s(d - c/3)} \frac{0.6d - c}{d - c} \tag{3.5}$$

$$c = d \cdot \rho_s \cdot \frac{E_s}{E_c}\left(\sqrt{1 + \frac{2E_c}{\rho_f \cdot E_s}} - 1\right) \tag{3.6}$$

where, $v_u = \frac{V}{bd}$ is the nominal shear strength, V the shear force resisted by the section (at failure, $V = V_R$ and $v_u = v_{uR}$), $d_{dg} = d_{g0} + d_g$ (the value of the reference aggregate size $d_{g0} = 16mm$ is used), d_g the nominal aggregate size, E_s the steel Young's modulus, E_c the concrete Young's modulus, d the effective depth, ρ_s the steel reinforcement ratio, ε the longitudinal strain at a critical section, c the depth of the centroid to the compression block, $\alpha_1 = \frac{1}{3}$ and $\alpha_2 = 120$ for the traditional CSCT whose success has been verified based on an experimental database of 269 majority steel-RC slender beams. Using the failure criterion given by Eq. (3.4) along with the strain ε—Eq. (3.5)—at critical section yields a quadratic relationship whose solution is the shear strength V. In other words, as illustrated in Fig. 3.2, the inter section between this failure criterion and the strain—that describes the load deformation response—is the solution for the section's capacity in shear.

3.3 ECSCT for FRP-Reinforced Slender Elements Under Shear

Table 3.2 shows the details and test results for the experimental for FRP-concrete elements, the performance of the original CSCT has been mainly demonstrated as good in the case of the steel-RC members, as shown in Fig. 3a. However, it demonstrated no such behavior for FRP-RC elements, as shown in Fig. 3b. In addition, the correlation coefficient (r) between the experimental shear strengths and the parameter $\frac{\varepsilon d}{d_{g0}+d_g}$ is indicated in the figures. The performance of the CSCT in steel-RC is consistent with the coefficient of correlation $r = 0.481$, while for FRP-RC elements, the correlation coefficient is 0.144, as indicated in Fig. 3b. Therefore, the CSCT

Table 3.1 Specimens database

Spec. name	Ref.	Width (mm)	Depth (mm)	Rft. ratio (%)	Steel Yield strength (MPa)	Compressive Strength (MPa)	a/d (–)	Shear Force (kN)	Normal Force (kN)
9	Elstner	175	284	0.41	343.4	23	3.69	19.68	86
10		175	284	0.41	343.4	23	3.69	24.13	68
4	Mattock	152	254	1.03	399.9	46	3	44.48	29
5		152	254	2.07	399.9	16	3	33.36	29
11		152	254	3.10	399.9	15	3	42.26	61
16		152	254	1.03	399.9	30	5.4	28.02	48
19		152	254	2.07	399.9	19	5.4	40.03	29
20		152	254	2.07	399.9	48	5.4	57.83	29
21		152	254	2.07	399.9	51	5.4	56.93	61
23		152	254	3.10	399.9	19	5.4	42.26	29
25		152	254	3.10	399.9	28	5.4	51.15	48
26		152	254	1.00	399.9	29	5.4	42.26	80
29		152	254	3.10	399.9	53	5.4	66.72	29
A1T	Haddadin	178	381	3.78	517.3	28	2.5	122.55	144
C1T		178	381	3.78	517.3	29	3.38	120.21	144
J1T		178	381	3.78	517.3	29	2.5	87	144
N3	Regan	152	272	1.46	427	33	2.8	42	120
N4		152	272	1.46	427	34	2.8	42	90
N5		152	272	1.46	427	32	2.8	48	60
N6		152	272	1.46	427	32	2.8	50	70
N7		152	272	1.46	427	35	2.8	45	130
N9		152	272	1.46	427	31	2.8	42	85
N11		152	272	0.97	427	33	2.8	37	75
N12		152	272	1.46	628	28	5.61	48	30
N13		152	272	1.46	628	31	5.61	50	40
N14		152	272	1.46	427	31	2.8	50	40
N15		152	272	1.46	427	32	2.8	50	20
N16		152	272	1.46	628	31	1.96	52	40
N18		152	272	1.46	427	31	2.8	45	60
N19		152	272	1.46	427	29	2.8	40	80
N20		152	272	1.46	427	46	2.8	42	60
N21		152	272	1.46	427	15	2.8	40	60
N22		152	272	1.46	427	32	1.96	85	60
N23		152	272	1.46	427	35	1.96	75	20
N24		152	272	1.46	427	22	2.8	37	60

Table 3.1 (continued)

Spec. name	Ref.	Width (mm)	Depth (mm)	Rft. ratio (%)	Steel Yield strength (MPa)	Compressive Strength (MPa)	a/d (–)	Shear Force (kN)	Normal Force (kN)
M5	Leonhardt	760	250	0.40	602	21	4	137.3	295
M6		760	250	0.50	643	27	4	137.3	393
T4	Soresen	200	262	1.80	534	53	2.5	94	327
T5		200	262	1.80	534	53	2.5	81.9	439
T6		200	262	1.80	534	53	2.5	126.5	223
PB4	Bhide	70	890	1.10	423	16	N/A	72.3	72
PB6		70	890	1.10	425	17	N/A	71.6	72
PB7		70	890	1.10	425	20	N/A	53.6	102
PB8		70	890	1.10	425	20	N/A	49.2	148
PB10		70	890	1.10	425	24	N/A	34.9	148
PB16		70	890	1.10	502	42	N/A	90.3	181
PB14		70	890	2.00	489	42	N/A	95.9	288
PB17		70	890	2.00	502	25	N/A	76	449
PB19		70	890	2.00	402	20	N/A	79.7	80
PB20		70	890	2.00	411	22	N/A	88.5	177
PB28		70	890	2.00	424	23	N/A	95.3	191
PB21		70	890	2.00	426	22	N/A	88.5	274
PB22		70	890	2.00	402	18	N/A	64.2	392
PB29		70	890	2.00	433	42	N/A	92.8	186
PB30		70	890	2.00	496	40	N/A	92.2	277
PB31		70	890	2.00	496	43	N/A	71.6	422
ZS2	Saul	600	164	4.00	500	40	3.05	356	1200
P1	Emrich	600	178	0.20	477	35	3.82	92	60
P2		600	178	0.20	477	35	3.82	92	60
P3		600	178	0.20	477	43	3.82	92	60
P4		600	178	0.60	506	43	3.82	92	60
P5		600	178	0.60	506	35	3.82	92	60
ST9	Adebar	290	278	1.95	536	46	3.6	69.9	280
ST10		290	278	1.95	536	46	3.6	65.6	525
ST11		290	278	1.95	536	46	3.6	65.6	776
ST12		290	278	1.95	536	46	3.6	47.1	1507
ST13		290	278	1.95	536	46	3.6	65.6	1050
ST25		290	278	1.00	484	59	3.6	82	165
ST26		290	278	1.00	484	59	3.6	58.9	191
S1	Tamura	80	204	0.87	356.5	37	2	32.75	30

Table 3.1 (continued)

Spec. name	Ref.	Width (mm)	Depth (mm)	Rft. ratio (%)	Steel Yield strength (MPa)	Compressive Strength (MPa)	a/d (–)	Shear Force (kN)	Normal Force (kN)
S2		80	204	0.87	356.5	37	2	28.85	50
S3		80	204	0.87	356.5	37	2	27.95	60
S4		80	204	0.87	356.5	37	2	23.85	70
S5		80	204	0.87	356.5	37	2.5	27	30
S6		80	204	0.87	356.5	37	2.5	23.8	50
S7		80	204	0.87	356.5	37	2.5	23.35	60
S8		80	204	0.87	356.5	37	2.5	22.3	70
S10		100	204	1.26	356.5	37	2	30.03	20
S11		100	204	1.26	356.5	37	2	24.34	30
S12		100	204	1.26	356.5	37	2	23	40
S14		100	204	1.26	356.5	37	2.5	24.15	20
S15		100	204	1.26	356.5	37	2.5	19.42	30
S16		100	204	1.26	356.5	37	2.5	15.43	40
A1	Ehmann	400	250	1.60	579	47	3	150	450
A2		400	250	1.60	579	47	3	146.6	340
A2'		400	250	1.60	579	47	5	122.9	340
A3		400	250	1.60	579	49	3	119.8	560
A3'		400	250	1.60	579	49	5	124.5	560
A4		400	250	2.50	559	49	3	162.5	340
A4'		400	250	2.50	559	49	5	134.1	340
A5		400	250	1.00	585	49	3	146.3	340
B2		400	250	2.00	558	46	3	122.5	200
B3		400	250	2.00	558	46	3	164.4	400
B3'		400	250	2.00	558	46	5	132.7	400
B4		400	250	2.00	558	46	3	109.8	600
B4'		400	250	2.00	558	46	5	125.2	600
B5		400	250	2.00	558	48	3	139.4	800
B5'		400	250	2.00	558	48	5	113.3	800
B6		400	250	1.00	572	46	3	137.3	200
B7		400	250	1.60	546	44	3	144.6	200
B7'		400	250	1.60	546	44	5	109	200
B8		400	250	2.50	570	45	3	150.2	200
B9		400	250	2.80	566	45	3	150.8	200
B9'		400	250	2.80	566	45	5	143.6	200
B10		400	250	1.00	572	48	3	94.1	600

(continued)

Table 3.1 (continued)

| Spec. name	Ref.	Width (mm)	Depth (mm)	Rft. ratio (%)	Steel Yield strength (MPa)	Compressive Strength (MPa)	a/d (–)	Shear Force (kN)	Normal Force (kN)
B11		400	250	1.60	546	47	3	160.1	600
B11'		400	250	1.60	546	47	5	126.3	600
B12		400	250	2.50	570	47	3	174	600
B12'		400	250	2.50	570	47	5	140.7	600
C1		400	250	1.60	559	43	3	249.6	200
C1'		400	250	1.60	559	43	5	149.7	200
C2		400	250	1.60	559	43	3	136.1	600
C2'		400	250	1.60	559	43	5	153.2	600
C4		400	250	1.60	559	44	4	144.2	150
C4'		400	250	1.60	559	44	4	136.1	150
C5		400	250	1.60	559	44	4	138.5	340
C7		400	250	1.60	559	44	4	129.8	150
C7'		400	250	1.60	559	44	4	125.1	150
C8		400	250	1.60	559	45	4	127.6	340
C8'		400	250	1.60	559	45	4	116.7	340
C9		400	250	2.00	554	27	4	105.2	500
C10		400	250	2.00	554	52	3	146	500
C11		400	250	1.50	550	45	3	146.4	340
C12		400	250	1.50	550	45	3	151.2	600
C12'		400	250	1.50	550	45	5	143	600
C13		400	250	2.00	554	46	3	111.2	900
C13'		400	250	2.00	554	46	5	134.5	900
ST-1	Jorgensen	200	165	1.10	1027	25	2.25	39.5	427
ST-2		200	165	1.10	1027	26	2.25	43.5	97
ST-3		200	165	1.10	1027	26	2.25	45.4	200
ST-6		200	165	1.10	1027	27	2.25	43	300
ST-7		200	165	1.10	1027	27	2.25	40.8	401
ST-8		200	165	1.10	1027	27	2.25	39.8	499
ST-9		200	165	1.10	1027	27	2.25	45.4	299
ST-10		200	165	1.10	1027	28	2.25	36.9	401
ST-12		200	165	1.10	1027	28	2.25	44	200
ST-13		200	165	1.10	1027	29	2.25	33.9	100
ST-14		200	165	1.10	1027	29	2.75	40.7	201
ST-15		200	165	1.10	1027	29	2.75	44.6	301
ST-17		200	165	1.10	1027	30	2.75	39.9	100

Table 3.1 (continued)

Spec. name	Ref.	Width (mm)	Depth (mm)	Rft. ratio (%)	Steel Yield strength (MPa)	Compressive Strength (MPa)	a/d (–)	Shear Force (kN)	Normal Force (kN)
ST-18		200	165	1.10	1027	30	2.75	32.8	200
ST-19		200	165	1.10	1027	30	2.75	32	300
ST-20		200	165	1.10	1027	30	2.75	30.2	500
ST-22		200	165	1.10	1027	30	2.75	37.5	501
ST-23		200	165	1.10	1027	30	2.25	34.5	602
ST-24		200	165	1.10	1027	30	2.25	35.2	600
V8-1	Fernandez-Montes	140	164	1.00	495	36	1.97	57.37	30
V8-2		140	164	1.00	495	82	1.97	75.73	51
V8-3		140	164	1.00	495	34	1.97	45.13	50
V8-4		140	164	1.00	495	34	1.97	50.91	102
V9-1		140	164	1.51	487	31	1.97	68.94	27
V9-2		140	164	1.51	487	74	1.97	71.95	47
V9-3		140	164	1.51	487	36	1.97	52.83	60
V9-4		140	164	1.51	495	74	1.97	109.9	69
V9-5		140	164	1.51	495	33	1.97	58.09	109
V9-6		140	164	1.51	487	82	1.97	52.63	154
ST1	Bui, T	4000	267	1.15	500	34	4.59	711	600
ST2		4000	267	1.15	500	35	4.59	742	780
ST3		4000	267	1.15	500	34	4.59	539	1200
ST4		4000	267	1.15	500	34	4.59	555	1440
SC8	Limam	4000	267	1.15	500	35	4.59	801	1200
SC9		4000	267	1.15	500	33	4.59	792	1800
N1-1	Adam, V	300	255	1.00	957	38	4.53	73	259
N1-2		300	255	1.00	957	39	4.53	70	258
N2-1		300	255	1.00	957	38	4.53	102	195
N2-2		300	255	1.00	957	39	4.53	55	195
N3-1		300	255	1.00	957	38	4.53	68	317
N3-2		300	255	1.00	957	39	4.53	116	317
4	Pham	200	280	1.65	550	33	3.57	68	147
5		200	280	1.65	550	33	3.57	51	147
6		200	280	1.65	550	35	3.57	59	148
7		200	280	1.65	550	33	3.57	60	298
8		200	280	1.65	550	33	3.57	48	297
9		200	280	1.65	550	35	3.57	56	297
10		200	280	1.65	550	34	3.57	43	397

(continued)

Table 3.1 (continued)

Spec. name	Ref.	Width (mm)	Depth (mm)	Rft. ratio (%)	Steel Yield strength (MPa)	Compressive Strength (MPa)	a/d (–)	Shear Force (kN)	Normal Force (kN)
11		200	280	1.65	550	34	3.57	61	397
12		200	280	1.65	550	35	3.57	62	397
13		200	280	1.65	550	34	3.57	63	596
14		200	280	1.65	550	34	3.57	60	596
15		200	280	1.65	550	35	3.57	73	594
Avg		370	296	1.50	563	37	3.35	100.05	292
Min		70	164	0.20	343	15	1.96	15.43	20
Max		4000	890	4.00	1027	82	5.61	801	1800

Fig. 3.2 Load deformation versus failure criteria
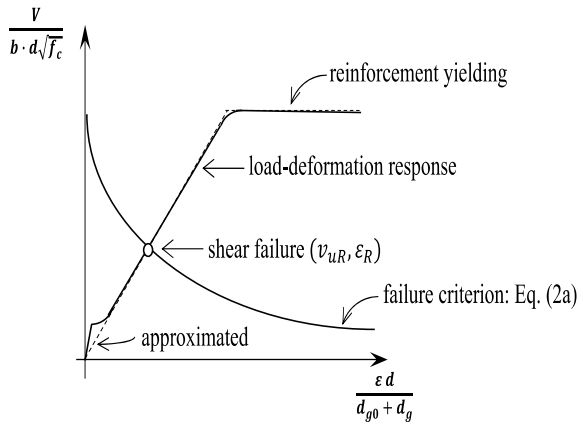
needs modification to account for the differences in behaviour for FRP. Plots for shear strength versus steel to FRP modular ratio, longitudinal reinforcement ratio E_s/E_f, width-to-effective depth ratio, b/d, and shear slenderness ratio, a/d are shown in Fig. 3.4. The coefficients of correlation between each parameter and its strength are also indicated in each plot.

Compared to the width-to-effective depth and shear slenderness ratios, the FRP reinforcement and modular ratios have the most significant values of (r). Such an observation is because FRP-RC members are characterized by a smaller young modulus and lesser ductility than those reinforced with steel, which manifests in their differing roles in resisting shear. In addition, wider and deeper critical shear cracks are observed, leading to a significant reduction in the compression zone depth, aggregate interlock, and transfer of tensile stresses across inclined cracks. Moreover, the dowel action is reduced due to the lower transverse strength of FRP bars. The CSCT is extended to the FRP-reinforced concrete elements while maintaining the

Table 3.2 Specimens database for FRP-concrete elements

Ref.	b mm	N	d mm	ρf %	a/d	fc' MPa	ffu Mpa	Ef Gpa	Shape	FRP Type
Nagasaka et al.	250	2	253	1.9	1.78	22–34	1295	56	R	A
Tottori and Wakui	200	9	325	0.7–0.9	3.2	44–47	700–1000	58–192	R	C, G
Maruyama and Zhao	150	4	250	0.55–2.2	3	27–35	1308	94	R	C
Okamoto et al.	250	1	253	1.71	1.19	37	1167	61	R	G
Nakamura and Higai	300	2	150	1.3–1.8	4	22–28	751	29	R	G
Zhao et al'.	150	3	250	1.5–3.0	3	34	1124	105	R	C
Maruyama and Zhao	150–300	2	250–500	1.04	2.5	29–34	1200	100	R	C
Vijay et al.	150	2	265	0.6–1.4	1.89	31–45	655	54	R	G
Duranovic et al.	150	2	210	1.36	3.65	38–33	1000	45	R	G
Mizukawa et al.	200	1	260	1.36	2.69	34.7	1185	130	R	C
Swamy and Aburawi	154	1	222	1.55	3.15	39	586	34	R	G
Michaluk et al.	1000	2	104	0.49–0.8	8.44–13	66	692	41	R	G
Deitz et al.	305	3	158	0.73	4.49–5.8	27–30	612	40	R	G
Alkhrdaji et al.	178	3	279–287	0.77–2.3	2.61–2.7	24	717	40	R	G
Massam	450	6	194–938	0.09–047	3.2–4.1	35–46	397–474	37	R	G
Yost et al.	178–305	21	192–225	0.27–2.3	4.06–4.1	36–38	690–830	41	R	G
Tureyen and Frosch	457	6	360	0.96–1.9	3.39	39.7–43.7	593–1421	38–47	R	G, A
Gross et al.	152–203	4	225	1.25–2.6	4.06	79	690	40	R	G
Tariq and Newhook	130–160	6	310–346	0.70–1.6	2.75–3.7	37.3–43	600–1551	42–120	R	G, C
Razaqpur et al.	150–200	12	163–262	0.25–1.4	2.5–4.2	29–50	676–1600	32–145	R	C, G
Gross et al.	89–159	4	141–143	0.33–0.8	6.36–6.5	60.3–81.4	2640	139	R	C
Yost et al.	121	2	190	1.1–1.65	7.96	40–74	690	40	R	G

(continued)

Table 3.2 (continued)

Ref.	b mm	N	d mm	ρ_f %	a/d	f_c' MPa	f_{fu} Mpa	E_f Gpa	Shape	FRP Type
Kilpatrick and Easden	420	12	78–83	0.61–2.6	3.61–6.4	61–93	630–780	40–42	R	G
El-Sayed et al.	1000	8	154–165	0.39–2.7	6.06–6.5	40	540–1536	40–114	R	C, G
Razaqpur and Isgor	200	7	225	0.22–0.8	1.82–4–5	40	2250	145	R	C
Ashour	150	6	168–263	0.45–1.4	2.54–4.1	29–50	650–705	32–38	R	G
El-Sayed et al. (a)	250	6	326	0.87–1.7	3.07	44–50	754–1536	39–134	R	C, G
El-Sayed et al. (b)	250	4	326	1.7–2.19	3.07	63	754–769	42–135	R	C, G
Guadagnini et al.	150	4	224	1.28	1.12–3.3	43	765	45	R	G
Kilpatrick and Dawborn	420	1	75	0.68	6	48	840	42	R	G
Dawborn and Kilpatrick	420	8	73	0.68–1.2	6.16	48–92	840	42	R	G
Matta et al.	114–457	15	146–883	0.12–0.3	3.1	29.5–60	476–849	41–48.2	R	G
Nehidi et al.	150	13	150–350	1.13–2.3	1.36–1.8	35	690–1180	41–134	R	C, G
Niewels	300	3	404–441	3–25–3.9	3.02–3.7	43	480–1000	44–63	R	G
Steiner et al.	457	2	889	1.19	3.1	29.6	600	41	R	G
Alam et al.	250–300	10	305–734	0.86–1.5	1.5–3.5	34.5–44.7	751	46	R	G
El-Sayed et al.	600	2	262	0.77–1.5	6.68	68	683	48	R	G
Jang et al.	150–200	29	215	0.33–0.8	1.5–4.50	30	980–2130	48–146	R	C, G
Caporale and Luciano	150	4	170	0.92–1.5	4.12	20	970	4	R	G
Olivito and Zuccarello	150	4	170	1.33–2.2	5.88	20	1725	113	R	C
Bentz et al.	450	6	188–937	0.51–2.5	3.2–16.2	35–46	397–474	37	R	G
Lee et al.	800	18	100–200	0.21–0.8	6–12	27.4–40	1130	49	R	G
Mohamed and Masmoudi	162	1	162	3.65	4	45	683	48	C	G
Zeidan et al.	150	4	280	0.11–0.2	1.25–2.5	28–54	2480	148	R	C

Table 3.2 (continued)

Ref.	b mm	N	d mm	ρf %	a/d	f′c MPa	ffu Mpa	Ef Gpa	Shape	FRP Type
Razaqpur et al.	200–500	6	230–530	0.28–0.36	3.5–6.5	52	1500	114	R	C
Alam and Hussien	250	12	296–455	0.86–1.4	2.5	37.4–44.7	786–1899	46–14	R	G, C
Alam and Hussien	250–300	5	291–594	0.65–1.3	2.5	65–74	751–1596	46–144	R	G, C
Elchabib and Alhamaydeh	200	9	300–400	0.92–1.8	1.04–1.52	34.4–52	1050	51	R	G
Liu and Pantelides	610–1830	8	209–247	0.79–0.9	3.90–4.6	53–84	715	43	R	G
Xiao-quan et al.	240	3	240	2.24	0.66–1	36	542	33	C	G
Matta et al.	114–457	14	146–883	0.12–0.3	3.1	30	476–849	41	R	G
Alam and Hussien	250–300	8	305–744	0.4–0.9	2.5	40	786–1986	46–144	R	G, C
Farghaly and Benmokrane	300	4	1106–1097	0.26–1.2	1.13	38.70–50	750–1899	47–144	R	G, C
Kim and Jang	150–200	53	216	0.33–0.8	1.5–4.5	30	980–2130	39–147	R	C, G
Kim et al.	200	12	190–310	0.38–0.6	1.4–1.7	26.1	1827–1956	80–120	R	A, C
ElRefai and Abed	152	8	216–224	0.31–1.5	2.50–3.3	49	1168	50	R	G
Tomlinson and Fam	150	3	245–270	0.39–0.8	4	60	1100	70	R	B
Abdul-Salam et al.	1000	16	175	0.62–3.7	4.86	42.9–86.2	588–1906	40–147	R	G, C
Ali et al.	500	4	500	1.5–3.5	2	36.3	1150–1670	64–141	C	C, G
Alam and Hussien	250–300	28	291–744	0.18–1.4	1.5–2.5	34.5–74.2	761–1747	47–132	R	G, C
Kazubska et al. (a)	150	7	379	0.99–1.8	2.9	31.4	1091	51.5	R	G
Kotyina et al. (b)	150	7	379	0.99–1.8	2.9	30.2	1091	51.5	R	G
Kazubska & Kotyina	150	13	379	0.99–1.4	2.9	30.1	1091	51.5	R	G
Mohamed et al.	500	3	500	1.6–3.84	2.09	40	1105	63.7	C	G
Jumaa and Yousif	200	12	234–635	0.71–2.7	2.62	42–73.4	1089	58	R	G
Hofmann et al.	150	9	150	0.19–1.1	2–5	33–60	1375	62	R	G

(continued)

Table 3.2 (continued)

Ref.	b mm	N	d mm	ρ_f %	a/d	f_c' MPa	f_{fu} Mpa	E_f Gpa	Shape	FRP Type
Maranan et al.	300	1	200	1.66	1.8	43	1184	63	R	G
Hosseini et al.	150	3	120	0.89	1.5	54	1015	49.8	R	G
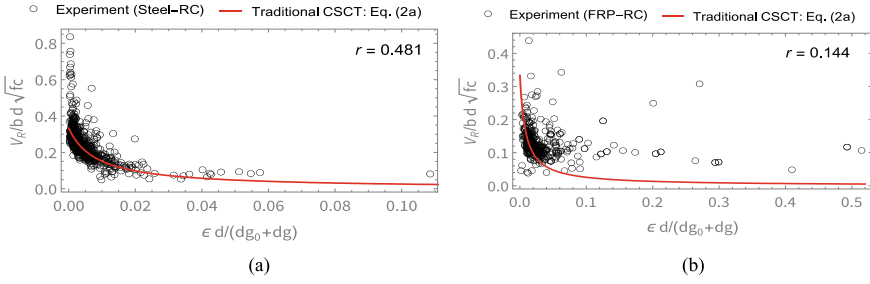
Fig. 3.3 Comparison between the CSCT for (**a**) steel and (**b**) FRP-RC elements
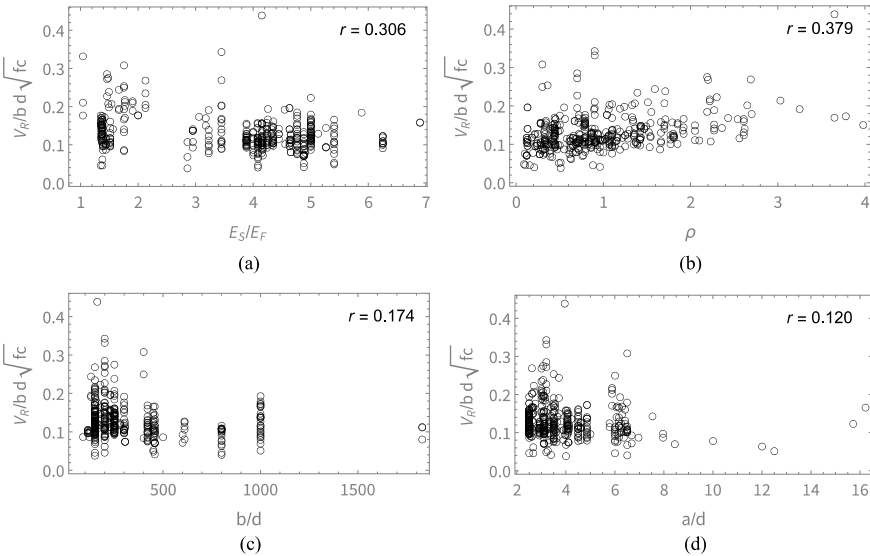
Fig. 3.4 Correlation between test results and (1) E_s/E_f (2) ρ (3) b/d (4) a/d

basic assumptions of the theory. However, the effect of the modular ratio is incorporated for Eq. (3.7) using nonlinear fitting (Deifalla and Mukhtar xxxxa), and thus the shear strength is such that:

$$\frac{v_u}{\sqrt{f_c'}} = \frac{0.000052\left(E_s/E_f\right)^2 + 0.008(E_s/E_f) + 0.26}{1 + 45\frac{\varepsilon d}{d_{dg}}} \tag{3.7}$$

3.4 ECSCT for Non-slender FRP-Reinforced Elements Under Shear

This The database of deep FRC-RC beams without stirrups shown in Table 3.2, followed by a mechanical model based on the CSCT developed for the deep FRC-RC beams without stirrups. Because of the erratic behavior of the deep FRP-RC beams highlighted, as well as the resulting gross deviation from code provisions, models derived from physical principles, rather than pure empirical fitting, are required. FRP rebars are characterized by linear elastic stress–strain behavior until rupture. In addition, due to the lower modulus of FRP rebars, the FRP-RC members are characterized by wider and deeper crack development, irrespective of the boundary and loading conditions, as well as larger deflections. In addition to the more pronounced arch action in deep beams, the assumptions of the critical shear crack theory are adjusted via the incorporation of FRP stiffness and shear span as an extension of the conventional CSCT model for steel-RC members to the case of deep FRP-RC members. Moreover, nonlinear regression and an ECSCT are arrived at Deifalla (Deifalla and Mukhtar xxxxb), a parabolic function yields the shear strength V of the member, such that:

$$\frac{v_u}{\sqrt{f_c'}} = \frac{\left[0.000052\left(E_s/E_f\right)^2 + 0.008(E_s/E_f) + 0.26\right]}{1 + 45\frac{\varepsilon d}{d_{dg}}}\left[5.52\left(\frac{d}{a}\right)^{1.78}\right] \quad (3.8)$$

This form allows one to account for the FRP material type in addition to the slenderness effect (a/d) using a hybrid physically based model coupled with minimal empirical fitting to address the changes in the assumptions. It should be noted that the original CSCT considers d/2 from the point load to be the critical section location in computing the critical shear crack width and effective strain.

3.5 Model Validation

Combining the information created by Deifalla (Deifalla and Mukhtar 2022; Deifalla and Mukhtar xxxxa; Deifalla and Mukhtar xxxxb), a sizable experimental database of materials tested under shear was compiled. roughly 700 specimens altogether, drawn from over 60 distinct research studies. Axially tensioned concrete, size, shear-span to depth ratio, concrete strength, flexure reinforcement ratio, and width to depth ratio were used to effectively gather the data, and it covered a wide range of values for all significant variables. Further details can be found in the literature by Deifalla and co-workers (Deifalla and Mukhtar 2022; Deifalla and Mukhtar xxxxa; Deifalla and Mukhtar xxxxb). The strength was calculated using existing design codes (ACI-318-19 2019; EC2 2004; Fib 2010; JSCE 2007) and compared with the measured strength.

Table 3.3 Comparison between ECSCT and exiting design codes for slender elements with FRP

Model/Code	Mean	COV (%)	99% conf. L.L
ECSCT	1.00	41	0.95
CSA-S806-12	1.07	27	1.04
ACI-440-15	2.03	21	1.93
CAN/CSA S6-14	0.76	48	0.73
CSCT	1.34	47	1.23

Table 3.4 Comparison between ECSCT and exiting design codes for non-slender elements with FRP

Model/Code	Mean	COV (%)	99% conf. L.L
ECSCT	1.16	40	1.04
CSA-S806-12	2.54	24	2.36
ACI-440-15	6.81	8.43	6.36
CAN/CSA S6-14	3.06	21	2.83
JSCE-1997	6.52	9.3	5.62
AASHTO LRFD	6.74	9.13	5.80
BISE	5.16	11.46	4.47
CNR-DT-203	3.87	16	3.32

The ECSCT outperformed the existing design codes. As a result, the following formula is used to determine the lower 99% confidence limit (Tables 3.3 and 3.4):

$$\text{Lower } 99\% = \text{Average} - 1.98 \left(\frac{\text{Standard deviation}}{\sqrt{\text{number of samples}}} \right)$$

3.6 Concluding Remarks

The following conclusions were established after accounting for all fundamental factors, including (1) Tension force, (2) Ratio of reinforcement of flexural resistance, (3) shear depth to span ratio, (4) width to depth ratio, and (5) Compressive strength of concrete.

- The creation and extensive analysis of a comprehensive database for deep FRP-RC beams without stirrups regarding different effective shear strength parameters. Despite some of them performing well in thin FRP-RC as reported in other studies, all the evaluated design codes and guidelines perform poorly in estimating the shear strength of deep FRP-RC beams without stirrups.

- Given that the ultimate shear strength of reinforced concrete elements is composed of the six major shear transfer actions (direct shear across the uncracked compression zone depth, dowel action across longitudinal reinforcing crossing the diagonal crack, aggregate interlocking across the diagonal shear crack, residual tensile stress across the diagonal crack, fiber strength, and arch action),
- The critical shear crack theory's development and support for special problems including shear strength of concrete elements reinforced with FRP. The ESCT is based on the principles of mechanics and its applicability to reinforced concrete elements under shear, and it was accurate and consistent with true behavior compared to existing database and design code.

References

Adam V, Claßen M, Hegger J (2020) Tests on Shear Behavior with Concurrent Normal Tensile Action. Versuche zum Querkrafttrag- verhalten bei gleichzeitiger Zugnormalkraft. Beton und Stahlbeton bau. https://doi.org/10.1002/best.202000003

Adebar P, Collins MP (1996) Shear strength of members without transverse reinforcement. Can J Civ Eng 23(1):30–41

ACI-318-19 (2019) ACI Committee 318. Building Code Requirements for Structural Concrete (ACI 318-19) and Commentary on Building Code Requirements (ACI 318-19). Farmington Hills (MI): American Concrete Institute

Ali, A, Hamady M, Chalioris C E, Deifalla A (2021). Evaluation of the shear design equations of FRP-reinforced concrete beams without shear reinforcement. Engineering Structures, Elsevier; 235

Bara HC (1971) Investigation on the effect of axial loads on the shear strength of reinforced concrete beams [PhD thesis]. Faculty of Engineering, Imperial College of Science and Technology, London.

Belletti B, Damoni C, Cervenka V, Hendriks MAN (2016) Catenary action effects on the structural robustness assessment of RC slab strips subjected to shear and tensile forces. Struct Concr 17(6):1003–1016

Biao H, Yu-Fei W (2018) Effect of shear span-to-depth ratio on shear strength components of RC beams. Eng Struct 168(2018):770–783

Bhide SB, Collins MP (1989) Influence of axial tension on the shear capacity of reinforced concrete members. ACI Struct J 86(5):570–581. https://doi.org/10.14359/3013

Bui TT, et al (2017) Influence of uniaxial tension and compression on shear strength of concrete slabs without shear reinforcement under concentrated loads. Constr Build Mater 146:86–101. https://doi.org/10.1016/j.conbu ildmat.2017.04068

Deifalla A, Awad A, El-Garhy M (2013) Effectiveness of externally bonded CFRP strips for strengthening flanged beams under torsion: an experimental study. Eng Struct Elsevier 56:2065–2075

Deifalla A, Ghobarah A (2014) Behavior and analysis of inverted T-shaped RC beams under shear and torsion. En Struct Elsevier 62:776–786

Deifalla A, Hamed M, Saleh A, Ali T (2014) Exploring GFRP bars as reinforcement for rectangular and L-shaped beams subjected to significant torsion: an experimental study. Eng Struct Elsevier 59:776–786

Deifalla A, Khalil MS, Abdelrahman A (2015) A simplified model for the torsional strength of concrete beams with GFRP stirrups. Compos Construct ASCE, 04014032. https://doi.org/10.1061/(ASCE)CC.1943-5614.0000498

Deifalla A, Awad A, Seleem H, AbdElrahman A (2020a) Investigating the behavior of lightweight foamed concrete T-beams under torsion, shear, and flexure. Eng Struct 219:110741. https://doi.org/10.1016/j.engstruct.2020.110741

Deifalla A, Awad A, Seleem H, AbdElrahman A (2020b) Experimental and numerical investigation of the behavior of LWFC L-girders under combined torsion. Structures 26:362–377. https://doi.org/10.1016/j.istruc.2020.03.070

Deifalla A (2020a) Design of lightweight concrete slabs under two-way shear without shear reinforcements: A comparative study and a new model. Eng Struct Elsevier 222:111076. https://doi.org/10.1016/j.engstruct.2020.111076

Deifalla A (2020b) Torsion design of lightweight concrete beams without or with fibers: A comparative study and a refined cracking torque formula. Structures 28:786–802. https://doi.org/10.1016/j.istruc.2020.09.004

Deifalla A (2020c). Strength and Ductility of Lightweight Reinforced Concrete Slabs under Punching Shear. Structures 27 (2020) 2329–2345; https://doi.org/10.1016/j.istruc.2020.08.002

Deifalla A, Ghobarah A (2010a) Full torsional behavior of RC beams wrapped with FRP: Analytical model. ACSE Compos Construct 14(3):289–300

Deifalla A, Ghobarah A (2010b) Strengthening RC T-beams subjected to combined torsion and shear using FRP fabrics—Experimental study. ASCE Compos Construct 14(3):301–311

Deifalla AF, Mousa E, Yehia D, Abdelrahman A (2021) Exploring the effect of in-plane tensile forces on the two-way shear strength: review, comparative study and future works. Future Eng J 2(1):5

Deifalla A (2021a) Assessment of one-way shear design of RC elements subjected to axial tension. case studies in construction materials. https://doi.org/10.1016/j.cscm.2021.e00620

Deifalla A (2021b) A comparative study and a simplified formula for punching shear design of concrete slabs with or without membrane tensile forces. Structures, Volume 33, October 2021, Pages 1936–1953.

Deifalla A (2021c) A mechanical model for concrete slabs subjected to combined punching shear and in-plane tensile forces. Engineering Structures, Elsevier March 2021 (231). 2021.

Deifalla A (2021d) A strength and deformation model for prestressed lightweight concrete slabs under two-way shear. Advances in Structural Engineering. 1–12. https://doi.org/10.1177/13694332211020408

Deifalla A (2022) Punching shear strength and deformation for FRP-reinforced concrete slabs without shear reinforcements. Case Studies in Construction Materials 16 (2022) e00925. https://doi.org/10.1016/j.cscm.2022.e00925

Deifalla A, Mukhtar FM (2022) A mechanical and simplified model for RC elements subjected to combined shear and axial tension. Sci Rep 12:7863. https://doi.org/10.1038/s41598-022-11577-y

Deifalla A, Mukhtar FM, A Shear strength of FRP reinforced deep concrete beams without stirrups: state-of-the-art experimental tests and a CSCT-based model. Compos Struct

Deifalla A, Mukhtar FM, A shear mechanical model for FRP reinforced concrete members based on the critical shear crack theory. In preparation

EC2 (2004) EN 1992-1-1:2004: Eurocode 2: Design of concrete structures – Part 1- 1: General rules and rules for buildings. Incl. Corrigendum 1: EN 1992-1-1:2004/AC:2008, incl. Corrigendum 2: EN 1992-1-1:2004/AC:2010, incl. Amendment 1: EN 1992-1-1:2004/A1:2014

Ebid A, Deifalla A (2021) Prediction of shear strength of FRP reinforced beams with and without stirrups using (GP) technique. Ain Shams Eng J. https://doi.org/10.1016/j.asej.2021.02.006. Elsevier

El-Meligy O, El-Nemr AM, Deifalla A (2017) Re-evaluating the modified shear provision of CAN/CSA S806-12 for concrete beams Reinforced with FRP Stirrups. AEI. https://doi.org/10.1061/9780784480502.027

Ehmann J (2003) Querkrafttragfahigkeit zugbeanspruchtwe Stahlbetonplatten in Verbundbrucken. Thesis submitted to Stuttgart Universty, Germany

Emrich H (1993) Zum Trgverhalten von Stahlbetonbauteilen unter Querkraft-unde Langszug-beansprunchung. Schriftenreihe des Instituts fur Massivbau und Bau stofftechnologie, Heft 20, Karlsruhe

Elstner RC, Hognestad E (1957) Laboratory investigation of rigid frame failure. J Proc 53(1):637–668

Fernandez-Montes D, Gonzalez VE, Diaz HE (2015) Influence of axial tension on the shear strength of floor joists without transverse reinforcement. Struct Concr 16(2):207–220

Fib MC (2010) Fédérationinternationale du béton. fib model code for concrete structures 2010. Lausanne; 2013

Haddadin MJ, Hong ST, Mattock AH (1971) Stirrup effectiveness in reinforced concrete beams with axial force. J Struct Div

Hassan MM, Deifalla A (2015) Evaluating the new CAN/CSA-S806–12 torsion provisions for concrete beams with FRP reinforcements. Mater Struct. https://doi.org/10.1617/s11527-015-0680-9

Hu B, Wu FY (2017) Quantification of shear cracking in reinforced concrete beams. Eng. Struct. 147(2017), 666–678 (2017).

Jorgensen HB, Hoang LC, Fabrin LS, Malgaard J (2013) Influence of high axial tension on the shear strength of non-shear RC beams. Poster Session Presented Proc. Int. IABSE Conf. Assess. Upgrading. Refurbishment. Infrastruct. vol 99, no (155), p 161

JSCE (2007) Standard Specifications for Concrete Structures-2007: Design. Japanese Society of Civil Engineering, No. 15, ISBN 978-4-8106-0752-0759

Mattock AH (1969) Diagonal tension cracking in concrete beams with axial forces. J Struct Div ASCE 95(ST 9):1887–1990

Muttoni A (2008) Punching Shear Strength of Reinforced Concrete Slabs without Shear Reinforcement. ACI Struct J 105(4):440–450. https://doi.org/10.14359/19858

Muttoni A, Fernández Ruiz M, Simões JT (2018) The theoretical principles of the critical shear crack theory for punching shear failures and derivation of consistent closed-form design expressions. Struct Concrete 19(1):174–190

Leonhardt F, Rostasy K, Macgregor J, Patzak M (1977) Schubversuche an Balken und Platten bei gleichzeitigem Langszug, dAfStb Heft 275, W. Ernst & Sohn

Limam S, Nanaa WSA, Bui TT, Limam A, Abouric S (2017) Experimental investigation and analytical calculations on shear strength of full-scale RC slabs with shear reinforcement for nuclear power plants. Nucl Eng Des 324(2017):143–157

Pham DT, Fouré B, Pinoteau N, Abouri S, Mège R (2020). Influence of axial tension on the shear strength of RC beams without stirrups. Struct Concr, 1–17. https://doi.org/10.1002/suco.202000077

Regan PE (1971) Beams subjected to axial loads. Imperial College Lond. 1971:93–118

Saleh A, Fathy A, Deifalla A, Nasser M (2019) Performance of steel fiber reinforced concrete corbels. Int Res J Innovat Eng Technol IRJIET 3(2):22–27

Sayani FHN (1968) Influence of axial tension on the shear strength of reinforced concrete beams. M. Phil. Thesis, Imperial College of Science and Technology, University of London, p 118

Saul R, Koch R (1989) Zur Schubtragfahigkeit von Stahlbetonplatten bei gleichzeitigem Langszug, Beton-und Stahlbetonbau 84, Heft 7 181–186, Ernst & Sohn Verlag

Soresen K, Loset O, Olsen T (1981) Investigation of the influence of axial tensile forces on the transverse shear strength. Report No. PP1-1-5, Det Norske Veritas, Oslo, Plus appendixes

Tamura T, Shigematsu T, Hara T, Maruyama K (1995) A study of proposed design equation for the shear strength of R/C beams subjected to axial tension. Doboku Gakkai Ronbunshu 520:225–234

Yu-Fei W, Biao H (2017) Shear strength components in reinforced concrete members. J Struct Eng 143(9):04017092–04017101. https://doi.org/10.1061/(ASCE)ST.1943-541X.0001832

Chapter 4
Large-Scale Shake Table Tests on Pounding Response of RC Buildings

Fezayil Sunca and Ahmet Can Altunışık

Abstract This study presents large-scale shake table test results to investigate the responses of RC structures exposed to earthquake-induced pounding effects. The effects of pounding on structural responses and damage were discussed by comparing the experimental results with and without interaction. In the shake table test, ½ scaled two-story RC specimens were used. To investigate structural responses under seismic excitations of different intensities, a series of shake table tests was organized. Hence, a sum of 15 tests were carried out. Due to the destructive effects caused by column and slab interaction, the collision between RC structures with different story heights was simulated in the experiments. Experimental results show that critical increases occur in acceleration values measured at floor level due to pounding, and column-slab poundings can cause significant damage to columns.

Keywords Damage · Earthquake · Pounding · RC structures · Shake table test

4.1 Introduction

Although many codes and guidelines suggest for the gap to be left between adjacent buildings, various reasons such as unplanned urbanization, land costs, and not taking into account the interaction between constructed buildings and adjacent buildings cause inadequate gaps to be left between buildings. However, researchers revealed that pounding was the source of much of the local damage in buildings and this can cause global damage (Abdel Raheem et al. 2018; Cole et al. 2012; Chouw and Hao 2012).

In the literature, pounding between adjacent buildings was generally handled with analytical models or by observations executed after earthquakes. Some experimental studies were carried out on this subject, but the interaction between small-scale structures was investigated in these experiments (Chau et al. 2003, 2004; Khatiwada

F. Sunca (✉) · A. C. Altunışık
Department of Civil Engineering, Karadeniz Technical University, Trabzon, Turkey
e-mail: fezayilsunca@ktu.edu.tr

and Chouw 2013; Khatiwada et al. 2013; Jankowski 2010; El-Khoriby et al. 2014; Takabatake et al. 2014; Sołtysik et al. 2017). A limited number of experimental studies were performed by considering test specimens of considerable size.

Papadrakakis and Mouzakis (Papadrakakis and Mouzakis 1995) studied collision between 2-story RC structures, one of which is more rigid than the other. As a result of the experimental study in which harmonic excitations were taken into account as input, it was revealed that pounding increased the displacements of the rigid structure and, on the contrary, decreased the displacements of the flexible structure. Also, critical increases in maximum acceleration measured at floor level were reported due to pounding. Crozet et al. (2019) performed large-scale shake table tests to study pounding effects by considering the two 2-story steel frames with concrete slabs. Also, they investigated the effectiveness of rigid links installed between adjacent specimens to prevent collisions. Masroor and Mosqueda (2012) and Du et al. (2021) handled the interaction between base-isolated structures and moat walls by using shake table tests. These studies showed that collision can significantly amplify structural responses. The contributions of this study to the existing literature are as follows. It can be seen from the literature review that the pounding effects between RC structures were not sufficiently examined. The interaction between small-scale structures was investigated in past studies. In this study, a large campaign of shake table tests was performed by using relatively large-scale test specimens. In most of the past studies, test specimens remained within elastic limits after tests and the pounding damages were adequately investigated. Therefore, the effects of collisions on damages were also investigated in detail.

This study presents large-scale shake table test results to investigate the structural responses of RC structures subjected to earthquake-induced pounding effects. The effects of pounding on structural responses and damage were discussed by comparing the experimental results with and without interaction. In the shake table test, ½ scaled two-story RC specimens were used. The experimental campaign was executed on the 4 × 4 m shake table of the Karadeniz Technical University in Trabzon, Turkey.

4.2 Experimental Study

4.2.1 Test Specimen and Experimental Setup

The capacity of the shake table and laboratory conditions were decisive in the selection of the characteristics of the test specimen and the scale factor. This uniaxial shake table has a 350kN payload capacity and has a mother platform of 4 × 4 m. It has a maximum acceleration range of ± 2 g, a displacement capacity of ± 400 mm, and a frequency range 0−50 Hz. ½ scaled two-story RC specimens were used. In the design of the building, the following deficiencies were considered to represent the existing RC buildings: (i) poor concrete quality, (ii) inadequate transverse reinforcement, and (iii) incorrect reinforcement details.

Artificial mass model employed in previous studies on shake table tests of RC structures (Zhang et al. 2017; Khan et al. 2021), was used. Thus, the material properties were unchanged for the scaled test specimens. The grades of concrete were C16 (f_{ck} = 16 MPa) for foundations and C12 (f_{ck} = 12 MPa) for other load-bearing elements. Longitudinal and transverse reinforcements were S420 (f_{yk} = 420 MPa).

The test specimen was designed as a two-bay in the longitudinal direction with 1.4 m. The height of each story was 1.7 m. As a result of scaling, the test specimen consists of columns with dimension 15 × 20 cm. Longitudinal and transverse bars 4Ø10 and 8Ø25 mm. The cross-section dimensions of the beams were 15 × 20 cm. Longitudinal bars of the beams 2Ø10 both in top and bottom zones. The diameter and center-to-center distance of the stirrup were 8 mm and 25 cm, respectively. The thickness and width of the foundation were 30 cm and 40 cm.

Most of the aforementioned studies investigated the pounding effects by considering one of the buildings to be more flexible or more rigid than the other. However, the evaluation of structural responses from the two test specimens during shake table experiments is a rather complex issue. To overcome this situation, a rigid collision wall was constructed by using HE200A profiles to represent the rigid building. To precisely adjust the gaps between the RC specimen and wall, adjustable collision elements were manufactured on each floor. During the experiments, a ball-bearing system was also used to prevent out-of-plane motion of the RC frame. Figure 4.1 presents test setup.

4.2.2 Instrumentation

After the test specimen is rigidly attached to the platform, it was placed with a total of five displacement transducers (LVDT), three wireless 3-axis accelerometers, and four uniaxial accelerometers. LVDTs were used to obtain displacements in foundations and each floor level and relative displacements between the test specimen and the collision wall.

During the shake table tests, 3-axis wireless accelerometers with an adjustable sampling rate up to 4 kHz and a maximum acceleration range of ± 40 g were used to capture sudden acceleration changes and peaks in acceleration due to the pounding. These were located in the interaction regions. In addition, four uniaxial accelerometers with a maximum acceleration range of ± 2 g were used to determine the in-plane and out-of-plane accelerations of the shaking table, each floor, and foundation. Table 4.1 briefs instrumentation layouts.

4.2.3 Test Procedures

Researchers commonly utilized both real earthquake data and sinusoidal waves in shake table experiments to assess the seismic behavior of RC structures (Ahmad

a. General view of the experimental setup for shake table tests

b. High-strength steel rods and profiles for connection between foundation and shake table

c. Adjustable collision element and collision wall

Fig. 4.1 Experimental setup

Table 4.1 Instrumentation layouts

No	ID	Model	Direction	Capacity	Location
1	Acc1	G-Link 200	In-plane out-of-plane	± 40 g	Interaction region at 1st floor level of specimen
2	Acc2				Interaction region at 2nd floor level of specimen
3	Acc3				Interaction region at 2nd floor level of collision wall
4	Acc4	SENSEBOX7001	In-plane	± 2 g	Shake table
5	Acc5				1st floor level of specimen
6	Acc6				2nd floor level of specimen
7	Acc7		Out-of-plane		2nd floor level of specimen
8	LVDT1	RTL-400	In-plane	400 mm	Foundation level of specimen
9	LVDT2				1st floor level of specimen
10	LVDT3				2nd floor level of specimen
11	LVDT4	RTL-200		200 mm	Between specimen and collision wall at 1st floor level
12	LVDT5				Between specimen and collision wall at 2nd floor level

et al. 2019; He et al. 2020; Henry et al. 2021; Koutromanos et al. 2013; Lu et al. 2018; Yuen et al. 2018). Selecting the seismic excitation is heavily dependent on the shaking table's capacity. During certain experiments utilizing real ground motions, despite input amplitudes nearing the shaking table's capacity threshold, the test specimens might not experience the desired level of damage. In these scenarios, the test procedures could incorporate sine-wave excitations (Tu et al. 2010). Additionally, these basic excitations offer the benefit of ensuring a simplified structural response, thereby making the test results more comprehensible (Mayorca et al. 2006). Therefore, a natural acceleration record obtained from the 1992 Erzincan Earthquake (EW component, Erzincan station) and three sinusoidal motions were used.

Time intervals of natural acceleration data were scaled based on similitude requirements. Similarly, peak acceleration values of both original and scaled records were kept the same (Fig. 4.2). The series of incremental shake table tests was established through a gradual escalation of the seismic excitation's intensity. Peak ground acceleration (PGA) values were selected as an intensity measure. 25% (PGA =
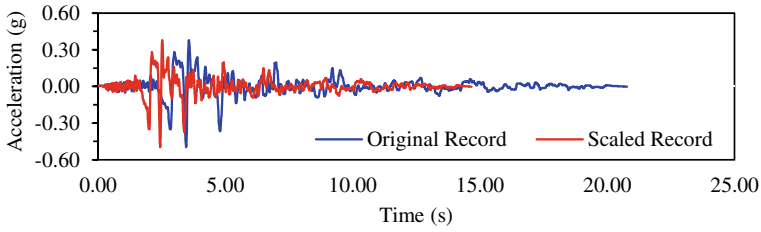
Fig. 4.2 The original and scaled 1992 Erzincan record

Table 4.2 Shake table test sequence

Test No	Scale factor	Input	Code	PGA (g)	PGD (mm)
1	25%	1992 Erzincan Earthquake	ERZ25%	0.125	35.05
2	50%		ERZ50%	0.250	70.10
3	75%		ERZ75%	0.375	105.16
4	100%		ERZ100%	0.500	140.21
5	100%	Sinusoidal motions	S1	0.500	5.00
6	100%		S2	0.500	50.00
7	100%		S3	0.750	50.00

0.125 g), 50% (PGA = 0.250 g), 75% (PGA = 0.375 g) and 100% (PGA = 0.500 g) of the scaled acceleration was applied. Three sinusoidal motions were carried out (Table 4.2).

4.3 Results and Discussions

This section illustrated the structural responses by analyzing the data yielded by the measurement systems. A relative comparison was undertaken for the relative displacements and absolute accelerations corresponding to each records.

Figures 4.3–4.4 present the changes in the time history of accelerations for each shake table test. To this aim, the accelerations measured at the 2nd floor level of the structure were comparatively investigated because the highest structural responses were obtained at this floor. The measured acceleration values increased significantly owing to increasing intensity in both the tests with and without considering the pounding effect. In the case where pounding was not taken into account, the maximum acceleration values were obtained as 0.61 g for ERZ25%, 0.89 g for ERZ50%, 1.12 g for ERZ75%, and 1.15 g for ERZ100%. In tests performed with sinusoidal ground motions, these values were between 1.07 g and 2.07 g. In tests where pounding effects were considered, the maximum acceleration values were obtained as 0.48 g for ERZ25%, 0.73 g for ERZ50%, 1.25 g for ERZ75%, 1.54 g for ERZ100%, 2.25 g

for S1, and 2.04 g for S2. During the test with S3, significant damage occurred to the test specimen. For this reason, no measurements were taken for the safety of the devices in the pounding test with S3 ground motion. As can be seen, in tests performed with relatively low-intensity seismic excitation (ERZ25 and ERZ50%), the pounding caused a decrease in the measured acceleration values. However, the pounding significantly fluctuated the measured acceleration with the increase of the seismic excitation intensity. By comparing the results obtained in the experiments with and without the pounding effect, it can be seen that the acceleration values increase by 11.61% for ERZ75, 33.91%, for ERZ100, 110.28% for S1, and 29.11% for S2, due to the collision effect.

On the other hand, three accelerometers with a maximum acceleration range of ± 40 g were used at the interaction region between specimen and collision wall, to capture sudden acceleration changes and peaks in acceleration due to the pounding. When comparing the data from these accelerometers, the increases in accelerations due to the collision were more pronounced (Fig. 4.5). The measurement of acceleration is a critical parameter for assessing the seismic forces impacting structural and non-structural elements. In past shake table experiments, acceleration values were correlated with the story and base shear forces. Therefore, increases in the accelerations due to the pounding might be caused significant structural responses and might
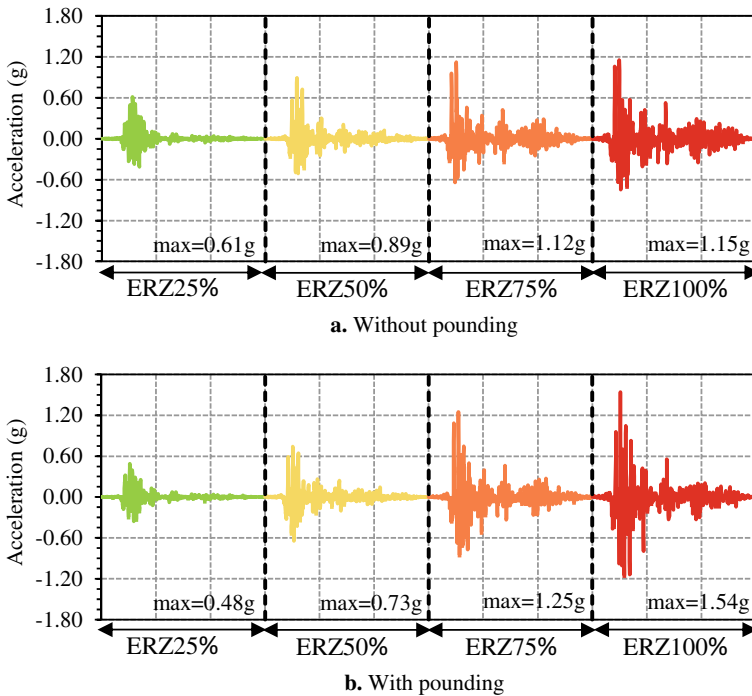
Fig. 4.3 Comparison of the acceleration responses recorded during shake table tests performed with natural ground motion
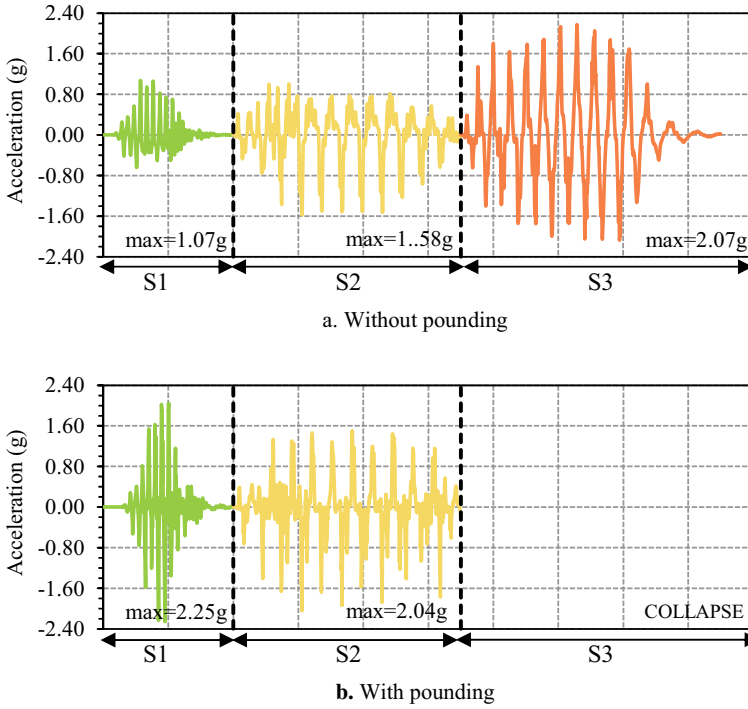
a. Without pounding

b. With pounding

Fig. 4.4 Comparison of the acceleration responses recorded during shake table tests performed with sinusoidal motion

be caused significant damage to columns in the column-slab interaction, as in this study (Fig. 4.8).

Figures 4.6 and 4.7 present the time history of relative displacements. The displacements recorded at the 2nd floor level of the structure were used. The trends determined for the accelerations were observed for the relative displacements.
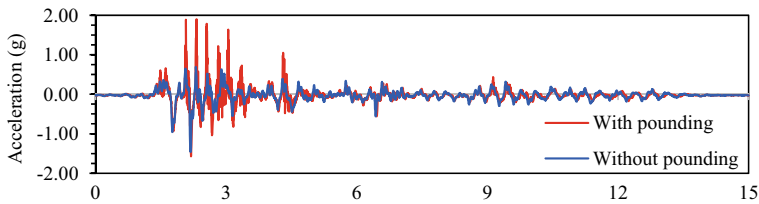

Fig. 4.5 Comparison of the acceleration responses recorded at the interaction region between specimen and collision wall during tests performed with ERZ100%
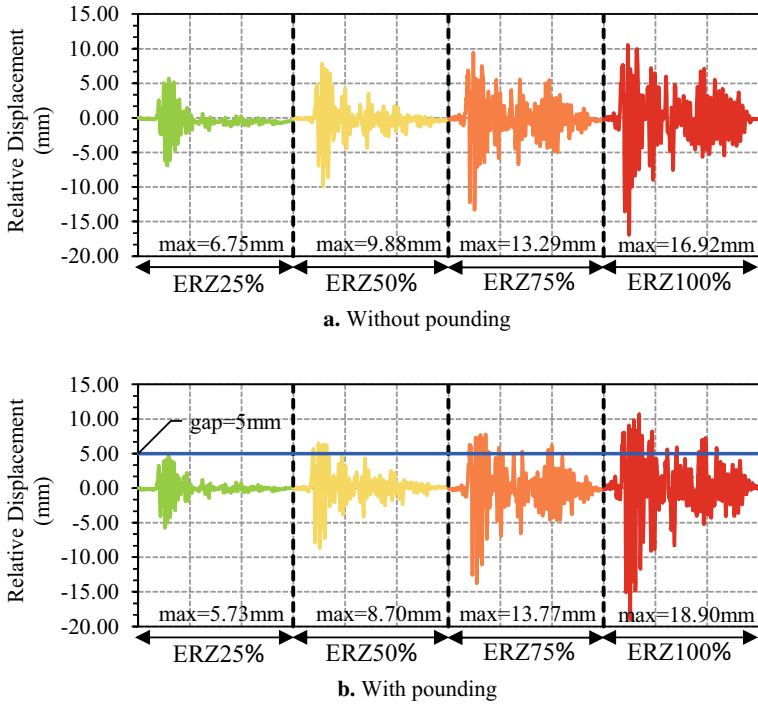
Fig. 4.6 Comparison of the relative displacements recorded during shake table tests performed with natural ground motion

4.4   Conclusions

This study presents large-scale shake table test results to investigate the responses of RC structures exposed to earthquake-induced pounding effects. The effects of pounding on structural responses and damage were discussed by comparing the experimental results with and without interaction. Experimental results show that critical increases occur in acceleration values measured at floor level due to pounding. This led to significant damage to columns in the column-slab interaction.
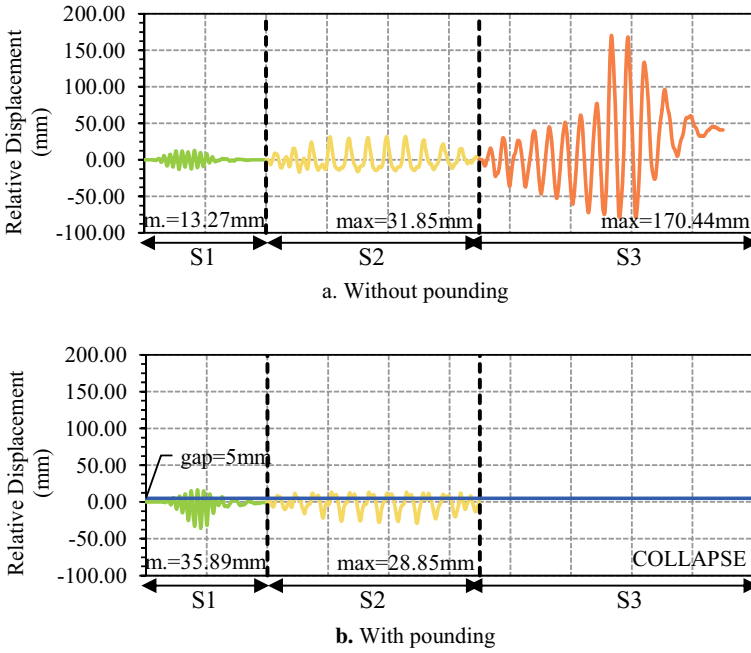
Fig. 4.7 Comparison of the relative displacements recorded during shake table tests performed with sinusoidal motion
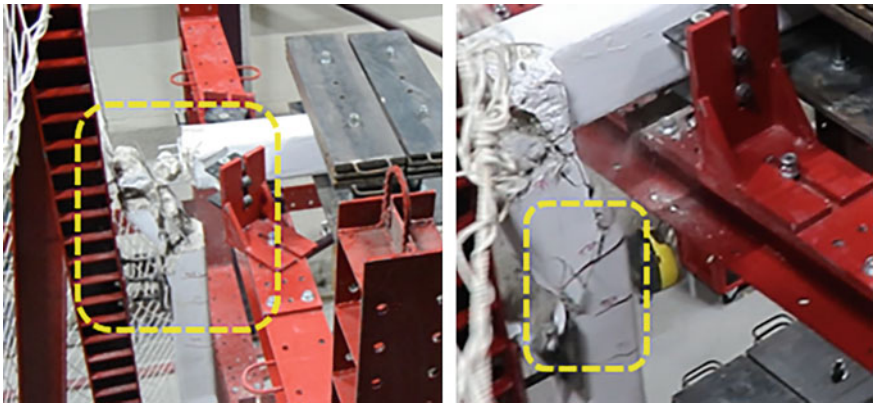
Fig. 4.8 Column collapse due to pounding during the shaking table test performed with the S3 motion

References

Abdel Raheem SE, Fooly MYM, Abdel Shafy AGA, Taha AM, Abbas YA, Abdel Latif MMS (2018) Numerical simulation of potential seismic pounding among adjacent buildings in series. Bull Earthq Eng 17:439–471. https://doi.org/10.1007/s10518-018-0455-0

Ahmad N, Shahzad A, Rizwan M, Khan AN, Ali SM, Ashraf M, Naser A, Ali Q, Alam B (2019) Seismic performance assessment of non-compliant SMRF-reinforced concrete frame: shake-table test study. J Earthquake Eng 23:444–462. https://doi.org/10.1080/13632469.2017.1326426

Chau KT, Wei XX, Guo X, Shen CY (2003) Experimental and theoretical simulations of seismic poundings between two adjacent structures. Earthquake Eng Struct Dynam 32:537–554. https://doi.org/10.1002/eqe.231

Chau KT, Wei XX, Shen CY, Wang LX (2004) Experimental and theoretical simulations of seismic torsional poundings between two adjacent structures. In: 13th world conference on earthquake engineering. pp 1–6

Chouw N, Hao H (2012) Pounding damage to buildings and bridges in the 22 February 2011 Christchurch earthquake. Int J Prot Struct 3:123–139. https://doi.org/10.1260/2041-4196.3.2.123

Cole GL, Dhakal RP, Turner FM (2012) Building pounding damage observed in the 2011 Christchurch earthquake. Earthquake Eng Struct Dynam 41:893–913. https://doi.org/10.1002/eqe.1164

Crozet V, Politopoulos I, Chaudat T (2019) Shake table tests of structures subject to pounding. Earthquake Eng Struct Dynam 48:1156–1173. https://doi.org/10.1002/eqe.3180

Du H, Wang Y, Han M, Ibarra LF (2021) Experimental seismic performance of a base-isolated building with displacement limiters. Eng Struct 244:112811. https://doi.org/10.1016/j.engstruct.2021.112811

El-Khoriby S, Seleemah A, Elwardany H, Jankowski R (2014) Experimental and numerical study on pounding of structures in series. Adv Struct Eng, 1073–1089. https://doi.org/10.1007/978-81-322-2193-7_84

He J, Chen J, Ren X, Li J (2020) A shake table test study of reinforced concrete shear wall model structures exhibiting strong non-linear behaviors. Eng Struct 212:110481. https://doi.org/10.1016/j.engstruct.2020.110481

Henry RS, Zhou Y, Lu Y, Rodgers GW, Gu A, Elwood KJ, Yang TY (2021) Shake-table test of a two-storey low-damage concrete wall building. Earthquake Eng Struct Dynam 50:3160–3183. https://doi.org/10.1002/eqe.3504

Jankowski R (2010) Experimental study on earthquake-induced pounding between structural elements made of different building materials. Earthquake Eng Struct Dynam 39:343–354. https://doi.org/10.1002/eqe.941

Khan I, Shahzada K, Bibi T, Ahmed A, Ullah H (2021) Seismic performance evaluation of crumb rubber concrete frame structure using shake table test. Structures 30:41–49. https://doi.org/10.1016/j.istruc.2021.01.003

Khatiwada S, Chouw N (2013) A shake table investigation on interaction between buildings in a row. Coupled Syst Mech 2:175–190. https://doi.org/10.12989/csm.2013.2.2.175

Khatiwada S, Chouw N, Butterworth JW (2013) Evaluation of numerical pounding models with experimental validation. Bull N Z Soc Earthq Eng. 46:117–130. https://doi.org/10.5459/bnzsee.46.3.117-130

Koutromanos I, Kyriakides M, Stavridis A, Billington S, Shing PB (2013) Shake-table tests of a 3-story masonry-infilled RC frame retrofitted with composite materials. J Struct Eng 139:1340–1351. https://doi.org/10.1061/(ASCE)ST.1943-541X.0000689

Lu X, Yang B, Zhao B (2018) Shake-table testing of a self-centering precast reinforced concrete frame with shear walls. Earthq Eng Eng Vib 17:221–233. https://doi.org/10.1007/s11803-018-0436-y

Masroor A, Mosqueda G (2012) Experimental simulation of base-isolated buildings pounding against moat wall and effects on superstructure response. Earthquake Eng Struct Dynam 41:2093–2109. https://doi.org/10.1002/eqe.2177

Mayorca P, Sathiparan N, Guragain R, Meguro K (2006) Comparison of the seismic performance of different strength masonry structures retrofitted with PP-band meshes. In: 5th international symposium on new technologies for urban safety of mega cities in Asia, Phuket, Thailand

Papadrakakis M, Mouzakis HP (1995) Earthquake simulator testing of pounding between adjacent buildings. Earthquake Eng Struct Dynam 24:811–834. https://doi.org/10.1002/eqe.4290240604

Sołtysik B, Falborski T, Jankowski R (2017) Preventing of earthquake-induced pounding between steel structures by using polymer elements–experimental study. Procedia Eng 199:278–283. https://doi.org/10.1016/j.proeng.2017.09.029

Takabatake H, Yasui M, Nakagawa Y, Kishida A (2014) Relaxation method for pounding action between adjacent buildings at expansion joint. Earthquake Eng Struct Dynam 43:1381–1400. https://doi.org/10.1002/eqe.2402

Tu YH, Chuang TH, Liu PM, Yang YS (2010) Out-of-plane shaking table tests on unreinforced masonry panels in RC frames. Eng Struct 32:3925–3935. https://doi.org/10.1016/j.engstruct.2010.08.030

Yuen TY, Zhang HH, Kuang JS, Huang Q (2018) Shake table tests on RC frame infilled by slitted masonry panels. Bull Earthq Eng 16:4027–4052. https://doi.org/10.1007/s10518-018-0339-3

Zhang H, Kuang JS, Yuen TYP (2017) Low-seismic damage strategies for infilled RC frames: shake-table tests. Earthquake Eng Struct Dynam 46:2419–2438. https://doi.org/10.1002/eqe.2911

Chapter 5
The Effect of Earthquake Damages Created by Shaking Table Tests on Dynamic Characteristics of Masonry Structures

Ali Kaya, Boudjamaa Roudane, Ahmet Can Altunışık, and Suleyman Adanur

Abstract Masonry constructions are edifices created through the amalgamation of fragile substances like stones, bricks, and pumice utilizing mortar. The masonry structures, which do not show the desired ductile behavior against dynamic effects, show a brittle behavior. In scenarios like earthquakes, when masonry structures surpass their load-bearing capabilities, this circumstance leads to heavy damage. Knowing the dynamic behavior of masonry constructions will help to take precaution to minimize the loss of life and property, since a significant part of people live in masonry buildings. Both analytical and experimental methods are employed to determine the damping ratios, natural frequencies and mode shapes of the buildings. which depend on the dynamic properties of the structures subjected to dynamic loads. This study explored variations in the dynamic attributes of a half-scale, single-span, and single-story masonry model constructed with hollow bricks under various damage scenarios. To acquire varying levels of damage cases, the model is tested on a shaking table with gradually different earthquake data. To observe the earthquake damages experimentally, the modal parameters of the masonry model were ascertained through ambient vibration tests conducted under both intact and impaired conditions. Also, A nonlinear analytical one-story masonry model is developed using finite element ABAQUS software with macro modelling methodology for examining the characteristics of masonry models subjected to different earthquakes. Six different test cases using same model are investigated analytically.

Keywords Masonry · Operational modal analysis · Abaqus · Macro model · Dynamic characteristics

A. Kaya
Department of Engineering, Artvin Coruh University, Artvin, Turkey

B. Roudane · A. C. Altunışık (✉) · S. Adanur
Department of Civil Engineering, Karadeniz Technical University, Trabzon, Turkey
e-mail: ahmetcan8284@hotmail.com

5.1 Introduction

Due to a series of earthquakes in recent times, the evaluation and safeguarding of the structural integrity of masonry constructions have grown into matters of heightened significance. Occurrences such as progressive deformations over time, abnormal and/or excessive loading, ground settlements, flooding, fires, and conflict significantly undermine the durability of masonry structures. Nevertheless, the primary challenge faced by masonry structures remained their susceptibility to earthquakes. Moreover, a majority of historical edifices are constructed using masonry techniques. In the recent past, the San Paolo cathedral and other historical masonry structures have been heavily damaged by earthquakes (Parisi and Augenti, 2013; Altunisik et al., 2016a).

The amount of uncertainty associated with various aspects impacting the construction's performance is one of the primary issues that must be addressed in the structural study of masonry structures. Considerations such as the mechanical characteristics of the building components, the structure construction methods, the connection types, or the structure's cracking state may generate significant differences between numerical and experimental findings (Atamturktur and Laman, 2012). Ground Vibration Testing, Modal Testing, Full-Field Vibration Testing, Modal Parameter Identification, Vibration Troubleshooting, Experimental Modal Analysis (EMA) and Operational Modal Analysis (OMA), and among others are some of the methods. In this regard, non-destructive techniques prove to be valuable tools for providing information on a building's structural behavior (Diaferio et al., 2015; Lacanna et al., 2016). The dynamic features offered by ambient vibration approaches, in particular, have proven to be especially well-suited for validating and updating numerical models (Friswell and Mottershead, 1995). Given that it is a non-invasive and non-destructive approach that can be done under service circumstances, OMA has established itself as one of the most appropriate techniques for estimating the modal characteristics of a construction. On this basis, OMA is now recognized as a very practical approach for dynamically characterizing masonry structures, as it does not need the use of the greater external stimulation (shakers or impact hammers) necessary for traditional EMA.

Atamturktur et al. (2010) provide a more detailed examination of the technical and practical distinctions between OMA and EMA when used for dynamic testing of masonry structures. Ivanovic et al (2015) also presented a comprehensive review of the subject matter. Altunişik et al. (2016) utilized OMA to examine the dynamic properties of the historic Zağanos Bastion. They then applied these findings to update the FE model of the structure. As a result, by using dynamic characteristics determined with OMA application, numerical models may be adjusted to achieve an accurate assessment of the structure's real behavior. This approach enables the utilization of updated FE models to conduct structural analyses based on current conditions or to predict the potential outcomes of diverse structural scenarios that the edifice might encounter. Many occurrences of using ambient vibration experiments to update numerical models in ancient structures have been documented in recent decades

(Aras et al., 2011; Gentile and Saisi, 2007; Ramos et al., 2013; Gentile et al., 2015). The utilization of OMA for assessing the structural performance of specific intricate elements within a construction, such as vaults or domes, is demonstrated in the work of (Atamturktur et al., 2011; Çalık et al., 2015). Compana et al. (2017) utilized OMA to provide dynamic characterization of the vaults within the Basilica chapel, aiming to enhance comprehension of this intricate construction. In subsequent research, they employed the obtained data to refine a finite element model, aiming to assess and analyze its current safety level.

In this study, the changes in the dynamic characteristics of a half scale single-span and single-story masonry model built with hollow brick for different damage conditions were investigated. To acquire varying levels of damage cases, the model is tested on a shaking table with gradually different earthquake data. To observe earthquake-induced damages experimentally, the masonry model's traits were established via ambient vibration tests. These tests were conducted to identify the modal parameters of the model under both undamaged and damaged conditions. Also, this study aims by formulating and validating a finite element modeling scheme using the ABAQUS software.

5.2 Experimental Campaign

The complete experimental plans consist of the material tests, ambient vibration tests, and the shake table tests. In experimental investigations conducted using a shaking table, constructing full-scale laboratory models is often not favored due to limitations in laboratory resources, construction challenges, and associated risks. Consequently, scaled-down laboratory structures or structural components are typically employed in these experimental endeavors. In this section, experimental research is conducted to explore the dynamic attributes of a half-scale masonry structure. To accomplish this, an specimen was constructed utilizing hollow brick components, followed by conducting shaking table tests under varied ground motions to induce diverse damage scenarios. Comparative analysis and discussion of the outcomes derived from ambient vibration tests were performed both before and after each experimental trial.

Shake table tests are the method that simulates the earthquake behavior of the structure in the same quality as the loads acting on the earthquake to understand the dynamic response of the structures in the most accurate way. In the shaking table method, the structure is forced by the loads closest to the earthquake loads with the loading mechanisms that apply forces that shake the structure, such as inertia forces acting on the structure during an earthquake. Shake table assemblies and installation are very costly. Therefore, testing can be carried out on scale models built in a laboratory environment by manufacturing shaking tables in various sizes. The cost of a shaking table that shakes a larger-scale structure or structural element with earthquake action is quite high. The shaking table artificially generates one,

two and three dimensional earthquake motions. Model structures should be rigidly attached to the shaking table prior to dynamic testing.

The bricks of $215 \times 102 \times 65$ mm (length $\times$ width $\times$ height) was constructed in 22 layers masonry model on a concrete foundation as shown in Fig. 5.1. The laboratory model had dimensions of $1800 \times 1800 \times 1600$ mm with a door opening of 450×1000 mm and a window opening of 450×550 mm, as shown in Fig. 5.1. Considering the stress concentration near the openings, the openings were placed symmetrically in the model buildings to evenly distribute the resistance and stiffness. Concrete lintels are used in the window and door openings of the building models. The void ratio for the brick elements was selected as 23%, adhering to the guidelines of the Turkish Building Earthquake Code (TBEC). A mortar blend consisting of a 1:3 ratio (cement to sand) was utilized for constructing the model, and the mortar was applied with a thickness of 7.5 mm. The model was constructed in accordance with standard construction practices prevalent in Turkey. A reinforced concrete foundation with dimensions of $2.1 \times 2.1 \times 0.2$ m was constructed. To secure the model to the shaking table during testing, 16 rod holes were integrated. The first row of bricks of the walls were embedded into the foundation to emulate a fixed boundary condition. This step was implemented to ensure that the model remained firmly attached to the foundation and to prevent any detachment or sliding during the testing procedure. Reinforced concrete slabs sized 1800 mm by 1800 and 100 mm were utilized. For the half-scale model designated for shaking table tests, a wall thickness of 100 mm was chosen. The material characteristics of the mortar and brick employed in the experiments can be found in Table 5.1.
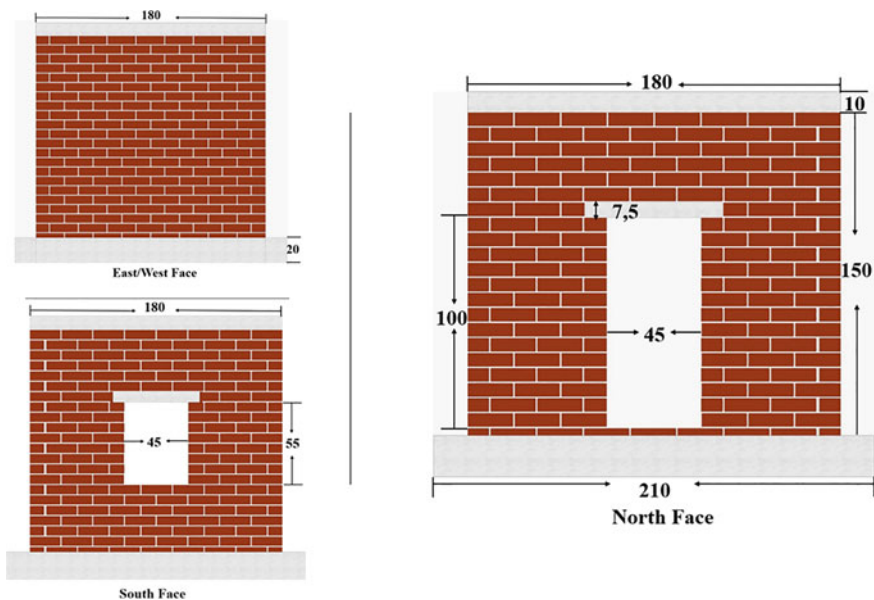

Fig. 5.1 Dimensions of the masonry building

Table 5.1 Mechanical properties of materials

Brick		Mortar	
Compressive strength	Density	Compressive strength	Tensile strength
45 *MPa*	1660 kg/m^3	14,22 *MPa*	1,77 *MPa*

During the process of experimentally ascertaining the dynamic attributes of models produced under carefully controlled laboratory conditions, the OMA (2006) technique is utilized. This method relies on conducting environmental vibration tests. System equipment to be used within the scope of measurements, single and three-axis accelerometers, data collection system, software, etc. B&K 4506 B 003 triaxial accelerometers are used during the experiments to determine the structural vibrations. The data collection system consists of a data collection unit and a computer. The data acquisition unit transfers the vibration signals from the accelerometers to the computer. Signals are processed with a computer program interface. B&K 3560 C type 17-channel data acquisition system is used. Within the scope of the experiments, PULSE (2006) software developed by Brüel & Kjaer Company is used to introduce the accelerometers to the data acquisition unit, to store the signals to the data acquisition unit, and to transfer the stored signals to the signal conditioning program. The OMA software is employed to process the signals obtained through experimental techniques and discern the dynamic properties of the model. Once the laboratory specimen was constructed and prior to inducing any damage, the OMA approach was employed to ascertain the dynamic properties of the specimen (refer to Fig. 5.2). Accelerometers were strategically positioned on the building walls to capture vibrations in both horizontal and vertical orientations. During the measurement process, the first three frequency values of the building model and the mode shapes represented by these frequencies were determined. Multiple measurements were conducted from various locations and using a greater number of accelerometers to acquire more comprehensive data. In this way, the necessary work before the damage will be completed. The dynamic characteristics of pre-damage OMA measurements are presented below.

Throughout the incremental shaking table tests, acceleration data sourced from previous earthquakes and sine wave signals were utilized as input ground motion data. This process was performed using peak ground accelerations (PGA). The seismic excitations for the shaking table test consisted of the 1994 Northridge Earthquake, the 2004 Parkfield Earthquake, and the 1979 Coyote Lake Earthquake. These acceleration data were sourced from the Pacific Earthquake Engineering Research Center Database (PEER, 2023). Furthermore, three distinct sine waves were employed, each with an amplitude of 50 mm, frequency of 2.00 Hz, and acceleration level of 0.80 g, taking into account various cycles. Table 5.2 summarizes the sequence and characteristics of the seismic excitations used in the 7 shaking table loading cases applied in this research. The accelerations of the selected records can be seen in Fig. 5.3.
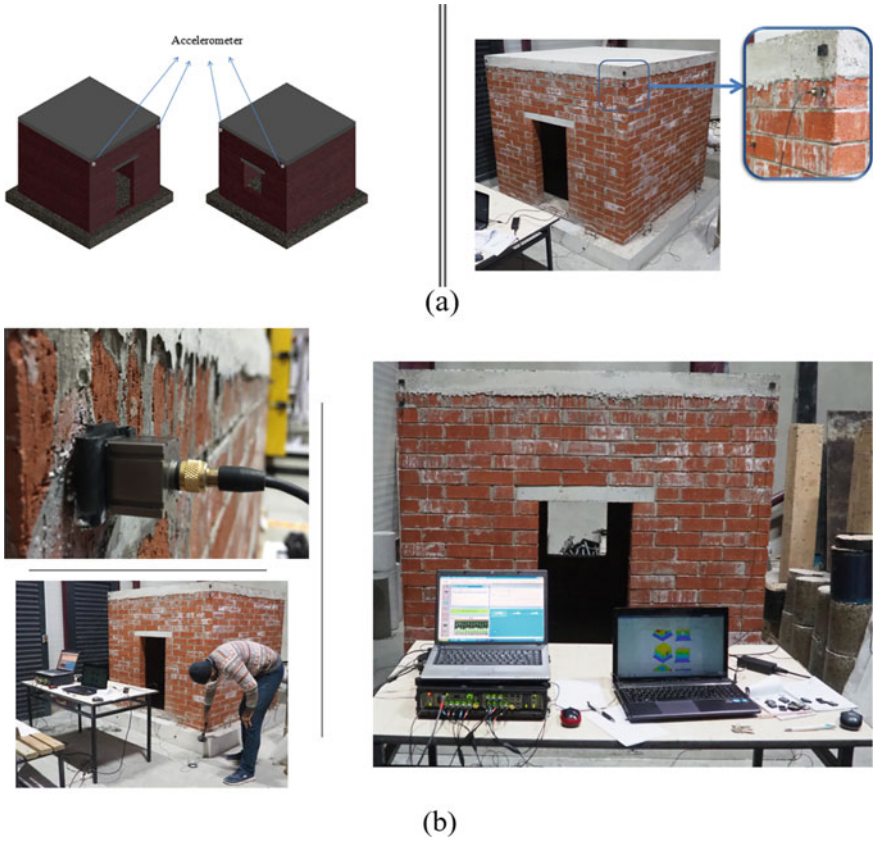
Fig. 5.2 **a** Location of accelerometers **b** Ambient vibration test measurements

Table 5.2 Earthquake sequence

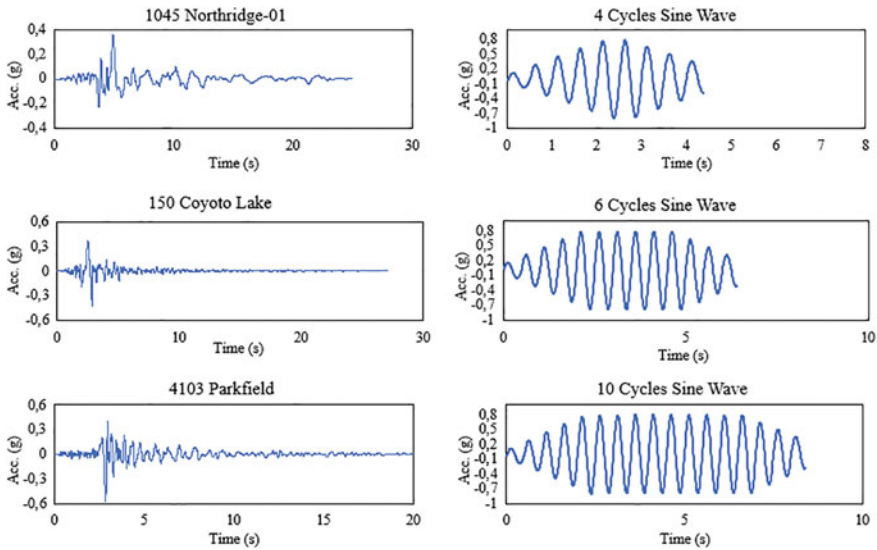| No	Name	Station	PGA (g)	PGV (cm/s)	PGD (cm)	Magnitude
GM-1	Northridge	W Pico Canyon Rd	0.35	59.22	16.03	6.7
GM-2	Coyote lake	Gilroy array #6	0.42	44.34	12.44	5.7
GM-3	Parkfield	Parkfield fault zone 1	0.6	63.77	8.46	6
GM-4	4 cycles sine wave	–	0.8	–	5.0	–
GM-5	6 cycles sine wave	–	0.8	–	5.0	–
GM-6	10 cycles sine wave	–	0.8	–	5.0	–

Fig. 5.3 The time-history plots depicting the chosen ground motion profiles

5.3   Results and Discussion

5.3.1   Ambient Vibration Test

Visual investigation of the model was carried out in the sequel to every loading condition imposed on the shake table. The development and propagation of cracks were carefully observed and noted. This aid in the evaluation of damage progression. Ambient vibration measurements conducted prior to and after each loading condition were utilized to determine the modal parameters representing the initial and current damage states of the model. These parameters were compared to evaluate the damage experimentally. No significant cracking was observed after the first two loading conditions (GM-1 and GM-2). After the GM-3 seismic loading condition, the first micro cracks began to be observed in the wall. Since there were no obvious cracks, DS-1 (No Structural Damage) was classified according to EMS-98 (Grünthal, 1998), where the damages were categorized.

The subsequent loading conditions (GM-4 and GM-5) revealed that existing micro-cracks had significantly expanded, and many new ones had developed on all external sides. A huge percentage of the cracks were almost horizontal at this point. They were caused by sliding motion at the first two layers of brick slightly below the slab. Previous experimental research conducted by Chellappa and Dubey (2017) on unreinforced masonry buildings found similar crack propagation. A diagonal crack which is attributed to in-plane deformation was also observed on the northern face of the masonry. Due to the significantly greater strength of the bricks

compared to the mortar, diagonal cracks emerged along the mortar bed joints. It stretched from the right top corner of the opening towards the right edge of the slab. The width of diagonal and nearly horizontal cracks was less than 1 mm. Furthermore, the observed damages were of a mild nature, resulting in the classification of damage as DS-2 (Slight Structural Damage) in type. The last test before the collapse results in the further expansion of the already existing cracks. Shear-sliding cracks were also discovered at the first two layers of brick, slightly above the foundation level and around the support over openings. As of the conclusion of the test, However, the residual widths of existing diagonal cracks and nearly horizontal fractures did not exhibit significant expansion by the conclusion of the shaking test. In contrast, videos recorded during the seismic testing phase indicated a different outcome. Notably, the breadth of the shear-stepped diagonal fracture at the upper corner of the door had undergone a substantial increase. The cracks were found to measure in the centimeter range. Consequently, the structural damage was reclassified as DS-4 (Heavy Structural Damage) type (refer to Fig. 5.4). Afterwards, the measuring systems (accelerometers and LVDTs) were removed from the test setup for security reasons. The final loading condition before collapse, a 10-cycles sine function wave was reapplied to the DS-4 model. This resulted in the complete collapse of the masonry model. The structural damage classification at this stage is obviously DS-5 (Total Collapse) type. The cumulative damage model on the outer surface of the model is shown in Fig. 5.5.

The correlations between the masonry structure's modal characteristics and the damage caused by progressive shake table tests were examined. After each loading condition, subsequent to the application of ambient vibration measurements, dynamic parameters were established. The ambient vibration tests were conducted utilizing identical accelerometer configurations and measurement specifications as those used

Fig. 5.4 The pattern of damage on the specimen's external surface for the DS-4 type
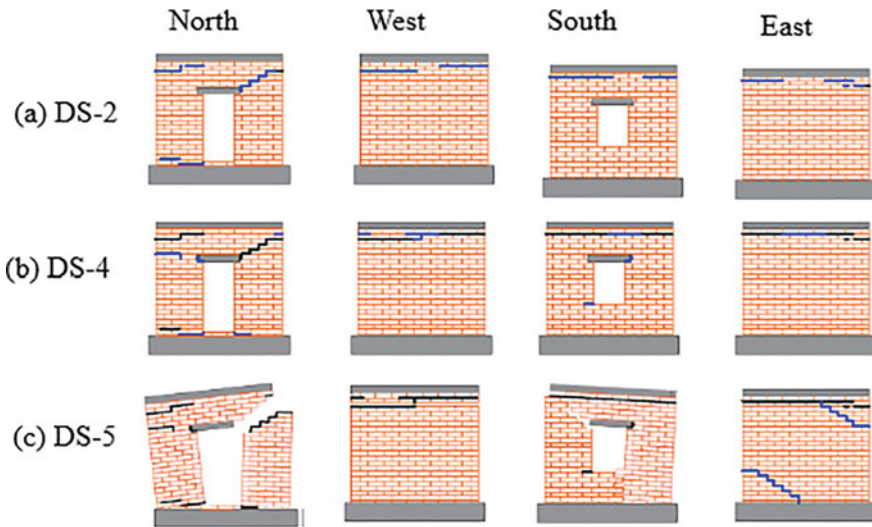
Fig. 5.5   The pattern of cumulative damage on the specimen's external surface

in the pre-damage assessment. Therefore, through a comparison of the modal characteristics before and after damage, the influence of the inflicted damages on the dynamic parameters was scrutinized.

For system identification of test specimens, the Enhanced Frequency Domain Decomposition (EFDD) approach in the frequency domain was used. The Singular Values of Spectral Density Matrices (SVSDM) corresponding to the initial three mode shapes and natural frequencies were presented due to the EFDD technique. The SVSDM graphs for both the before and after damaged conditions of the model are illustrated in Fig. 5.6. The initial three natural frequencies for the condition before the damages occurred were found as 22.07, 27.49 and 45.16 Hz. These corresponded to the transverse, longitudinal, and torsional mode shapes. Figure 5.7 provides a comparison between the first three mode shapes extracted from assessments prior to testing and the post-test damaged conditions. Transverse and longitudinal mode shapes were found to have altered considerably to incorporate torsional behavior with structural degradation. Furthermore, no consistency exists between the undamaged and damaged states. Modal characteristics after each shaking table test were determined (Table 5.3). The comparison between the natural frequencies determined for the pre-damage and post-damage cases is shown in Fig. 5.8.

5.3.2   Finite Element Modeling

In these analyses, three-dimensional solid element with 8 nodes and 3 degrees of freedom was modeled with C3D8R in modeling of concrete and masonry walls, the
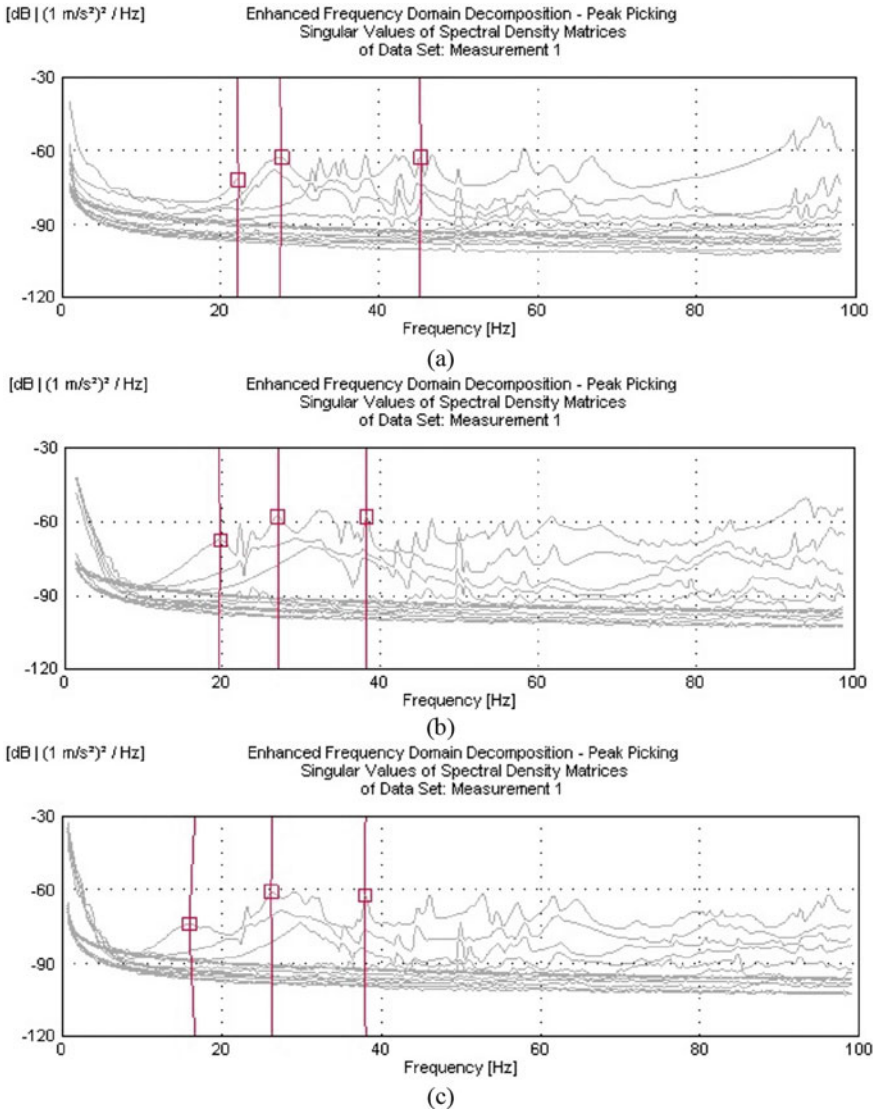
Fig. 5.6 SVSDM **a** undamaged; **b** DS-2; **c** DS-4

shape of this element is shown in Fig. 5.9. The reinforcement element types are T3D2. While the number of elements in the model is 3447 and the number of nodes is 5168, the weight of the model is 21.74 tons.

Using the single-storey model macro-modeling technique in ABAQUS software based on finite element modeling, brick and mortar were represented as a single homogenous material, as illustrated in Fig. 5.9. How the elements are chosen carefully
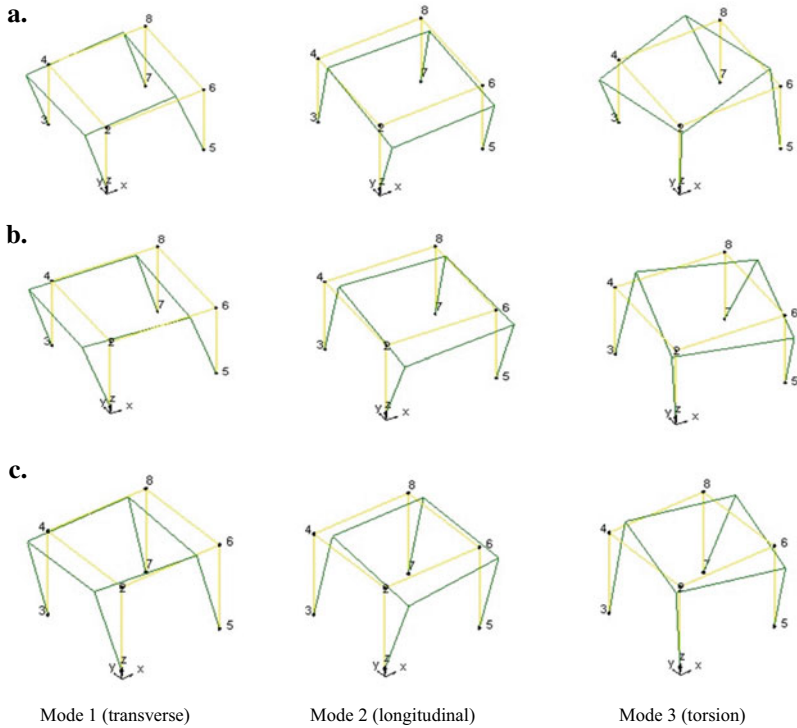
a.

b.

c.

Mode 1 (transverse)   Mode 2 (longitudinal)   Mode 3 (torsion)

Fig. 5.7 The initial three mode shapes determined through ambient vibration tests **a** undamaged; **b** DS-2; **c** DS-4

Table 5.3 The modal characteristics after every loading conditions

EQ	1st mode (Hz)	2nd mode (Hz)	3rd mode (Hz)
GM-0	22.07	27.49	45.16
GM-1	22	27.45	44.8
GM-2	21.71	27.38	44
GM-3	21.24	27.31	41.55
GM-4	20.81	27.27	40.93
GM-5	19.51	27.06	38.28
GM-6	16.69	26.46	38.11
GM-6	–	–	–

has significant impacts on the computational efficiency and result correctness of FE analysis. Therefore, the application of fine meshes and rational element types is highly crucial to achieving acceptable accuracy in ABAQUS modeling results. If the mesh is divided too finely, the computing capabilities required to execute the model will increase, resulting in very high costs. For this reason, it is divided into finite elements
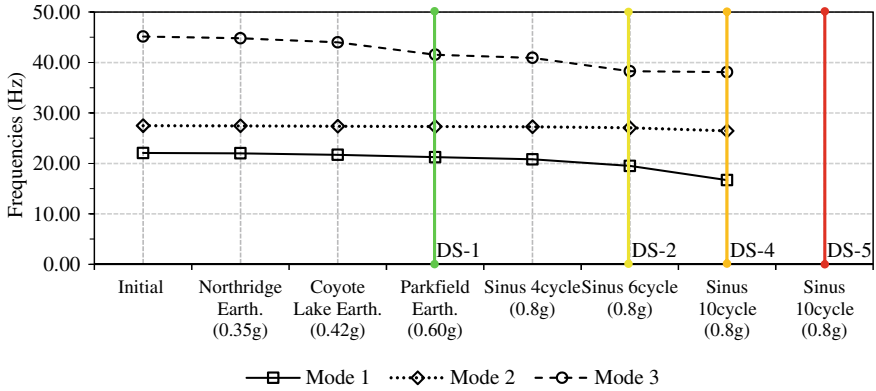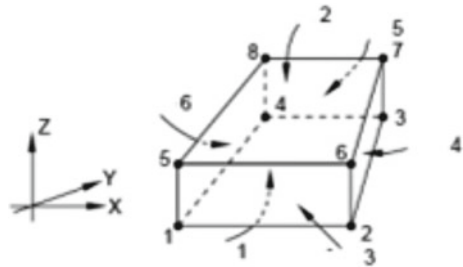
Fig. 5.8 Variations in the first three natural frequencies of the model across different damage states

Fig. 5.9 C3D8R model

of 50 mm size. It can be seen in Fig. 5.10. Non-linear analysis was performed using an explicit dynamic procedure implemented in ABAQUS software. The results of the first three modes of the undamaged and heavy structural damaged (DS-4) model obtained by analytical and experimental studies are presented in Table 5.4.
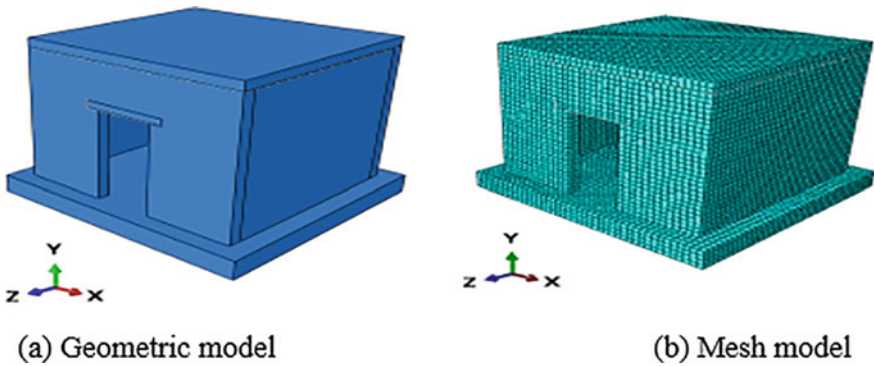

(a) Geometric model   (b) Mesh model

Fig. 5.10 Geometric model and mesh model of single-story model

Table 5.4 Comparison of the characteristics of the main modes

Damage state	Mode no	Mode direction	Frequency (Hz)		Relative difference (%)
			Analytical	Experimental	
Undamaged	1	Transverse	22.61	22.07	2.45
	2	Longitudinal	27.89	27.49	1.46
	3	Torsional	43.24	45.16	4.25
DS-4	1	Transverse	16.87	16.69	1.10
	2	Longitudinal	26.33	26.46	0.50
	3	Torsional	38.05	38.11	0.20

The results of the ABAQUS software were remarkably comparable to the laboratory findings when the analytical results were compared to the results of the experimental studies. While the natural frequency values were quite well predicted by analytical modeling, they found an average of 5% errors when looking at Fig. 5.11. Thus, a FE models that accurately represents the real structure was produced using the dynamic parameters of the FE models. Yet, it appears that the fundamental reason for the disparity between the findings of the FE model and OMA lies in the material properties of the masonry walls.

The damage patterns were successfully developed by the numerical simulation (Fig. 5.12). An illustration of the tensile damage obtained by the brick building
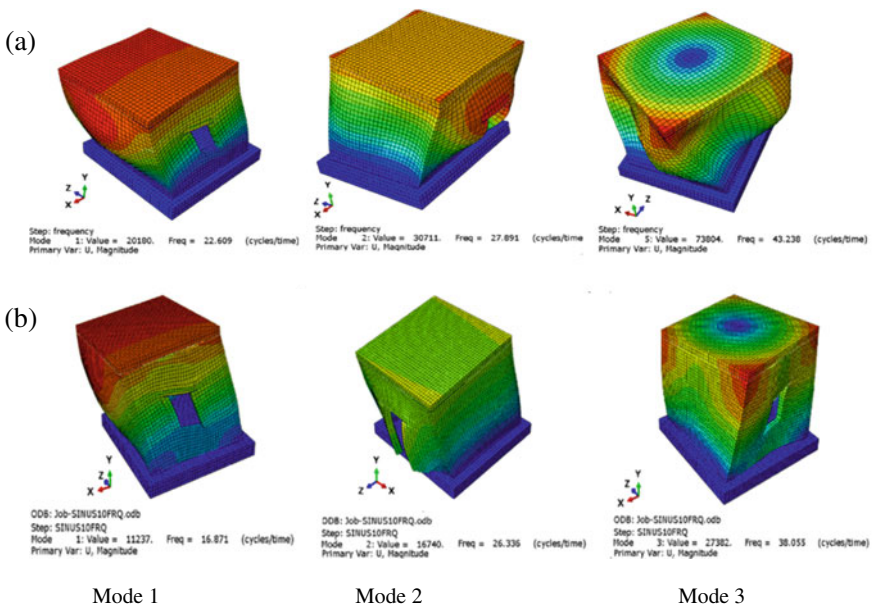

Fig. 5.11 Mode shapes obtained analytically; **a** Undamaged, **b** Heavy damaged (SD-4)

during the non-linear time history analysis investigation. For north and south faces, diagonal cracks were created from four corners of the window to the four corners of the wall induced by in-plane shearing. The cracks appeared obviously in the case of the considerable excitation amplitude of last case. The left and right faces have many longitudinal cracks generated by the out-of-plane loading. The damage patterns determined by the finite element analysis can coincide with the cracks of the model in the experimental studies. It is evident that damage from compression does not have a substantial impact on the determination of failure behavior in masonry buildings subjected to shear or seismic stimulation. This fact provides an argument to exclude an analysis of this specific issue from the scope of the current paper.
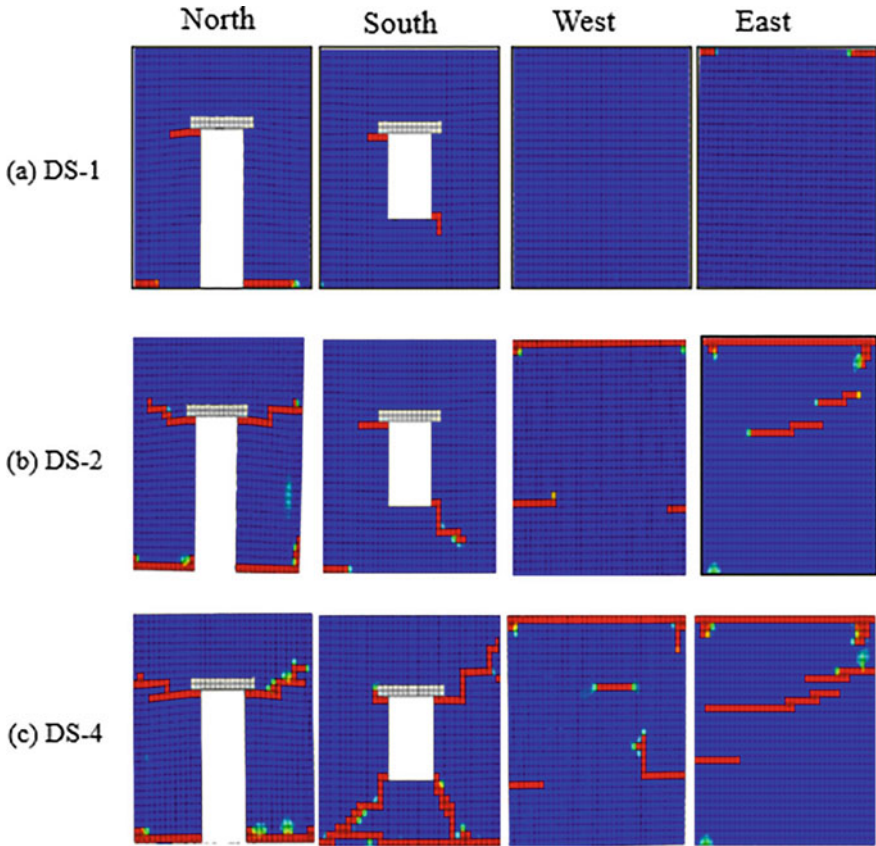

Fig. 5.12 Cumulative damage model on the outer surface of the model (analytical)
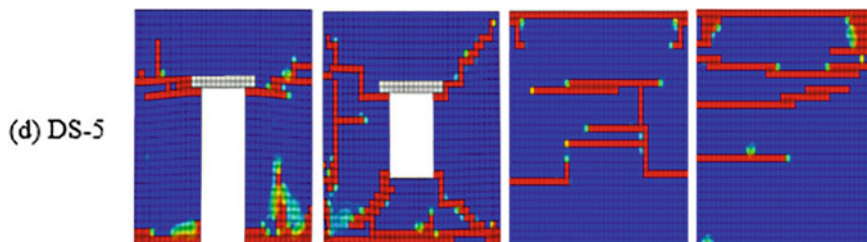
(d) DS-5

Fig. 5.12 (continued)

References

Altunisik AC, Bayraktar A, Genc AF (2016) A study on seismic behaviour of masonry mosques after restoration. Earthq Struct 10(6):1331–1346

Altunişik AC, Adanur S, Genç AF, Günaydin M, Okur FY (2016) Non-destructive testing of an ancient masonry bastion. J Cult Herit 22:1049–1054

Aras F, Krstevska L, Altay G, Tashkov L (2011) Experimental and numerical modal analyses of a historical masonry palace. Constr Build Mater 25:81–91

Atamturktur S, Laman J (2012) Finite element model correlation and calibration of historic masonry monuments. Struct Des Tall Spec Build 21(2):96–113

Atamturktur S, Fanning P, Boothby T (2010) Traditional and operational modal testing of masonry vaults. ICE Eng Comput Mech 163:213–223

Atamturktur S, Luke B, François H, Sezer A (2011) Vibration characteristics of vaulted masonry monuments undergoing differential support settlement. Eng Struct 33(9):2472–2484

Çalık İ, Bayraktar A, Türker T, Karadeniz H (2015) Structural dynamic identification of a damaged and restored masonry vault using ambient vibrations. Meas 55:462–472

Chellappa S, Dubey RN (2017) Performance evaluation of a reinforced masonry model and an unreinforced masonry model using a shake table testing facility. J Perform Constr Facil 32(1).

Compana V, Pachónb P, Cámarac M (2017) Ambient vibration testing and dynamic identification of a historical building. Basilica of the fourteen holy helpers (Germany). X Int Conf Struct Dyn, EURODYN 2017. Rome

Diaferio M, Foti D, Giannoccaro N (2015) Identification of the modal properties of a building of the Greek heritage. Key Eng Mater 628:150–159

Friswell M, Mottershead J (1995) Finite element model updating in structural dynamics. Kluwer Academic Publishers, Amsterdam

Gentile C, Saisi A (2007) Ambient vibration testing of historic masonry towers for structural identification and damage assessment. Constr Build Mater 21:1311–1321

Gentile C, Saisi A, Cabboi A (2015) Structural identification of a masonry tower based on operational modal analysis. Int J Arch Herit 9:98–110

Grünthal G (1998) European Macroseismic Scale 1998. LUXEMBOURG

Ivanovic SS, Trifunac MD, Todorovska MI (2015) Ambient vibration tests of structures-a review. ISET J Earthq Technol 37(4):165–197

Lacanna G, Ripepe M, Marchetti E, Coli M, Garzonio C (2016) Dynamic response of the Baptistery of San Giovanni İn Florence, Italy, based on ambient vibration test. J Cult Herit (2016).

OMA (2006) Release 4.0 computer software. Aalborg, Denmark, Structural Vibration Solution

Parisi F, Augenti N (2013) Earthquake damages to cultural heritage constructions and simplified assessment of artworks. Eng Fail Anal 34:735–760

PEER (2023) (Pacific Earthquake Engineering Research Centre). https://ngawest2.berkeley.edu/.

PULSE, Analyzers and Solutions (2006) Release 11.2., Denmark: Bruel and Kjaer (sound and vibration measurement A/S)

Ramos LF, Aguilar R, Lourenço PB, Moreira S (2013) Dynamic structural health monitoring of Saint Torcato church. Mech Syst Signal Process 35:1–15

Part II
Fiber Reinforced Polymeric (FRP) Composite Structures

Chapter 6
Numerical Modeling of DCB Mode 1 Delamination Propagation in Composite Laminates Using Cohesive Zone Model

Mouad Bellahkim, Ahmed Ouezgan, Nawal Achak, Aziz Maziri, El Hassan Mallil, and Jamal Echaabi

Abstract   In this study, utilizing relatively refined meshes, we present a novel Cohesive Zone Model (CZM) to predict delamination propagation precisely and reliably in composite laminates under static loads. This finite element analysis consists to define elements at the interface between two composite plates and an interface damage law. This analysis was conducted using ABAQUS software, where we employed the guidelines outlined in the ASTM D5528 standard for composite Double Cantilever Beam (DCB) testing to numerically simulate the propagation of delamination under pure mode 1 conditions. We have compared the outcomes of this numerical model with existing literature and engaged in a discussion regarding their validity.

6.1   Introduction

Laminated composites find extensive use in applications necessitating weight reduction. As usage grows, the likelihood of eventual breakage also increases. Ensuring the integrity of components in service and the future product design necessitates the capability to characterize failures, such as identifying failure modes, parameters, or critical failure thresholds (Reddy 2003). It is a mechanism of decohesion between the layers which appears on the free edge or/and inside the specimen (Lorriot et al.

M. Bellahkim (✉) · A. Ouezgan · A. Maziri · E. H. Mallil · J. Echaabi
Laboratory of Mechanics, Engineering and Innovation (LM2I), ENSEM, Hassan II University of Casablanca, Casablanca, Morocco
e-mail: mouad.bellahkim@ensem.ac.ma

N. Achak
Team of Modeling and Simulation of Mechanical and Energetic, Faculty of Sciences, Mohammed V University, Rabat, Morocco

2003). Because of the high interlaminar stresses near the edges, the delamination generally begins there, then progresses by separating the layers. In many situations, especially during an impact, matrix cracking and delamination are strongly coupled phenomena (Wisnom and Hallett 2009).

Design engineers are very interested in FE modeling of delamination propagation to better understand a structure's failure process. Finite element software offers three established approaches for studying crack propagation across various materials. These methods include the Virtual Crack Closure Technique (VCCT) (Irwin 1957; Karimi et al. 2022), Cohesive Zone Model (CZM) (Elices et al. 2002; Lu et al. 2019), and Extended Finite Element Method (XFEM) (Sosa and Karapurath 2012). Delamination can be categorized as across the width or in a narrow strip (Yeh and Fang 1999; Yin et al. 1986; Bruno 1988; Bruno and Grimaldi 1990; Kardomateas 1993; Kardomateas and Pelegri 1994; Sheinman et al. 1998; Bruno and Greco 2000), circular (Kim 1997; Bottega and Maewal 1983; Cochelin and Potier-Ferry 1991), elliptic (Chai and Babcock 1985), rectangular (Whitcomb and Shivakumar 1989), or capricious (Kim 1997; Bottega and Maewal 1983) contingent on their shape. Delaminations can be categorized into three distinct types: thin film, symmetric split, and general delaminations, depending on their location within the laminates thickness. Additionally, an extensive investigation encompassing both buckling and propagation was conducted for laminated composite plates featuring multiple delaminations occurring under in-plane compressive stress, as detailed in references (Cochelin and Potier-Ferry 1991; Chai and Babcock 1985). (Whitcomb and Shivakumar 1989; Bottega 1983) describe experimental findings on delamination buckling. Another delamination configuration explored in the literature involves beam-type delamination specimens submitted to various loading conditions, including bending, axial, and shear loading (Whitcomb and Shivakumar 1989; Bottega 1983; Storåkers and Andersson 1988; Larsson 1991; Kouchakzadeh and Sekine 2000; Comiez et al. 1995; Kardomateas 1990; Allix and Corigliano 1996; Bruno and Greco 2001; Point and Sacco 1996). These specimens serve as the foundation for experimental methodologies employed to assess interlaminar fracture strength across a range of loading modes, including pure mode 1, mode 2, and mixed mode conditions, within laminated materials, adhesive joints, and other composites.

In this paper, the delamination propagation through a composite laminate interface is investigated numerically using a cohesive element model implanted in Abaqus/Standard. This laminate subjected to double cantilever beam (DCB) test (A. AC09036782 2007) to study the propagation under pure mode 1. This modeling is based on the interface elements characterized by traction–separation law combined with a damage evolution law. When the findings were compared to those in the literature (Alfano and Crisfield 2001), a strong correlation was found.

6.2   Numerical Simulation Method

6.2.1   Cohesive Zone Method

The cohesive zone method (CZM) relies on the concept that the stress transmission capability between the two adjacent layers of a delamination is not entirely lost at the onset of damage. Instead, it diminishes gradually due to a cumulative reduction in stiffness at that interface (Fig. 6.1).

Without considering the coupling effects, the relationship between the normal and shear tractions, as well as the normal and shear separations, of a cracked element is defined by Eq. (6.1) within the elastic constitutive model. In this equation, T represents the cohesive stress vector, δ stands for the displacement vector, and K represents the stiffness matrix of the elements

$$\overrightarrow{T} = \begin{Bmatrix} t_n \\ t_s \\ t_t \end{Bmatrix} = \begin{bmatrix} K_n & 0 & 0 \\ 0 & K_s & 0 \\ 0 & 0 & K_t \end{bmatrix} \begin{Bmatrix} \delta_n \\ \delta_s \\ \delta_t \end{Bmatrix} = K \overrightarrow{\delta} \tag{6.1}$$

In addition to specifying the interface stiffness, this model necessitates the definition of both an initiation criterion for predicting crack initiation and a propagation criterion grounded in energy considerations. The criterion of initiation of the damage by interlaminar delamination adopted is based on a traction–separation law and is given by the quadratic function:

$$f = \left\{ \frac{\langle t_n \rangle}{t_n^0} \right\}^2 + \left\{ \frac{t_s}{t_s^0} \right\}^2 + \left\{ \frac{t_t}{t_t^0} \right\}^2 \tag{6.2}$$

Using the Benzeggagh-Kenane energy criterion (B-K), we predict delamination propagation under mixed-mode loading, where tn, ts, and tt represent the tensile stresses in the normal direction *n* and shear stresses *s* and *t*, while t0n, t0s, and t0t represent their corresponding critical values (Benzeggagh and Kenane 1996).

Fig. 6.1 Cohesive zone method to simulate delamination propagation

Elastic zone   Stress transfer   Stress-free
(D = 0)   zone (0 < D < 1)   zone (D = 1)
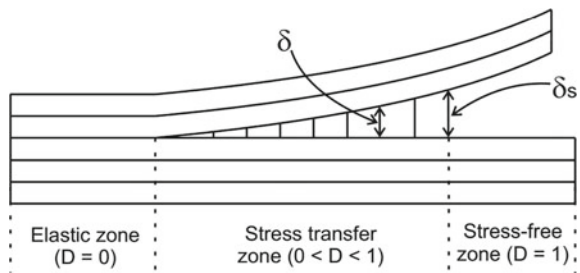
$$G = G_{IC} + (G_{IIC} - G_{IC}) \cdot \left(\frac{G_{II} + G_{III}}{G} \right)^{\eta} \tag{6.3}$$

In Eq. (6.3), G stands for the total strain energy release rate, encompassing mode 1 (GI), mode 2 (GII), and mode 3 ($GIII$) contributions. The parameter η is derived from experimental data obtained through a mixed-mode delamination test, allowing for the determination of the B-K parameter. A numerical reproduction of the DCB test made it possible to estimate the value of η at 2.284 and to calibrate the values of the interlaminar resistances.

6.2.2 Modeling of Delamination in Composites Materials

We utilize recommendations derived from a double cantilever beam (DCB) test to model the onset and progression of delamination in laminated composites. The numerical model comprises two half-layers of identical dimensions, with a very small separation distance of 0.001 mm between the two composite layers. The cohesive rule is introduced in the form of the cohesive elements defined in Abaqus while guaranteeing the pre-crack length $a_0 = 30$ mm. The geometry is described in.

Figure 6.2 and the mechanical characteristics of composite ply and cohesive interface are listed respectively in Tables 6.1 and 6.2.

The adhesive stiffness at the interface is intentionally selected to provide a level of rigidity that ensures a quasi-rigid connection between the plies. The values used are those reported in the work of Alfano & Crisfield (Alfano and Crisfield 2001).
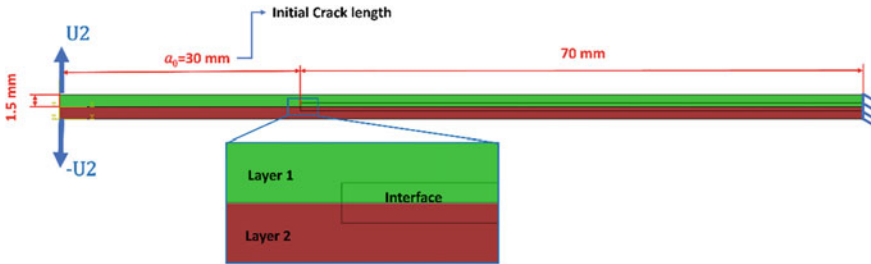

Fig. 6.2 DCB geometry

Table 6.1 Mechanical characteristics of composite layer (Alfano and Crisfield 2001)

Elastic modulus (GPa)		Shear modulus (GPa)		Poisson coefficients	
E_{11}	$E_{22} = E_{33}$	$G_{12} = G_{23}$	G_{13}	$\nu_{12} = \nu_{13}$	ν_{23}
153.3	9.0	5.2	3.3	0.24	0.46

Table 6.2 Mechanical characteristics of cohesive interface (Alfano and Crisfield 2001)

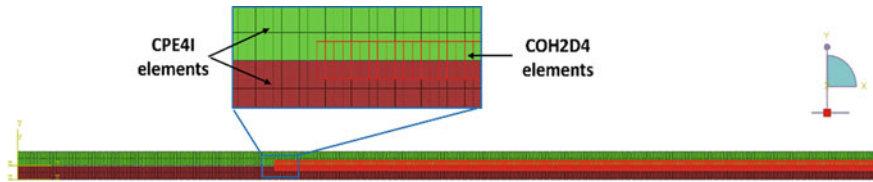| Adhesive stiffness (Pa)			Adhesive strength (Pa)			Critical fracture energies (J/m^2)		
Mode 1	Mode 2	Mode 3	Mode 1	Mode 2	Mode 3	Mode 1	Mode 2	Mode 3
$K_I = E/$ K_{nn}	$K_{II} = E/$ K_{ss}	$K_{III} = E/$ K_{tt}	t^0_n	t^0_s	t^0_t	G_{IC}	G_{IIC}	G_{IIIC}
570×10^{12}	570×10^{12}	570×10^{12}	5.7×10^7	5.7×10^7	5.7×10^7	280	280	280

Fig. 6.3 Mesh assignment and choice of elements

A refined mesh is used to discretize the composite plate by CPE4I Linear Quadri-lateral elements with 496 elements. However, the interface is meshed by two-dimensional cohesive elements (COH2D4) available in Abaqus. This element is used in conjunction with a viscosity parameter to hasten the convergence of the iter-ative solution. The sweep technique is employed for the interface meshing because the cohesive elements length depends on their orientation, since their elongation will signify the separation of the laminates in this instance, specifications should be made in the order across the entire thickness of the adhesive layer, spanning from the lower surface to the upper surface (Fig. 6.3).

A geometrical nonlinearity for large displacements is chosen in the static analysis with 1000 for the maximum number of increments. An imposed displacement U2 and -U2 are applied in the left extremity (U2 = 6 mm at x = 100 mm) while the other extremity is totally clamped (U1 = U2 = UR3 = 0 at x = 0 mm) (see Fig. 6.2).

6.3 Results and Discussion

In this part, the obtained numerical results will be presented and discussed for the DCB test to simulate mode 1 delamination. A comparison is also made with the published results (Alfano and Crisfield 2001) and an excellent consistency is found. The (Fig. 6.4 shows a load–displacement curve of layers separation plotted at the loaded extremity. The first slope of the curve indicates the separation of the layers along the pre-crack a_0. When the cohesive elements begin to deteriorate (damage), the reaction force decreases. At the second part of the decreasing curve, the response

force constantly decreases as the cohesive elements degrade (damaged response) (Fig. 6.4).

The Fig. 6.5 presents the Von Mises stress distribution for U2 = 6 mm, this distribution shows that the stress concentration is located at the cohesive interface. The Fig. 6.6 gives the separation displacement between composites layers. This separation has reached the maximum value given in the software. This implies that an increase in the separation displacement value results in greater damage to the cohesive zones.
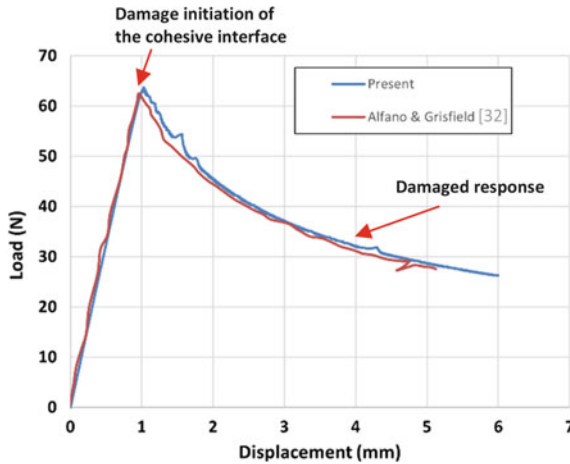

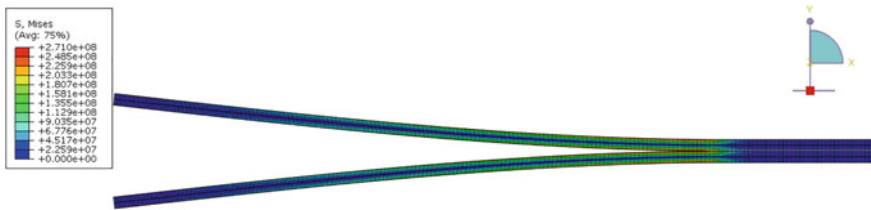**Fig. 6.4** Load–displacement curve of DCB test

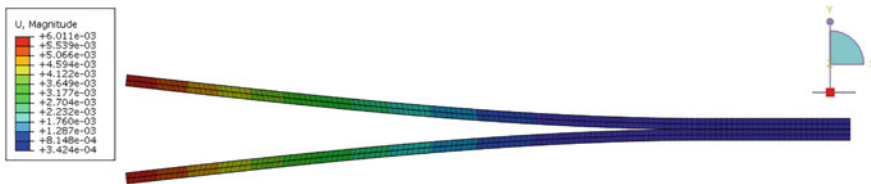**Fig. 6.5** Von mises stress distribution

Fig. 6.6 Separation displacement distribution, Umax = 6 mm

6.4 Conclusion

In this work, we have developed a 2D numerical model for simulating mode 1 delamination propagation under DCB test conditions using the cohesive zone model. This approach aims to identify an effective method for simulating delamination growth in composite laminates. This modeling approach involves incorporating an interface element Distinguished by a traction–separation relationship that relies on damage initiation and evolution criteria. The results are then compared to a previously published method in the literature, revealing a strong correlation.

References

A. AC09036782 (2007) ASTM D5528-standard test method for mode I interlaminar fracture toughness of unidirectional fiber-reinforced polymer matrix composites. ASTM Internat

Alfano G, Crisfield MA (2001) Finite element interface models for the delamination analysis of laminated composites: mechanical and computational issues. Int J Numer Methods Eng 50(7):1701–1736. https://doi.org/10.1002/nme.93

Allix O, Corigliano A (1996) Modeling and simulation of crack propagation in mixed-modes interlaminar fracture specimens. Int J Fract 77(2):111–140

Benzeggagh ML, Kenane M (1996) Measurement of mixed-mode delamination fracture toughness of unidirectional glass/epoxy composites with mixed-mode bending apparatus. Compos Sci Technol 56(4):439–449

Bottega WJ (1983) A growth law for propagation of arbitrary shaped delaminations in layered plates. Int J Solids Struct 19(11):1009–1017

Bottega WJ, Maewal A (1983) Delamination buckling and growth in laminates. J Appl Mech Trans ASME 50(1):184–189

Bruno D (1988) Delamination buckling in composite laminates with interlaminar defects. Theor Appl Fract Mech 9(2):145–159

Bruno D, Greco F (2000) An asymptotic analysis of delamination buckling and growth in layered plates. Int J Solids Struct 37(43):6239–6276

Bruno D, Greco F (2001) Delamination in composite plates: influence of shear deformability on interfacial debonding. Cem Concr Compos 23(1):33–45

Bruno D, Grimaldi A (1990) Delamination failure of layered composite plates loaded in compression. Int J Solids Struct 26(3):313–330

Chai H, Babcock CD (1985) Two-dimensional modelling of compressive failure in delaminated laminates. J Compos Mater 19(1):67–98

Cochelin B, Potier-Ferry M (1991) A numerical model for buckling and growth of delaminations in composite laminates. Comput Methods Appl Mech Eng 89(1–3):361–380

Comiez JM, Waas AM, Shahwan KW (1995) Delamination buckling; experiment and analysis. Int J Solids Struct 32(6–7):767–782

Elices M, Guinea GV, Gomez J, Planas J (2002) The cohesive zone model: advantages, limitations and challenges. Eng Fract Mech 69(2):137–163

Irwin GR (1957) Analysis of stresses and strains near the end of a crack traversing a plate.

Kardomateas GA (1990) Postbuckling characteristics in delaminated kevlar/epoxy laminates: an experimental study. J Compos Technol Res 12(2):85–90

Kardomateas GA, Pelegri AA (1994) The stability of delamination growth in compressively loaded composite plates. Int J Fract 65(3):261–276

Kardomateas GA (1993) The initial post-buckling and growth behavior of internal delaminations in composite plates.

Karimi S, Haji Aboutalebi F, Heidari-Rarani M (2022) Developments in remeshing-free fatigue crack growth simulation including a new adaptive virtual crack closure technique. Fatigue Fract. Eng. Mater. Struct. 45(8):2293–2312.

Kim H-J (1997) Postbuckling analysis of composite laminates with a delamination. Comput Struct 62(6):975–983

Kouchakzadeh MA, Sekine H (2000) Compressive buckling analysis of rectangular composite laminates containing multiple delaminations. Compos Struct 50(3):249–255

Larsson P-L (1991) On multiple delamination buckling and growth in composite plates. Int J Solids Struct 27(13):1623–1637

Lorriot T, Marion G, Harry R, Wargnier H (2003) Onset of free-edge delamination in composite laminates under tensile loading. Compos Part B Eng 34(5):459–471. https://doi.org/10.1016/S1359-8368(03)00016-7

Lu X, Ridha M, Chen BY, Tan VBC, Tay TE (2019) On cohesive element parameters and delamination modelling. Eng Fract Mech 206:278–296

Point N, Sacco E (1996) Delamination of beams: an application to the DCB specimen. Int J Fract 79(3):225–247

Reddy JN (2003) Mechanics of laminated composite plates and shells: theory and analysis. CRC press

Sheinman I, Kardomateas GA, Pelegri AA (1998) Delamination growth during pre-and post-buckling phases of delaminated composite laminates. Int J Solids Struct 35(1–2):19–31

Sosa JLC, Karapurath N (2012) Delamination modelling of GLARE using the extended finite element method. Compos Sci Technol 72(7):788–791

Storåkers B, Andersson B (1988) Nonlinear plate theory applied to delamination in composites. J Mech Phys Solids 36(6):689–718

Whitcomb JD, Shivakumar KN (1989) Strain-energy release rate analysis of plates with postbuckled delaminations. J Compos Mater 23(7):714–734

Wisnom MR, Hallett SR (2009) The role of delamination in strength, failure mechanism and hole size effect in open hole tensile tests on quasi-isotropic laminates. Compos Part A Appl Sci Manuf 40(4):335–342. https://doi.org/10.1016/J.COMPOSITESA.2008.12.013

Yeh M-K, Fang L-B (1999) Contact analysis and experiment of delaminated cantilever composite beam. Compos Part B Eng 30(4):407–414

Yin W-L, Sallam SN, Simitses GJ (1986) Ultimate axial load capacity of a delaminated beam-plate. AIAA J 24(1):123–128

Chapter 7
Durability of High-Performance Fiber Reinforced Cementitious Composites Subjected to Freeze–Thaw Cycles

Luciano Feo, Enzo Martinelli, Rosa Penna, and Marco Pepe

Abstract The application of high-performance fibre-reinforced cementitious composites (HPFRCCs) represents one of the most advanced solutions in the civil engineering field for both mitigating the criticisms of ordinary concrete while ate the same time enhancing its overall mechanical performances. Moreover, due to its significant durability resistance, HPFRCC material is highly recommended also in the view of reducing the cost for the long-term maintenance of reinforced concrete elements. More specifically, the capability of resisting against freezing promotes its possible use in cold regions where freeze–thaw cycling can lead to significantly degradation of cement-based composites. In this context, this study summarized the key results of an experimental campaign aimed at investigating the degradation processes generated by freeze–thaw actions on the resulting HPFRCCs. Furthermore, a numerical simulation is also performed for unveiling the degradation effect induced by the freeze–thaw cycles.

Keywords HPFRCC · Steel fibers · Experimental activity · Freeze–thaw cycles · Durability · Meso-scale model · Cracked-hinge approach

7.1 Introduction

Due to its improved rheology at the early age, significant mechanical behavior (i.e., compressive-tensile strengths), relevant ductility and durability coupled with low permeability, High-Performance Fiber-Reinforced Concrete (HPFRC) represent one of the major innovations in the rehabilitation and repair of existing buildings (Elsayed et al. 2022; Carlos Zanuy et al. 2021; Cheng et al. 2020; Elmorsy and Hassan 2021;

L. Feo (✉) · E. Martinelli · R. Penna · M. Pepe
Department of Civil Engineering, University of Salerno, Fisciano, SA, Italy
e-mail: lfeo@unisa.it

E. Martinelli · M. Pepe
TESIS Srl, Fisciano, SA, Italy

Sharma and Pal 2022; Pereiro-Barceló et al. 2019; O'Hegarty et al. 2021). Compared to a traditional concrete, the addition of fibers of different nature in HPC (Savino et al. 2019, 2018; Ashkezari et al. 2020; Caggiano et al. 2017, 2016; Joo Kim 2008; Uchida et al. 2010; Foti 2013; Choi et al. 2016; Savastano and Warden 2003; Li et al. 2006; Wenjie 2017; Smarzewski 2018, 2019; Reis and Ferreira 2004; Wang et al. 2019), allows to have a composite material with a higher resistance in the post-cracking phase: this also depends on the type and geometric characteristics of the employed fibers. In particular, thanks to the great capacity to withstand tensile load, HPFRC are widely used to control crack propagation, while their high durability and low permeability allows these concretes to be used even to harsh environment as well as to resist freezing and thawing cycles (Jang et al. 2014; Zhang et al. 2016; Song and Kwon 2009; Ismail and Ohtsu 2006). Many experimental studies about HPFRC subject to freeze and thaw cycled have been presented in literature (Feo et al. 2020; Zhao et al. 2018; Ameri et al. 2020; Lee et al. 2021; Vivek et al. 2021) but there aren't predictive models able to predict the mechanical response. In this paper, the experimental results obtained in Feo et al. (2020) related to the analysis of the durability of HPFRC (reinforced with short steel fibers) when subjected to freeze-thawing cycles, are employed for implementing a theoretical model recently proposed in the literature by the authors (Martinelli et al. 2021). The above-mentioned model in is based on a meso-scale formulation of the cracked hinge approach and it is implemented in dedicated a Matlab code (Martinelli et al. 2020) by considering the behavior of the two significant "phases" in FRCCs: distribution and orientation of the spread reinforcement (i.e., fibers) and their possible crack-bridging capacity. Moreover, the model is also capable to furnish an estimation of the cracking, post-cracking strength and toughness of a HPFRC beams subjected to bending load. As a matter of fact, the proposed comparison between experimental observations and the numerical results demonstrates the mechanical consistency and the reliability of the above-mentioned model.

7.2 Experimental Campaign

7.2.1 Raw Materials and Preparation of Specimens

High performance concrete (*GeoLite® Magma*) and short steel fibers (*Dramix OL 13/0.20*, see Fig. 7.1), with length (l_f) equal to 13.0 mm, equivalent diameter (d_e) equal to 0.2 mm and the corresponding aspect ratio of 65, were used for the production of High Performances Fiber Reinforced Cementitious Composites (HPFRCCs) mixture. In this study, steel fibers were used instead of other possible synthetic fibers such as carbon, basalt due to the mechanical performances to be achieved.

Fixing the High-Performance Concrete (i.e., HPC) matrix composition and considering the volume fraction (V_f) variation of the employed fibers in the range of 0%, 1.25% and 2.50%, three HPFRCC types of mixtures, labelled CM0, CM1

Fig. 7.1 Representative sample of the employed steel fibers (*Dramix® OL 13/0.20*). Adapted from Feo et al. (2020)

and CM2, respectively, were produced and tested. The experimental program was designed so that for each type of the above HPFRC mix, eight prismatic samples characterized by a dimension (mm) of $150 \times 150 \times 600$ and five cubic specimens with dimension (mm) of $150 \times 150 \times 150$ were cast. After 24 h, both the twenty-four prismatic samples and the fifteen cubic specimens were demolded and immersed in water for additional 27 days of curing at an average temperature of 20 °C (± 2 °C).

7.2.2 Test Methods and Procedure

After curing period, and in accordance with the EN 12,390–4 (E.N. 2000), all cubic samples were subjected to axial compression loading for measuring the possible variation of the corresponding mechanical behavior (i.e., compressive load, F_u, and compressive strength, f_c). Meanwhile, with the aim of evaluating the resulting durability of HPFRCCs produced herein, five (prismatic $150 \times 150 \times 600$ mm) specimens for each produced mix, were firstly subjected to a thermal stabilization in water (see Fig. 7.2) at temperature of 5 °C (± 2 °C).

Subsequently, the stabilized samples were conditioned to 75 rapid freeze–thaw cycles (refer to Fig. 7.3) following the UNI 7087–2017 (UNI 2017) procedure.

The others nine prismatic specimens were kept in water by keeping a reference temperature of 20 °C (± 2 °C). Later, both non-conditioned (Non Freeze–Thaw, NFT) and conditioned (Freeze–Thaw, FT) samples referred to each type of HPFRCC

Fig. 7.2 Thermal stabilization of prismatic specimens

Fig. 7.3 Freeze–thaw cycling apparatus. Adapted from Ismail and Ohtsu (2006)

mixture were subjected to (four-point) bending tests according to UNI 11,039–2 (2003) (see Fig. 7.4) from which the vertical load (P) versus Crack-Tip-Opening-Displacement (CTOD) trends were obtained.

Fig. 7.4 Experimental set-up for 4-point bending test. Adapted from Ismail and Ohtsu (2006).
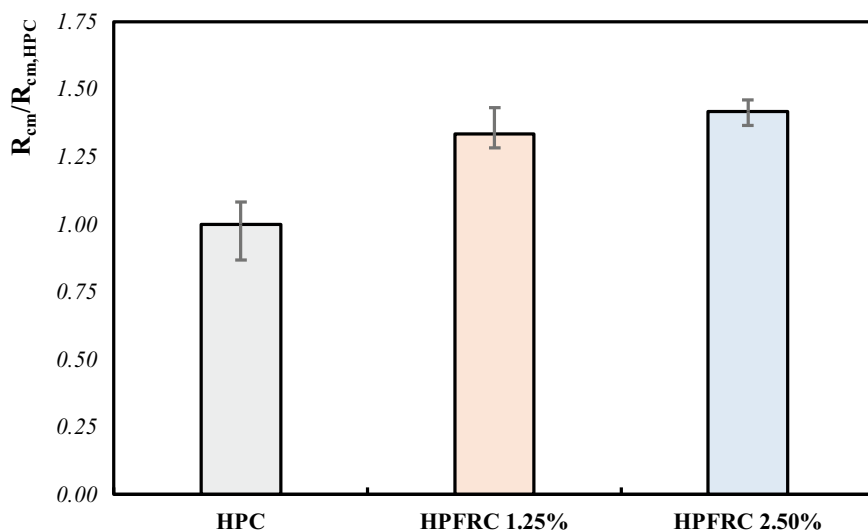
Fig. 7.5 Cubic compressive strength results

7.2.3   Experimental Results

Figure 7.5 summarizes the results registered in terms of average cubic compressive strength. The figure shows the role of the fibers on improving overall mechanical performances at 28-days curing period. Experimental results indicate that the presence of fibers at 1.25% volume fraction increases the compressive strength of around 30% while, for specimens with higher fiber volume fraction (i.e., 2.50%), the resulting compressive strength was increased by more than 40% then compared to reference (i.e., around 65 MPa) mixture specimens.

Figure 7.6 reports the Load-CTOD curves for the three unconditioned specimens. This figure shows the significant enhancement of the compressive ultimate load capacity of FRC as compared to HPC mixture, it emerges the significantly higher mechanical performances of the FRC mixtures in comparison with the plain HPC reference mix.

Figure 7.7 presents the Load-CTOD curves for the conditioned specimens subjected to freeze–thaw cycles. The figure remarks the fundamental role of the fiber on mitigating the possible detrimental effect on the HPC due to the presence of a relevant amount of spread reinforcement. The shaded area proposed in the aforementioned figures (Figs. 7.6 and 7.7) represent the scatter of three tested samples.

Following the UNI-11039–2 procedure, the average CTOD values (i.e., $CTOD_{0,avg}$) which corresponds to the maximum applied vertical load (P_{max}) of the reference HPC samples (i.e., CM0) was evaluated first. Afterwards, the following representative indices of the HPFRC concrete mixes, whose expressions are given

Fig. 7.6 Results of the 4-point bending tests: **a** NFT-Plain, **b** NFT-HPFRC 1.25 and **c** NFT-HPFRC 2.50
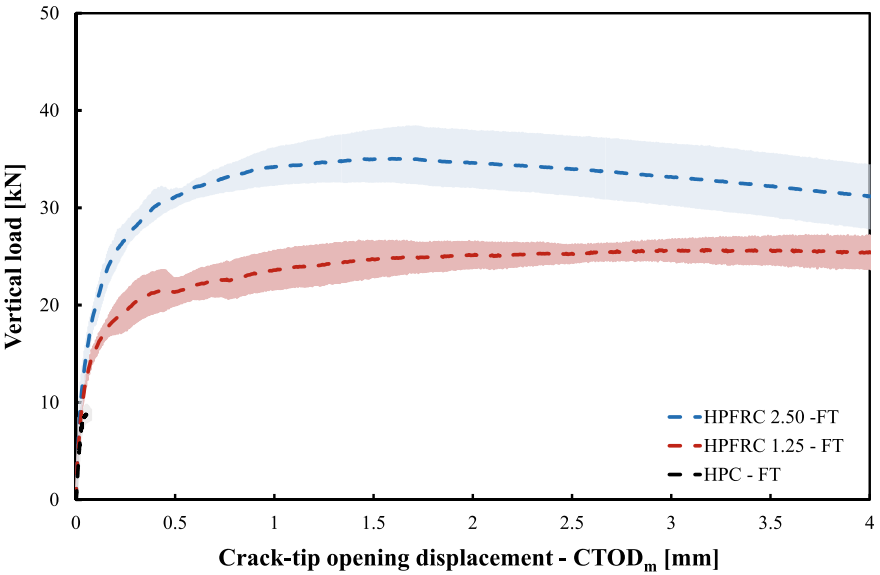
Fig. 7.7 Results of the 4-point bending tests: **a** FT-Plain, **b** FT-HPFRC 1.25 and **c** FT-HPFRC 2.50
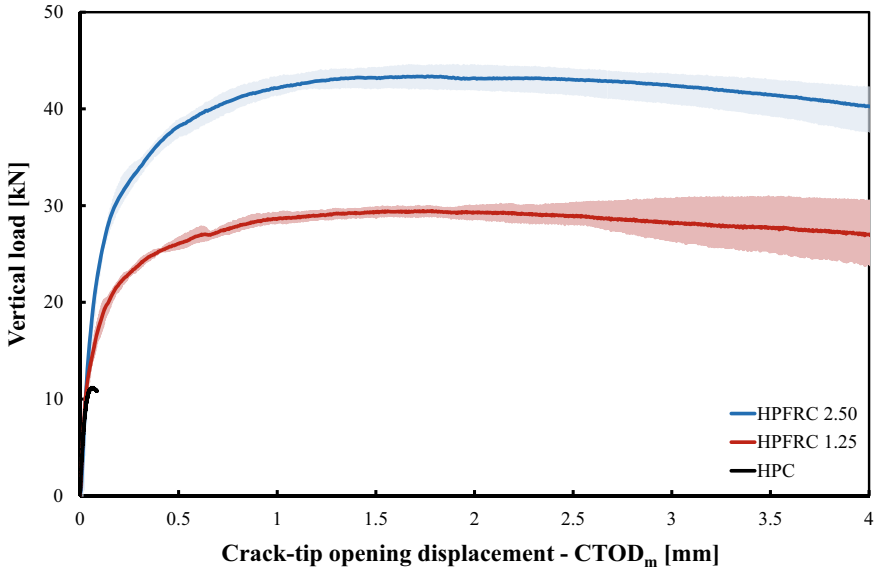
by Eqs. (7.1) through (7.5), were evaluated: first crack load (P_{lf}) and strength (f_{lf}), work capacity (U_1, U_2), equivalent post-cracking strengths ($f_{eq(0-0.6)}$, $f_{eq(0.6-3)}$) and ductility (D_0 and D_1):

$$f_{lf} = \frac{P_{lf} \cdot l}{h \cdot (b - a_0)^2} \tag{7.1}$$

$$D_0 = \frac{f_{eq(0-0.6)}}{f_{lf}} \tag{7.2}$$

$$D_1 = \frac{f_{eq(0.6-3)}}{f_{eq(0-0.6)}} \tag{7.3}$$

$$f_{eq(0-0.6)} = \frac{l}{b(h - a_0)^2} \cdot \frac{U_1}{0.6} \tag{7.4}$$

$$f_{eq(0.6-3)} = \frac{l}{b(h - a_0)^2} \cdot \frac{U_2}{2.4} \tag{7.5}$$

where: l, h and b are, respectively, the length (expressed in mm), the height (expressed in mm) and the width (expressed in mm) for the produced prismatic samples while a_0 represents the notch depth (expressed in mm). The equivalent post-cracking strengths $f_{eq(0-0.6)}$ and $f_{eq(0.6-3)}$ correspond, respectively, to $CTOD_{0,avg+0.6}$ and $CTOD_{0,avg+3.0}$ and the parameters U_1 and U_2 represents areas under the P-CTOD curves in the range $CTOD_0$-$CTOD_{0,+0.6}$, and in the range $CTOD_{0,+0.6}$–$CTOD_{0,+3.0}$, respectively.

The average values of the aforementioned parameters for each HPFRC reference (i.e., NFT), and after exposure to freeze-thaw cycles (i.e., FT), are summarized in Tables 7.1 and 7.2.

7.3 Numerical Modelling

Aimed at unveiling the possible effect of freezing–thawing cyclic exposure on both cracking and post-cracking resistance of HPFRC samples with varying fibers volume fractions, the experimental results are used to implement the theoretical model developed previously by the authors following a meso-mechanical approach (Martinelli et al. 2021, 2020). More specifically, the proposed modelling approach introduces a transition zone length and a modified bond-slip law of the spread reinforcement

Table 7.1 Representative parameters for reference HPC and HPFRC mixtures in NFT and FT conditions

	$P_{1f,avg}^{NFT}$ [kN]	$P_{1f,avg}^{FT}$ [kN]	$f_{1f,avg}^{NFT}$ [MPa]	$f_{1f,avg}^{FT}$ [MPa]	$f_{eq(0-0.6),avg}^{NFT}$ [MPa]	$f_{eq(0-0.6),avg}^{FT}$ [MPa]	$f_{eq(0.6-3),avg}^{NFT}$ [MPa]	$f_{eq(0.6-3),avg}^{FT}$ [MPa]
CM0	11.213	9.105	3.05	2.477	–	–	–	–
CM1	14.489	12.538	4.013	3.475	6.617	5.435	7.99	6.845
CM2	18.595	16.175	5.06	4.327	9.15	7.537	11.473	9.255

Table 7.2 Work capacity and ductility indices for HPFRC mixtures in NFT and FT condition

Mix	$U_{1,avg}^{NFT}$	$U_{1,avg}^{FT}$	$U_{2,avg}^{NFT}$	$U_{2,avg}^{FT}$	$D_{0,avg}^{NFT}$	$D_{0,avg}^{FT}$	$D_{1,avg}^{NFT}$	$D_{1,avg}^{FT}$
	[kNmm]	[kNmm]	[kNmm]	[kNmm]	[−]	[−]	[−]	[−]
CM1	14,283.43	11,742.40	69,226.73	59,175.15	1.647	1.565	1.265	1.265
CM2	20,508.47	16,895.83	102,877.93	82,992.00	1.837	1.747	1.257	1.250

embedded within the HPC surrounding matrix. The principle of the kinematics of the model is inspired to the so-called "cracked-hinge" approach (Hillerborg 1991; Kytinou et al. 2020; Hillerborg et al. 1976; Olesen 2001; Armelin and Banthia 1997): it was able to simulate the crack-bridging effect of fibers, by also specifically considering the possible random spatial distribution and the orientation of steel fibers while at same time considering the performances of both the cement-based matrix and the spread reinforcement, as well as with their possible interaction. Details on the geometric beam representation, on the kinematic assumptions and on the constitutive laws used for concrete both in compression and in tension and for short steel fibers are presented in ref. (Penna et al. 2022).

The model was aimed at calibrating the bond-slip law curve (between the HPC matrix and the steel fibers) by minimizing the difference between measured and predicted values and considering the variation of key parameters used in designing and fabricating the different HPFRC specimens. In order to evaluate how the freeze–thaw cycles could influence these parameters, several numerical simulations were carried out.

The following figures show comparisons between average experimental and numerical P-CTOD curves. As shown in these figures, good agreement between numerical and experimental results is achieved (Figs. 7.8 and 7.9).
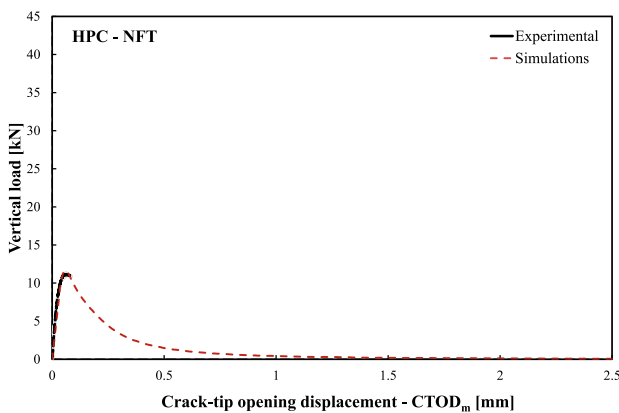
(a)

Fig. 7.8 Numerical simulation for unconditioned specimens

(b)

(c)
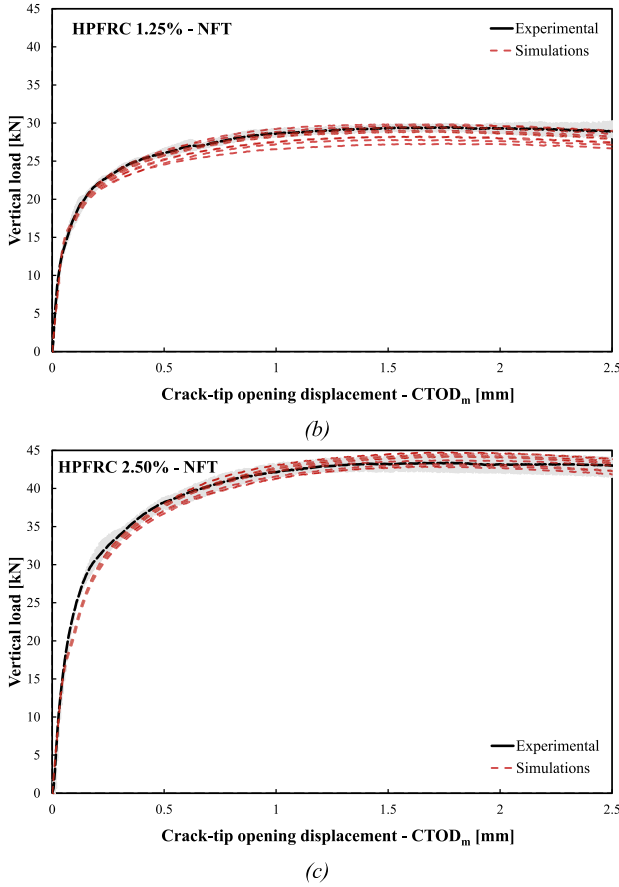
Fig. 7.8 (continued)

7.4 Conclusion

Based on the results obtained from this study, the following main conclusions can be drawn:

– The presence of the steel fibres significantly improves the mechanical performances of the produced mixtures and, moreover, mitigate the detrimental effect induced by the degradation freeze-thaws cycles;
– The model previously developed by the authors has been proposed and applied in the current study to assess the possible influence of freezing–thawing action on the resulting bending response of a HPFRC specimens as a function of the employed volume of fibres;
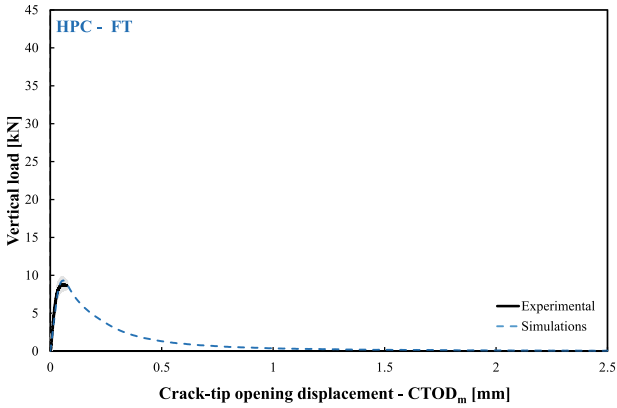
(a)
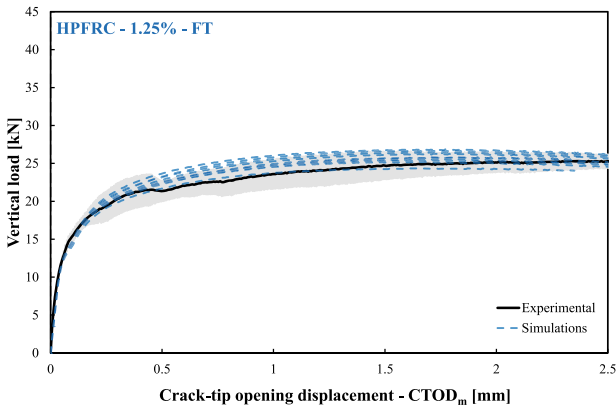
(b)
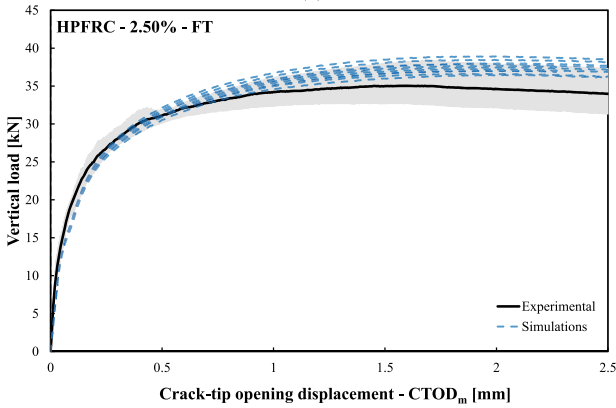
(c)

Fig. 7.9 Numerical simulation for conditioned specimens

– The freezing–thawing actions effected the mechanical compressive strength and the resulting bond slip resistance, confirming the key role as predictive parameters for the proposed model;
– A good agreement between predicted and experimental data confirms that the capability of the proposed model in predicting both cracking and post-cracking strengths as well as, its toughness indices and that a low standard deviation between the registered experimental values and theoretical ones was observed.

References

Ameri F, de Brito J, Madhkhan M, Ali TR (2020) Steel fibre-reinforced high-strength concrete incorporating copper slag: Mechanical, gamma-ray shielding, impact resistance, and microstructural characteristics. J Build Eng 29:101118

Armelin HS, Banthia N (1997) Predicting the flexural postcracking performance of steel fiber reinforced concrete from the pullout of single fibers. Mater J 94(1):18–31

Ashkezari GD, Fotouhi F, Razmara M (2020) Experimental relationships between steel fiber volume fraction and mechanical properties of ultra-high performance fiber-reinforced concrete. J Build Eng 32:101613

Caggiano A, Gambardelli S, Martinelli E, Nisticò N, Pepe M (2016) Experimental characterization of the post-cracking response in hybrid steel/polypropylene fiber-reinforced concrete. Construct Build Mater 125:1035–1043

Caggiano A, Folino P, Lima C, Martinelli E, Pepe M (2017) On the mechanical response of hybrid fiber reinforced concrete with recycled and industrial steel fibers. Construct Build Mater 147:286–295

Carlos Zanuy C, Irache PJ, García-Sainz A (2021) Composite behavior of RC-HPFRC tension members under service loads. Materials 14:47

Cheng J, Luo X, Xiang P (2020) Experimental study on seismic behavior of RC beams with corroded stirrups at joints under cyclic loading. J Build Eng 32:101489

Choi JI, Song KI, Song JK, Lee BY (2016) Composite properties of high-strength polyethylene fiber-reinforced cement and cementless composites. Compos Struct 138:116–121

E.N. Uni 12390–4 (2000) Testing hardened concrete. Part 4: compressive strength-specification for testing machines 2000.

Elmorsy M, Hassan WM (2021) Seismic behavior of ultra-high performance concrete elements: state-of-the-art review and test database and trends. J Build Eng 40:102572

Elsayed M, Tayeh BA, Elmaaty MA, Aldahsoory YG (2022) Behaviour of RC columns strengthened with ultra-high performance fiber reinforced concrete (UHPFRC) under eccentric loading. J Build Eng 103857

Feo L, Ascione F, Penna R, Lau D, Lamberti M (2020) An experimental investigation on freezing and thawing durability of high performance fiber reinforced concrete (HPFRC). Compos Struct

Foti D (2013) Use of recycled waste pet bottles fibers for the reinforcement of concrete. Compos Struct 96:396–404

Hillerborg A, Modéer M, Petersson PE (1976) Analysis of crack formation and crack growth in concrete by means of fracture mechanics and finite elements. Cem Concr Res 6(6):773–781

Hillerborg A (1991) Application of the fictitious crack model to different types of materials. Mater Today: Proc 51:95–102

Ismail M, Ohtsu M (2006) Corrosion rate of ordinary and high-performance concrete subjected to chloride attack by AC impedance spectroscopy. Constr Build Mater 20:458–469

Jang JG, Kim HK, Kim TS, Min BJ, Lee HK (2014) Improved flexural fatigue resistance of PVA fiber reinforced concrete subjected to freezing and thawing cycles. Constr Build Mater 59:129–135

Joo Kim D, Naaman AE, El-Tawil S (2008) Comparative flexural behavior of four fiber reinforced cementitious composites. Cem & Concr Compos 30:917–928

Kytinou VK, Chalioris CE, Karayannis CG (2020) Analysis of residual flexural stiffness of steel fiber-reinforced concrete beams with steel reinforcement. Materials 13(12):2698

Lee S-T, Park S-H, Kim D-G, Kang J-M (2021) Effect of freeze–thaw cycles on the performance of concrete containing water-cooled and air-cooled slag. Appl Sci 11:7291. https://doi.org/10.3390/app11167291

Li Z, Wang X, Wang L (2006) Properties of hemp fibre reinforced concrete composites. Compos A Appl Sci Manuf 37(3):497–505

Martinelli E, Pepe M, Fraternali F (2020) Meso-scale formulation of a cracked-hinge model for hybrid fiber-reinforced cement composites. Fibers 8:56

Martinelli E, Pepe M, Penna R, Feo L (2021) A cracked-hinge approach to modelling high performance fiber-reinforced concrete. Compos Struct 273:114277

O'Hegarty R, Kinnane O, Newell J, West R (2021) High performance, low carbon concrete for building cladding applications. J Build Eng 43:102566

Olesen JF (2001) Fictitious crack propagation in fiber-reinforced concrete beams. J Eng Mech 127(3):272–280

Penna R, Feo L, Martinelli E, Pepe M (2022) Theoretical modelling of the degradation processes induced by freeze-thaw cycles on bond-slip laws of fibres in high-performance fibre-reinforced concrete. Materials 15:6122

Pereiro-Barceló J, Bonet JL, Cabañero-Escudero B, Martínez-Jaén B (2019) Cyclic behavior of hybrid RC columns using high-performance fiber-reinforced concrete and Ni-Ti SMA bars in critical regions. Compos Struct 212:207–219

Reis JML, Ferreira AJM (2003) Assessment of fracture properties of epoxy polymer concrete reinforced with short carbon and glass fibers. Constr Build Mater 18:523–8

Savastano H, Warden PG, Coutts RSP (2003) Mechanically pulped sisal as reinforcement in cementitious matrices. Cem Concr Compos 25:311–9

Savino V, Lanzoni L, Tarantino AM, Viviani M (2018) Simple and effective models to predict the compressive and tensile strength of HPFRC as the steel fiber content and type changes. Compos Part B 137:153–162

Savino V, Lanzoni L, Tarantino AM, Viviani M (2019) An extended model to predict the compressive, tensile and flexural strengths of HPFRCs and UHPFRCs: definition and experimental validation. Compos Part B 163:681–689

Sharma R, Pal BP (2022) Experimental investigation of initially damaged beam column joint retrofitted with reinforced UHP-HFRC overlay. J Build Eng 49:103973

Smarzewski P (2018) Flexural toughness of high-performance concrete with basalt and polypropylene short fibers. Adv Civ Eng 2018(5024353):1–8

Smarzewski P (2019) Influence of basalt-polypropylene fibres on fracture properties of high performance concrete. Compos Struct 209:23–33

Song H-W, Kwon S-J (2009) Evaluation of chloride penetration in high performance concrete using neural network algorithm and micro pore structure. Cem Concr Res 39:814–824

Uchida Y, Takeyama T, Dei T (2010) Ultra high strength fiber reinforced concrete using aramid fiber fracture mechanics of concrete and concrete structures–high performance. In: Oh BH et al (eds) Fiber reinforced concrete, Special loadings and structural applications. pp 1492–1497

UNI 11039–2 (2003) Steel, fibre reinforced concrete–test method for determination of\first crack strength and ductility indexes 2003

UNI 7087–2017 (2017) Concrete–determination of the resistance to the degrade due to freeze-thaw cycles

Vivek D, Elango KS, Gokul Prasath K, Ashik Saran V, Ajeeth Divine Chakaravarthy VB, Abimanyu S (2021) Mechanical and durability studies of high performance concrete (HPC) with nano-silica. Mater Today: Proc. Available online 23 September 2021.

Wang X, He J, Mosallam AS, Li C, Xin H (2019) The effects of fiber length and volume on material properties and crack resistance of basalt fiber reinforced concrete (BFRC). Adv Mater Sci Eng

Wang W, Chouw N (2017) The behaviour of coconut fibre reinforced concrete (CFRC) under impact loading. Constr Build Mater 134:452–61

Zhang WM, Zhang N, Zhou Y (2016) Effect of flexural impact on freeze–thaw and deicing salt resistance of steel fiber reinforced concrete. Mater Struct 49(12):5161–5168

Zhao Y-R, Wang L, Lei Z-K, Han X-F, Shi J-N (2018) Study on bending damage and failure of basalt fiber reinforced concrete under freeze-thaw cycles. Constr Build Mater 163:460–470

Chapter 8
Numerical Simulation of Fatigue Delamination Growth of Adhesively-Bonded Pultruded GFRP Double Cantilever Beam Joints Under Mode I Loading

Haohui Xin, Qinglin Gao, Ayman S. Mosallam, Dan Wang, and Jielin Liu

Abstract Fiber Reinforced Polymer (FRP) is widely used in the industrial field. Delamination damage is one of the main failure forms of FRP laminates. In-depth exploration of fatigue-induced delamination behavior in laminates offers valuable insights for the structural design of FRP composites. The behavior of fatigue delamination hinges significantly on factors such as the stress ratio R. In this paper, experimental data on the relationship between the fatigue delamination growth rate and the strain energy release rate of the adhesively-bonded pultruded glass fiber reinforced polymer double cantilever beam (GFRP DCB) joints were fitted based on the Walker equation. A 2D finite element model based on Virtual Crack Closure Technology (VCCT) is adopted to simulate the fatigue delamination propagation behavior. Finally, the fatigue delamination propagation behavior of the adhesively-bonded pultruded GFRP DCB joints under Mode I loading was successfully simulated by two sets of finite element models.

Keywords Fatigue delamination · Finite element simulation · Walker equation · Virtual crack closure technology

H. Xin (✉) · Q. Gao · D. Wang · J. Liu
Department of Civil Engineering, School of Human Settlements and Civil Engineering, Xi'an Jiaotong University, Xi'an, Shaanxi, P. R. China
e-mail: xinhaohui@xjtu.edu.cn

A. S. Mosallam
Department of Civil and Environment Engineering, University of California, Irvine, CA, USA

8.1 Introduction

Fiber-reinforced polymer (FRP) composite materials enjoy extensive utilization across diverse industrial sectors owing to their remarkable attributes, including high strength, good fatigue resistance, and good design ability. As the utilization of FRP composites continues to expand, the structural forms (Xin et al. 2017a), the loading types (Xin et al. 2017b), and the service environment (Xin et al. 2016) become more complex. Hence, how to ensure the safety of composite structures is also more challenging.

Generally speaking, FRP composites are applied to structures in the form of laminates, which are made of orthotropic monolayers laid up in different stacking sequences. However, a significant limitation arises from the absence of reinforcement in the thickness direction. This results in interlaminar properties of composite laminates that are notably inferior to their in-plane properties. Consequently, delamination emerges as a primary mode of structural damage within composite laminate constructions (Zhao et al. 2019). Delamination-induced damage causes a substantial decline in both strength and stiffness, thereby precipitating the potential for catastrophic failure. This critical issue severely restricts the application for applying FRP laminates effectively. In practical applications, fatigue delamination growth is a common and complex delamination form of laminates. Although laminates have good resistance to in-plane fatigue loads, delamination can propagate even below fracture toughness under cyclic action of normal stress perpendicular to the laminate plane. Therefore, to meet the design requirements of composite structures, it is necessary to investigate the law of delamination of laminates under fatigue loads.

The fatigue behavior of composites is related to several parameters, such as loading type, service environment, loading history, etc. Investigating the fatigue response of composite materials across all conceivable loading scenarios via experimental means becomes a formidable task. Only standard experiments are generally carried out in the laboratory, thereby necessitating the development of appropriate models to replicate the fatigue characteristics of composite materials.

Researchers have proposed an array of mathematical models to explore the behavior of fatigue crack growth. Among these, the fatigue crack growth model grounded in the principles of fracture mechanics stands out as the most extensively employed and acknowledged approach. Building upon the remarkable success of the Paris criterion in describing fatigue crack propagation in metallic materials (Xin et al. 2021), researchers continue to leverage this criterion as a foundational framework for investigating the growth of fatigue-induced delamination in composite materials. Considering the equivalence between the stress intensity factor K and the strain energy release rate G, and recognizing the challenges in precisely computing the stress intensity factor near the crack tip within anisotropic heterogeneous composites, the exploration of fatigue delamination growth in composites will rely on the strain energy release rate as the central mechanical governing parameter dictating crack propagation. This approach offers a more viable means of characterizing the driving force behind crack advancement in such complex materials.

Drawing from available experimental data, it becomes apparent that the fatigue delamination growth in FRP composites is influenced not only by stress amplitude but is also significantly impacted by stress ratio (Roundi et al. 2017; Rans et al. 2011). Nevertheless, the original Paris Criterion, as initially formulated, does not account for the influence of mean stress. This limitation prompted Walker to introduce the notion of stress ratio's effect on aluminum fatigue crack propagation in 1970. Walker's findings suggested an elevated crack growth rate with increasing stress ratio. Subsequently, an empirical model featuring three distinct material parameters was devised to address the role of stress ratio in fatigue crack growth rate-an approach termed the Walker equation (Walker 1970). The mean stress effect on the fatigue crack growth rate is not considered yet in the current commercial software ABAQUS® (ABAQUS 2021).

In this paper, the Walker equation is used to effectively fit experimental data concerning the correlation between the fatigue delamination growth rate (da/dN) and the strain energy release rate (G) for pultruded glass fiber-reinforced polymer double cantilever beam (GFRP DCB) joints. This application of the Walker equation accounts for the influence of stress ratio on crack growth rate. To realize this, a customized fatigue crack growth subroutine is employed. On this basis, a two-dimensional (2D) finite element model based on the Virtual Crack Closure Technology (VCCT) is adopted to simulate the fatigue delamination propagation behavior. Finally, the fatigue delamination propagation patterns in adhesively-bonded pultruded GFRP DCB joints subjected to Mode I loading are successfully simulated, accomplished through the utilization of two distinct sets of finite element models.

8.2 Determination of Fatigue Delamination Parameters

8.2.1 Experimental Details in the Literature

The GFRP laminate is composed of 7 layers of symmetrical single-layer boards, which are made of glass fiber and isophthalic acid polyester resin. The width of the laminate is 40.0 mm and the thickness is 6 mm. Its specific internal structure is shown in Table 8.1 (Shahverdi et al. 2012).

Table 8.1 Structure of pultruded GFRP laminate (Shahverdi et al. 2012)

Layers	Average thickness (mm)
Veil	$2 \times 0.05^{\text{a}}$
First mat	2×0.63
Second mat	2×1.07
Roving	1×2.5
Total	6

[a] "$2x$" means on each side of the symmetry axis

Fig. 8.1 Specimen
configuration, dimensions in
mm (Shahverdi et al. 2012)
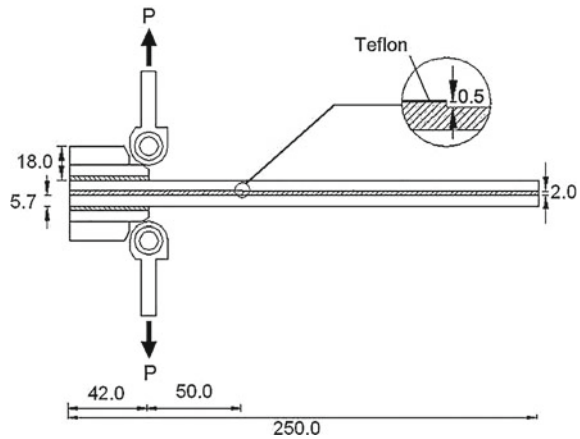
The geometrical dimensions of the double cantilever beam (DCB) specimen are shown in Fig. 8.1. The DCB is made of two identical laminates bonded by a 2.0 mm adhesive layer. The total length is 250.0 mm, and the length of the pre-crack is 50.0 mm from the loading position, which is 42.0 mm from the left end of the DCB. The two keys are bonded to the upper and lower parts of the DCB by an adhesive to facilitate the application of load. The function of Teflon is to induce pre-crack, which is located between the first mat layer and the second mat layer.

To start the experiment, the crack is firstly propagated by 15.0–30.0 mm by static loading, and the crack length reaches the plateau of the R curve of the corresponding specimen (Shahverdi et al. 2011). Then, the fatigue loading is carried out by the displacement control method of 5.0 Hz, and the loading stress ratio is 0.1, 0.5, and 0.8. The maximum displacement value is equal to the maximum displacement value of the DCB specimen opening during static loading.

8.2.2 Processing of Experimental Data

Fracture mode

According to the existing experiment, when the pre-crack's location lies between the first mat layer and the second mat layer, two distinct fracture modes emerge. The crack progression occurs amidst the upper Continuous Strand Mat (CSM) and the first mat layer, termed as Path II-A. The crack extends between the lower CSM and the second mat layer, referred to as Path II-B (Shahverdi et al. 2012). It is noteworthy that the crack growth rate and the strain energy release rate diverge substantially between these two fracture modes. In this study, the chosen specimen for fitting experimental data is specimen No. 6, characterized by a stress ratio of 0.5. Additionally, the fracture mode under consideration is Path II-B.
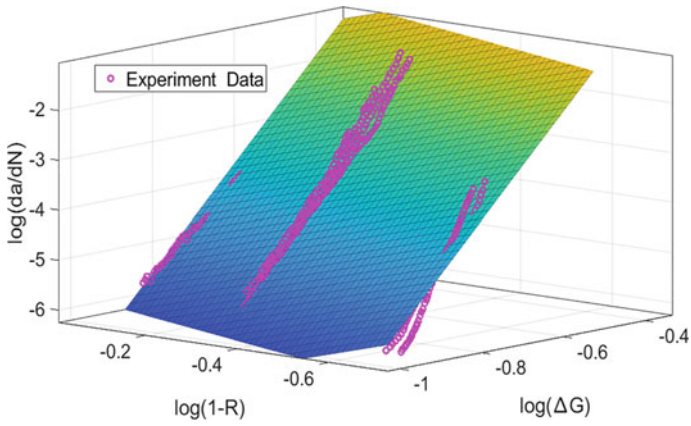
Fig. 8.2 Comparison between fitted results and experimental data

Table 8.2 Coefficients of Walker equation

Parameters	Statistical values	
$\log (D)$	Average	1.768
Γ	Average	0.6932
M	Average	9.291
R^2		0.8975
$RMSE$		0.3655
SSE		61.85
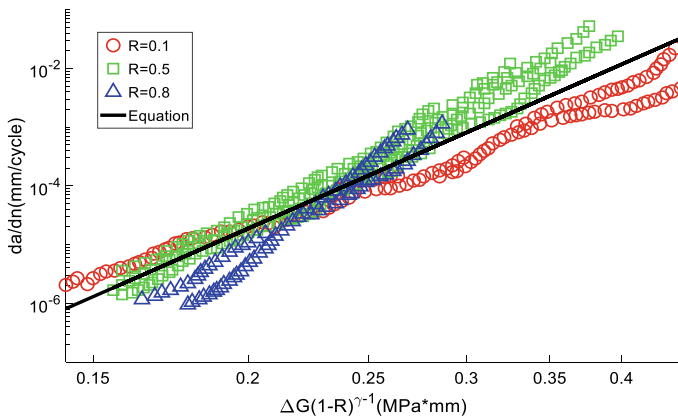
Fig. 8.3 Walker equation fit experimental data of DCB

Equation fitting

As shown in Eqs. (8.1) and (8.2), the Walker equation incorporates the stress ratio (*R*) to address the effect of stress ratio on the progression of fatigue delamination. As shown in Fig. 8.2, experimental data is transformed into the Walker equation within a double logarithmic coordinate system for linear regression fitting. Employing MATLAB (Higham and Higham 2016) software, this procedure yields three material parameters. The coefficients obtained through fitting the Walker equation for double cantilever beam (DCB) joints are documented in Table 8.2, and these coefficients will be instrumental in calculating fatigue delamination propagation. The Walker equation exhibits the capability to unify data across various R-ratios onto a singular line when plotting the delamination propagation rate (*da/dN*) against the equivalent $\overline{\Delta G}$ (Walker 1970), as illustrated in Fig. 8.3.

$$\frac{da}{dN} = D(\overline{\Delta G})m \tag{8.1}$$

$$\overline{\Delta G} = \frac{\Delta G}{(1 - R)^{1-\gamma}} \tag{8.2}$$

where: *D, m, γ* are material parameters of fatigue delamination propagation in the Walker equation.

8.3 Numerical Simulation of DCB Fatigue Delamination Growth

8.3.1 Finite Element Model

Based on the experimental data, two sets of 2D finite element models were adopted for simulation. As shown in Fig. 8.4, the total length of the first DCB model is 250.0 mm and the thickness is 14.0 mm. The position of the pre-crack is between the first mat and the second mat, and the length is 68.0 mm from the loading point (including 50.0 mm prefabricated crack and 18.0 mm static loading crack), the delamination interface is set to be plane, as shown in red. Nonetheless, the conventional pultrusion process, often employed for fabricating pultruded profiles intended for construction purposes, tends to exhibit a comparatively less stringent quality control when juxtaposed with the meticulous standards upheld in the production of advanced aerospace composite components. This discrepancy leads to an irregular and relatively variable distribution of reinforcements within the material, imparting a certain level of instability to the final product. As shown in Fig. 8.5, fabric folds of a typical pultruded FRP perpendicular to pultrusion direction is a common question (Xin et al. 2017c). The second model is shown in Fig. 8.6 where delamination interface is set to a curved surface, as shown in the red curved part. The rest is the same as for the first model.
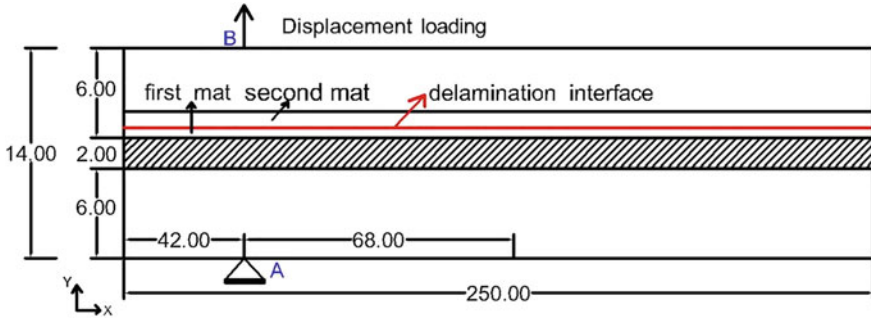
Fig. 8.4 Schematic diagram of the model with the delamination interface as a plane

(a) high-quality laminates   (b) pultruded laminates
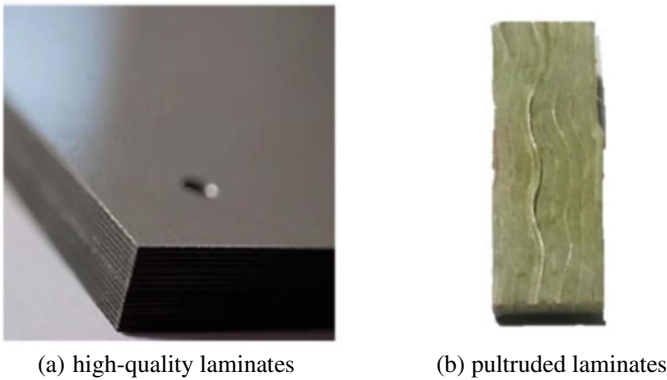
Fig. 8.5 Difference in quality and accuracy of stacking sequence of composite laminates (Xin et al. 2017c)
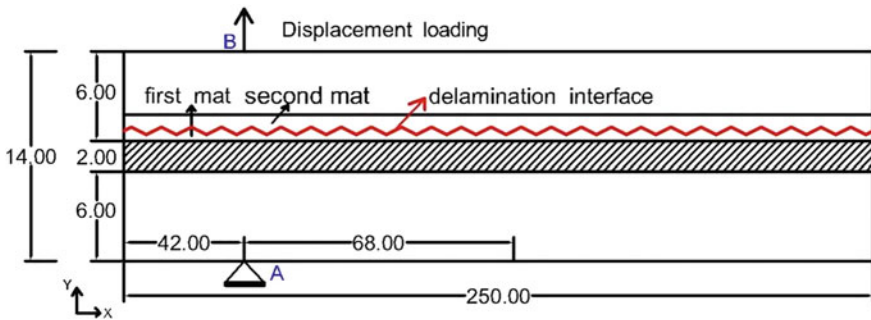
Fig. 8.6 Schematic diagram of the model with the delamination interface as a curved surface

Table 8.3 Properties used for FE model

Material data	Veil	Adhesive	First mat	Second mat	Roving
E1 (MPa)	3200	4600	12,800	15,100	38,900
E2 (MPa)	3200	4600	3200	3200	3200
E3 (MPa)	3200	4600	12,800	15,100	3200
Nu12	0.38	0.37	0.36	0.36	0.35
Nu13	0.38	0.37	0.27	0.27	0.32
Nu23	0.38	0.37	0.36	0.36	0.27
G12 (MPa)	1200	1700	1400	1400	2700
G13 (MPa)	1200	1700	6200	6700	2700
G23 (MPa)	1200	1700	1400	1400	1400

The material properties of the two groups of models are presented in Table 8.3. The mesh type of the two groups of models is a 2D plane stress element, namely CPS4R, which is a 2D, 4-node element. The mesh size used in the analysis is 1.0 mm. The boundary conditions of the experiment are defined at nodes *A* and *B*. As shown in Fig. 8.4, fixed-end constraints are used to limit the movement in the *UX* and *UY* directions and plane rotation Rotz at node *A*. The displacement is applied in the *Y*-direction of node *B*. The *X*-direction movement and plane rotation of node *B* are restricted (Shahverdi et al. 2012). In the model, debonding setting is defined at the pre-crack position of the first mat and second mat layers, and both the master and slave surfaces are connected at the delamination propagation interface through Bonded Nodes, and crack propagation is then achieved through Debonding method. With the exception of the distinct configuration governing the interaction at the interface between the first and second mat layers, the contact surface interactions across all remaining layers are uniformly defined as 'Tie' constraints.

8.3.2 Debond Technique

Debonding analysis technique is one of the techniques used by ABAQUS® (ABAQUS 2021) to simulate and calculate crack growth. The main idea is to define a master and slave surfaces, and define a set of nodes on the slave surface so that both master and slave surfaces are bonded together through these nodes. Subseqently, the bonding contact property and fracture criterion and under load or displacement loading are specified. When the critical value, based on this criterion is reached, the node breaks away from the master surface, resulting in crack propagation. In ABAQUS® (ABAQUS 2021) finite element software, debond analysis technique provides four fracture criteria, namely: (i) critical stress criterion, (ii) critical crack opening displacement criterion (COD), (iii) crack length and time failure criterion,
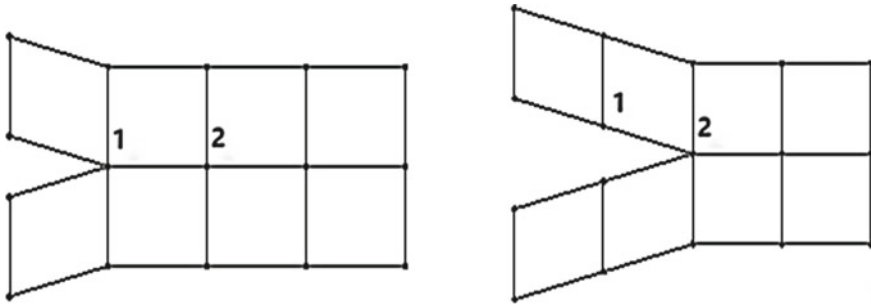
Fig. 8.7 Schematic diagram of the state before and after crack propagation (ABAQUS 2021)

and (iv) virtual crack closure technical criterion (VCCT). In this paper, the debonding criterion based on VCCT technology is adopted.

The VCCT operates on the assumption that the energy released by the crack as it progresses is equivalent to the energy necessitated to close the crack. Fig. 8.7 shows a schematic diagram of the state before and after crack propagation. The hypothesis posits that the contour of the leading edge of the crack remains unchanged, hence, the aperture dimensions of the crack post-propagation mirror those prior to propagation. In the context of the crack advancing from the left to the right (as depicted in Fig. 8.7), the presumption entails an energy release rate of G_I, an association concisely formulated through Eq. (8.3) (ABAQUS 2021). The critical energy release rate requisite for crack advancement is shown as G_{IC}. The equivalent energy release rate is used for mixed-mode fatigue delamination.

$$G_I = \frac{1}{2}\left(\frac{\upsilon_{1,2}F_{\upsilon,3,4}}{bd}\right) \tag{8.3}$$

where: b and d represent the width and length of the crack tip of the unit, respectively (see Fig. 8.8), $F_{\upsilon,3,4}$ refers to the normal force between nodes 3 and 4, $\upsilon_{1,2}$ refers to the normal displacement between nodes 1 and 2.

Fig. 8.8 Schematic finite element representation of the VCCT method (ABAQUS 2021)
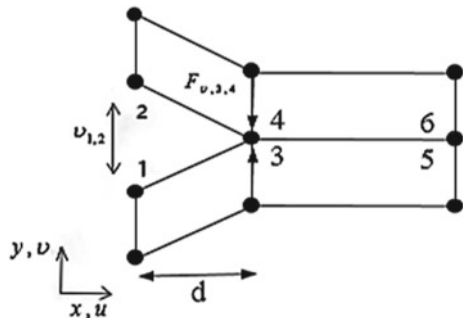
8.4 Experimental Results and Discussion

A summary of simulation results are presented in Fig. 8.9. The simulation results of the delamination interface modeled as a curved surface are in a good agreement with the experimental data in the entire crack propagation stage. However, results indicated that simulation results from the model where the delamination interface is modeled as a plane surface shows better correlation with experimental results in the early stage of crack propagation, where at the middle and late stages results have poor correlation. Regardless of whether the delamination interface is curved or plane, it can be seen that the crack growth rate of the simulation results has a higher rate as compared to that observed in the tests. This can be attributed to two main reasons. The first reason is the nature and limitation used in the experiments. For example, the loading regime used in the experiments was in the form of a displacement-control that was dictated by the test machine displacement, rather than the crack mouth opening displacement. For this reason, the real force transmitted to the specimen is smaller than the theoretical value. The second reason is that the loading position of the experiment was not set directly on the specimen itself, but is transmitted to the specimen indirectly via a piano keys like fixture, that was bonded to the specimen by room-temperature cured adhesives. This may caused the debonding between the piano keys fixture and the specimen in the later stage of the experiment, resulting in less and less force transmitted to the specimen during crack propagation later stage. Consequently, a notable discrepancy emerged between the simulation outcomes and the experimental findings, particularly in the advanced phase of crack propagation.

Comparing the two sets of simulation results, one can see that the crack growth rate of the plane is relatively higher than that of the curved surface, which may be due to the fact that the curved surface increases the crack propagation path contact area. Overall, the crack growth simulation is shown to have in good agreement with the experimental values in the early stage of crack growth.
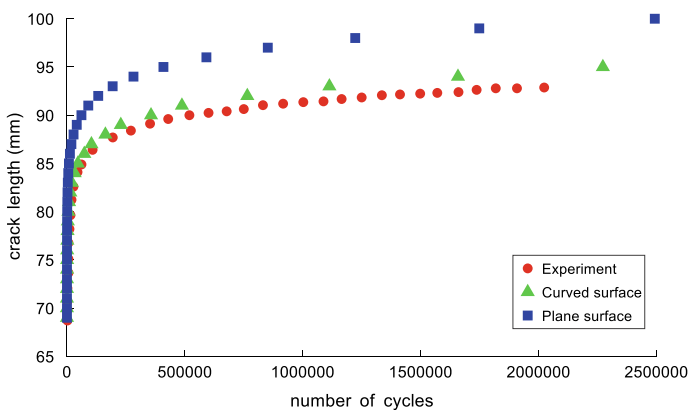
Fig. 8.9 A comparison between the simulation results and the experimental data

8.5 Conclusions

This paper employs the Walker equation to fit the experimental data pertaining to fatigue-induced delamination growth within adhesive pultruded double cantilever beam (DCB) joints. Moreover, a user-defined fatigue crack growth subroutine, UMIXMODEFATIGUE, is used. Built upon the principles of the Walker equation, this subroutine assumes the responsibility of simulating the progression of fatigue delamination in DCB structures when subjected to Mode I loading conditions. Drawing from the results of this investigation, the subsequent conclusions are drawn:

- By comparing the simulation results with experimental data and considering the influence of stress ratio on fatigue crack propagation, the three material parameters obtained by fitting the experimental data with Walker equation can simulate the delamination propagation behavior of DCB.
- Through the comparison of the two sets of simulation results, the simulation effect of the delamination surface as a curved surface is better than that of the delamination surface as a plane.

References

ABAQUS (2021) Analysis user's manual. Dassault Systèmes Simulia Corp., Providence, RI, USA

Higham DJ, Higham NJ (2016) MATLAB guide. Soc Ind Appl Math

Rans C, Alderliesten R, Benedictus R (2011) Misinterpreting the results: how similitude can improve our understanding of fatigue delamination growth. Compos Sci Technol 71(2):230–238

Roundi W, El Mahi A, El Gharad A, Rebière JL (2017) Experimental and numerical investigation of the effects of stacking sequence and stress ratio on fatigue damage of glass/epoxy composites. Compos Part b: Eng 109:64–71

Shahverdi M, Vassilopoulos AP, Keller T (2011) A phenomenological analysis of Mode I fracture of adhesively-bonded pultruded GFRP joints. Eng Fract Mech 78(10):2161–2173

Shahverdi M, Vassilopoulos AP, Keller T (2012) Experimental investigation of R-ratio effects on fatigue crack growth of adhesively-bonded pultruded GFRP DCB joints under CA loading. Compos Part a: Appl Sci Manuf 43(10):1689–1697

Walker K (1970) The effect of stress ratio during crack propagation and fatigue for 2024-T3 and 7075-T6 aluminum, 1–14

Xin H, Liu Y, Mosallam A, Zhang Y (2016) Moisture diffusion and hygrothermal aging of pultruded glass fiber reinforced polymer laminates in bridge application. Compos Part b: Eng 100:197–207

Xin H, Mosallam A, Liu Y, Xiao Y, He J, Wang C, Jiang Z (2017a) Experimental and numerical investigation on in-plane compression and shear performance of a pultruded GFRP composite bridge deck. Compos Struct 180:914–932

Xin H, Mosallam A, Liu Y, Wang C, Zhang Y (2017b) Analytical and experimental evaluation of flexural behavior of FRP pultruded composite profiles for bridge deck structural design. Constr Build Mater 150:123–149

Xin H, Liu Y, Mosallam AS, He J, Du A (2017c) Evaluation on material behaviors of pultruded glass fiber reinforced polymer (GFRP) laminates. Compos Struct 182:283–300

Xin H, Correia JA, Veljkovic M (2021) Three-dimensional fatigue crack propagation simulation using extended finite element methods for steel grades S355 and S690 considering mean stress effects. Eng Struct 227:111414

Zhao LB, Gong Y, Zhang JY (2019) A survey on delamination growth behavior in fiber reinforced composite laminates. Acta Aeronaut Astronaut Sin 40(01):171–199

Chapter 9
Fire Damage Prevention Using Innovative Insulation Systems

Yunus Emrahan Akbulut, Ahmet Can Altunışık, Süleyman Adanur, Ayman S. Mosallam, and Ashraf Abdel Khalek Agwa

Abstract Energy consumption is rising alongside the associated danger of fire due to the increased industrialization and urbanisation of previously rural areas. An example of a building that is predisposed to fire has a furnace on the bottom floor, one that is used in the production of iron and steel, or thermal power plants. It's difficult, time-consuming, and potentially hazardous to intervene in a fire from the exterior of a high-rise structure, whose number is expanding every day with construction technology. It's hard to forecast how long a fire will burn or how far it will spread. Complete fire safety practices are especially important in densely populated buildings to prevent fire dangers to people and property. Because of the high temperatures produced by the fire, the structural system's parts may lose stiffness and strength, resulting in structural damage. A wide variety of insulation materials are utilised to shield the elements of the building carrier system and the materials on which they are constructed from extreme heat and flame. A combination of these materials is utilised to create the insulation systems in use today. Although there are a variety of insulation applications that may be developed for fire protection, covering the environment is more frequent these days. To insulate anything, you can use the wrapping technique, which is wrapping or covering the outside of the item to be protected with insulation. Three cutting-edge insulation technologies, all suitable for application in fire prevention, are presented within the framework of this research.

Keywords Fire · High temperature · Damage · Fire protection · Insulation

Y. E. Akbulut · A. C. Altunışık (✉) · S. Adanur
Department of Civil Engineering, Karadeniz Technical University, Trabzon, Turkey
e-mail: ahmetcan@ktu.edu.tr

A. S. Mosallam
Civil and Environmental Engineering, The Henry Samueli School of Engineering, University of California, Irvine, USA

A. A. K. Agwa
Valley Higher Institute for Engineering & Technology, Cairo, Egypt

9.1 Introduction

One of the fundamental requirements for human survival is a safe place to live in which to retreat from the elements. Humanity needs refuge from bad weather, external hazards and threats, and natural disasters, therefore people constructed many types of structures to suit this need. Throughout their service life, engineered buildings will be threatened not just by earthquakes and floods, but also by fires caused by the spread of urban sprawl and a rise in people's propensity to waste energy.

The frequency of fires has decreased because of significant efforts put into the development of fire-resistant construction materials and the refinement of fire suppression methods. But the rising quantity and wealth of structures have more than countered these advancements in terms of property destruction.

The number of fires that required assistance from local fire departments in the United States was projected to reach 1.4 million in 2020. Over a third (490,500) of the fires were started inside or on buildings. These fires were responsible for 2,730 civilian deaths (or 78% of all fire deaths), 13,000 civilian injuries (86% of all fire injuries), and $12.1 billion in direct property damage (55%). Another $9.8 billion in property damage was incurred due to fires started by vehicles, fires in the open, and fires in the wildland-urban interface in California, bringing the total property losses from fires to $21.9 billion. Undoubtedly, building fires were responsible for a sizable percentage of the damage. Fires inflict a lot of damage and loss of life in other industrialised nations as well, especially to the environment and the economy.

A fire is a chemical and physical process that affects its surroundings. There are often three distinct phases to a fire's life cycle: ignition, growth, and extinguishment. Due to their unique qualities, the hazards and dangers associated with each stage vary. Damage from fires to buildings can be extensive.

From ancient times to the present, architects have had their pick of a wide variety of materials with which to construct their masterpieces. When considering the current state of the building industry, the creation of concrete and the subsequent development of reinforced concrete stand out as the two most important discoveries. Parallel to the expansion of technological possibilities, there has been a corresponding expansion in the range of available construction materials, with the emergence of several new options alongside the more conventional varieties. The fact that reinforced concrete buildings are still the most popular choice despite this is astonishing. When compared to other construction materials, reinforced concrete has several benefits, including a low total cost of ownership, a long service life, and simple, inexpensive maintenance and repair.

Mechanical systems may fail to function as intended if they sustain wear and tear or are subjected to a sudden shock from an outside source. Due to high-temperature impacts such as fire, reinforced concrete structures can lose a lot of their strength and stiffness. The reinforced concrete structural parts that make up the building's structural system suffer severe damage, degradation, bursting, and stripping as a result of these losses. If the building hasn't collapsed from these forces, assessing the damage and deciding whether to utilise it again is urgent.

Where structural analyses reveal a decline in building performance that is not catastrophic, repairs or reinforcements may be possible. If the results of the economic evaluations do not pose a significant barrier to eliminating this performance loss, then the service life of the structure can be ensured to continue with these improvements by applying repair/reinforcement applications to the existing structure rather than demolishing and reconstructing. In tandem with the advancement of technology, a plethora of structural strengthening techniques have been developed and put into practice in the market to avert the financial and reputational fallout of structural damage.

Increasing the axial load-bearing capacity, bending, and shear strengths of the structural element to which FRP (Fiber Reinforced Polymers) composites are applied significantly impacts the durability and ductility of the associated structure. Despite all their positive qualities, FRPs can deteriorate when exposed to elements including moisture, heat, and UV light. Due to the breakdown of the resin material under the impact of temperature, which affects the mechanical characteristics of FRP composites, they are not typically appropriate for long-term usage at high temperatures.

Despite all of FRP composites' benefits, when exposed to high temperatures (from fire, for example), it was found that their mechanical qualities degraded significantly.

In the presence of high temperatures, FRP composites that lack an insulating coating do not add to the structural strength, as indicated by Al-Salloum et al. (2011). This experiment included considering a variety of factors, including different composite kinds (carbon and glass-based), temperature levels (100 and 200 °C), and exposure lengths (1, 2, and 3 h). They found that carbon fiber reinforced polymer (CFRP) composites lost a lot of strength after being heated to 200 °C. Al-Kamaki et al. (2015) used experimental and computational approaches to study the behaviour of charred carbon fiber reinforced concrete columns. According to the findings, applying CFRP wrapping to either the non-heat-treated reference columns or the reinforced concrete columns that have suffered thermal damage significantly improves the components' strength and ductility. The numerical and experimental results have been found to correspond rather well. Lenwari et al. (2016) explored the use of CFRP for reinforcement and its performance after being subjected to 300, 500, and 700 °C for 2 h. On top of that, tests were run for a whole three hours at a temperature of 700 °C. Various strengths of conventional cylindrical concrete samples were used in this experiment (20, 35 and 50 MPa). The research showed that FRP composites failed under high heat conditions. In their work, Li et al. (2017) evaluated the effects

of exposure to different temperatures (80, 160, and 240 °C) on the performance of FRP composites across different periods (1.5 and 3 h). It was concluded that longer periods of exposure at higher temperatures resulted in a weakening of the substance. According to research by Bisby et al. (2005) determined the columns' resilience to fire thanks to the wrapping and fire insulation treatments made possible by FRP composites. Researchers found that FRP composites retained some of their original strength even after being heated to 200 °C. Also, this research found that for up to 4 h, the FRP composite's temperature may be maintained at or below 100 °C thanks to the insulating material that shields the FRP composite-reinforced column from high temperatures. Without any kind of fire protection and when exposed to fire, FRP composites have been seen to catch fire within minutes. Therefore, FRP composite materials can be used for fire, and it is of critical importance to apply insulation processes to protect them from high-temperature effects and to increase their durability against these effects, especially since it is not clear when it will occur and how severe the effects will be.

Applications of insulation for fire protection can take several forms, including mass, wrapping, boxing, and chilling the item to be protected via water circulation. In most cases, the mass insulation approach involves embedding the insulating material into the concrete itself. When using the boxing technique, insulating plates are used to cover the materials. The wrapping technique involves encasing or covering the exposed surface of the material with insulation. It's possible that the insulation technique to be used will change based on the type of building component being insulated or the required level of insulation. These days, it's more common for insulation to be made by wrapping the environment.

This study is a series of experiments in which CFRP and GFRP composites are used to strengthen cylinders of concrete formed in a controlled setting, with the aim of using these samples in a variety of fire prevention applications. Insulation applications will be made using one of three cutting-edge fire protection technologies (FireWrap, FireCoat, or RealRock) as part of the research. The research takes into account the many configurations that might arise from combining the various application forms of the components of these systems in the insulation applications that fall under its purview. Temperature tests at varying levels and for varying durations were performed on the reference samples, which had been reinforced and insulated within the scope of the project but had not used any reinforcing or insulation treatment. All the variable characteristics evaluated in the study have been used to calculate the efficacy of the various insulation types described within the project's scope. In this context, assessments are done using data from fire tests, as well as other temperature tests at relatively low temperatures based on standard fire curve ASTM E119 (2012), and data from compressive strengths acquired from pressure testing on the samples.

FRP composites and engineering constructions or structural elements enhanced using these materials are subjected to fire, etc., as is evident from a review of the relevant literature. One can observe that various research has been conducted to ascertain the extent to which high-temperature impacts lead to performance drops. Yet, it has been pointed out that there is a dearth of experimental research on the many insulating techniques that may be used to safeguard FRP composite materials against

these temperature impacts. It was found that only a small subset of possible insulating configurations was tested in these investigations. Since the study encompasses a wide range of novel fire protection techniques and diverse applications of these insulation strategies, it is believed to have special relevance.

9.2 Methodology

The conducted experimental evaluation comprises 5 main steps of fabrication of the specimens, FRP wrapping, thermal insulating the specimens, high temperature test, and post fire evaluation.

9.2.1 Fabrication and Strengthening

Initially, cylindrical concrete specimens with 45 cm height and 20 cm diameter were constructed. All constructed specimens, except reference samples, were reinforced using fiber polymer composites. In both sets, 2 layers of FRP were wrapped and an overlap length of 20 cm has been considered. The fabricated specimens were divided into three groups of CFRP, GFRP and reference specimens. The utilized materials for strengthening the specimens are described in Table 9.1.

9.2.2 Insulation Types and Application Procedures

After strengthening the specimens, thermal insulation materials with different schemes were applied on some of the specimens. The utilized materials for each system are detailed in Table 9.2. The procedure related to preparation and applying the three different insulation systems are described below.

System A–FireWrap. Multiple To assess the effectiveness of System A, 4 different insulation schemes reflecting various combination forms of Dymat®RS and Dymatherm insulation materials were considered. The procedure related to applying the System A are shown in Fig. 9.1.

System B–FireCoat. System B consists of Dymat®DCF-D approved test by ICC-AC125 by IAPMO. FCI-APP11 A&B components and final coating FireFree 88 (Dymat®D8) were used for this system.

Mix A&B contain Dymat®DCF "A" Epoxy Resin and Dymat®DCF "B" Curing Agent (Hardener). Prior to application of mix A&B, specimens' surfaces were cleaned. To prepare the mix, A and B materials were mixed with a ratio of 1:1 by volume and were rolled on specimens with an equal amount of 310.56 g for

Table 9.1 Utilized materials for strengthening the specimens

Scope	Materials		
	Component	Name	Image
Strengthening	Fiber reinforced polymers	DYMAT® Carbon Fiber System DHC-190	
		DYMAT® Glass Fiber System DHE-272	
	Epoxy matrix	DYMAT® BT-D "A" Epoxy Resin	
		DYMAT® BT-D "B" Curing Agent - Hardener	
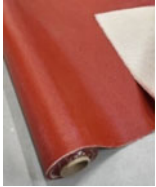
each layer (0.225 lb/ft^2). The FireFree 88 was applied on the outer surface of the specimens with the amount of 55.2 g (0.04 lb/ft^2) for each layer (Fig. 9.2).

System C–RealRock. System C consists of 60 min fire-resistant setting compound Fire Set 60 (Dymat®Fireset) and %100 acrylic interior/exterior plaster Acrylic Vella Fino as coating material. To evaluate the effectiveness of this system 3 different insulation schemes were considered.

To prepare Fire Set 60 setting compound, 0.615 L of clean water and 1 kg of setting compound were mixed and applied on the prepared specimens. Then, Vella Fino was mixed and applied on dried surface of the specimens. The layer thickness in each configuration was 0.25 inches (Fig. 9.3).

The details of the employed insulation schemes for each system and the layering information are presented in Table 9.3.

Table 9.2 Utilized materials for thermal insulations

Scope	Materials		
	Component	Name	Image
Fire insulation system "A" (FireWrap)	RS material (red)	Dymat®RS	
	DYMAT® super wool	Dymatherm	
Fire insulation system "B" (FireCoat)	FCI-APP11 A&B components	DYMAT® DCF "A" Epoxy Resin	
		DYMAT® DCF "B" Curing Agent - Hardener	
	Final coating FireFree 88	Dymat®D8	

(continued)

Table 9.2 (continued)

Scope	Materials		
	Component	Name	Image
Fire insulation system "C" (RealRock)	DYMAT® plaster (acrylic paint)	Acrylic Vella Fino Coating	
	DYMAT® fire-resistant joint compound (60 min)	FIRE SET 60 (DYMAT® Fire Set)	

Fig. 9.1 Wrapping applications of the insulation layers

Fig. 9.2 Preparation and application of the System B components

9.2.3   Temperature Tests and Measurements

To assess the performance of all systems, all insulated specimens undergone the temperature tests with different temperature levels and exposure durations. The fire tests were done with respect to 30 and 60 min of the ASTM E119 standard fire curve. The high temperature tests were done using a constant heating rate of 2.5 °C/min till reaching the target temperatures of 200 and 400 °C. To measure the temperature developments within the test durations, thermocouples were embedded into different locations of the specimens.

Upon completion of temperature test, a pyrometer was used to measure the surface temperature of specimens. Then, the samples were placed outside the furnace and cooled naturally to be prepared for compression tests. Using the data obtained from compressive tests and recorded visual observations, the effectiveness of each insulation method was evaluated. The overview of the some conducted temperature tests are depicted in Fig. 9.4.
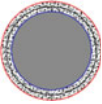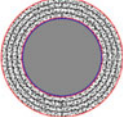
Fig. 9.3 Preparation and application of the System C components

9.2.4 Uniaxial Compression Tests

Thereafter cooling phase, all fire exposed specimens were subjected to a uniaxial compression test with a loading rate of 0.6 MPa/s. The procedure and the observation for the performed compression tests are illustrated (Fig. 9.5).

Table 9.3 Utilized insulation schemes

Insulation system	Insulation type ID	Layer information (*from inner to outer layer*)			Schematization
A	I1	✗	Dymatherm 2 layers	Dymat®RS	
	I2	✗	Dymatherm 4 layers	Dymat®RS	
	I3	Dymat®RS	Dymatherm 2 layers	Dymat®RS	
	I4	Dymat®RS	Dymatherm 4 layers	Dymat®RS	
B	I1	FCI-APP11 A&B components 1 layer	FireFree 88 (Dymat®D8) 3 layers		
	I2	FCI-APP11 A&B components 2 layers	FireFree 88 (Dymat®D8) 6 layers		
C	I1	✗	Acrylic Vella Fino 2 layers		

Table 9.3 (continued)

Insulation system	Insulation type ID	Layer information (*from inner to outer layer*)		Schematization
	I2	Fire set 60 1 layer	Acrylic Vella Fino 1 layer	
	I3	Fire set 60 2 layers	Acrylic Vella Fino 2 layers	

9.3 Conclusion

This study has evaluated the effectiveness of different insulation materials under high temperature. for this purpose, a set of concrete specimens were constructed and wrapped using CFRP and GFRP and were thermally insulated using three different insulation systems with different configurations. The insulated specimens were exposed to high temperature and fire for different durations and the remaining strength of the specimens were evaluated. From the post fire evaluations, it was observed that the System C that had more affordable price can also provide a better protection for both concrete and FRP layers. While the System C had the lowest price and had the easiest application procedure, it had also provided a better protection for both concrete and FRP wraps. So, using this system can provide the balance between cost and protection.

Fig. 9.4 The overview of the some conducted temperature tests
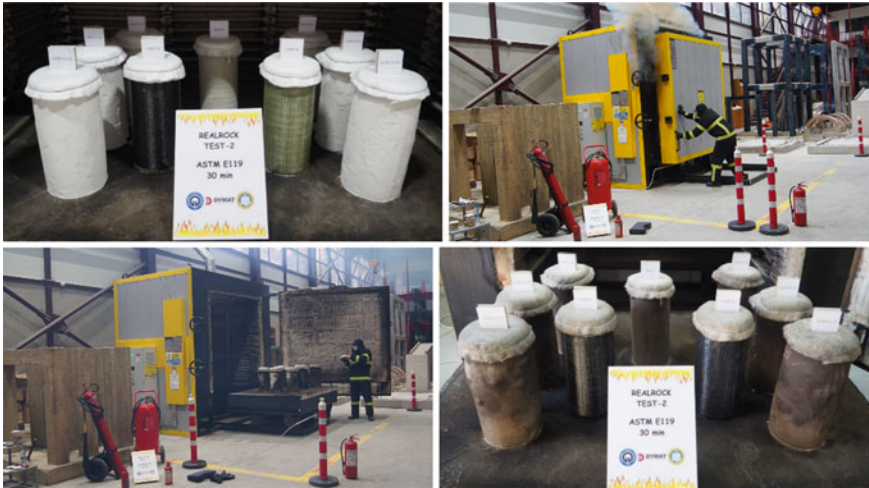
Fig. 9.4 (continued)

Fig. 9.5 The overview of the compressive strength of some specimens before and after fire tests

References

Al-Kamaki YSS, Al-Mahaidi R, Bennetts I (2015) Experimental and numerical study of the behaviour of heat-damaged RC circular columns confined with CFRP fabric. Compos Struct 133:679–690. https://doi.org/10.1016/j.compstruct.2015.07.116

Al-Salloum YA, Elsanadedy HM, Abadel AA (2011) Behavior of FRP-confined concrete after high temperature exposure. Constr Build Mater 25(2):838–850. https://doi.org/10.1016/j.conbuildmat.2010.06.103

ASTM E119 (2012) Standard fire test of building construction and materials. ASTM standards, American Society for Testing and Materials. West Conshohocken, PA, United States

Bisby LA, Kodur VKR, Green MF (2005) Fire endurance of fiber-reinforced polymer-confined concrete columns. ACI Struct J 102(6):883–891. https://doi.org/10.14359/14797

Lenwari A, Rungamornrat J, Woonprasert S (2016) Axial compression behavior of fire-damaged concrete cylinders confined with CFRP sheets. J Compos Constr 20(5). https://doi.org/10.1061/(asce)cc.1943-5614.0000683

Li Y, Liu X, Wu M (2017) Mechanical properties of FRP-strengthened concrete at elevated temperature. Constr Build Mater 134:424–432. https://doi.org/10.1016/j.conbuildmat.2016.12.148

Part III
Smart Building Systems

Chapter 10
Importance of Parametric Modeling in New Generation Civil Engineering Projects

Fatih Yesevi Okur, Ebru kalkan Okur, and Ahmet Can Altunışık

Abstract Parametric modeling allows a new form to be obtained automatically by changing parameters with variable properties without the need to redraw a geometric form. This situation shortens the project design time and enables the most suitable model to be put forward in a short time. In this paper, it is aimed to explain the importance and latest situation of parametric modeling in the world and to present the parametric modeled turbine structure as an example. The double-sided turbine is designed with the roof system created by integrating the sea wave and bird wing forms, which are the symbols of the football team of Trabzon. Parametric modeling method is used to create the static project of the 13 m wide, 108.5 m long and 5.89 m high tribune structure with an extreme architecture and to determine the optimum structural elements. The tribune structure modeled in the Dynamo program is transferred to the SAP2000 program, which is a structural analysis program, with the add-on named "DynamicSap" developed by the project team. Thus, the transferred model is used as a reference model in the creation of the finite element model, and the analysis parameters are defined in the program. Optimization analysis is carried out in which parameters such as wave width and height are constantly changed for both the preservation of the architectural form and minimum cost. The tribune, which is brought to the city with the project prepared using the parametric modeling method and optimization analysis, is interesting with its aesthetic appearance and contributed to the economy of the city with its affordable cost.

Keywords Modeling parameters · Optimization analysis · Parametric modeling

F. Y. Okur (✉) · E. Okur · A. C. Altunışık
Department of Civil Engineering, Karadeniz Technical University, Trabzon, Turkey
e-mail: yesevi@ktu.edu.tr

131

10.1 Introduction

If the designer wants to change any parameter in a structural model prepared with the traditional method, the whole process during the modeling must be repeated, which is quite time consuming. However, in parametric design, the design parameters are integrated simultaneously, allowing the design to be changed and developed easily and in a short time. Thus, any parameter that is desired to be edited or developed can be automatically and instantly updated in the model. The optimum design that offers the best solution requires a plan and coordination process for designers, and changes or adjustments are made to the envisaged model in this process. This process can lead to complexity, especially in large companies' interdisciplinary comprehensive projects. Parametric modeling method is used to facilitate the relationship between different disciplines and to apply changes instantly (Suyoto et al. 2015).

The difficulties experienced in the periods when the drawings of structural designs were made by hand using traditional methods increased the need for technological approaches. Ivan Sutherland, the inventor of Sketchpad, which can be considered the pioneer of today's design interfaces, developed the first computer-aided two-dimensional modeling tool (Sutherland 1963). Sutherland stated that error-free and repeatable drawings can be created with computer-aided modeling, so that much faster results can be obtained than traditional drawing techniques (Stouffs et al. 2013). The first version of the AutoCAD program, which is widely used especially for architectural design with access to the personal computer, was published in 1982 and has developed rapidly by updating its versions until today (Weisberg 2008, Chap. 8). Later, with the development of three-dimensional modeling methods and tools, the modeling of designs became easier.

Luigi Moretti, who first used the expression parametric architecture in the 1940s, defined parametric architecture as the study of architectural systems that aim to describe the relationships between dimensions depending on various parameters (Moretti et al. 2000). On the other hand, Gerber (2007) stated in his thesis that the term parametric was used for the first time in 1988 in Maurice Ruiter's book (de Ruiter 1988), Reddy et al. (2015) stated in their study that the first parametric modeling software called Pro/ENGINEER was created by the mathematician Professor Samuel Geisberg in 1988. With this object-based modeling tool, the qualitative properties of objects have come to the fore (History of CAD CAM 2004). This gave users the opportunity to design the relationship of the data in addition to the geometry-based design process.

CAD systems, in the twentieth century, played a major role in the development of the construction industry with its contributions to the project design process. However, with the differentiation of architectural designs and the design of more complex systems, new systems have emerged. Thus, with the developing technologies in the twenty-first century, the CAD system has become ineffective. In order to keep up with the technology, new systems have been created in the construction industry, different from the traditional methods.

While designing projects in the construction sector with parametric modeling methods is effective both in reducing the project time and in determining the optimum modeling, in case 3D modeling is insufficient, the 4th dimension has been added to the design, enabling it to turn into a system where cost-energy calculations can be made. All these developments have contributed to the development of BIM (Building Information Modeling) systems. BIM is a system that brings together structured and multi-disciplinary data to create a digital representation of the entire planning, design, construction and operation phase of a building (URL-1).

Within the scope of this study, it is aimed to present up-to-date information about the occurrence and development of the parametric modeling method and to explain the tribune project, whose project was created and whose construction was completed in Turkey, with the parametric modeling method. What disadvantages will be encountered in case of modeling with traditional methods and the advantage of the parametric modeling method have been expressed.

10.2   Parametric Modeling

With the development of technology, traditional methods are widely used in the project and analysis of computer-aided projects. However, it is required to redesign in the event that the project is altered. It takes a long time to complete this procedure, especially for huge and complicated constructions. However, because parametric modeling is done based on the established variable parameters, required adjustments may be performed instantaneously without the need for remodeling. When compared to standard modeling techniques, this saves a ton of time. Text and visual algorithm editors are the two categories of parametric modeling tools. Rhinoscript (McNeel), Generative Components (Bentley), and Mayascript (Autodesk) are examples of textual algorithm editors, whereas Grasshoopper (McNeel) and Dynamo are examples of visual algorithm editors (Autodesk). Given that it demands coding skills, the text algorithm editor is difficult to use (Stouffs et al. 2013; Yu et al. 2013). Visual algorithm editors are utilized more frequently as a result (Çinici et al. 2008).

When a dimension value is changed, parametric modeling, a modeling technique, can alter the geometry of the model (Fig. 10.1). The implementation of parametric modeling involves writing design computer programming code, such as a script, to specify the model's dimensions and shape. To modify the characteristics of the system, parametric models employ design tools for feature-based, solid, and surface modeling. The fact that attributes with links modify their properties automatically is one of the most significant characteristics of parametric modeling. Parametric modeling, in other words, enables the designer to specify entire classes of forms rather than simply particular instances. Editing the form was a difficult undertaking for designers before the introduction of parametrics. For instance, the designer needed to alter the 3D solid's length, breadth, and height. With parametric modeling, the designer only needs to change one parameter; the other two are changed automatically.
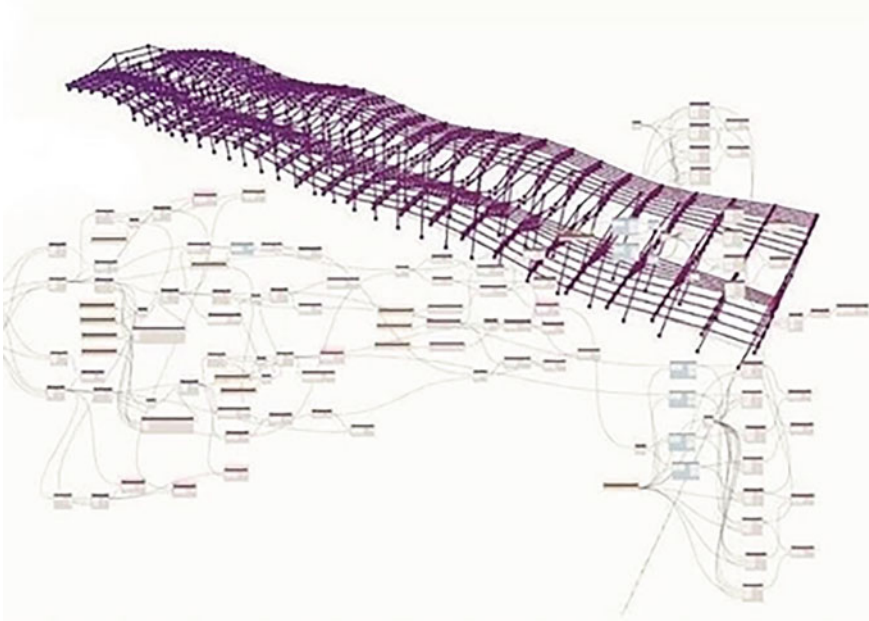
Fig. 10.1 Parametric modeling example

Advantages of parametric modeling method compared to traditional methods;

- *Structure*: All parametric 3D modeling aspects are controlled by dimensions, allowing for new, enhanced changes and more precision in modeling motions.
- *Design intent*: Until a model is finished, its parameters will continue to change from the initial version or design intent.
- *Feature tree*: Record List contains all of the features that have been saved, these features are always available.
- *Automated updates*: Whenever changes a dimension, the visual model immediately updates to reflect the changes. This allows the model to update successively on all changed features.

Disadvantages;

- *File size*: The list of the feature tree grows longer as a model's number of features rises. Therefore, the longer the list, the longer it will take to power the computer to resolve the model.
- *Model sharing*: Due to the vast array of CAD packages on the market, distributing the 3D model via site-specific CAD might be challenging. Files may be exchanged across computers by simply converting them to a generic CAD application, which is extremely simple to do.

10.3   Tribune Design and Analysis with Parametric Modeling Method

Parametric model can be created by automatically changing many parameters such as length, span and height of any extreme design. By transferring this model to structural analysis programs, in addition to static and dynamic analyzes, optimization analyzes can be made in a short time to determine the most suitable geometric properties of the model, and sections can be obtained. At the stage of realizing the extreme designs created with parametric modeling, steel material provides great advantages in obtaining the desired form.

Parametric modeling was used to create the proposal and analysis for the steel carrier system for amateur tribunes at the Şenol Güneş Sports Complex in Turkey's Ortahisar District of the Trabzon Province. The Tribune Project was modeled using the parametric modeling technique in the Dynamo program, including wave and wing forms, which are symbols of Trabzon province (Fig. 10.2). Real-time data transfer was carried out between the structural analysis program SAP2000 and the Dynamo program by using the add-on named "DynamicSap" developed by the project team. Thus, as a result of thousands of analysis and optimization algorithms performed on the finite element model, the dimensions and sections of the most suitable wing and waveform were determined. The tribune is architected in wave form with a width of 13 m, a length of 108.5 m and a height of 5.89 m. Some visuals of the tribune project, which was created by considering the wing and wave form, are given in Fig. 10.3. Views of the finite element models created are given in Fig. 10.4.

After the finite element analysis, the connection details and drawings of the tribune project transferred to Tekla Structures program were created (Fig. 10.5).

After the completion of the tribune project and construction process, the design and analysis of which were made with the parametric modeling method, it was put into use (Fig. 10.6). The tribune project, which has become the focus of attention with its aesthetic appearance in the region where it is located, has created awareness in terms of using the parametric modeling approach in different projects with its innovative application. In addition, considering its high strength, elastic behavior throughout the entire cross-section, ductility and lightness, the use of steel, an earthquake resistant building material, has enabled the aesthetic tribune design to be realized at low cost. Especially in earthquake regions, the lightness of the steel structure will ensure that the structure is exposed to less earthquake forces, and the life of the structure will increase under appropriate maintenance conditions.
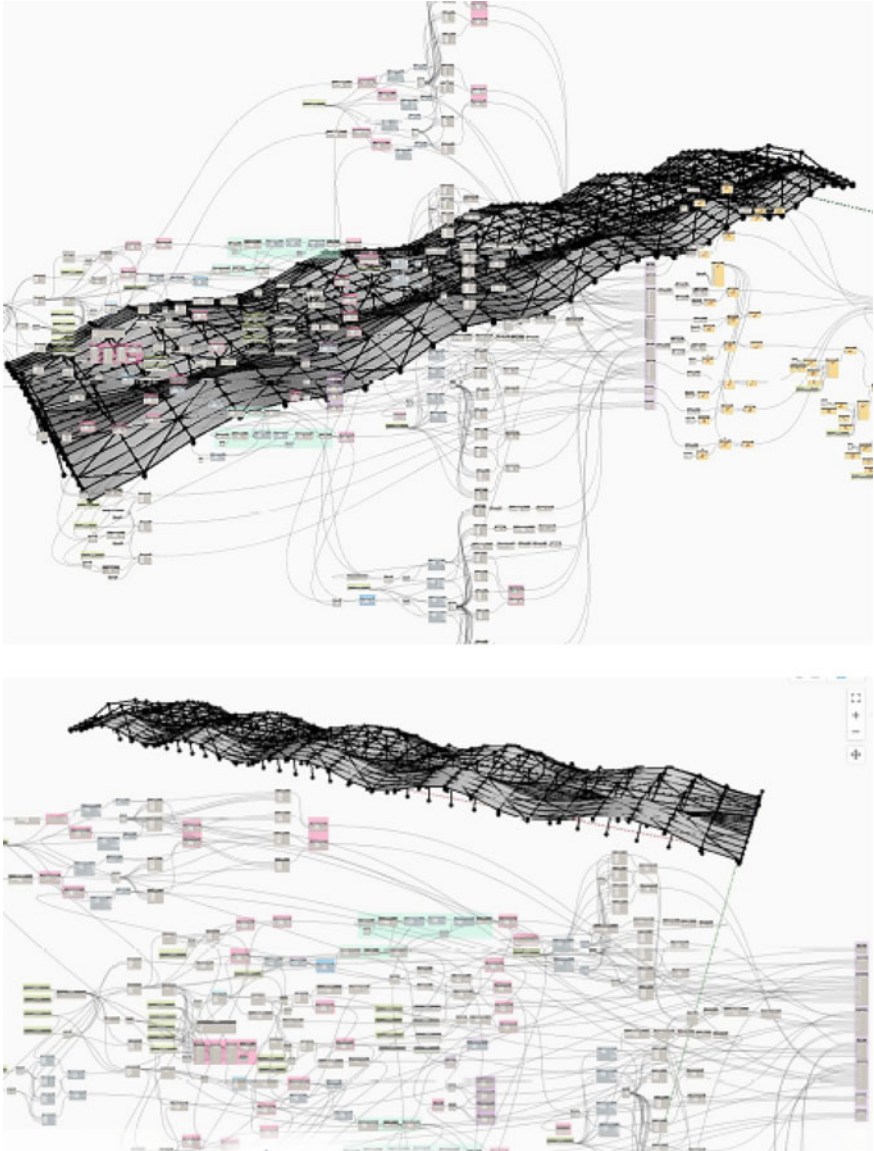
Fig. 10.2 Dynamo model of the tribune created in wave and wing form
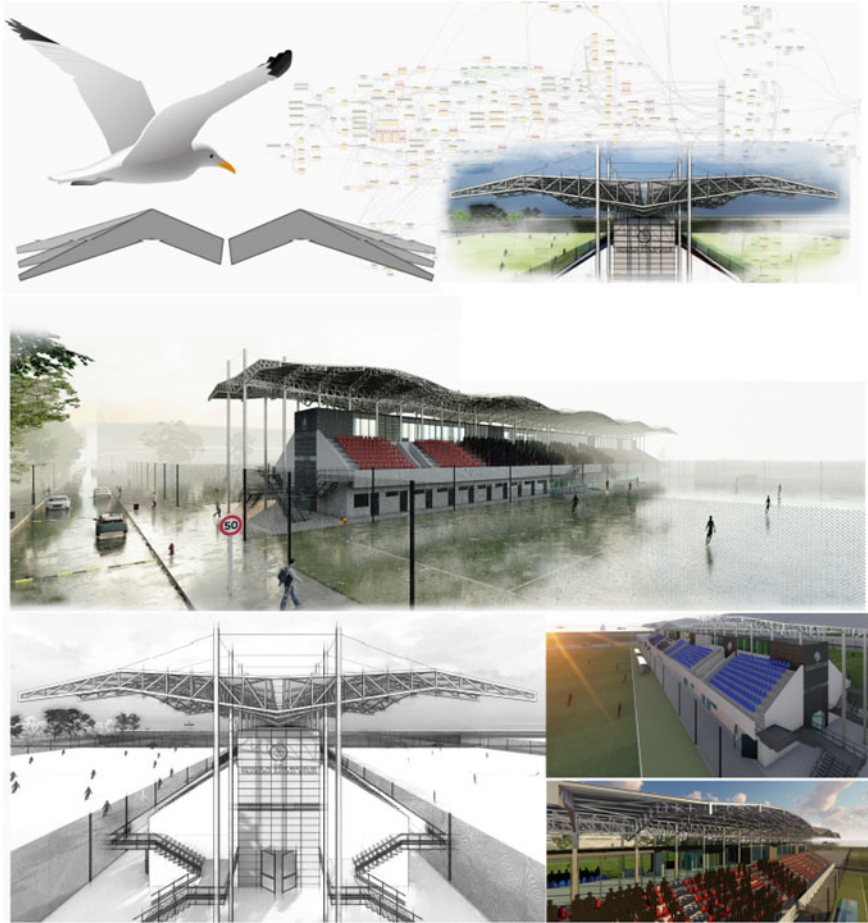
Fig. 10.3   Images of the tribune created in wave and wing form
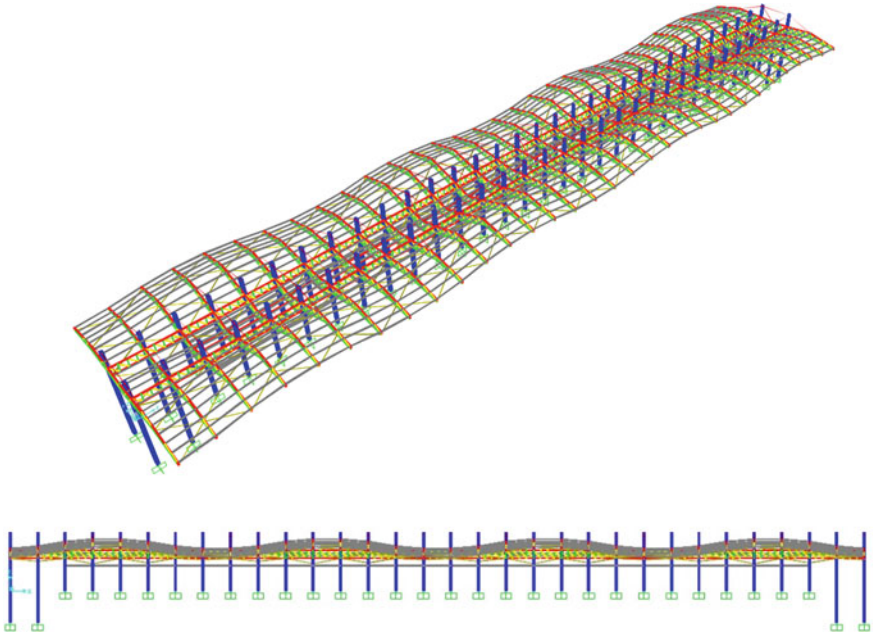
Fig. 10.4 Tribune project transferred to finite element program by parametric modeling
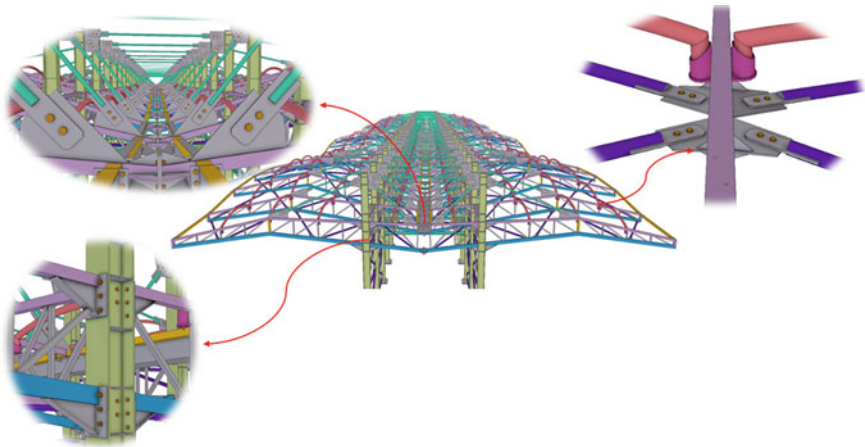
Fig. 10.5 Connection details and drawings of the tribune project in Tekla Structures program

Fig. 10.6 Pictures after the completion of the tribune project

References

Çinici SY, Akipek FÖ, Yazar T (2008) Computational design, parametric modelling and architectural education. Arkitekt 518:16–23

de Ruiter MM (1988) Advances in computer graphics III. Springer Science & Business Media

Gerber DJ (2007) Parametric practices: models for design exploration in architecture. Harvard University

History of CAD CAM (2004) CADAZZ. http://www.cadazz.com/cad-software-history.htm. Accessed 20 April 2014

Moretti L, Bucci F, Mulazzani M (2000) Luigi Moretti: opere e scritti. Electa, Milano

Reddy EJ, Sridhar C, Rangadu VP (2015) Knowledge based engineering: notion, approaches and future trends. Am J Intell Syst 5(1):1–17

Stouffs R, Janssen P, Roudavski S, Tunçer B (2013) A method for comparing designers' behavior in two environments: parametric and geometric modeling. In: Conference on computer-aided architectural design research in Asia (CAADRIA 2013) vol 479, pp 488

Sutherland I (1963) Sketchpad: a man-machine graphical communication system. PhD dissertation, Massachusetts Institute of Technology

Suyoto W, Indraprastha A, Purbo HW (2015) Parametric approach as a tool for decision-making in planning and design process. Case study: office tower in Kebayoran Lama. Procedia Soc Behav Sci 184:328–337

URL-1. https://www.autodesk.eu/solutions/bim. Accessed 28 July 2022

Weisberg D (2008) The engineering design revolution: the people, companies and computer systems that changed forever the practice of engineering. http://www.cadhistory.net. Accessed 23 July 2011

Yu R, Gu N, Ostwald M (2013) Comparing designers' problem-solving behavior in a parametric design environment and a geometric modeling environment. Buildings 3(3):621–638

Chapter 11
Beyond Codes: Enhancing Infrastructure Resilience Through Creative Design

Rajan Sen

Abstract An unprecedented surge in urban population has led to the creation of megacities characterized by heavy traffic, pollution, uncontrolled growth, changes in land use, leading to accelerated environmental degradation. The vulnerability of the urban infrastructure is exacerbated by the hazards of climate change. Increasingly, code-specified worst case scenarios appear obsolete. Evidence of this is found in escalating global incidences of severe storms, record high temperatures, raging forest fires and floods alternating with drought exposing critical infrastructure to large scale damage. With our current inability to predict the impact of climate change, there is an urgent need to explore affordable alternatives to overcome this shortcoming. This paper profiles creative design ideas developed in US and elsewhere to counter intense environmental loads on existing infrastructure. They provide an alternative approach that relies on engineering insight, effective policies, smart technologies and new materials rather than mere code compliance. The goal is to restore functionality of disaster prone critical infrastructure with minimal disruption to the populace. Awareness and application of the varied approaches used can assist licensed design professionals and policy makers to make better informed decisions for building stronger resilient communities.

Keywords Climate · Design · Infrastructure · Resilience · Novel

11.1 Introduction

The safety and integrity of structures relies on loads used for design, e.g., ASCE 7/ 16 (2017). Loads and their combinations are typically determined from a statistical analysis of historical data. Recent events suggest that the records are out of date. Over a 12-day period this summer (2022), news media reported four occurrences of 1 in 1000 year flood events in the United States (St. Louis on July 25–26, Eastern

R. Sen (✉)
University of South Florida, Tampa, FL, USA
e-mail: Rajan.Sen@springernature.com

Kentucky on July 28, Southern Illinois on August 2 and Death Valley on August 5). Elsewhere, there have been reports of wildfires in France, heatwaves in England and drought conditions that have led to water levels in the Rhine drop to unseen levels threatening the transport of critically important bulk material.

Historically, lack of accurate information did not deter early builders from designing resilient structures to meet the challenges of their time. A notable example is the design of the five-story, 37 m tall Horyu-Ji pagoda built in Japan more than 1300 years ago. Its structural form consists of a central wood column made from a single tree trunk ("*shinbashira*") anchored deep into the ground. Each of the five stories of the pagoda are cantilevered from this column.

The Horyu-Ji pagoda has survived 46 magnitude 7.0 or greater earthquakes since it was built. Analysis revealed that this performance was no accident; its design and construction embodied many core principles of modern seismic resistant design such as symmetry, base isolation (separating the structure from the soil), and seismic damping (increasing frictional resistance against ground shaking by using sliding joints), Nakahara et al. (2006).

The insights displayed by the early builders have been replicated by modern designers though their achievements are seldom recognized and therefore not widely known. The goal of this paper is to address this gap. It highlights creative design ideas and accompanying policies developed in US and elsewhere that address extreme events. Knowledge of successful world-wide practices will provide decision makers new perspectives that can lead to improved community resilience at an affordable cost.

11.2 Objectives

Civil engineers are responsible for planning, design, construction, operation and maintenance of physical infrastructure expected to remain functional, durable and safe over a 50–100 year lifespan, ASCE (2015). Problems affecting urban resilience vary widely depending on location, hazards faced, environmental degradation, population density and the potential impact of climate change. A generic one-size-fits all design strategy is therefore not optimal.

This paper presents examples of creative infrastructure solutions developed by the modern-day counterparts of early builders. The ingenuity of the design complemented by imaginative policies made it possible for infrastructure to better withstand extreme events. The hallmark is the simplicity of the design concept and its focus on speedy functional restoration. New materials and technologies (not addressed) can further expedite repair and re-construction.
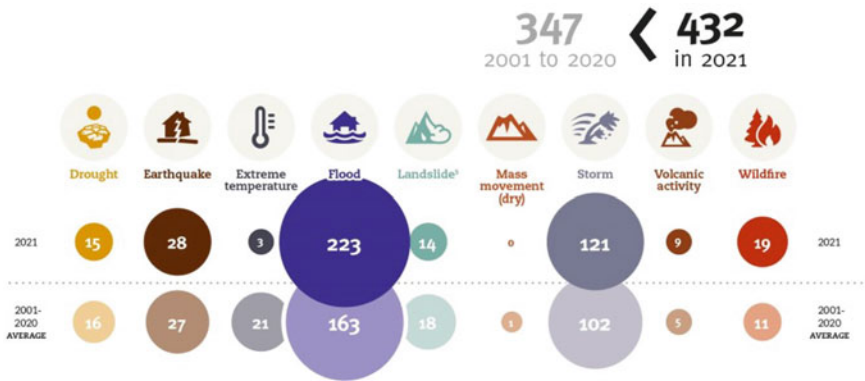
Fig. 11.1 Occurrence by disaster type: 2021 compared to 2001–2020 annual average. *Source* EM-DAT (2022)

11.3 Background

11.3.1 Disaster Data

The global incidence of extreme events is summarized in Fig. 11.1. This compares the occurrence of different disaster types in 2021 with the average over twenty years from 2001 to 2020. The overall number of disasters (432) in 2021 was 24% higher than in the preceding 20 years (347). The types of disaster showing the greatest increase were wildfire (72%), flood (37%) and storm (20%) (EM-DAT 2022).

As extreme weather events become more common, the question facing society is how infrastructure can be economically designed for this uncertain environment, particularly in urban areas where the majority of the world's population now reside.

11.3.2 Climate Change

Climate change has been identified as the principal driver for recent extreme weather events. The United Nations (UN) has defined climate change as "*long-term shifts in temperatures and weather patterns*" (UN 2022). Weather refers to the short term state of the atmosphere at a location whereas climate is the average weather pattern over 30 years.

Geological records show that the Earth's climate has undergone significant change during its 4.5 billion year existence. Current changes are attributed to the accumulation of greenhouse gases (GHG) that trap solar radiation and increase global temperature. Industrialization, population growth, urbanization, deforestation and pollution over the past two centuries, have altered the planet's environmental eco-system.

Informally, it is referred to as the "*era of the Anthropocene*" in recognition of the role of human activity for the change.

Though there are several greenhouse gases, e.g., carbon dioxide, methane, nitrous oxide and others, carbon dioxide is the most damaging since it is retained in the atmosphere for over 100 years (Sachs 2015). Carbon dioxide (CO_2) levels in the atmosphere were first measured in Mauna Loa, Hawaii in 1958 and has since increased continually from 316 to 419 ppm in August 2022. 85.5% of global CO_2 emissions are attributed to fossil fuels and industry (Simply 2022; NASA 2022).

The sustained increase in the atmospheric concentration of carbon dioxide has led to a rise in average global temperature. Figure 11.2 plots this change relative to the 30-year baseline from 1951 to 1980. According to NASA's Goddard Institute of Space Studies, as of August 2022, the average temperature rise is 1.01 C with the majority of the warming taking place after 1975. The global average surface temperature in 2016 and 2020 was tied as the hottest on record.

Temperature increase has led to melting of ice sheets contributing to rising ocean levels. Since 1993 the average global ocean level rise is 101 ± 4 mm as of May 2022 (NASA 2022) though local effects can be higher. This impacts coastal cities such as Miami FL where streets now routinely flood during "king" tide.

Climate models available are used to predict the impact of climate change. In modeling the entire Earth is idealized as a 3-dimensional grid and supercomputers used to determine energy exchange due to dynamic motion in the vertical and horizontal directions (Simply 2022). Unfortunately, the 100 km grid possible in modeling is too coarse to accurately predict climate change effects at the granular local level required for safe design, ASCE (2015). The absence of reliable predictions and the lack of historical data means that creative conceptual designs may be only means available for economically designing resilient infrastructure.

Source: climate.nasa.gov
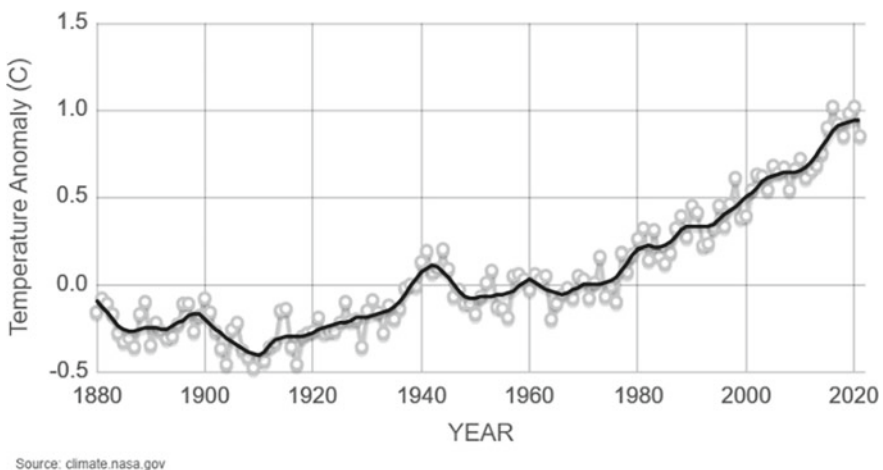
Fig. 11.2 Change in global surface temperature relative to 1951–1980 baseline (NASA 2022)

11.3.3   Urbanization

The year 2008 marked a turning point because the urban population exceeded the rural population for the very first time. Whereas there were only two megacities (>10 m), Tokyo and New York in 1950, their number is currently over 30 and projected to exceed 40 by 2030 with the majority in the developing world (Sachs 2015; Simply 2022). A high population density and a coastal location makes megacities extremely vulnerable to climate shocks as evidenced by the multi-billion dollar damage inflicted on New York by Hurricane Sandy (HUD 2013).

Cities are engines of growth, occupying only three percent of the land surface yet contributing about 60% of the global GDP, McKinsey Global Institute (2011). In the aftermath of a disaster there is urgent need to quickly restore function to minimize economic loss. Delayed recovery can permanently impair competitive advantage. This was the case with Kobe, Japan which was, until the 1995 Great Hanshin Earthquake, the world's busiest seaport. For this reason, the US Department of Transportation committed more than half of the $12.4 billion allocated for immediate repairs following hurricane Sandy, HUD (2013). Almost certainly, re-built structures were designed to prevailing standards. Though there was a 're-build by design component' that took a holistic approach to making the entire region resilient, funding assigned for the six projects that were part of this effort was less than $1 billion, McKee (2014).

11.3.4   Infrastructure Interdependency

Infrastructure systems, whether privately owned such as utilities, or publicly owned such as highways, are characterized by interdependency, e.g., traffic signals require communication systems and electric power. Thus, disruption to one sector can have a cascading effect on multiple sectors, evident in the devastation following catastrophic natural events.

Hurricane Sandy disrupted power generation impairing transportation, communications, water supply and sewage treatment sectors among others in northeastern US. The 2013 HUD Task Force report provides statistics on this impact: average commute time in Brooklyn doubled from 42 to 86 min, 100 million gallons of raw sewage were released into Hewlett Bay in 2 days, and 25% of cell sites in ten states were out of service (HUD 2013). A systems-based design can take interdependency into account. But this is an emerging research topic, e.g., NSF (2014), and it will be years before a systems design approach is feasible. In the interim re-built structures will continue to be designed at best, for the previous worst case scenario. An inevitable outcome is a decline in infrastructure resilience relative to the unknown impact of climate change.

11.4   UN Action

The stabilization and ultimately reduction in the atmospheric levels of GHG responsible for temperature rise is a difficult, complex problem requiring political action and cooperation at the national and international level. For context, the US was only able to pass climate change legislation in August 2022 after decades of effort. The legislation includes financial incentives geared to accelerate innovation and influence consumer behavior that is expected to significantly reduce carbon emission by 2030.

Serious attempts at the international level were first made at the UN sustainability conference in Rio (1992) and culminated in the historic 2015 Paris Agreement. Its goal was aspirational, to limit global temperature increase this century to "*well below 2 degrees, preferably 1.5 °C*" above pre-industrial levels through reductions in GHG emission (UN Climate Change 2022). The international commitment to pursue this goal was made at the Glasgow Climate Pact in November 2021 (UN Climate Change 2022). Relative to 2010, this targets a 45% reduction in carbon emission levels by 2030 and net zero emission by 2050.

11.5   Creative Design Examples

Brief descriptions of a small sample of creative engineering solutions are presented. These are taken from disparate applications worldwide. More detailed information may be found in the relevant cited references.

The examples highlight how innovative approaches can provide resilient solutions even when the scale and extent of an extreme event is unknown. A common thread in all the applications is avoidance of "complexity risk" that arises because of reliance on sophisticated controls geared for improving operational efficiency. These usually require power and telecommunication support that are non-existent during extreme events rendering them ineffective, Zolli and Healey (2013).

11.5.1   Resilient Drinking Water Supply

New York City gets its drinking water from 19 reservoirs and three controlled lakes spread across 518,000 ha (nearly 2,000 square miles) watershed north of the city. It is one of the few US cities where water is not filtered but disinfected using chlorine and UV light (NYC EPA 2021).

At the turn of the twenty-first century, this watershed was threatened by contamination caused by upstate farm run-off. City planners decided to solve this problem by offering financial incentives to stop activities that led to the contamination (Sachs 2015) and focus instead on watershed management and protection. It opted to buy land around the 19 reservoirs and three controlled lakes making it unnecessary to

construct a sophisticated electric-powered water filtration plant that would have cost about \$8 billion to build and \$300–400 million to operate annually, Sachs (2015), UN Habitat (2012). To ensure water of the highest quality was delivered to its millions of customers a comprehensive sampling and testing is in place deploying robotic stations where necessary.

The resilience of New York City's water supply was proven in the aftermath of Hurricane Sandy when there was loss of electric power. The city's water distribution was unaffected because it is gravity fed and unfiltered. It is also economical; according to the 2021 report, the annual combined water and sewer charge for an average New York City household using 265,000 L (70,000 gallons) is \$994 calculated at 2022 fiscal rates. Of this the water component is \$384 (NYC EPA 2021).

11.5.2 Dual Use Structures

To solve the twin problems of flash flooding and rush hour traffic, Kuala Lumpur designed a dual purpose storm water management and road tunnel system that was opened to traffic (2007). The tunnel cross-section has an upper channel for a freeway and a lower channel for diverting flood waters. Under normal operating conditions, the upper channel housing is open to motorists. For moderate storms, the upper channel is still available to motorists but floodwaters are diverted into the lower channel that drain into a reservoir. In the event storms are very severe, the tunnel is closed to motorists altogether and automatic water-tight gates are opened to allow floodwaters to pass through.

The tunnel handles 30,000 cars per day and has been used 44 times to divert floodwaters, SMART (2022). Note that this design was feasible because of the availability of a reservoir in close proximity to the tunnel. In designing the system, it was assumed that flooding was inevitable and therefore the solution focused on rapidly restoring services necessitating allowing the tunnel to serve as a drain during severe flooding events.

Similar dual concepts have been successfully used for other infrastructure, e.g., lower levels of multistory parking garages serving as temporary reservoirs to accommodate flood waters and ease street flooding. Rotterdam's "water square", is a public space that doubles up as a reservoir that can store up to two million liters of rain water run-off. This capacity prevents the sewer system from being overwhelmed and streets from being waterlogged in a heavily built-up urban area.

11.5.3 Protecting Transportation Infrastructure

Intense rainfall events lead to street flooding and the overflow can enter tunnels and subway stations creating havoc. This was the case with the Brooklyn Battery Tunnel whose entrances were unprotected. Flood waters from Hurricane Sandy

caused significant damage to its lighting and ventilation systems. Watertight doors protecting the entrances to Houston's underground tunnels connecting buildings that are part of the Medical complex prevented similar damage, Rosenthal (2012). The severe floods that submerged Bangkok in 2011 did not affect their Metro system because their entrances were designed to be at a higher elevation. These examples highlight how simple measures such as elevating entrances or providing watertight gates can greatly enhance urban transportation resilience for a relatively modest cost.

11.5.4 Managing Highway Flooding

The Danish National Road network constitutes 5% of all public roads but carries almost 50% of the country's total traffic. Heavy rainfall over 2010–12 waterlogged sections of the highway necessitating extended road closure.

The Danish authorities initiated a detailed hydrological analysis to identify optimal solutions. Stake holders were consulted and it was decided that the efficiency of the highway system would not be adversely impaired if flooded highways could be cleared within one hour (Danish Road Directorate 2013). Highway regions prone to flooding were identified and arrangements made to provide additional mobile pumps to complement those already in place to facilitate rapid removal of flood waters.

Denmark controlled flooding using a three-pronged strategy (Fig. 11.3). Safety was addressed by teaming up with a company that could enforce road closures as needed. Users were kept informed on impending flooding and resulting traffic disruption. Improvements were undertaken during scheduled construction, e.g., when carriageways were widened to minimize cost. Additionally, research and development measures were instituted to identify optimal short and long term flood prevention strategies.

The most innovative action was the deployment of mobile pumps to minimize the impact of localized flooding rather than elevate the road or replace existing drainage pipes with ones having a greater capacity. The pumps used were carefully vetted to ensure they could operate optimally in extreme conditions. The positioning of

Fig. 11.3 Flooded Danish highway and three-prong strategy to minimize impact (Courtesy Danish Road Directorate)

the pumps was determined from hydrological studies to ensure the waters could be safely discharged without causing flooding elsewhere. This provided a cost effective solution without incurring large capital expenditures.

11.5.5 Earthquake Mitigation

The Alaska pipeline project was completed during 1974–1977. The 1.2 m pipeline transports crude oil from Prudhoe Bay in the Arctic Ocean to the ice-free Valdez Marine Terminal 1290 km away crossing the active Denali fault in its path.

Nearly 25 years after its construction, a magnitude 7.9 earthquake struck in November 2002. The intensity of the shaking, shifted the pipeline 4.3 m horizontally and 0.76 m. vertically. It survived intact because it had been designed to withstand a magnitude 8.0 earthquake and accommodate a 6.1 m movement horizontally and 1.52 m movement vertically. Over the fault zone, bends were deliberately introduced to limit the displacements the pipe segment would encounter. The movement itself was accommodated by supporting the pipe on Teflon shoes that were free to slide on the sloping steel beams placed in the transverse direction (Fig. 11.4). This creative design solution only added about $3 million to the original cost, US Geological Survey (2022).

This application exemplifies a highly creative, cost effective engineering solution for a critically important pipeline at a vulnerable location. It illustrates the effectiveness of gravity based solutions (both horizontal and vertical movements were accommodated because steel beams were placed at a slope), system was passive (no power was needed because the Teflon shoes minimized friction allowing the supports to move freely even when there was some snow on the ground at the time of the earthquake) complemented by superb analysis that accurately predicted the expected movement.

The financial implications of an oil-spill at an environmentally fragile location meant that many safeguards were in place to limit the extent of any spillage and also to continuously monitor performance so that necessary action could be speedily undertaken. Such careful maintenance undoubtedly allowed the pipeline to displace in the manner envisaged by its designers 25 years earlier.

11.6 Resilience Enhancing Policies

Codes have traditionally provided a framework for safe, durable and resilient infrastructure design. To this end, the American Society of Civil Engineers issued a white paper on climate adaptation in 2015. However, uncertainty associated with predictions about future climate change effects led to guarded recommendations such as: use engineering judgment, low-regret adaptive strategies (regret is the difference between a plan pay-off and the best performing plan under the same scenario) and

Fig. 11.4 Alaska pipeline crossing at Denali Fault (*Source* US Geological Survey)

engineering economic analysis, ASCE (2015). Examples of policies enhancing urban resilience found in the literature fall under two broad categories: policies that increase resilience through retrofit or insurance coverage and those that employ "low regret" adaptive strategies to mitigate the effect of climate change.

The US government's accountability office reported that in Berkeley CA it is mandated that a portion of the taxes resulting from a real estate transaction be made available to the buyer provided seismic retrofitting of a home is completed within a year of purchase. This program has had an 80–90% participation rate (GAO 2014). But, overall participation for insuring homes against earthquakes in CA is estimated to be only ten percent, WSJ (2015), possibly because the deductible is a very high 15%.

France has a nationwide catastrophic insurance program whose premium is paid for as an add-on to home insurance, Dumitrescu (2010). The flat-rate premium set by the state and collected by private insurance industry covers all homeowners of any risk exposure regardless of location.

The flood management strategies used in Denmark and Malaysia are examples of "low regret" adaptive strategies. Rather than incur heavy capital expenditure by installing large diameter drainage pipes to prevent flooding, dual use tunnels and mobile pumps provided solutions that adequately met the community's needs.

11.7 Concluding Remarks

The role of good design is rarely celebrated and their existence remains invisible. In contrast, poor design is given wide publicity, e.g., heavy key rings that accidentally switched off automobile engines and disabled airbags. This paper presents examples of creative designs that minimized the impact of extreme effects ensuring a rapid return to normalcy. Awareness of the novel concepts embodied in the design and the underlying supportive policies will allow other communities to use them effectively.

Climate change effects are long lasting because carbon dioxide is retained in the atmosphere for over 100 years. The venture capitalist John Doerr has developed a detailed action plan to meet UN emission targets (Doerr 2021). His calculations show that attaining net zero emissions at the global scale will require annual investments of up to $1.7 trillion for the next 20 years or more. It will also require life style changes for reasons eloquently stated by the writer Ghosh (2016) who observed "*… the patterns of life that modernity engenders can only be practiced by a small minority of the world's population… not because of technical or economic limitations but because humanity would asphyxiate in the process*".

References

ASCE (2015) Adapting infrastructure and civil engineering practice to a changing climate, ASCE, Reston, VA 2015

ASCE 7-16 (2017) Minimum design loads and associated criteria for buildings and other structures (ASCE/SEI 7-16), ASCE, Reston, VA

Danish Road Directorate (2013) Strategy for adapting to climate change, Vejdirektoratet, Denmark

Doerr J (2021) Speed and scale: an action plan for solving our climate crisis now. Portfolio, Penguin, New York, NY, p 263

Dumitrescu B (Oct 2010) French natural catastrophe insurance and reinsurance regime, Boston

EM-DAT (2022) CRED/UCLouvain, Brussels, Belgium–www.emdat.be

GAO (14 May 2014) Disaster resilience, GAO-14-603T, Washington DC

Ghosh A (2016) The great derangement. The University of Chicago Press, p 92

HUD (Aug 2013) Hurricane Sandy rebuilding strategy, Rebuilding task force, Washington DC

McKee B (Jun 2014) Rebuild by design: the winners. Landscape Architecture Magazine

McKinsey Global Institute (Mar 2011) Urban world: mapping the economic power of cities

Nakahara K, Hisatoku T, Nagase T, Takahashi Y (2006) Earthquake response of ancient five-story pagoda structure of Horyu-Ji temple in Japan. In: Proceedings, 12th world conference on earthquake engineering, Auckland, New Zealand, 6 pp

NASA (2022) https://climate.nasa.gov/vital-signs/

NSF (Mar 2014) Program solicitation 14-524, Resilient interdependent infrastructure processes and systems

NYC EPA (2021) Drinking water supply and quality report 2021, NY

Rosenthal E (9 Nov 2012) Hurricanes exposed flaws in protection of tunnels, New York Times

Sachs J (2015) The age of sustainable development. Columbia University Press, NY

Simply DK (2022) Simply climate change. DK Publishing, NY

SMART (2022) Kuala Lumpur, Malaysia. http://www.roadtraffic-technology.com/projects/smart/, http://www.visionlondon.com/news-press/interview-ricj=hard-coutts-baca-architect/

UN Climate Change (2022) https://ukcop26.org/the-glasgow-climate-pact

UN Habitat (2012) Urban patterns for a green economy: working with nature. Nairobi, Kenya

UN Climate Change (2022) https://unfccc.int/process-and-meetings/the-paris-agreement/the-paris-agreement

UN (2022) https://www.un.org/en/climatechange/what-is-climate-change

United Nations conference on environment and development, Rio de Janeiro, Brazil, 3–14 June 1992

US Geological Survey (2022) The trans-Alaska oil pipeline survives the quake. Fact Sheet 014-03

WSJ (2015) Quake coverage gets a push, August 31, page C3

Zolli A, Healy A (2013) Resilience: why things bounce back. Simon and Schuster, NY

Chapter 12
Punching Shear Strength of FRP-Reinforced-Concrete Using a Machine Learning Model

Nermin M. Salem and **Ahmed F. Deifalla**

Abstract The aim of this research is to investigate the strength behavior of Fiber reinforced polymers (FRP) - Reinforced-concrete using supervised Machine Learning (ML) techniques. Based on previous studies by the authors, two machine learning modes were found to be the most effective in terms of accuracy and consistency, namely, the ensembled boosted regression model and the medium Gaussian SVM. The ensembled boosted model showed the most accurate predictions. To assess the performance of the two suggested ML models: the 15-held-out validation method and statistical analysis techniques including metrics such as the coefficient of variation (R^2), mean absolute error (MAE), and root mean square error (RMSE) are used. The ensembled boosted ML model demonstrated the most accurate predictions, achieving $R^2 = 0.97$, MAE = 43.352, and least RMSE = 71.963. Also, the variation of strength versus effective parameters was captured and discussed.

Keywords FRP · Strengthening · Torsion · ML

12.1 Introduction

Fiber-reinforced polymer (FRP) had been utilized in the construction industry, while showing success due to its interesting characteristics, especially, being highly resistant to corrosion (Alkhatib and Deifalla 2022a, 2022b; Deifalla 2022, 2021a, 2021; Deifalla et al. 2021; Ebid and Deifalla 2021; Ali et al. 2021). In addition, punching shear of concrete elements is an area of many unsolved mysteries, thus, a need for

N. M. Salem (✉)
Electrical Engineering Department, Future University in Egypt (FUE), Cairo, Egypt
e-mail: nfawzy@fue.edu.eg

A. F. Deifalla
Structural Engineering and Construction Management Department, Future University in Egypt (FUE), Cairo, Egypt
e-mail: ahmed.deifalla@fue.edu.eg

further digging is a mandate (Deifalla 2020, 2020b; ElMeligy et al. 2017; Hassan and Deifalla 2015).

Artificial Intelligence (AI) and Machine Learning (ML) algorithms have gained a lot of attention recently due to their significantly superior more accurate results in many applications such as (Salem et al. 2020, 2019, 2018; Salem 2021; Salem and Deifalla 2022; Deifalla and Salem 2022) and in solving complex structural problems (Badra et al. 2022; Li et al. 2022; Khan et al. 2022; Shen et al. 2022; Ebid and Deifalla 2022). There are various ML techniques that showed very good potential in solving such a complex problem and producing accurate prediction results such as ensembled trees, decision trees, gene expression programming and artificial neural networks, and support vector machines.

The idea of ML techniques is the employment of pattern recognition methodologies using datasets and statistical analysis. The focal point is to extract the required data from the used dataset in training in order to produce and obtain various relations which simplify the complex patterns found in the original dataset.

This paper aims to evaluate the two best models from our research papers, (Salem and Deifalla 2022; Badra et al. 2022). Model development was briefly described and evaluated. An additional parametric study was conducted using the predictions of the suggested ML models. Concluding remarks were delineated and discussed.

12.2   Machine Learning Model

To develop and analysis the two models, a dataset composed of 189 records from experimental studies was used in training and testing (Salem and Deifalla 2022; Badra et al. 2022). The model had been trained using 80% of the dataset with holdout validation of 15% and testing with the remaining of 20%. The training of our model consists of main four sub-processes:

- The dataset had been divided into two main sets: training and testing.
- ML methodologies are applied on the training set with holdout validation.
- Evaluate the accuracy of the trained model.
- Predict the final output.

12.2.1   Support Vector Machine (SVM) Model

SVM is a supervised machine learning technique that has been employed for both classification and regression problems. This technique is used in solving and generalizing problems such as high input dimensional space, small datasets, and non-linearity problems. SVM techniques can have the ability to transform the input data into a higher dimensional vector via a non-linear transformation using an inner product function (Badra et al. 2022). The model first maps the input data into an n-dimensional space function followed by a non-linear kernel function to improve

the difference in the original input data. The goal is to find the function $F(wi, yi)$ that has the maximum derivation ε of the real output y_i for all samples in the training set. the linear regression function $F(w, y)$ could be defined as:

$$F(w_i, y_i) = \sum_{i=1}^{n} w_i H_i(y) + b \tag{12.1}$$

where, w_i is the vector transformation weight, $H_i(y)$ is the non-linear space and b is the bias. The loss function between the actual output x and the model output $F(w, y)$ could be defined by:

$$L = \begin{cases} 0 & if \, |x - F(w, y)| \leq \varepsilon \\ |x - F(w, y)| & otherwise \end{cases} \tag{12.2}$$

the final computed function is defined by:

$$F(y) = \sum_{i=1}^{n} \sigma_i K(Y, \, y_i) + b \tag{12.3}$$

where, σ_i is LaGrange multiplier, $K(Y, y_i)$ b is the bias and n is the number of support vectors.

There are several kernel types used for SVM such as linear, quadratic, cubic, fine, medium, and coarse SVMs. In this research, the medium Gaussian kernel is used as in Badra et al. (2022).

12.2.2 Ensemble Boosted Machine

The ensemble technique is used for enhancing the prediction accuracy by computing several separate, weak models and then merging them by averaging and voting techniques to obtain a single powerful model. Ensemble tree has two main techniques; boosted and bagged. The study will concentrate on the boosted algorithm as it showed the most accurate results for the used dataset (Salem and Deifalla 2022). In the boosted algorithm, several cumulative models are produced, and many components are made to have higher accuracy than single models. Afterward, all sub-models are augmented based on a weighted average technique into one final single model.

12.2.3 Results and Discussions

The two ML models were tested using the testing set, i.e., the model was not trained using this part of the dataset, composed of 20% of the experimental dataset. To guarantee that there is no overfitting potential: (1) Random splitting of the dataset among training and testing sets with the defined percentage; (2) evaluation performance on the test set.

In assessing the effectiveness of our proposed models, three statistical measures were employed for the randomly selected testing set: coefficient of determination (R^2), mean square error (MAE), and the root mean square error (RMSE). These three statistical measures are computed as:

$$R^2 = 1 - \frac{\sum_{i=1}^{m} (Z_p - Z_o)^2}{\sum_{i=1}^{m} Z_o - \frac{1}{m} \sum_{i=1}^{m} Z_o} \tag{12.4}$$

$$MAE = \frac{1}{m} \sum_{i=1}^{m} |Z_p - Z_o| \tag{12.5}$$

$$RMSE = \sqrt{\frac{1}{m} \sum_{i=1}^{m} (Z_p - Z_o)^2} \tag{12.6}$$

where, Z_p is the model output and Z_o is the actual output.

The boosted ensemble model produced the highest R^2, lowest MAE and RMSE with values of 0.97, 43.452, and 71.963, respectively. While medium gaussian SVM scored 0.69, 116.613, and 245.066, respectively for the testing set. Results are summarized in Table 12.1. Both RMSE and MAE are measured in KN.

Although Medium Gaussian SVM showed promising statistical results in the training phase, in the testing phase, it couldn't keep the same good results. this could be justified by the following reasons:

- SVM algorithms work by classifying data points, any other points below or above them, the model will not be able to give a reasonable predicted value.
- These algorithms also may not work well in case the number of features of each data point outnumbers the training samples.

Table 12.1 Metrics results

	R^2		RMSE		MAE		Training time
Models	Training	Testing	Training	Testing	Training	Testing	(seconds)
Medium gaussian	0.96	0.69	57.815	236.587	46.092	109.372	1.4165
Boosted	0.98	0.97	44.12	71.963	35.95	43.452	1.1991
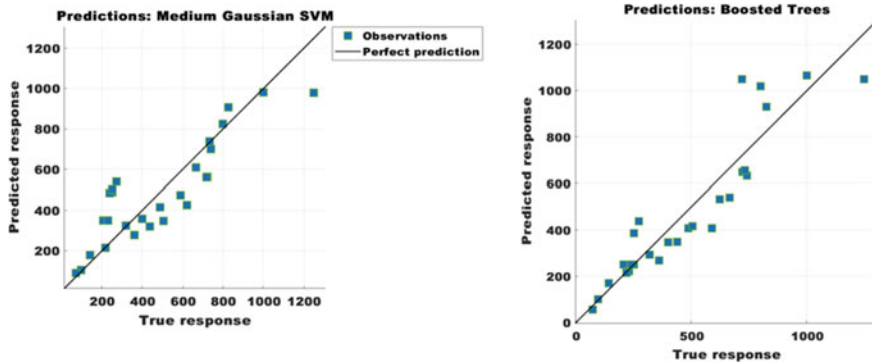
Fig. 12.1 Models predictions

- Also, it may not be suitable for large datasets.

Therefore, Boosted Ensemble ML technique could easily adapt to a large dataset, such as the one used in our research, and maintain the same accurate results predictions in both training and testing phases.

The two suggested models were trained using MATLAB 2022a with the Statistical and Machine learning toolbox. The training and testing were conducted on an Intel(R) Core (TM) i5-7200U CPU @ 2.50 GHz equipped with 16 GB RAM.

Figure 12.1 illustrates the predictions generated from the two suggested models, respectively, and the actual output from the employed testing set. Ideally, all prediction points would be exactly located on the diagonal line and any divergence or deviation between the predicted data points and the diagonal line indicated the prediction error.

12.3 Effect of Various Parameters on Punching Shear Strength of FRP-Reinforced Concrete Elements

Figure 12.2 shows a parametric study for the strength calculated using the two proposed models versus the values of the effective parameters including the size, the concrete compressive strength, the flexure reinforcement ratio, and the FRP modulus of elasticity.

12.3.1 Versus Size

From Fig. 12.2, the impact of the size was captured by the proposed models, showing the presence of two nonlinear folds occurring at the effective depth of value 200
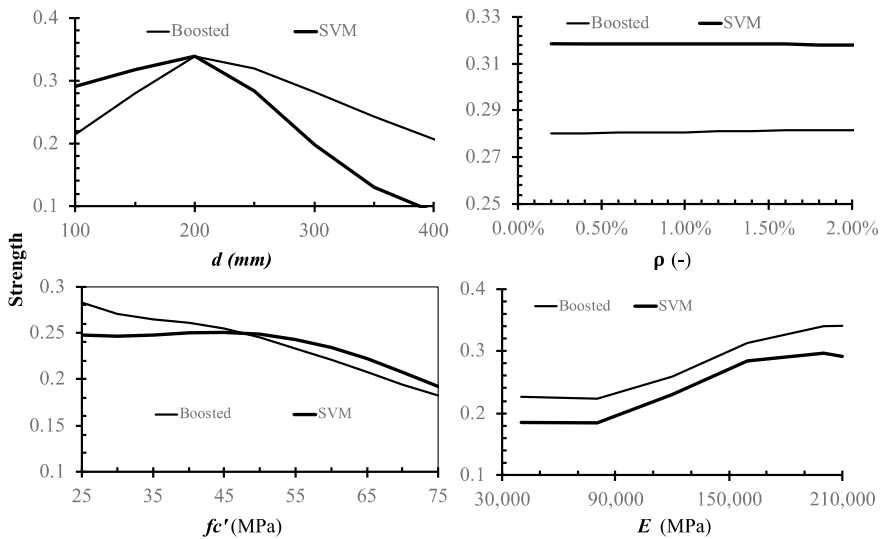
Fig. 12.2 Strength versus selected effective parameters (modulus of elasticity (**E**) of 80,000 MPa, effective depth (**d**) set as 150 mm, concrete compressive strength (**f'$_c$**) of 30 MPa, flexure reinforcement ratio (**ρ**) at 1%, and column dimensions (**C**) set to 100 mm.)

mm. Prior to this effective depth, the strength increased with the increase of the size. Conversely, after the effective depth value exceeded 200 mm, the strength is significantly decreased with the deeper depth (i.e., size effect). However, the Boasted model displays a gentler less gradient of decrease after the 200 mm value compared to the SVM model.

12.3.2 Versus Flexure Reinforcement Ratio

Although methods have proposed a cubic root or a square root relation between strength and flexure reinforcement ratio, the data depicted in Fig. 12.2 shows that the strength computed using the proposed model shows a constant pattern without any variation of strength versus the flexure reinforcement ratio. This is attributed to the fact that the transversal resistance of FRP reinforcements is much lower than that of steel reinforcement. Thus, diminishing the dowel action component.

12.3.3 Versus Concrete Compressive Strength

Although methods have proposed a cubic root or a square root relation between strength and concrete compressive strength. From Fig. 12.2, the strength was

computed from the data of the proposed model showed a completely different variation versus the concrete compressive strength.

12.3.4   Versus Modulus of Elasticity

Although methods have proposed a cubic root or a square root relation between strength and modulus of elasticity. From Fig. 12.2, the strength calculated using the proposed model showed three-fold variation versus the value of modulus of elasticity. Small variation up to modulus of elasticity value of 80 GPa, followed by an increase in the strength versus the value of modulus of elasticity up to 160. Then, almost no change up to 210 GPa value for modulus of elasticity.

12.4   Summary and Conclusions

For concrete FRP-Reinforced-Concrete elements, two models were suggested and integrated into a parametric study aiming at assessing the impact of various parameters on the strength. The following findings are summarized as follows:

- The boosted model showed more accurate and consistent performance compared to the SVM model.
- The size effect was clearly identified at a value of 200 mm by both models, while the boosted model offered a more refined distinction.
- No variation of strength versus the flexure reinforcement ratio was confirmed by either models. This is because the transversal resistance of FRP reinforcements is much lower than that of steel reinforcement. Thus, resulting in a lower dowel action component.
- The strength calculated using the proposed models did not show the traditional cubic root or a square root relation with the concrete compressive strength, however, they showed a completely distinctive variation with respect to the concrete compressive strength.
- The strength calculated using the suggested models also did not show the traditional cubic root or a square root relation with the modulus of elasticity, however, they showed a three-fold variation versus the value of modulus of elasticity. Small variation up to modulus of elasticity value of 80 GPa, followed by an increase in the strength versus the value of modulus of elasticity up to 160 GPa. Then, almost no change up to 210 GPa value for modulus of elasticity.

References

Ali A, Hamady M, Chalioris CE, Deifalla A (2021) Evaluation of the shear design equations of FRP-reinforced concrete beams without shear reinforcement. Eng Struct 235. Elsevier

Alkhatib S, Deifalla A (2022a) Punching shear strength of FRP-reinforced concrete slabs without shear reinforcements: a reliability assessment. Polymers 14:1743. https://doi.org/10.3390/polym14091743

Alkhatib S, Deifalla A (2022b) Reliability-based assessment and optimization for the two-way shear design of lightweight reinforced concrete slabs using the ACI and EC2. Case Stud Constr Mater 17:e01209. https://doi.org/10.1016/j.cscm.2022.e01209

Badra N, Haggag S, Deifalla A, Salem NM (2022) Development of machine learning models for reliable prediction of the punching shear strength of FRP-reinforced concrete slabs without shear reinforcements. Meas 201:111723. ISSN 0263–2241. https://doi.org/10.1016/j.measurement.2022.111723.

Deifalla A (2020) Design of lightweight concrete slabs under two-way shear without shear reinforcements: a comparative study and a new model. Eng Struct 222:111076. Elsevier. https://doi.org/10.1016/j.engstruct.2020.111076

Deifalla A (2020b) Strength and ductility of lightweight reinforced concrete slabs under punching shear. Structures 27:2329–2345. https://doi.org/10.1016/j.istruc.2020.08.002

Deifalla A (2022) Punching shear strength and deformation for FRP-reinforced concrete slabs without shear reinforcements. Case Stud Constr Mater. https://doi.org/10.1016/j.cscm.2022.e00925

Deifalla AF, Zapris AG, Chalioris CE (2021) Multivariable regression strength model for steel fiber-reinforced concrete beams under Torsion. Materials 2021(14):3889. https://doi.org/10.3390/ma14143889

Deifalla A (2021) A strength and deformation model for prestressed lightweight concrete slabs under two-way shear. Adv Struct Eng, 1–12. https://doi.org/10.1177/13694332211020408

Deifalla A (2021a) Refining the torsion design of fibered concrete beams reinforced with FRP using multi-variable non-linear regression analysis for experimental results. Eng Struct 224. Elsevier

Deifalla A, Salem NM (2022) A machine learning model for torsion strength of externally bonded FRP-reinforced concrete beams. Polymers 14(9):1824

Ebid A, Deifalla A (2021) Prediction of shear strength of FRP reinforced beams with and without stirrups using (GP) technique. Ain Shams Eng J. 12(3):2493–2510. Elsevier. https://doi.org/10.1016/j.asej.2021.02.006

Ebid A, Deifalla A (2022) Using artificial intelligence techniques to predict punching shear capacity of lightweight concrete slabs. Materials 15:2732. https://doi.org/10.3390/ma15082732

ElMeligy O, El-Nemr AM, Deifalla A (2017) Reevaluating the modified shear provision of CAN/CSA S806–12 for concrete beams reinforced with FRP stirrups. AEI 2017. https://doi.org/10.1061/9780784480502.027

Hassan MM, Deifalla A (2015) Evaluating the new CAN/CSA-S806-12 torsion provisions for concrete beams with FRP reinforcements. Mater Struct. Accepted: 18 July 2015, https://doi.org/10.1617/s11527-015-0680-9

Khan MA, Aslam F, Javed MF, Alabduljabbar H, Deifalla AF (2022) New prediction models for the compressive strength and dry-thermal conductivity of bio-composites using novel machine learning algorithms. J Clean Prod 350:131364. ISSN 0959–5526. https://doi.org/10.1016/j.jclepro.2022.131364

Li Y, Zhang Q, KamiÑski P, Deifalla A, Sufian M, Dyczko A, Kahla N, Atig M (2022) Compressive strength of steel fiber-reinforced concrete employing supervised machine learning techniques. Materials 15(12):4209. https://doi.org/10.3390/ma15124209

Salem NMF (2021) A survey on various image inpainting techniques. Futur Eng J 2(2), Article 1. https://digitalcommons.aaru.edu.jo/fej/vol2/iss2/1

Salem NM, Deifalla A (2022) Evaluation of the strength of slab-column connections with FRPs using machine learning algorithms, Polymers 2022 14(8):1517. https://doi.org/10.3390/polym14081517

Salem NM, Mahdi HMK, Abbas H (2018) Semantic image inpainting using self-learning encoder-decoder and adversarial loss. In: Proceeding of 13th international conference on computer engineering and systems (ICCES)

Salem NM, Mahdi HMK, Abbas HM (2019) Random-shaped image inpainting using dilated convolution. Int J Eng Adv Technol (IJEAT) 8(6)

Salem NM, Mahdi HMK, Abbas HM (2020) A novel face inpainting approach based on guided deep learning. In 4th international conference on communications, signal processing and their applications (ICCSPA '20)

Shen Z, Deifalla AF, Kamiński P, Dyczko A (2022) Compressive strength evaluation of ultra-high-strength concrete by machine learning. Materials 15:3523. https://doi.org/10.3390/ma15103523

Chapter 13
Structural Collapse Visualization Using Blender and BCB

Ridwan Adebayo Bello, Murat Günaydin, and Ahmet Can Altunişik

Abstract   In recent years, unfavourable actions such as excessive deflection, uneven settling of the soil beneath foundations, structural loads, deterioration of materials, poor maintenance, landslides, deficiency in the initial builder's structural knowledge, flood, earthquake and explosive blast have led to the collapse of structures and loss of human life. It has often been reported that these events do not kill people but rather the affected structures do. Hence, the collapse of engineering structures is a contemporary and critical topic all over the world. However, to simulate these phenomena, a great number of input data and failure criterion definitions are required which have an elaborated form owing to the interaction between several elements of engineering structure. Also, the computational cost is relatively high and time-consuming. Hence the justification for an alternative simplified method using Blender software and Bullet Constraints Builder (BCB). Blender software and BCB add-on work in harmony to simulate collapse scenarios. Blender and BCB averaged a large number of structural features in simplified engineering formulas. Consequently, the time it takes to develop an executable simulation model is much reduced with approximately the same accuracy and debris formation. The debris formulation of the simplified method could be used to trace victims in the event of a collapse in reality. This study aims to review the alternative simplified method that could be used for visualizing collapse. The review is supported by masonry structure as a case study.

Keywords   Blender · BCB · Collapse · Masonry · Visual simulation

R. A. Bello · M. Günaydin · A. C. Altunişik (✉)
Department of Civil Engineering, Karadeniz Technical University, Trabzon, Turkey
e-mail: ahmetcan@ktu.edu.tr

13.1 Introduction

Structures are safely designed based on an accurate understanding of their collapse condition. The knowledge of ductility is relied upon in the design of a modern structure to signal looming collapse. Also, in the occurrence of overloading, the ductility property enables the absorption of energy. With this in mind, engineers can design and analyze the safety of reinforced concrete and steel structures with confidence in their failure mechanisms. Although structural collapse could be attributed to unfavourable actions such as excessive deflection, uneven settling of the soil beneath foundations, structural loads, deterioration of materials, poor maintenance and deficiency in the initial builder's structural knowledge. The Tower of Pisa with the Mexico City Cathedral are famous instances of masonry structures at the risk owing to soil settlements, whereas the Cathedral of Pavia and the Cathedral of Florence are examples of masonry monuments at risk due to a lack of structural design (Roca et al. 1998). By far, the most common cause of the structural collapse is an earthquake. Yet the multitude of structures that are to this day in operation are built with little or no regard for earthquake action. This was evident about 20 years after the Erzurum Earthquake, the 7.6 magnitude Izmit Earthquake (otherwise known as the Kocaeli earthquake) shocked Turkey again with over 300,000 homes reported as either damaged, partially or totally collapsed resulting in the death of over 17,480 people (Reilinger et al. 2000).

As a direct consequence of this fact, the problem of designed constructions collapsing is one that is of the utmost significance in the modern world. Several scholars have great done great work regarding this contemporary subject. The collapse mechanism of masonry structures when subjected to seismic actions was studied by Tamaam Bakeer (Bakeer 2009). The research entails the creation of numerical tools to recreate the real behaviour of masonry from the point of linear elasticity to the progression of damage till the collapse. The numerical models were created with an open-source programme called LsDyna. Dolatshahi and Aref (Dolatshahi and Aref 2015) proposed a constitutive material model that is compatible with commercially available finite element software such as ABAQUS, TNO DIANA, and LS-DYNA and is based on both implicit and explicit formulations. Seyedrezai (Seyedrezai 2011) utilised the commercially available FE programme LS-DYNA to simulate the collapse behaviour of unreinforced, one-way arching walls under blast stress. Oliveira (Oliveira 2003) made it a point to clarify the responses of masonry buildings to cyclic loads. A constitutive model was suggested and implemented in a prototype version of the DIANA finite element code. Unfortunately, because of the intricate nature of the interactions between the numerous engineering structures, the simulation of such events requires a huge quantity of input data as well as failure criterion definitions. The amount of time it takes to accomplish the work in addition to the expense of the computations is considerable. However, the use of Blender and BCB eliminates difficulties relating to high computational requirements. Also, it requires a little description of the structures making it user-friendly as well as less time consuming.

13.2 Blender and BCB

With Bullet Constraint Builder (BCB) is a simulation add-on tool that is based on the Discrete Element Method (DEM) in a broader term. It enables the simulation of collapse scenarios using the freely available software Bullet Physics engine and Blender. The software package is made up of three program modules that work in harmony. Each software unit is released under an open-source license, allowing third-party programmers to use and alter the source code (Ghezelbash et al. 2020). This collaborative effort enables continuing quality assurance cross-check and consistent software enhancements. The Components of the program include:

- Bullet Physics Engine (Failed 2017)
- Blender (Couman 2021)
- The BCB script (T. B. institute 2021)

DEM predicts how deformable and/or rigid moving objects interact. Newton's motion theories specify object trajectories and routes. DEM may be employed when several objects interact and frictional, electromagnetic, and cohesive forces can be used. DEM simulates building collapse by automatically creating a model and reducing simulation time. DEM is used to design agricultural equipment that can handle bulk materials like seeds and grains and to analyse the viscosity and geomechanics of gravel and sand in soil processing (LUAS 2021; Roessler et al. 2019; Hustrulid and Graham 1996). DEMs are used as methods in "Interactive Rigid Body Dynamics." It allows easy user-simulation interaction and "real-time" outcomes. Speed is more important than accuracy (Clearly 1998).

13.2.1 The Benefits and Drawbacks in Terms of Collapse Simulations

The Rigid Body Dynamic (RBD) simulation approach offers several advantages over continuum approaches, which estimate each element's material behaviour. Since only rigid bodies are addressed and they mostly relate using Newton's equations, the numerical effort to define and analyse the problem is reduced. The RBD is a fast approach that may be used in real-time.

A huge number of structural characteristics are averaged in engineering calculations, and the geometry is approximated coarsely. Thus, developing an executable simulation model is faster. These gains come with the caveat that ongoing deformations within bodies can only be observed as a relative distance change. Along with a coarsely discretized structure, this lowers accuracy. Not paying attention to structure is undesirable. The governing equations apply the physics of structural dynamic behaviour to discrete objects alone. They're not applicable to the continuum in collapse conditions. Bakeer (Seyedrezai 2011) has described successful efforts to utilise RBD to model and simulate masonry construction collapse.

The RBD is a good choice for brick constructions, which have a grid of regular blocks and fail at the mortar joints. Mortar characteristics can be used in force modelling. The same is true for reinforced concrete constructions when numerical and structural parts lose their link. All approaches of this type require to modify the main algorithm. In the utilized application, the physics engine's existing capabilities were explored. So, the limitations between dissolved items are evaluated after a certain level. They are used in addition to physical threshold knowledge.

13.2.2 Bullet Physics Engine

Physics Engine (commercial or open-source) implements DEM and RBD. It solves the discrete-time model. It simulates physical and mechanical processes to deliver realistic game experiences. Physics engines employ a variety of ways to simulate physical processes in games, such as stiff bodies (like rocks and dirt), soft bodies (like clothes), fluids (like water), and their interactions. PhysX can simulate realistic particles (Mirinavičius et al. 2010). It's used to produce physics-based visual effects and animations in movies. NASA's tensegrity robotics simulator (He et al. 2019) and BBZ medical technologies' robotic surgical simulation (National Aeronautics and Space Administration 2022) use its application.

13.2.3 Blender Softwares

Blender is a free 3D modelling programme that allows user interactivity. It's related to the physics engine and allows modelling and simulation visualisation. It was NeoGeo's 1995 proprietary application. This programme has gained game logic, real-time physics simulation, powerful texture mapping, video editing, route tracing rendering, sculpting, and animation capabilities. Blender's functionality is regularly improved by programmers and users. Blender allows interactive "walkthroughs" of simulation results with lighting, texturing, and realistic shading. It covers cavity identification and victim tracing in a collapse situation. Custom extensions can be utilised using a Python script interface.

13.2.4 BCB

RBD was created to imitate moving things. Rigid bodies must be linked to show building members. Because rigid bodies don't include material behaviour, components must be connected by constraints to define the material's strength. BCB enhances Blender's Bullet physics. It combines discrete rigid entities with advanced constraint arrangements to simulate complex collapses by considering

the materials' mechanical characteristics. The BCB's fundamental principles are as follows: Multiple Constraints, Precise Placement of Constraints and Calculation of Admissible Forces.

13.2.5 Fracture Modifier

The DEM approach aims to solve "real-time" simulation challenges quickly. Despite using RBD, which reduces computation time, Blender's current simulations fall short. The Northridge earthquake model with 625 simulation frames took 13,620 seconds to bake (actual simulation time) (almost four hours). Discretized models and their restrictions clutter Blender scenes, making them difficult to handle. Blender's object management performance diminishes as the scene's object count rises. Cameras, lighting, limitations, and rigid bodies are examples of Blender objects. Fracture Modifier (FM) is a custom-made Blender mode.

13.3 Collapse Visualization and Conclusion

For this study, a half-scaled masonry structure was utilized. The half-scale masonry model is made from perforated engineering brick. Brick measures 102 mm, 215 mm, and 65 mm. Figure 13.1 shows the masonry model with unit geometry. The Turkish Building Earthquake Code (2019) requires that 23% of bricks be hollow. Construction used stretcher bond with toothing texture. The mortar is 7.5 mm thick and 1:3. (cement: sand). 1800 mm square and 1600 mm height. The north and south masonry apertures have RC supports. The South door measures 100 mm × 45 mm. From the first block, it's 65 mm above the notch. The north window is 55 mm by 45 mm. The opening supports are 650 mm long, 75 mm tall, and 8 mm thick. Overhead was an 1800 mm RC square slab. It's 100 mm thick 25-grade concrete reinforced in both directions with 8 mm steel. Masonry was built on RC squares. 35-grade concrete with 14 mm rebar is used for the base. The base is 2100 × 200 mm. Bricks at a building's base slip, shear, or bounce away. To avoid this, the base has a 100 mm wide, 30 mm deep slot for brickwork (Figs. 13.2, 13.3, 13.4, 13.5, 13.6 and Table 13.1).

The structure was modelled using mesh cubes and rigidity was enabled during the preprocessing of the model. However, BCB uses a "convex hull" as a standard collision shape for all elements which does not allow for concave shapes like the notch presented in the base. Hence, the base was split into blocks so that every sub-element is convex and can easily be discretized. This topology modification was necessary to avoid problems with the shape collision. Also scaling of objects (Ctrl + A) was applied since Boolean operations in the preprocessing stage work better when the scaling is unity. The ground motion was added as a ".csv" file in the preprocessing

Fig. 13.1 The masonry model utilized as a case study

Fig. 13.2 An illustration of Visual Simulation in comparison to Experiment result-1

stage. To reduce the computational time the FM version of the blender was used for the simulation (Ghezelbash et al. 2020; T. B. institute 2021; Wikipedia xxxx).

The proposed DEM system cannot visualise internal forces because Blender's Python API links add-ons like BCB to core Blender functionalities and data. Hence, there's no way to access the Bullet engine's simulation forces directly. Conversely, the displacements of neighbouring rigid bodies caused by these forces may be examined by using a python script. Blender's deformation visualizer v1.10 python script (written by Kai Kostack) generates element displacements relative to start frame coordinates. It is important to note that displacement values aren't accessible due to the aforementioned reasons, and hence could only be visualized using the deformation visualizer. Bodies with low relative displacements are represented with blue colours, whereas those with high displacements are represented in red. Figure 13.7 shows the model's relative displacement.
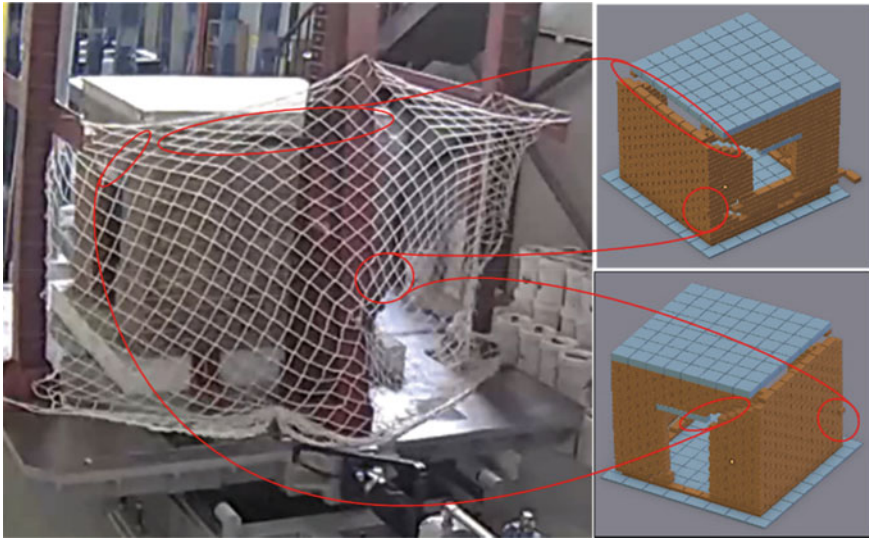
Fig. 13.3 An illustration of Visual Simulation in comparison to Experiment result-2
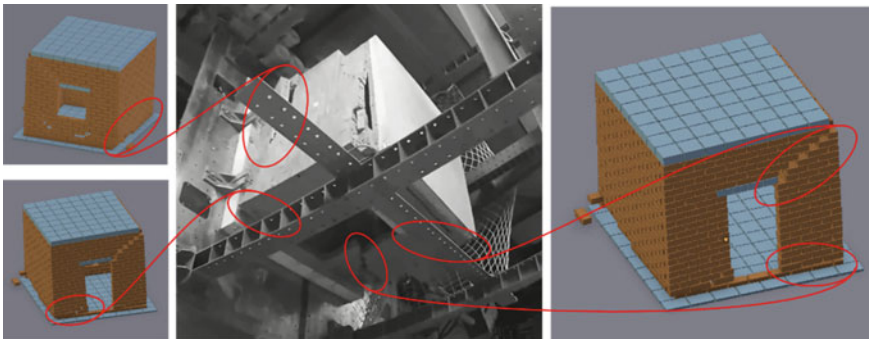
Fig. 13.4 An illustration of Visual Simulation in comparison to Experiment result-3
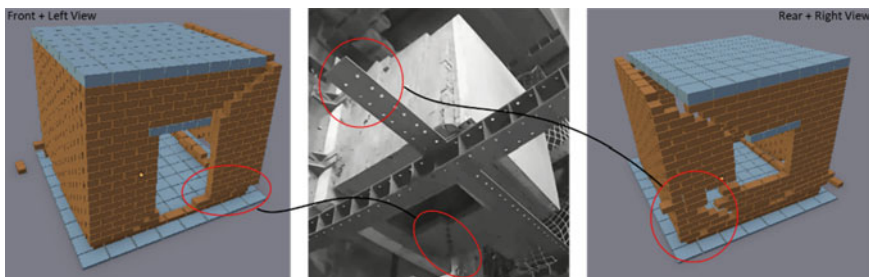
Fig. 13.5 An illustration of Visual Simulation in comparison to Experiment result-4
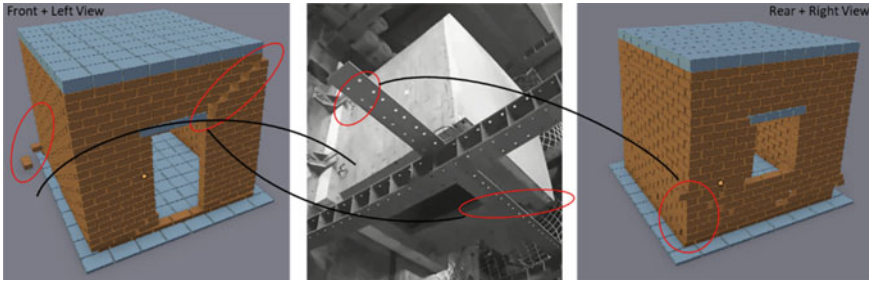
Fig. 13.6 An illustration of Visual Simulation in comparison to Experiment result-5

Table 13.1 Values used for analysis

Parameter	Unit	Value
Discretization Size	m	0.3
Connection Type	–	15
Compressive	N/mm^2	10
Tensile	N/mm^2	0.1
Shear	N/mm^2	$0.1 + \text{abs}\,(1.85 - z) \times 0.1$
Bend	N/mm^2	0.1
Density	kg/m^3	1800
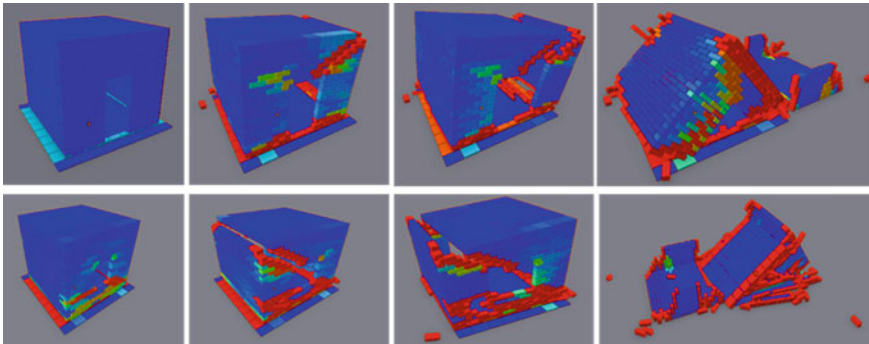
Fig. 13.7 A visualization of the relative displacement

13.4   Conclusion

The primary goal of the method presented in this study is to provide a visual representation of the effects of the EQ on the structure. This method not only allows us to recreate past earthquakes but also to foresee the devastating effects of quakes yet to come. Using the methods outlined in this study, one may visualise the structural behaviour in advance of seismic movements. The simulation was carried out by

subjecting a half-scale model of the stone building to escalating seismic activity until it collapsed, and it was found to be both realistic and effective. The damage pattern seems to be a perfect match, although the debris formation slightly differs. For this reason, this method may help engineers make better decisions on reinforcement and retrofitting. This approach might potentially be expanded to landslide effects on engineering structure as well as explosion analysis for investigation of various risk/threat situations (although not explored within the scope of this paper). Important factors like Elasticity modulus, Poisson ratio, Shell object, etc. should be incorporated into the streamlined programme to maximise its exploitation for structural application. The relative displacement visualisation python script also needs an update to allow for the extraction of displacement data, which will be further extended to the extraction of force and stress values.

References

Bakeer T (2009) Collapse analysis of masonry structures under earthquake actions, PhD thesis, TU Dresden, Dresden

Clearly PW (1998) Discrete element modeling of industrial granular flow applications. In: Task—quarterly scientific bulletin of academic computer centre, vol 2, no 3, pp 385–416. Nazir S, Dhanasekar M (2013) Modelling the failure of thin layered mortar joints in masonry. Eng Struct 49:615–627

Couman E (2021) GitHub, https://github.com/-bulletphysics/bullet3. 23 June 2021

Dolatshahi KM, Aref AJ (2015) Computational, analytical, and experimental modeling of masonry structures, MCEER thrust area 2. Sustainable and Resilient Buildings, New York

Ghezelbash A, Beyer K, Dolatshahi KM, Yekrangnia M (2020) Shake table test of a masonry building retrofitted with shotcrete. Eng Struct 219:110912

He H, Zheng J, Sun Q, Li Z (2019) Simulation of realistic particles with bullet physics engine. In E3S web of conferences 92, Glasgow

Hustrulid AI, Graham GWM (1996) Engineering analysis of transfer points using discrete element analysis. Geomechanics Research Center, Colorado School of Mines, Colorado,.

Kai K, Oliver W (2017) Final release of the Blender and Bullet physics engine based on fast on-site assessment tool. INACHUS

LUAS (2021) GitHub, https://github.com/KaiKostack-/bullet-constraints-builder. 23 June 2021.

Mirinavičius A, Markauskas D, Kačianauskas R (2010) Computational Performance of Contact Search During DEM Simulation of Hopper Filling. In: 10th international conference of modern buildings materials, structures and techniques, Vilnius, Lithuania

National Aeronautics and Space Administration, Autonomous Systems-NASA Tensegrity Robotics Toolkit (NTRT) v1 (ARC-17093-1), https://software.nasa.gov/software/ARC-17093-1 06 May 2022.

Oliveira DVC (2003) Experimental and numerical analysis of blocky masonry structures under cyclic loading, PhD Thesis, Universidade do Minho, Minho

Reilinger R, Toksoz N, McClusky S, Barka A (2000) 1999 Izmit, Turkey earthquake was no surprise. GSA Today 10(1):1–6

Roca P, Gonzálcz J, Dilate E, Lourenço PB (1998) Experimental and numerical issues in the modelling of the mechanical behaviour of masonry. Struct Anal Hist Constr Il:58–91

Roessler T, Katterfeld A (2019) DEM parameter calibration of cohesive bulk materials using a simple angle of repose test, Particuology 45:105–115

Seyedrezai S (2011) Modeling of arching unreinforced masonry walls subjected to blast loadings, MSc Thesis, McMaster University, Ontario

T. B. institute (2021), Blender, https://www.blender.org-/download

Turkish Earthquake Code (2019) Specifications for Building Design Under Earthquake Effects, Ankara

Wikipedia, the free encyclopedia, Bullet (software), Wikipedia®. https://en.wikipedia.org/wiki/Bullet_(software). Accessed 28 Nov 2021

Part IV
Mechanical Performance of Composite Structural Systems

Chapter 14
FRP-RC Slabs Under Punching Shear: Assessment of Existing Models

Maged Tawfik, Taha Ibrahim, Mahmood Ahmad, Ahmed F. Deifalla (ID)**,
Ahmed Awad, and Amr El-Said**

Abstract The purpose of this study is to examine the punching shear behavior of concrete slabs reinforced with FRP. We compared and quickly described 21 strength models. In addition, based on overall performance, strength models were contrasted with one another in terms of the experimentally observed strength. Conclusions were made and discussed, which may help future design codes evolve more effectively, It was decided where to focus future studies. This might aid in the development of future design codes. The ACI is the least realize model, although taking into account the effects of size, dowel action, depth-to-control perimeter ratio, concrete compressive strength, and shear span-to-depth ratio.

M. Tawfik · A. El-Said
Department of Civil Engineering, The Higher Institute of Engineering, El Shrouk, Cairo, Egypt
e-mail: m.nashaat@sha.edu.eg

A. El-Said
e-mail: a.elsayed@sha.edu.eg

T. Ibrahim
Benha University in Egypt, Banha, Egypt
e-mail: taha.ibrahim@feng.bu.edu.eg

M. Ahmad
University of Engineering and Technology Peshawar, Peshawar, Pakistan
e-mail: ahmadm@uetpeshawar.edu.pk

A. F. Deifalla (✉)
Future University in Egypt, New Cairo, Egypt
e-mail: Ahmed.deifalla@fue.edu.eg

A. Awad
Faculty of Engineering, October University for Modern Sciences and Arts, Giza, Egypt

14.1 Introduction

Figure 14.1 depicts the victims of a parking garage collapse in 2021 that happened unexpectedly on a playground in Spain. Additionally, much of the reinforced concrete (RC) slab Punching shear design is empirical or semi-empirical. As a result, extensive research is being conducted to better understand the punching shear. However, the process of the slabs' punching shear is intricate, making further research into it necessary (Deifalla 2020, 2021a, b; FIB 2007). The following list of resistance mechanisms makes up the punching shear resistance of concrete slabs lacking shear reinforcements: Flexural reinforcements, aggregate, and uncracked concrete are resisting the shear in different ways. Flexural reinforcements resist the shear by dowels shear, aggregate resist the shear across the sides of diagonal concrete cracks through the aggregate interlock, and uncracked concrete resists the shear through direct shear (Yooprasertchai et al. 2021a, b; Wu et al. 2022; Bywalski et al. 2020).

Fiber-reinforced polymer (FRP) reinforcements are frequently used in place of traditional reinforcement in concrete slabs to prevent corrosion issues (Ebid and Deifalla 2021). FRP reinforcements also offer a good strength-to-weight ratio and are magnetically neutral. As a result, it is the greatest option for structures exposed to harsh weather factors, including freeze thaw cycles, deicing salts, and wet dry cycles. Numerous researchers have examined, mostly through experimental studies, the behavior of brand-new and preexisting beams and slabs reinforced with FRP bars or textiles under one-way and punching shear as well as torsion (Ali et al. 2021; Hassan and Deifalla 2015; Deifalla 2015; Deifalla et al. 2014, 2015). Punching

Fig. 14.1 Parking garage atop a playground collapsed (Deifalla 2022)

shearing of concrete FRP reinforcements was the subject of several research projects, but very few mechanical models were created for this situation (Wu et al. 2022). Because the FRP failure is brittle, the fissures in FRP-reinforced concrete are larger before failure than in traditional RC (Elmeligy et al. 2017; Failed 2021), or (Deifalla et al. 2021). Wider fractures have a considerable impact on the different punching shear strength processes.

The early 1960s ideas served as the foundation for the conventional punching shear design formulae for RC slabs. These models were based on time tested specimens, but extensive testing over the last few decades has shown various flaws in this approach, including, and not limited to the effect of size and the models' extreme lack of conservatism in many circumstances (Shen et al. 2022). Because of this, there is opportunity for advancements in the punching shear design models, which could aid in design code development (Kuchma et al. 2019; Collins 2001).

In this work, the punching shear strength of concrete slabs reinforced with FRP will be evaluated using the methods currently in use. The punching shear strength of FRP-reinforced concrete slabs was reviewed using the most recent design regulations, manuals, and models. A detailed analysis of slabs made of FRP reinforced concrete that were subjected to two way load during experimental testing. The strength estimated using each model is contrasted with the strength determined through testing. There was a discussion and sketch of the closing comments.

14.2 Simplified Strength Models

Several streamlined strength models have been put up for the Punching shear strength of FRP and RC slabs, either via adaptations for ordinary concrete slabs or empirical based on scant tested data. The North American design codes' punching shear design requirements ignored the impact of flexure reinforcement on strength. They concentrated on the compression zone's direct shear resistance. This could make sense for traditional steel reinforcements that are substantially stiffer than FRP ones. Therefore, the Punching shear strength is governed by the direct shear component. Dowel motion, however, could be a bigger contributor to the strength because the FRP is substantially less rigid than the steel one. In this section, many models' specifics and histories are detailed.

V is the failure load for punching shears. E Is the modulus of elasticity for FRP. Effective depth is d. Compressive strength of concrete is f_c'. The dimensions of the slab are A and B, the dimensions of column are c, b, and the ratio of flexure reinforcement is ρ. The modulus of elasticity of the steel is E_s. The control perimeter at 0. 5d, denoted as $b_{0.5d}$, is equal to $2(b + c + 2d)$. The control perimeter at 1. 5d, denoted as $b_{1.5d}$, is equal to $2(b + c + 6d)$. The control perimeter at $b_{2.0d}$, denoted by the symbol 2.0d, is equal to $2(b + c + 8d)$.

The models included the following: Gardner (1990), JSCE (1997), El-Ghandour et al. (2003); Mattys and Taerwe (2000), Ospina et al. (2003), Zaghloul and Razaqpur (2003), Jacbson et al. (2005), ACI (2015), El-Gamal et al. (2005); Zhang (2006a, b);

Theodorkopoulos and Swamy (2007), CSA-S806-12 (2012), Nguyen and Rovnak (2013), Hassan et al. (2017), Kara and Sinani (2017), Oller et al. (2018), CCCM (Kara and Sinani 2017), Hemzah et al. (2019), El-Gendy and El-Salakawy (2020), Ju et al. (2021), Alrudaini (2022).

Table 14.1 compares the different design models, and it is evident that there is no consensus among researchers on the factors that should be considered and the approach to do so. The impact of compressive strength of concrete in terms of $\left(f_c^{'}\right)^{1/3}$ or $\left(f_c^{'}\right)^{1/2}$ was considered in all design methodologies. For flexure reinforcement, the majority of systems used a dowel action.

It was seen as $(\rho)^{1/3}$ or $(\rho)^{1/2}$. In terms of modulus of elasticity, which was regarded as $(E)^{1/3}$, or $(E)^{1/2}$. More than half of the approaches contained the FRP type. In terms of the size effect, almost half the ways $(1/d)^{1/4}$, $(1/d)^{1/5}$, $(1/d)^{1/2}$, or $\frac{2}{\sqrt{1+d/200}}$. included the ratio of $(0.44 + 20.8d/b_{0.5d})$, $(1 + 8d/b_{0.5d})$, $(0.19 + 4d/b_{0.5d})$, $(0.65 + 4d/b_{0.5d})$, $(1 + 8d/b_{0.5d})$, $(0.65 + 4d/b_{0.5d})$, $(d/b_{0.5d})^{1/2}$, or $(d/b_{0.5d})^{1/5}$. between the critical perimeter and depth, the compression zone and the shear span to depth ratio were two highly restricted models.

14.3 Tested Database Profile

Punching shear has caused a considerable number of experimentally tested specimens to fail during the past 30 years. the largest experimental database in comparison to earlier research (Deifalla 2022; Marí et al. 2015; El-Gendy and El-Salakawy 2020; Alrudaini 2022). 248 slabs reinforcement with FRP in all were gathered from 50 distinct research trials. All the grouping slabs were loaded with punching shear, and they all abruptly failed. The database's specifics are covered in other publications. Although FRP reinforcements can take various forms and arrangements, these differences were considered in terms of ρ and E. All variables are regularly distributed and have a large range of values. Table 14.2 shows RC slabs with FRP reinforcements under two way shear loads for experimental database. The tested column and slab connections' frequencies and ranges when using FRP is shown Fig. 14.2.

14.4 Evaluation of Chosen Models

The strength of the slab-column connection in the experimental data base was calculated using all the gathered models. The terms are graphical, statistical goodness, and central tendency of fit were used to define three areas of comparison. The safety ratio (SR) was determined as the difference between the measured and calculated strengths. A SR value that is almost one indicates that the estimate is correct. A SR

Table 14.1 Comparisons between designed models

Model designed	Location of critical perimeter	Effect of size	Dowel action	Modulus of elasticity	Strength of concrete
G	$1.5d$	$(d)^{-1/4}$	$(\rho)^{1/3}$	–	$\left(f_c'\right)^{1/3}$
JSCE	$0.5d$	$(d)^{-1/4}$	$(\rho)^{1/3}$	$(E)^{1/3}$	$\left(f_c'\right)^{1/2}$
Gd	$1.5d$	$(d)^{-1/4}$	$(\rho)^{1/3}$	$(E)^{1/3}$	$\left(f_c'\right)^{1/3}$
MT	$1.5d$	$(d)^{-1/4}$	$(\rho)^{1/3}$	$(E)^{1/3}$	$\left(f_c'\right)^{1/3}$
O	$1.5d$	–	$(\rho)^{1/3}$	$(E)^{1/2}$	$\left(f_c'\right)^{1/3}$
Z	$0.5d$	–	$(\rho)^{1/3}$	$(E)^{1/3}$	$\left(f_c'\right)^{1/3}$
Jb	$1.5d$	$(d)^{-1/4}$	$(\rho)^{1/2}$	–	$\left(f_c'\right)^{1/2}$
ACI	$0.5d$	–	–	–	$\left(f_c'\right)^{1/2}$
EG	$0.5d$	–	$(\rho)^{1/3}$	$(E)^{1/3}$	$\left(f_c'\right)^{1/2}$
Zg	$1.5d$	$(d)^{-1/5}$	$(\rho)^{1/2}$	$(E)^{1/2}$	$\left(f_c'\right)^{1/3}$
TS	$0.5d$	$(d)^{-1/6}$	–	–	$\left(f_c'\right)^{2/3}$
CSA	$0.5d$	–	$(\rho)^{1/3}$	$(E)^{1/3}$	$\left(f_c'\right)^{1/3}$
NR	$0.5d$	$(d)^{-1/2}$	$(\rho)^{1/3}$	$(E)^{1/3}$	$\left(f_c'\right)^{1/3}$
H	$0.5d$	$(d)^{-1/6}$	$(\rho)^{1/3}$	$(E)^{1/3}$	$\left(f_c'\right)^{1/3}$
KS	$1.5d$	–	$(\rho)^{1/3}$	$(E)^{1/3}$	$\left(f_c'\right)^{1/3}$
CCCM	$0.5d$	$2/\sqrt{1+d/200}$	$(\rho)^{1/3}$	$(E)^{1/3}$	$\left(f_c'\right)^{2/3}$
Hz	$0.5d$	–	$(\rho)^{0.39}$	$(E)^{0;3}$	$\left(f_c'\right)^{1/6}$
EE-(a)	$0.5d$	–	$(\rho)^{1/3}$	$(E)^{1/3}$	$\left(f_c'\right)^{1/2}$
EE-(b)	$0.5d$	$(d)^{-1/6}$	$(\rho)^{1/3}$	$(E)^{1/3}$	$\left(f_c'\right)^{1/3}$
Ju	$0.5d$	–	$(\rho)^{1/2}$	$(E)^{1/2}$	$\left(f_c'\right)^{1/2}$
A	$0.5d$	–	$(\rho)^{1/3}$	$(E)^{1/3}$	$\left(f_c'\right)^{1/3}$

Table 14.2 Experimental database of shear loads under two way on RC slabs with FRP reinforcements

Spec. title	References	Failure load (kN)	Modulus of elasticity (GPa)	FRP Type	Rft ratio	Cylindrical comp. strength (MPa)	Width of column (mm)	Length of column (mm)	Depth of slab (mm)	Width of slab (mm)	Length of slab (mm)
CFRC,SN1	Ahmad et al. (1993)	93	113	CFRP	0.95	42.3	75	75	60	690	690
CFRC,SN2		78	113	CFRP	0.95	44.5	75	75	60	690	690
CFRC,SN3		96	113	CFRP	0.95	39	100	100	60	690	690
CFRC,SN4		99	113	CFRP	0.95	36.5	100	100	60	690	690
1	Banthia et al. (1995)	65	100	CFRP	0.3	41	100	100	55	600	600
2		61	100	CFRP	0.3	53	100	100	55	600	600
3		72	100	CFRP	0.3	41.7	100	100	55	600	600
1	Bank and Xi (1995)	186	143	CFRP	2.1	30	250	250	75	1500	1800
2		179	143	CFRP	2.1	30	250	250	75	1500	1800
3		199	143	CFRP	1.8	30	250	250	75	1500	1800
4		198	156	CFRP	2.1	30	250	250	75	1500	1800
5		201	156	CFRP	1.8	30	250	250	75	1500	1800
6		190	156	CFRP	1.5	30	250	250	75	1500	1800
1	Louka (1999)	500	41.3	GFRP	1	45	575	225	175	1800	3000
2		1050	41.3	GFRP	1	45	575	225	175	1800	3000
3		875	39.3	GFRP	1	45	575	225	175	1800	3000
4		1090	39.3	GFRP	1	45	575	225	175	1800	3000
5		1180	39.3	GFRP	1	45	575	225	175	1800	3000
C1		1000	100	CFRP	1	55	575	225	175	1800	3000

(continued)

Table 14.2 (continued)

Spec. title	References	Failure load (kN)	Modulus of elasticity (GPa)	FRP Type	Rft ratio	Cylindrical comp. strength (MPa)	Width of column (mm)	Length of column (mm)	Depth of slab (mm)	Width of slab (mm)	Length of slab (mm)
C2		1200	100	CFRP	1	55	575	225	175	1800	3000
C3		1328	100	CFRP	1	55	575	225	175	1800	3000
H2		1055	160	Hybrid	1	45	575	225	175	1800	3000
H4		1096	160	Hybrid	1	45	575	225	175	1800	3000
H5		1183	160	Hybrid	1	45	575	225	175	1800	3000
C1	Ospina et al. (2003)	181	91.8	CFRP	0.25	37	150	150	95	1000	1000
C1'		189	91.8	CFRP	0.25	35.8	230	230	95	1000	1000
C2		255	95	CFRP	1.05	36.5	150	150	95	1000	1000
C2'		273	95	CFRP	1.05	36.5	230	230	95	1000	1000
C3		347	92	CFRP	0.55	33.5	150	150	125	1000	1000
C3'		343	92	CFRP	0.55	34.2	230	230	125	1000	1000
CS		142	148	CFRP	0.2	32.5	150	150	95	1000	1000
CS'		150	148	CFRP	0.2	33.3	230	230	95	1000	1000
H1		207	37.3	HFRP	0.65	35.7	150	150	95	1000	1000
H2		231	40.7	HFRP	3.75	35.7	150	150	90	1000	1000
H2'		171	40.7	HFRP	3.75	35.7	80	80	90	1000	1000
H3		237	44.8	HFRP	1.25	32	150	150	120	1000	1000
H3'		217	44.8	HFRP	1.25	32	80	80	120	1000	1000
1	Rahman et al. (2000)	622	85	GFRP	0.3	42	250	150	160	2500	2000
2		698	85	GFRP	0.3	42	250	150	160	2500	2000

(continued)

Table 14.2 (continued)

Spec. title	References	Failure load (kN)	Modulus of elasticity (GPa)	FRP Type	Rft ratio	Cylindrical comp. strength (MPa)	Width of column (mm)	Length of column (mm)	Depth of slab (mm)	Width of slab (mm)	Length of slab (mm)
3		575	85	GFRP	0.3	42	250	150	160	2500	2000
4		534	85	GFRP	0.3	42	250	150	160	2500	2000
5		584	85	GFRP	0.3	42	250	150	160	2500	2000
1	Hassan et al. (2000)	1000	147	CFRP	0.58	59	575	225	165	3000	1800
2		1200	147	CFRP	0.58	59	575	225	165	3000	1800
3		1328	147	CFRP	0.58	59	575	225	165	3000	1800
1	Khanna et al. (2000)	756	42	GFRP	2.5	35	500	250	145	4000	2000
SG1	Matthys and Taerwe (2000)	170	45	GFRP	0.25	33.5	200	200	145	2000	2000
SC1		229	110	CFRP	0.2	34.8	200	200	145	2000	2000
SG2		271	45	GFRP	0.48	46.5	200	200	145	2000	2000
SG3		237	45	GFRP	0.48	30	200	200	145	2000	2000
SC2		317	110	CFRP	0.45	29.7	200	200	145	2000	2000
GFR-1	Zaghloul and Razaqpur (2003)	217	34	GFRP	0.75	29.7	250	250	120	2150	2150
GFR-2		260	34	GFRP	1.45	29.7	250	250	120	2150	2150
NEF-1		206	28.4	GFRP	0.88	37.5	250	250	120	2150	2150
ZJF5	Jacobson et al. (2005)	234	100	CFRP-	1	45	250	250	75	1760	1760

Table 14.2 (continued)

Spec. title	References	Failure load (kN)	Modulus of elasticity (GPa)	FRP Type	Rft ratio	Cylindrical comp. strength (MPa)	Width of column (mm)	Length of column (mm)	Depth of slab (mm)	Width of slab (mm)	Length of slab (mm)
G-S1	Hussein et al. (2004)	249	42	GFRP	1.2	40	250	250	100	1830	1830
G-S2		218	42	GFRP	1.05	35	250	250	100	1830	1830
G-S3		240	42	GFRP	1.65	29	250	250	100	1830	1830
G-S4		210	42	GFRP	0.95	26	250	250	100	1830	1830
1	ACI (2015)	537	33	GFRP	0.95	27.5	635	250	175	2000	2300
2		536	33	GFRP	0.95	27.5	635	250	175	2000	2300
3		531	33	GFRP	0.95	27.5	635	250	175	2000	2300
7		721	33	GFRP	0.95	27.5	635	250	175	2000	2000
8		897	33	GFRP	0.95	27.5	635	250	175	2000	2000
G-S1	Zhang (2006a)	740	44.6	GFRP	1	49.5	600	250	160	2500	3000
G-S2		712	38.5	GFRP	2	44.2	600	250	160	2500	3000
G-S3		732	46.5	GFRP	1.2	49.2	600	250	160	2500	3000
C-S1		674	122.5	CFRP	0.35	49.5	600	250	165	2500	3000
C-S2		799	122.5	CFRP	0.7	44.5	600	250	165	2500	3000
GS2	Zhang et al. (2005)	218	42	GFRP	1.05	35	250	250	100	1830	1830
GSHS		275	42	GFRP	1.2	71	250	250	100	1830	1830

(continued)

Table 14.2 (continued)

Spec. title	References	Failure load (kN)	Modulus of elasticity (GPa)	FRP Type	Rft ratio	Cylindrical comp. strength (MPa)	Width of column (mm)	Length of column (mm)	Depth of slab (mm)	Width of slab (mm)	Length of slab (mm)
CS1	Zhang (2006b)	251	120	CFRP	0.4	31	250	250	100	1900	1900
CS2		293	120	CFRP	0.55	33	250	250	100	1900	1900
CS3		285	120	CFRP	0.75	25.5	250	250	100	1900	1900
CSHD1		325	120	CFRP	0.55	36	250	250	100	1900	1900
CSHD2		360	120	CFRP	0.75	38.5	250	250	100	1900	1900
CSHS1		399	120	CFRP	0.35	85.6	250	250	150	1900	1900
CHSHS2		446	120	CFRP	0.5	98.5	250	250	150	1900	1900
1	Tom (2007)	282	41	GFRP	1	70	250	250	110	1900	1900
2		319	41	GFRP	1.2	70	250	250	110	1900	1900
3		384	41	GFRP	1.5	70	250	250	110	1900	1900
4		589	41	GFRP	1.2	70	250	250	160	1900	1900
5		487	41	GFRP	1.2	70	250	250	145	1900	1900
6		437	41	GFRP	1.2	70	250	250	135	1900	1900
ZJEF1	Zaghloul (2007)	188	100	CFRP	1.35	25	250	250	120	1000	1760
ZJEF2		156	100	CFRP	0.95	27	250	250	120	1000	1760
ZJEF3		211	100	CFRP	1.38	55	250	250	120	1000	1760

(continued)

Table 14.2 (continued)

Spec. title	References	Failure load (kN)	Modulus of elasticity (GPa)	FRP Type	Rft ratio	Cylindrical comp. strength (MPa)	Width of column (mm)	Length of column (mm)	Depth of slab (mm)	Width of slab (mm)	Length of slab (mm)
ZJEF5		97	100	CFRP	1.38	28	250	250	80	1000	1760
ZJEF7		196	100	CFRP	1.38	26	450	250	120	1000	1760
ZJF8		178	100	CFRP	1.48	28	350	250	100	1760	1760
ZJF9		272	100	CFRP	1.48	57.5	250	250	100	1760	1760
G-S4	El-Gamal et al. (2007)	707	44.5	GFRP	1.2	44	600	250	155	2500	3000
G-S5		735	44.5	GFRP	1.2	44	600	250	155	2500	3000
F1	Zaghloul et al. (2008)	165	46	GFRP	1.1	37.5	200	200	80	1200	1200
F2		170	46	GFRP	0.8	33	200	200	110	1200	1200
F3		210	46	GFRP	1.3	38.5	200	200	80	1200	1200
F4		230	46	GFRP	1.55	39.5	200	200	80	1200	1200
GFU1	Lee et al. (2009)	222	48.2	GFRP	1.18	36.5	225	225	110	2300	2300
GFB2		246	48.2	GFRP	2.15	36.5	225	225	110	2300	2300
GFB3		248	48.2	GFRP	3	36.5	225	225	110	2300	2300
GFBF3		330	48.2	GFRP	3	33.9	225	225	110	2300	2300
S3	Zhu et al. (2010)	145	100	BFRP	0.3	33.5	150	150	135	1500	1500
S4		275	100	BFRP	0.55	35.5	150	150	135	1500	1500

Table 14.2 (continued)

Spec. title	References	Failure load (kN)	Modulus of elasticity (GPa)	FRP Type	Rft ratio	Cylindrical comp. strength (MPa)	Width of column (mm)	Length of column (mm)	Depth of slab (mm)	Width of slab (mm)	Length of slab (mm)
S5		235	100	BFRP	0.45	32.9	150	150	135	1500	1500
S6		225	100	BFRP	0.45	32.5	150	150	135	1500	1500
S7		170	100	BFRP	0.45	22.5	150	150	135	1500	1500
S8		235	100	BFRP	0.45	41.8	150	150	135	1500	1500
S9		200	100	BFRP	0.45	40.6	150	150	135	1500	1500
NC-G-45	Min et al. (2010)	44	76	GFRP	0.78	48	25	25	45	300	300
NC-G-0/90		45	76	GFRP	0.78	48	25	25	45	300	300
NC-C-45		39	230	CFRP	0.25	48	25	25	45	300	300
NC-C-0/90		45	230	CFRP	0.25	48	25	25	45	300	300
SFRC-C-45		63	230	CFRP	0.25	48	25	25	45	300	300
UHPC-C-45		97	230	CFRP	0.25	180	25	25	45	300	300
UHPC-C-0/90		98	230	CFRP	0.25	180	25	25	45	300	300
A	Xiao (2010)	176	45.6	GFRP	0.42	22.2	150	150	130	1500	1500
B-2		209	45.6	GFRP	0.42	32.5	150	150	130	1500	1500
B-3		245	45.6	GFRP	0.55	32.5	150	150	130	1500	1500
B-4		167	45.6	GFRP	0.3	32.5	150	150	130	1500	1500

(continued)

Table 14.2 (continued)

Spec. title	References	Failure load (kN)	Modulus of elasticity (GPa)	FRP Type	Rft ratio	Cylindrical comp. strength (MPa)	Width of column (mm)	Length of column (mm)	Depth of slab (mm)	Width of slab (mm)	Length of slab (mm)
B-5		217	45.6	GFRP	0.42	33.5	150	150	130	1500	1500
B-6		222	45.6	GFRP	0.42	28.4	150	150	130	1500	1500
B-7		253	45.6	GFRP	0.42	46	150	150	130	1500	1500
G200n	Bouguerra et al. (2011)	732	43	GFRP	1.2	49.1	600	250	155	2500	3000
G175N		484	43	GFRP	1.2	35	600	250	135	2000	3000
G150N		362	43	GFRP	1.2	35	600	250	110	2000	3000
G175h		704	43	GFRP	1.2	65	600	250	135	2000	3000
G175n0.7		549	43	GFRP	0.7	53	600	250	135	2000	3000
G175n0.35		506	43	GFRP	0.35	53	600	250	137	2000	3000
C175N		530	122	GFRP	0.4	40.5	600	250	140	2000	3000
A	Zhu and Wang (2012)	176	45.6	GFRP	0.42	22.5	150	150	130	1500	1500
B-2	Nguyen-Minh and Rovnak (2013)	209	45.6	GFRP	0.42	32.5	150	150	130	1500	1500
B-3		245	45.6	GFRP	0.55	32.5	150	150	130	1500	1500
B-4		167	45.6	GFRP	0.3	33	150	150	130	1500	1500
C		252	45.6	GFRP	0.42	44.5	150	150	130	1500	1500
GSL-PUNC-0.4		180	48	GFRP	0.48	49	200	200	130	2200	2200

Table 14.2 (continued)

Spec. title	References	Failure load (kN)	Modulus of elasticity (GPa)	FRP Type	Rft ratio	Cylindrical comp. strength (MPa)	Width of column (mm)	Length of column (mm)	Depth of slab (mm)	Width of slab (mm)	Length of slab (mm)
GSL-PUNC-0.5		212	48	GFRP	0.68	49	200	200	130	2200	2200
GSL-PUNC-0.6		244	48	GFRP	0.92	49	200	200	130	2200	2200
G (0.7) 30/20	Hassan et al. (2017)	329	48.2	GFRP	0.7	34.5	300	300	135	2500	2500
G (1.6) 30/20		431	48.1	GFRP	1.55	38.5	300	300	130	2500	2500
G (1.6) 30/20-H		547	57.4	GFRP	1.55	76	300	300	130	2500	2500
G (1.2) 30/20		438	64.9	GFRP	1.2	37.5	300	300	130	2500	2500
G (0.3) 30/35		825	48.2	GFRP	0.35	34.5	300	300	285	2500	2500
G (0.7) 30/35		1071	48.1	GFRP	0.75	39.5	300	300	285	2500	2500
G (1.6) 30/35		1492	56.7	GFRP	1.6	38.5	300	300	275	2500	2500
G (1.6) 30/35-H		1600	56.7	GFRP	1.6	76	300	300	275	2500	2500
G (0.7) 30/20-B		386	48.2	GFRP	0.7	38.5	300	300	135	2500	2500
G (0.7) 45/20		400	48.2	GFRP	0.7	45	300	300	135	2500	2500
G (1.6) 45/20-B		511	48.1	GFRP	1.55	39.5	300	300	130	2500	2500
G (0.3) 30/35-B		781	48.2	GFRP	0.35	39.5	300	300	285	2500	2500
G (0.7) 30/35-B-2		1195	48.1	GFRP	0.75	46.5	300	300	280	2500	2500
G (0.3) 45/35		911	48.2	GFRP	0.35	48.5	300	300	285	2500	2500

(continued)

Table 14.2 (continued)

Spec. title	References	Failure load (kN)	Modulus of elasticity (GPa)	FRP Type	Rft ratio	Cylindrical comp. strength (MPa)	Width of column (mm)	Length of column (mm)	Depth of slab (mm)	Width of slab (mm)	Length of slab (mm)
G (1.6) 30/20-B		451	48.1	GFRP	1.55	32.5	300	300	130	2500	2500
G (1.6) 45/20		504	48.1	GFRP	1.55	32.5	300	300	130	2500	2500
G (0.7) 30/35-B-1		1027	48.1	GFRP	0.75	29.5	300	300	180	2500	2500
G(0.3) 45/35-B		1020	48.2	GFRP	0.35	32.5	300	300	285	2500	2500
G (0.7) 45/35		1248	48.1	GFRP	0.75	29.5	300	300	280	2500	2500
GSC-0.9-XX-0.4	El-Gendy and El-Salakawy (2015)	251	60.505	GFRP	0.9	41	300	300	160	1500	2800
GSC-1.35-XX-0.4		268	60.505	GFRP	1.35	41	300	300	160	1500	2800
GSC-1.8-XX-0.4		277	60.505	GFRP	1.7	41	300	300	160	1500	2800
GSC-0.9-XX-0.2		239	60.505	GFRP	0.85	41	300	300	160	1500	2800
GSC-0.9-XX-0.3		159	60.505	GFRP	0.9	41	300	300	160	1500	2800
GRD-0.9-XX-0.4		191	59.877	GFRP	0.9	41	300	300	160	1500	2800
G-0.6%-12-125T&B	Tharmarajah et al. (2015)	344	67.4	GFRP	0.6	68	500	25	120	500	1425
G-0.6%-16-300T&B		365	67.4	GFRP	0.6	65	500	25	117	500	1425
B-0.6%-12-125T&B		300	54	BFRP	0.6	69.5	500	25	120	500	1425
B-0.6%-16-300T&B		295	54	BFRP	0.6	66	500	25	117	500	1425

(continued)

Table 14.2 (continued)

Spec. title	References	Failure load (kN)	Modulus of elasticity (GPa)	FRP Type	Rft ratio	Cylindrical comp. strength (MPa)	Width of column (mm)	Length of column (mm)	Depth of slab (mm)	Width of slab (mm)	Length of slab (mm)
GSC-0.9-XX-0.4	Mostafa (2016)	251	60.505	GFRP	0.88	81	300	300	160	1450	2600
GSC-1.35-XX-0.5		272	60.505	GFRP	1.28	85	300	300	160	1450	2600
GSC-1.8-XX-0.4		288	60.505	GFRP	1.7	80	300	300	160	1450	2600
S2-B	Fareed et al. (2016)	548	69.3	BFRP	0.8	48.7	600	250	160	2000	3000
S3-B		665	69.3	BFRP	0.8	42.5	600	250	160	2000	3000
S4-B		566	69.3	BFRP	0.8	42.5	600	250	160	2000	3000
S5-B		716	69.3	BFRP	1.2	48	600	250	160	2000	3000
S6-B		576	69.3	BFRP	0.4	48	600	250	160	2000	3000
S7-B		436	69.3	BFRP	0.4	48	600	250	160	2000	3000
GN-0.65	Gouda and El-Salakawy (2016a)	363	69.3	GFRP	0.65	42	300	300	160	2600	2600
GN-0.98		378	68	GFRP	0.98	38	300	300	160	2600	2600
GN-1.30		425	68	GFRP	1.3	39	300	300	160	2600	2600
GH-0.65		380	68	GFRP	0.65	70	300	300	160	2600	2600
G-00-XX	Gouda and El-Salakawy (2016b)	421	68	GFRP	0.65	38	300	300	160	2800	2800
G-15-XX		363	68	GFRP	0.65	42	300	300	160	2800	2800
G-30-XX		296	68	GFRP	0.65	42	300	300	160	2800	2800
R-15-XX		320	68	GFRP	0.65	40	300	300	160	2800	2800

(continued)

Table 14.2 (continued)

Spec. title	References	Failure load (kN)	Modulus of elasticity (GPa)	FRP Type	Rft ratio	Cylindrical comp. strength (MPa)	Width of column (mm)	Length of column (mm)	Depth of slab (mm)	Width of slab (mm)	Length of slab (mm)
NW59	Oskouei et al. (2017)	719	68	GFRP	0.7	59	250	250	175	800	800
SG1	Abduljaleel et al. (2017)	136	47	GFRP	0.22	30	150	150	60	1100	1100
SO1		68	47	GFRP	0.13	37.5	150	150	60	1100	1100
SO2		85	47	GFRP	0.13	32.5	150	150	60	1100	1100
SO3		80	47	GFRP	0.22	30.5	150	150	60	1100	1100
SO4		100	47	GFRP	0.22	35.5	150	150	60	1100	1100
SO5		102	47	GFRP	0.22	30	150	150	60	1100	1100
GFS1	Ju et al. (2018)	410	47	GFRP	1.55	36.5	200	200	180	2200	3000
GFS2		360	47	GFRP	1.2	36.5	200	200	180	2200	3000
GFS3		370	47	GFRP	0.8	36.5	200	200	180	2200	3000
H-1.0-XX	Hussein and El-Salakawy (2018)	461	65	GFRP	0.98	80	300	300	160	2800	2800
H-1.5-XX		541	65	GFRP	1.45	84	300	300	160	2800	2800
H-2.0-XX		604	65	GFRP	1.93	87	300	300	160	2800	2800
C-F-S-10-4	Hemzah et al. (2019)	103	144	CFRP	0.3	51	100	100	80	600	600
C-F-S-10-6		127	144	CFRP	0.45	52	100	100	80	600	600
S-F-D-10-4		112	144	CFRP	0.6	46	100	100	80	600	600

(continued)

Table 14.2 (continued)

Spec. title	References	Failure load (kN)	Modulus of elasticity (GPa)	FRP Type	Rft ratio	Cylindrical comp. strength (MPa)	Width of column (mm)	Length of column (mm)	Depth of slab (mm)	Width of slab (mm)	Length of slab (mm)
S-F-D-10-6		129	144	CFRP	0.9	60	100	100	80	600	600
S-F-S-10-4		79	144	CFRP	0.3	52	100	100	80	600	600
S-F-S-10-6		107	144	CFRP	0.45	48	100	100	80	600	600
S-F-S-7.5-4		57	144	CFRP	0.4	49	100	100	60	600	600
S-F-S-7.5-6		79	144	CFRP	0.6	49	100	100	60	600	600
G	Salama et al. (2019)	314	65	GFRP	1.55	41.5	300	300	160	1350	2500
G1 (1.06)	Eladawy et al. (2019)	140	62.6	GFRP	1.05	52.5	300	300	150	2500	2500
G2 (1.51)	Gu (2020)	140	62.6	GFRP	1.5	92.2	300	300	150	2500	2500
G3 (1.06)-SL		180	62.6	GFRP	1.05	45.2	300	300	150	2500	2500
A30-1		191	51.1	GFRP	1.28	27.5	300	300	90	1500	1500
A30-2		289	51.1	GFRP	1.05	27.5	300	300	110	1500	1500
A30-3		413	51.1	GFRP	0.82	26.5	300	300	140	1500	1500
A30-4		209	51.1	GFRP	1.31	27	350	350	85	1500	1500
A40-1		232	51.1	GFRP	1.28	28	350	350	85	1500	1500
A40-2		221	51.1	GFRP	0.88	26.5	350	350	85	1500	1500
A40-3		236	51.1	GFRP	1.28	28.5	300	300	85	1500	1500

(continued)

Table 14.2 (continued)

Spec. title	References	Failure load (kN)	Modulus of elasticity (GPa)	FRP Type	Rft ratio	Cylindrical comp. strength (MPa)	Width of column (mm)	Length of column (mm)	Depth of slab (mm)	Width of slab (mm)	Length of slab (mm)
A50-1		253	51.1	GFRP	1.28	29.5	300	300	85	1500	1500
A50-2		237	54.1	GFRP	0.88	32.5	300	300	85	1500	1500
A50-3		280	51.1	GFRP	1.28	26.5	350	350	85	1500	1500
S40-1	Zhou (2020)	314	51.1	GFRP	0.98	32.5	300	300	85	1500	1500
S50-1		187	54.4	GFRP	0.7	43.5	300	300	85	1500	1500
G4 (1.06)-H	Eladawy et al. (2020)	134	62.6	GFRP	1.05	92	300	300	150	2500	2500
F1	Huang et al. (2020)	262	123	CFRP	0.88	25	200	200	125	1600	1600
G-N-0.3	Salama et al. (2021)	260	65	GFRP	1.05	37	300	300	160	1300	2500
G-H-0.3		306	65	GFRP	1.05	86	200	200	160	2200	3000
G-N-0.6		178	65	GFRP	1.05	39	200	200	160	2200	3000
G-H-0.6		213	65	GFRP	1.05	86	200	200	160	2200	3000
0F-605	AlHamaydeh and Orabi (2021)	463	50.6	GFRP	2.8	38.5	250	250	125	2000	2000
0F-80F		486	50.6	GFRP	2.1	38.5	250	250	125	2000	2000
0F-1105		436	50.6	GFRP	1.55	38.5	250	250	125	2000	2000
1.25F-60S		455	50.6	GFRP	2.8	38.5	250	250	125	2000	2000
1.25F-80S		506	50.6	GFRP	2.1	38.5	250	250	125	2000	2000

(continued)

Table 14.2 (continued)

Spec. title	References	Failure load (kN)	Modulus of elasticity (GPa)	FRP Type	Rft ratio	Cylindrical comp. strength (MPa)	Width of column (mm)	Length of column (mm)	Depth of slab (mm)	Width of slab (mm)	Length of slab (mm)
1.25F-110S		498	50.6	GFRP	1.55	38.5	250	250	125	2000	2000
SA1	Mohmmad et al. (2022)	30	50	BFRP	0.85	45.2	55	55	35	500	500
SA2		28	42	GFRP	0.85	45.2	55	55	35	500	500
SA4		26	50	BFRP	0.55	45.2	55	55	35	500	500
SA5		24	42	GFRP	0.55	45.2	55	55	35	500	500
SA7		35	50	BFRP	0.85	45.2	55	55	35	500	500
SA0		28	50	BFRP	0.85	45.2	55	55	35	500	500
CFRP1	Shill et al. (2022)	169	140	CFRP	0.35	29.5	1075	1075	50	1670	1670
CFRP2		178	140	CFRP	0.35	34.5	1075	1075	50	1670	1670
CFRP3		208	140	CFRP	0.35	34.5	1075	1075	50	1670	1670
BFRP1		103	55	BFRP	0.35	29.5	1075	1075	50	1670	1670
BFRP2		120	55	BFRP	0.35	34.5	1075	1075	50	1670	1670
BFRP3		144	55	BFRP	0.35	34.5	1075	1075	50	1670	1670
Minimum		24.34	28.4		0.13	22.2	25	25	35	300	300
Maximum		1600	230		3.75	179	1075	1075	285	4000	3000
Mean		372	75		1	44	303	235	125	1715	1915
Variation		82%	55%		65%	45%	65%	65%	39%	39%	40%
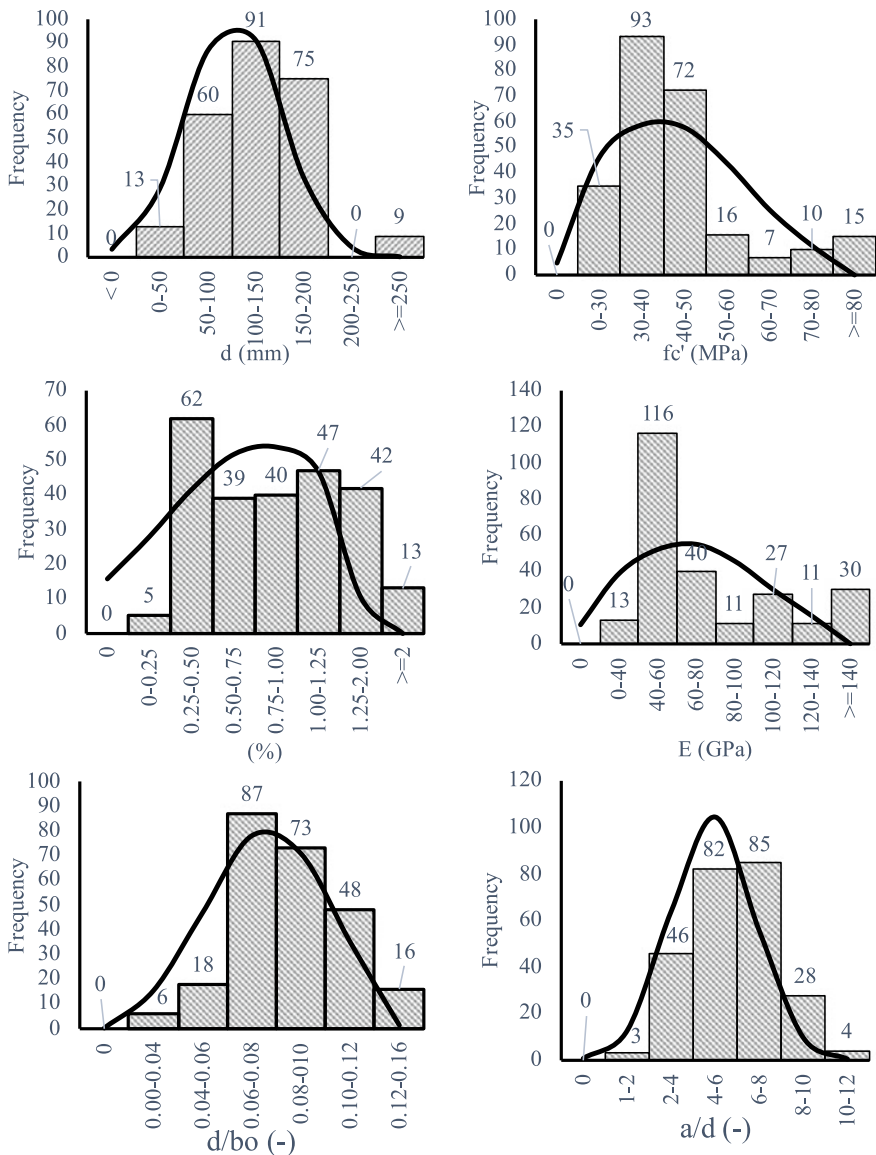
Fig. 14.2 The tested column-slab connections' frequencies and ranges when using FRP

value greater than unity implies a conservative estimate. If the SR value is less than 1.0, the prediction is cautious, and the shear strength was underestimated.

As indicated in Table 14.2 and Fig. 14.3, lower values with a 95% accuracy level (lower 95%), maximum values, and minimum–maximum values were applied to the SR for each model that was chosen. For furthering the development of the design
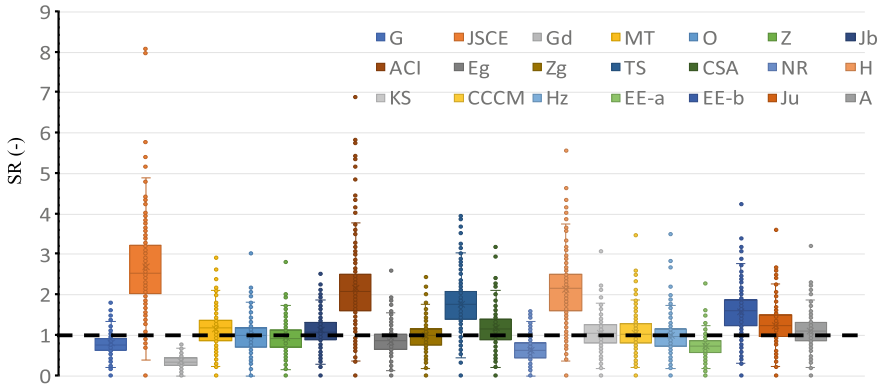
Fig. 14.3 The effectiveness of chosen models

models, Table 14.2 displays the statistical goodness and central tendency of fit of all chosen models. With an average value of 2.71, 2.16, and 2.18 respectively, the JSCE, H models, and ACI, are overly cautious. In comparison to other models with coefficients of variation of 35%, 35%, 36%, and 36%, respectively, the models, and Zg, EE-b, Ju are more consistent.

For each of the chosen models, a box plot is shown in Fig. 14.2. Extreme values and a wide range are shown in the ACI. Furthermore, when the GD and NR were used, extremely un-conservative predictions were produced. The strength (Mean near to 1.0) is accurately predicted by the current models (i.e., Ju, EE-a, Hz, and A) as illustrated in Fig. 14.3. As indicated in Table 14.3, the consistency is still deficient (i.e., C.O.V. is higher than 35.0%). In comparison to mechanically based models (CCCM) and fracture-based models, models that consider fundamental factors in a power form equation appear the most exact and consistent (NR). Furthermore, it is evident from Fig. 14.3 that each technique was created or calibrated with a nonsystematic margin of safety determined by the discretion and expertise of each develop. d NR. An evaluation of dependability that takes resistance and load uncertainty into account should be used to control this. Although it is a fascinating issue, it is outside the purview of this study and may be explored further. Further enhanced mechanically based models that make physical sense and are easy to construct are also required.

14.4.1 Effective Depth

Figure 14.4 plots the computed SR value against the effective depth using the American code model, the CSA model, the Ju model, the JSCE model, the model of CCCM, and the model of EE-B. Additionally, the slopes of the best fit line were presented for the JSCE model, the ACI model, the CSA model, the CCCM model, the EE-B model, and the Ju model, respectively. These slopes were 0.0011, 0.003, 0.0016,

Table 14.3 For all strength in models, statistical measurements

Model designed	Determination coefficients mean	Error of mean square root	Mean error	C.O.V	Average	Min	Max	Lower 95%
G	0.66	205	143	0.37	0.81	0.15	1.85	0.78
JSCE	0.69	335	237	0.38	2.7	0.69	8.07	2.58
Gd	0.7	775	653	0.37	0.35	0.08	0.78	0.35
MT	0.68	182	120	0.36	1.18	0.24	2.93	1.12
O	0.71	171	110	0.38	1	0.17	3.02	0.94
Z	0.68	201	125	0.38	0.95	0.16	2.8	0.91
Jb	0.66	181	110	0.38	1.15	0.2	2.6	1.1
ACI	0.69	273	194	0.45	2.18	0.37	6.9	2.05
Eg	0.68	222	136	0.36	0.85	0.14	2.6	0.83
Zg	0.71	166	105	0.35	1	0.18	2.44	0.95
TS	0.7	255	175	0.35	1.78	0.34	3.95	1.7
CSA	0.72	165	111	0.4	1.2	0.2	3.18	1.15
NR	0.55	360	253	0.45	0.64	0.15	1.6	0.6
H	0.7	291	205	0.36	2.16	0.4	5.55	2.08
KS	0.72	165	104	0.38	1.06	0.18	3.06	1.03
CCCM	0.66	198	127	0.44	1.06	0.22	3.47	1
Hz	0.73	166	105	0.45	1	0.19	3.55	0.95
EE-a	0.66	302	195	0.37	0.75	0.12	2.27	0.7
EE-b	0.71	232	160	0.35	1.6	0.3	4.25	1.55
Ju	0.7	173	118	0.35	1.25	0.22	3.6	1.2
A	0.71	164	105	0.36	1.15	0.2	3.2	1.08

0.0019, 0.0003, and 0.0025. Except for the JSCE, the safety of the chosen models declines as depth increases. The SR value that was determined using the EE-B model has the lowest best fit line, making it the most consistent regarding depth. The ACI model, however, produced the greatest SR value, making it the least consistent. This could be because the American code model doesn't account for size effects.

14.4.2 Concrete Compression Strength

Figure 14.5 compares the computed SR value to the concrete compressive strength using the American code model, the CSA model, the JSCE model, the Ju model, the CCCM model, and the EE-B model. The best fit line was also displayed, and its slopes for the JSCE model, the CSA model, the ACI model, the EE-B model, the
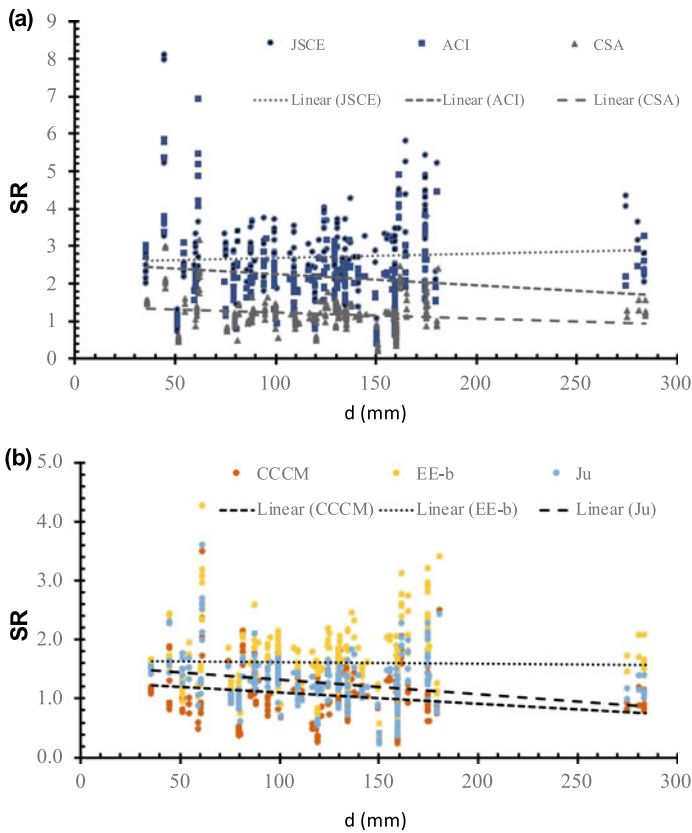
Fig. 14.4 The impact of depth on the SR value

CCCM model, and the Ju model, respectively, were 0.0019, 0.0174, 0.0046, 0.0017, 0.0031, and 0.0027. The CCCM model, the EE-B model, and the Ju model are less safe as concrete compressive strength increases. On the other hand, if compressive strength of concrete grows, the safety of the JSCE, ACI, and CSA models also does. It is most consistent with the concrete compressive strength since the more fit line for the SR value that was determined using the EE-b model is the lowest. Though it is the least reliable, employing the CSA model produced the greatest SR value.

14.4.3 Ratio of Flexure Reinforcement

In comparison to the flexure reinforcement ratio, Fig. 14.6 displays the value of SR estimated using the Ju model, American code model, the CSA model, the JSCE model, the CCCM model, and the EE-B model. The best fit line was also displayed,
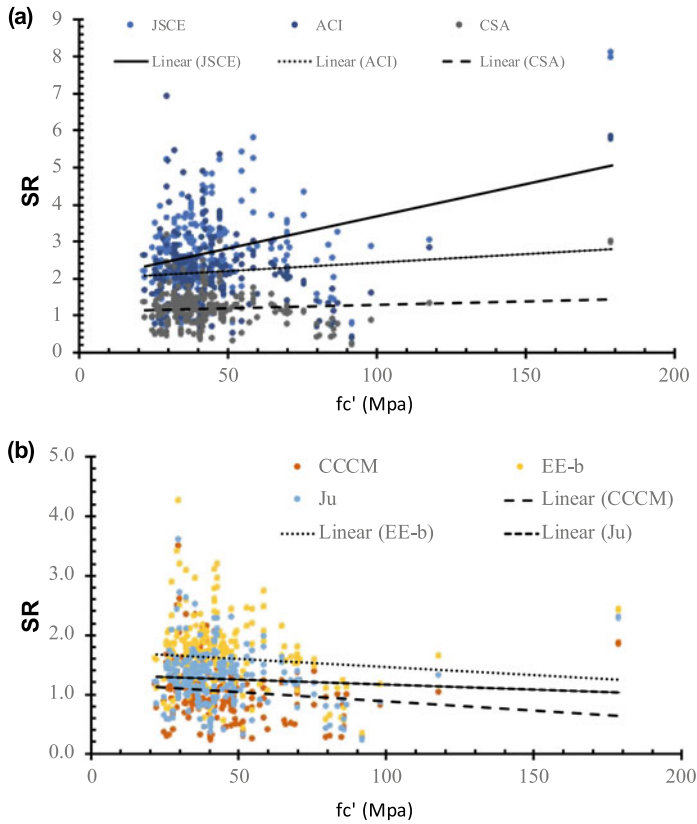
Fig. 14.5 The impact in compressive strength of concrete on the value of SR

and its slopes for the JSCE model, the ACI model, the CSA model, the Ju model, the EE-B model, and the CCCM model, respectively, were 0.2529, 0.6244, 0.1844, 0.0328, 0.1817, and 0.2229. Except for the JSCE model, the safety of the chosen models declines as the flexural reinforcement ratio increases. It is most consistent with the flexure reinforcement ratio that the more fit line for the SR value that was determined using the CCCM model is the lowest. The least consistent model, however, is the one that used the American code model since it produced the greatest value of SR. This may be because of the American code model leaving out the flexure reinforcement ratio.

14.4.4   Young's Modulus

In contrast to the Young's modulus, Fig. 14.7 displays the value of SR estimated using the EE-B model, the American code model, the JSCE model, the CCCM
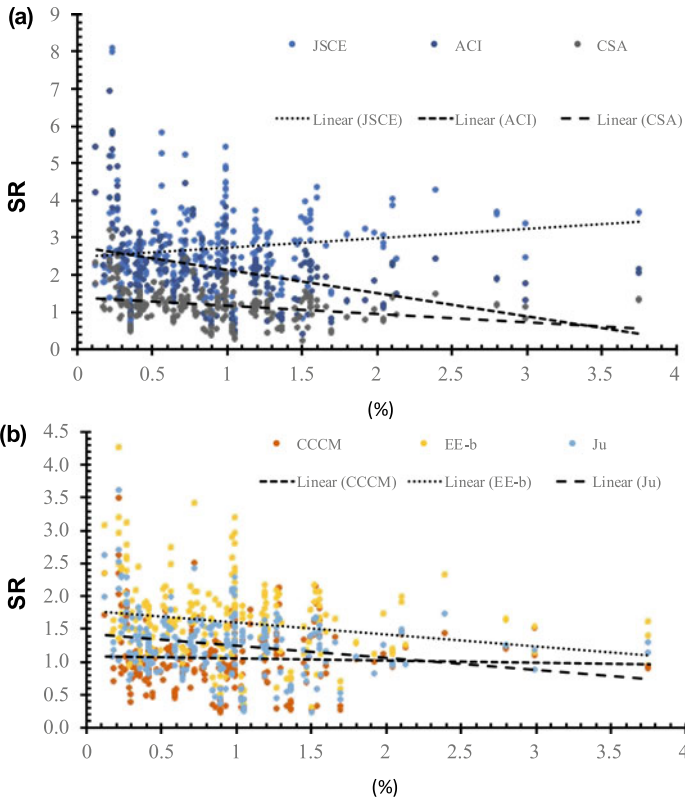
Fig. 14.6 The impact of the reinforcement in flexural ratio on the value of SR

model, the CSA model, and Ju model them. Additionally, the slopes of the best fit line were presented for the JSCE model, the American code model, the CSA model, the CCCM model, the EE-B model, and the Ju model, respectively. Slopes 0.0002, 0.0012, 0.0013, 0.002, 0.0011, and 0.0075were used. Except for the EE-b model and the CCCM model, the safety of chosen models rises as Young's modulus increases. The value of SR that was estimated using the Ju model has the lowest best fit line, making it the Young's modulus most consistently constant. The least consistent model was the one that used the JSCE model since it produced the greatest SR value.

14.4.5 Ratio of Depth to Control Perimeter

The SR value estimated using the American code model, the CCCM model, the CSA model, the JSCE model, the Ju model, and the EE-B model is displayed in Fig. 14.8
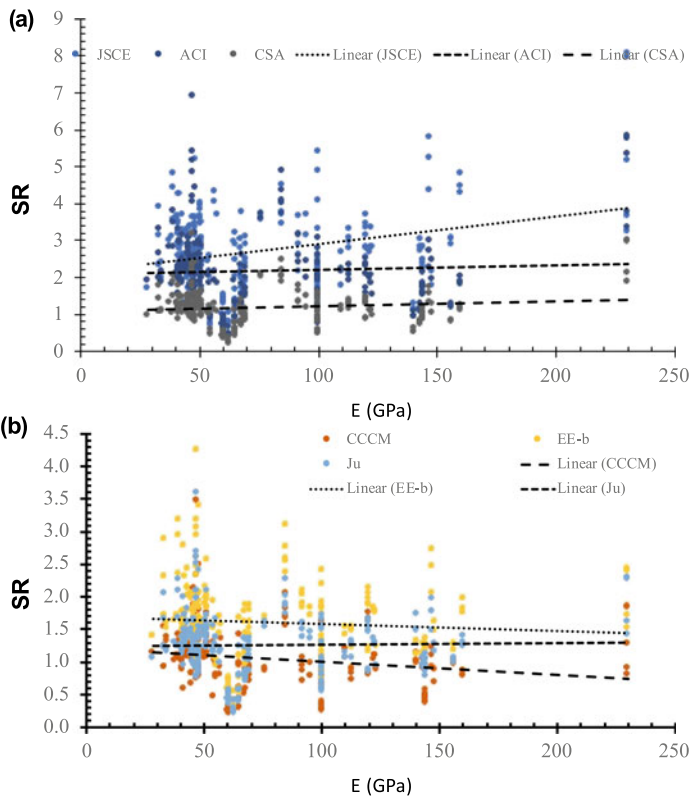
Fig. 14.7 The Young's modulus' impact on the value of SR

in comparison to the depth-to-control perimeter ratio. For the JSCE model, the ACI model, the CSA model, the CCCM model, the EE-B model, and the Ju model, the best fit line was also drawn. Its slope was 8.5935, 2.4433, 6.8699, 13.86, 0.8117, and 1.6327, respectively. As the depth-to-control perimeter ratio rises, the safety of the EE-b model, the CCCM model, and the Ju model also declines. However, when the ratio of depth to control perimeter grows, the safety of the ACI, JSCE, and CSA models also rises. It is most consistent with the depth to control perimeter ratio since the more fit line for the value of SR that was derived using the EE-b model is the lowest and is as a result. The American code model, however, produced the greatest SR value, making it the least consistent. The American code model might not have taken this parameter's influence into account, for whatever reason.
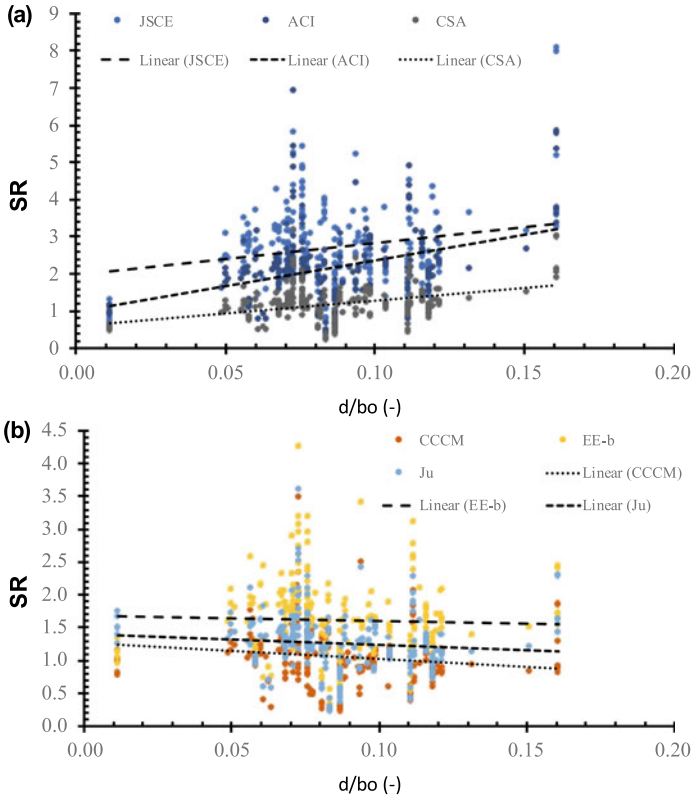
Fig. 14.8 The impact of the between depth and control perimeter on the value of SR

14.4.6 Span-to-Depth Ratio for Shear

Figure 14.9 compares the computed the value of SR to the shear span-to-effective depth ratio using the American code model, the JSCE model, the CSA model, the EE-B model, the Ju model, and the CCCM model. The slope of the best fit line, which was plotted separately for the JSCE model, the American code model, the CSA model, the CCCM model, the EE-b model, and the Ju model, was 0.0507, 0.0475, 0.0224, 0.0213, 0.023, and 0.1353. With an increase in the shear span-to-effective depth ratio, the safety of the JSCE model, the ACI model, and the CSA model declines. On the other hand, when the ratio of shear span to effective depth rises, the safety of the CCCM model, the EE-b model, and the Ju model also rises. They are the most consistent regarding the shear span-to-effective depth ratio since the CSA model, the Ju model, and the EE-b model have the lowest best fit line for the SR value. However, the CCCM model produced the greatest results; hence, it is the least consistent.
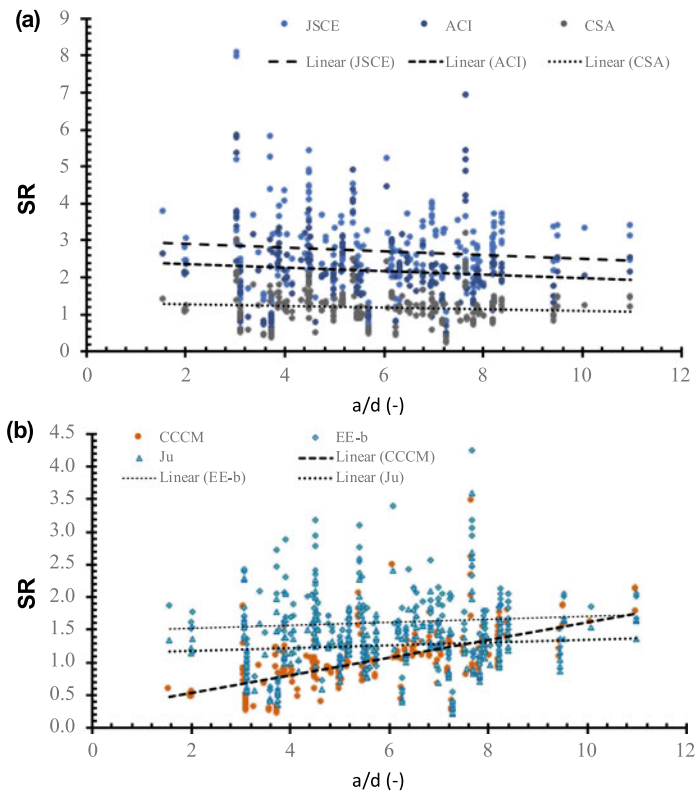
Fig. 14.9 The impact of the shear depth-to-span ratio on the value of SR is determined

14.5 Future Research

Future research studies might focus on a number of these areas, which were noted: (1) A reliability-based examination of the design's safety that takes into account the loads' variability as well as that of the geometry, the materials, and the constructions; (2) A simple-to-design mechanical model that is more dependable and consistent and makes sense in terms of physics.

14.6 Conclusions

Twenty-one concrete slabs chosen approaches for expected punching shear strength were evaluated for accuracy. Comparisons between forecasts and measured strengths from a large experimental database, including 248 slabs from more than 50 research

papers, were used to examine for the method's capacity to predict the two way strength in un-reinforcement concrete slabs in shear.

1. In terms of the effect of size, concrete compressive strength, depth to control perimeter ratio, and shear span-to-depth ratio, the EE-B model exhibits the greatest consistency. This is because it is based on the mechanical principles and uses empirically observed behavior.
2. A number of statistical techniques were used, and the impact of the different fundamental factors was explored. Because of this, the JSCE, ACI, and H models, which have average values of 2.71, 2.18, and 2.16, respectively, are too cautious. In comparison to other models, where the variational coefficients are 35%, 35%, 36%, and 36%, respectively, the Ju, Zg, EE-b, and A models are more consistent.

References

A. C. I. ACI-440 (2015) Guide for the design and construction of concrete reinforced with FRP bars (ACI 440.1R-15). ACI, Farmington Hills, Michigan, USA

Abduljaleel MT, Mahmoud AS, Yousif A (2017) Experimental investigation of two-way concrete slabs with openings reinforced with glass fiber reinforced polymer bars. J Eng Sci Technol 12:889–912

Ahmad HS, Zia P, Yu TJ, Xie Y (1993) Punching shear tests of slabs reinforced with 3-dimensional carbon fiber fabric. Concr Int 16:36–41

AlHamaydeh M, Orabi MA (2021) Punching shear behavior of synthetic fiber-reinforced self-consolidating concrete flat slabs with GFRP bars. J Compos Constr 25:04021029

Ali AH, Mohamed HM, Chalioris CE, Deifalla A (2021) Evaluation of the shear design equations of FRP-reinforced concrete beams without shear reinforcement. Eng Struct 235. Elsevier

Alrudaini TMS (2022) A rational formula to predict punching shear capacity at interior columns connections with RC flat slabs reinforced with either steel or FRP bars but without shear reinforcement. Structures 37:56–68

Bank L, Xi Z (1995) Punching shear behavior of pultruded FRP grating reinforced concrete slabs. In: Proceedings of the non-metallic (FRP) reinforcement for concrete structures. CRC Press, Boca Raton, FL, USA, pp 360–367

Banthia N, Al-Asaly M, Ma S (1995) Behavior of concrete slabs reinforced with fiber-reinforced plastic grid. ASCE J Mater Civ Eng 7:252–257

Bouguerra K, Ahmed EA, El-Gamal S, Benmokrane B (2011) Testing of full-scale concrete bridge deck slabs reinforced with fiber-reinforced polymer (FRP) bars. Constr Build Mater 25:3956–3965

Bywalski C, Drzazga M, Kamiński M, Kaźmierowski M (2020) A new proposal for the shear strength prediction of beams longitudinally reinforced with fiber-reinforced polymer bars. Buildings 10(5):86. https://doi.org/10.3390/buildings10050086

Collins MP (2001) Evaluation of shear design procedures for concrete structures. A CSA Technical Committee Reinforced Concrete Design Report by the Canadian Standards Association, Canada

CAN/CSA S806-12 (2012) Design and construction of building structures with fiber reinforced polymers (CAN/CSA S806-12). Canadian Standards Association: Rexdale, ON, Canada

Deifalla A (2015) Torsional behavior of rectangular and flanged concrete beams with FRP. J Struct Eng. ASCE. https://doi.org/10.1061/(ASCE)ST.1943-541X.0001322

Deifalla A (2020) Strength and ductility of lightweight reinforced concrete slabs under punching shear. Structures 27:2329–2345. https://doi.org/10.1016/j.istruc.2020.08.002

Deifalla A (Mar 2021a) A mechanical model for concrete slabs subjected to combined punching shear and in-plane tensile forces. Eng Struct 231. Elsevier

Deifalla A (2021b) A strength and deformation model for prestressed lightweight concrete slabs under punching shear. Adv Struct Eng 1–12. https://doi.org/10.1177/13694332211020408

Deifalla A (2022) Punching shear strength and deformation for FRP-reinforced concrete slabs without shear reinforcement. Case Stud Constr Mater 16:e00925. p. j. cscm. e00925

Deifalla AF, Zapris AG, Chalioris CE (2021) Multivariable regression strength model for steel fiber-reinforced concrete beams under torsion. Materials 14:3889. https://doi.org/10.3390/ma14143889

Deifalla A, Khali MS, Abdelrahman A (2015) Simplified model for the torsional strength of concrete beams with GFRP stirrups. Compos Constr, ASCE 19(1):04014032. https://doi.org/10.1061/(ASCE)CC.1943-5614.0000498

Deifalla A, Hamed M, Saleh A, Ali T (2014) Exploring GFRP bars as reinforcement for rectangular and L-shaped beams subjected to significant torsion: an experimental study. Eng Struct 59:776–786

Ebid A, Deifalla A (2021) Prediction of shear strength of FRP reinforced beams with and without stirrups using (GP) technique. Ain Shams Eng J. Elsevier. https://doi.org/10.1016/j.asej.2021.02.006

Eladawy B, Hassan M, Benmokrane B (2019) Experimental study of interior glass fiber-reinforced polymer-reinforced concrete slab-column connections under lateral cyclic load. ACI Struct J 116:165–180

Eladawy M, Hassan M, Benmokrane B, Ferrier E (2020) Lateral cyclic behavior of interior two-way concrete slab–column connections reinforced with GFRP bars. Eng Struct 209:109978

El-Gamal S, El-Salakawy E, Benmokrane B (2005) Behaviour of concrete bridge deck slabs reinforced with fiber-reinforced polymer bars under concentrated loads. ACI Struct J 102(5):727–735

El-Gamal S, El-Salakawy E, Benmokrane B (2007) Influence of reinforcement on the behaviour of concrete bridge deck slabs reinforced with FRP bars. J Compos Constr ASCE 11:449–458

El-Gendy MGS, El-Salakawy EF (2020) Assessment of punching shear design models for FRP-RC slab–column connections. J Compos Constr 24:04020047. https://doi.org/10.1061/(ASCE)CC.1943-5614.0001054

El-Gendy M, El-Salakawy E (2015) Punching shear behaviour of GFRP-RC edge slab-column connections. In: Proceedings of the 7th international conference on FRP composites in civil engineering, pp 1–6

El-Ghandour AW, Pilakoutas K, Waldron P (2003) Punching shear behavior of fiber reinforced polymers reinforced concrete flat slabs: experimental study. J Compos Constr 7(2003):258–265

Elmeligy O, El-Nemr A, Deifalla A (2017) Reevaluating the modified shear provision of CAN/CSA S806-12 for concrete beams reinforced with FRP stirrups. In: AEI Conference, ASCE, Oklahoma City

Zhang Q (2006) Behavior of two-way slabs reinforced with CFRP bars. A thesis submitted to the school of graduate studies in partial fulfillment of the requirement for the degree of Master Engineering, Faculty of engineering and Applied Science, Memorial University of Newfoundland, New Found land, Canada

Deifalla A (2021) Refining the torsion design of fibered concrete beams reinforced with FRP using multi-variable non-linear regression analysis for experimental results. Eng Struct 224. Elsevier

Fareed E, Ahmed EA, Benmokrane B (2016) Experimental testing WMCAUS IOP conference series: materials science and engineering; IOP Publishing, Bristol, UK, p 032064. https://doi.org/10.1088/1757-899X/245/3/032064

FIB (2007) FRP reinforcement in RC structures, Technical report prepared by a working party of Task Group 9.3: Fib Bulletin 40

Gardner NJ (1990) Relationship of the punching shear capacity of reinforced concrete slabs with concrete strength. ACI Struct J 87(1):66–71

Gouda A, El-Salakawy E (2016a) Behavior of GFRP-RC Interior Slab-Column Connections with Shear Studs and High-Moment Transfer. J Compos Constr 20:04016005. https://doi.org/10.1061/(ASCE)CC.1943-5614.0000663

Gouda A, El-Salakawy E (2016b) Punching shear strength of GFRPRC interior slab-column connections subjected to moment transfer. J Compos Constr ASCE 20:04015037. https://doi.org/10.1061/(ASCE)CC.1943-5614.0000597

Gu S (2020) Study on the punching shear behavior of FRP reinforced concrete slabs subjected to concentric loading. Master's thesis, Zhejiang University of Technology, Zhejiang, China

Hassan T, Abdelrahman A, Tadros G, Rizkalla S (2000) Fibre reinforced polymer reinforcing bars for bridge decks. Can J Civ Eng 27:839–849. https://doi.org/10.1139/l99-098

Hassan MM, Deifalla A (2015) Evaluating the new CAN/CSA-S806-12 torsion provisions for concrete beams with FRP reinforcements. Mater Struct. https://doi.org/10.1617/s11527-015-0680-9

Hassan M, Fam A, Benmokrane B (2017) A new punching shear design formula for frp-reinforced interior slab-column connections. In: Proceedings of the 7th international conference on advanced composite materials in bridges and structures, Vancouver, BC, Canada

Hemzah SA, Al-Obaidi S, Salim T (2019) Punching shear model for normal and high-strength concrete slabs reinforced with CFRP or steel bars. Jordan J Civ Eng 13:250–268

Huang Z, Zhao Y, Zhang J, Wu Y (2020) Punching shear behavior of concrete slabs reinforced with CFRP grids. Structures 26:617–625

Hussein AF, El-Salakawy E (2018) Punching shear behavior of glass fiber-reinforced polymer-reinforced concrete slab-column interior connections. ACI Struct J 115:1075–1088. https://doi.org/10.14359/51702134

Hussein A, Rashid I, Benmokrane B (2004) Two-way concrete slabs reinforced with GFRP bars. In: Proceedings of the 4th international conference on advanced composite materials in bridges and structures, CSCE, Calgary, AB, Canada

Jacobson DA, Bank LC, Oliva MG, Russel JS (2005) Punching shear capacity of double layer FRP grid reinforced slabs. ACI, Specs. Publication. SP. 230–49, pp 857–876

JSCE (1997) Recommendation for design and construction of concrete structures using continuous fiber reinforcing materials. Machida A (ed). Concrete Engineering Series 23, Tokyo, Japan, pp 325

Ju M, Park K, Park AC (2018) Punching shear behavior of two-way concrete slabs reinforced with glass-fiber-reinforced polymer (GFRP) bars. Polymers 10:893. https://doi.org/10.3390/polym10080893

Ju M, Ju J, Sim JW (2021) A new formula of punching shear strength for fiber reinforced polymer (FRP) or steel reinforced two-way concrete slabs. Compos Struct 258:113471. https://doi.org/10.1016/j.compstruct.2020.113471

Kara IF, Sinani B (2017) Prediction of punching shear capacity of two-ways FRP reinforced concrete slabs. Int J Bus Technol 5:57–63

Khanna O, Mufti A, Bakht B (2000) Experimental investigation of the role of reinforcement in the strength of concrete deck slabs. Can J Civil Eng 27:475–480

Kuchma D, Wei S, Sanders D, Belarbi A, Novak L (2019) The development of the one-way shear design provisions of ACI 318-19. ACI Struct J 116(4)

Lee JH, Yoon YS, Cook WD, Mitchell D (2009) Improving punching shear behavior of glass fiber-reinforced polymer reinforced slabs. ACI Struct J 106:427–434

Louka HJ (1999) Punching behavior of a hybrid reinforced concrete bridge deck. Master's thesis, University of Manitoba, Winnipeg, MB, Canada

Marí A, Bairán J, Cladera A, Oller E, Ribas C (2015) Shear-flexural strength mechanical model for the design and assessment of reinforced concrete beams. Struct Infrastruct Eng 11:1399–1419

Matthys S, Taerwe L (2000) Concrete slabs reinforced with FRP grids. II: punching resistance. J Compos Constr ASCE 4(3):154–161

Min KH, Yang JM, Yoo DY, Yoon YS (27–29 Sep 2010) Flexural and punching performances of FRP and fiber reinforced concrete on impact loading. In: Proceedings of the CICE 2010–the 5th international conference on FRP composites in civil engineering, Beijing, China

Mohmmad SH, Gülsan ME, Çevik A (2022) Punching shear behaviour of geopolymer concrete two-way slabs reinforced by FRP bars under monotonic and cyclic loadings. Adv Struct Eng 25:453–472

Mostafa A (2016) Punching shear behavior of GFRP-RC slab-column edge connections with high strength concrete and shear reinforcement. Master's thesis, Manitoba University, Winnipeg, MB, Canada, p 51

Nguyen-Minh L, Rovnak M (2013) Punching-shear resistance of interior GFRP reinforced slab-column connection. ASCE J Compos Constr 17:2–13

Oller E, Kotynia R, Marí A (2018) Assessment of the existing formulations to evaluate shear-punching strength in RC slabs with FRP bars without transverse reinforcement. In: High tech concrete: where technology and engineering meet; Springer, Cham, Switzerland. https://doi.org/10.1007/978-3-319-59471-2_91

Oskouei AV, Kivi MP, Araghi H, Bazli M (2017) Experimental study of the punching behavior of GFRP reinforced lightweight concrete footing. Mater Struct 50:256. https://doi.org/10.1617/s11527-017-1127-2

Ospina CE, Alexander SDB, Cheng JJR (2003) Punching of two- way slabs with fiber-reinforced polymer reinforcing bars or grids. ACI Struct J 100(2003):589–598

Rahman AH, Kingsley CY, Kobayashi K (2000) Service and ultimate load behavior of bridge deck reinforced with carbon FRP grid. J Compos Constr 4:16–23

Salama AE, Hassan M, Benmokrane AB (2019) Effectiveness of glass fiber-reinforced polymer stirrups as shear reinforcement in glass fiber-reinforced polymer-reinforced concrete edge slab-column connections. ACI Struct J 116:165–180

Salama AE, Hassan M, Benmokrane B (2021) Punching-shear behavior of glass fiber-reinforced polymer-reinforced concrete edge column-slab connections: experimental and analytical investigations. ACI Struct J 118:147–160

Shen Y, Sun J, Liang S (2022) Interpretable machine learning models for punching shear strength estimation of FRP reinforced concrete slabs. Crystals 12:259. https://doi.org/10.3390/cryst12020259

Shill S, Garcez E, Al-Ameri R, Subhani M (2022) Performance of two-way concrete slabs reinforced with basalt and carbon FRP rebars. J Compos Sci 6:74

Tharmarajah G, Taylor ES, Cleland J., Robinso D (2015) Corrosion-resistant FRP reinforcement for bridge deck slabs. In: Proceedings of the institution of civil engineers. Bridge Engineering; ICE Publishing, London, UK, vol 168, pp 208–217. https://doi.org/10.1680/jbren.13.00001

Theodorakopoulos DD, Swamy RN (2007) Analytical model to predict punching shear strength of FRP-reinforced concrete flat slabs. ACI Struct J 104:257–266

Tom EE (2007) Behavior of two-way slabs reinforced with GFRP bars. Master's thesis, Memorial University of Newfoundland, St. John's, NF, Canada, p 169

Wu L, Huang T, Tong Y, Liang S (2022) A modified compression field theory based analytical model of RC slab-column joint without punching shear reinforcement. Buildings 12:226. https://doi.org/10.3390/buildings12020226

Xiao Z (2010) Expremental study on two-way concrete slab subjected to punching shear. Master's thesis, Zhengzhou University, Zhengzhou, China

Yooprasertchai E, Dithaem R, Arnamwong T, Sahamitmongkol R, Jadekittichoke J, Joyklad P, Hussain Q (2021ab) Remediation of punching shear failure using glass fiber reinforced polymer (GFRP) rods. Polymers 13:2369. https://doi.org/10.3390/polym13142369

Yooprasertchai E, Tiawilai Y, Wittayawanitchai T, Angsumalee J, Joyklad P, Hussain Q (2021b) Effect of shape, number, and location of openings on punching shear capacity of flat slabs. Buildings 11:484. https://doi.org/10.3390/buildings11100

Zaghloul A (2007) Punching shear strength of interior and edge column slab connections in CFRP rein-forced flat plate structures transferring shear and moment. Ph.D. thesis, Department of Civil and Environmental Engineering, Carleton University, Ottawa, ON, Canada

Zaghloul A, Razaqpur A (2003) Punching shear behavior of CFRP reinforced concrete flat plates. In: Proceedings of the international conference on, composites in construction, pp 1–726

Zaghloul E, Mahmoud Z, Salama T (2008) Punching behavior and strength of two-way concrete slabs reinforced with glass fiber reinforced polymer (GFRP) rebars. In: Proceedings of structural composites for infrastructure applications, Hurghada, Egypt

Zhang Q (2006) Behaviour of two-way slabs reinforced with CFRP bars. Master's thesis, Memorial University of Newfoundland, St. John's, NF, Canada

Zhang Q, Marzouk H, Hussein A (2005) A preliminary study of high-strength concrete two-way slabs reinforced with GFRP bars. In: Proceedings of the 33rd CSCE annual conference: general conference and international history symposium, CSCE, Toronto, ON, Canada

Zhou X (2020) Expremental study on the punching shear behavior of square GFRP reinforced concrete slabs. Master's thesis, Zhejiang University of Technology, Zhejiang, China

Zhu HY, Wang JL (2012) Plastic analysis on punching shear capacity of two-way BFRP rebar reinforced concrete slabs under central concentrated load. J Zhengzhou Univ (Eng Sci) 33:1–5. (in Chinese)

Zhu H, Zhang Y, Gao D, Xiao Z (27–29 Sep 2010) Deformation behavior of concrete two-way slabs reinforced with BFRP bars subjected to eccentric loading. In: Proceedings of the CICE 2010: the 5th international conference on FRP composites in civil engineering, Beijing, China

Chapter 15
Assessment of Compression Design of CFST

Ibrahim S. Hussein, Mona M. Fawzy, M. F. Shaker, Ahmed F. Deifalla, and Gouda M. Ghanem

Abstract Design codes disagree on the design of Concrete filled steel tubes (CFST). Thus, in this current study, a comparison between the main international design codes for the design of CFST is presented. The considered codes include: AIJ 1997, AISC, EC4, ECP (ECP 205-2007 in Design of steel structures. National research center for housing and construction, Cairo, Egypt). Concluding remarks are outlined and discussed.

Keywords AIJ · AISC · EC4 · ECP · CFST

15.1 Introduction

Design codes in different countries provide general provisions for the design of concrete filled tube columns which are extended from traditional design provisions for concrete or steel structures. Thus, the main aim of this chapter is to provide a clear comparison between different codes from the obtained experimental results. In the late 1870's, the first CFST was used as axially loaded columns for the construction of road bridges in Great Britain. Later in 1967, the Architectural Institute of Japan, (AIJ) recommended CFST columns (AIJ 2008). The standards for composite sections were

I. S. Hussein · M. M. Fawzy
Civil Engineering Program, The Higher Institute of Engineering, El-Shorouk Academy, Nakheel District, Cairo 11837, Egypt

M. F. Shaker · G. M. Ghanem
Faculty of Engineering, Department of Structural Engineering, Helwan University, Cairo 11795, Egypt

A. F. Deifalla (✉)
Faculty of Engineering, Department of Structural Engineering and Construction Management, Future University in Egypt, End of 90Th St., Fifth Settlement, Cairo 11865, Egypt
e-mail: Ahmed.deifalla@fue.edu.eg

G. M. Ghanem
The Higher Institute of Engineering, El-Shorouk Academy, Cairo, Egypt

written for circular composite sections, and then it was revised in 1980 to include the square composite sections. In 1987, a revised design method was included in AIJ standards that accounts for the strength of the confined concrete and the width-to-thickness ratio, Nishiyama et al. (2002). The first high-rise building in U.S. used CFT columns was First Street Plaza in San Francisco, California. The building consisted of 27 stories and the lateral bracing system consisted of a braced frame with moment connections and CFST columns at the four corners of the braced core.

Most design codes introduced specific formulas which helped in predicting the axial capacity and strength of composite steel–concrete columns. The formulas depend on both analytical and experimental studies. Leon et al. (2007, 2011) provided an overview of the historical development of the design of CFST in the American codes. The work of Kloppel and Goder in 1970 was the base for the first design equation for CFST columns. Their work reported the detailed the internal strain and stress in both the concrete and steel for a series of CFST tested until collapse. Roik and Bergmann (1989, 1990) collected the experimental data from 208 tests, which were implemented for the calibration and development of the Eurocode provisions for CFST (Eurocode 4 2004). The work of Wakabayashi, Roik and Bergman is the base for the J11apanese provisions (Roik and Bergmann 1989). Leon et al. (2007) evaluated the CFST provisions for CFST in AISC (2010), and EC4 (2004). The authors concluded that in general EC4 give good predictions for CFST columns. While AISC design method performs well for beam columns. Potty et al. (2009) conducted 36 tests to investigate the effect of using high strength concrete in CFT columns. The authors recommended modifying the formulas given in EC4 to consider the confinement effect in circular CFST columns. Roik and Bergmann (1990) extended the design method in EC4 to account for unsymmetrical CFST. The proposed design method was verified via an experimental program of 6 specimens (Deifalla et al. 2019; Shaker et al. 2022). Thus, in this current study, a comparison between the main international design codes for the design of CFST is presented. The considered codes include: AIJ 1997, AISC, EC4, ECP (ECP 205-2007 2007).

15.2 Brief Recount of Experimental Testing

15.2.1 General

Steel plates longitudinally welded with electric welding were used to fabricate circular steel sections. The external diameter of pipes was 127 mm and D/t ratios are equal to 63.5 and 31.75, to avoid the local buckling effect according to the limitation of different codes as shown in Table 15.1. (EC4, AISC, AIJ, ECP).

Table 15.1 Tested CFST (Deifalla et al. 2019; Shaker et al. 2022)

Sample name	D/t	H/D	N_u (kN)
C40-2	63.5	3.14	860
C100-2		7.87	743
C200-2		15.75	724
C40-4	31.8	3.14	1260
C100-4		7.87	1098
C200-4		15.75	1078

Table 15.2 Comparisons of ultimate axial loads between measured and calculated using AISC

Sample name	D/t	H/D	N_u (kN)	AISC	
				P (KN)	Ratio
C40-2	63.5	3.14	860	743.8	0.87
C100-2		7.87	743	707.8	0.95
C200-2		15.75	724	593	0.82
C40-4	31.8	3.14	1260	980	0.78
C100-4		7.87	1098	939	0.86
C200-4		15.75	1078	807	0.75

15.2.2 Studied Parameters

Specimens were characterized with letters and numbers as per load application, length, steel pipe thickness, extra parameter and its positioning along the length is shown in Table 15.2. The main parameter was the impact of utilizing shear connectors and through bolts on the behavior of CFST. Three different groups were prepared; each one had three various H/D proportions. Different studied lengths were 400 mm, 1000 mm, and 2000 mm, corresponding to H/D proportions 3.14, 7.874, and 15.748, respectively. Also, the D/t proportion was equal to 63.5 and 31.75. Subgroup A specimens were utilized as control groups with neither shear connectors nor thorough bolts. Loading was at either steel only or loaded on both the concrete core and the steel pipe sections.

15.2.3 Testing Program

The loading frame comprised fundamentally of horizontal I–beam fixed to two vertical column I–beams by bolts. The I–beam column was placed on the floor. The columns were vertically placed, and the upper and lower ends were hinged at a solid frame. The upper end of column was laterally supported by elastic anchors just

Fig. 15.1 Specimens
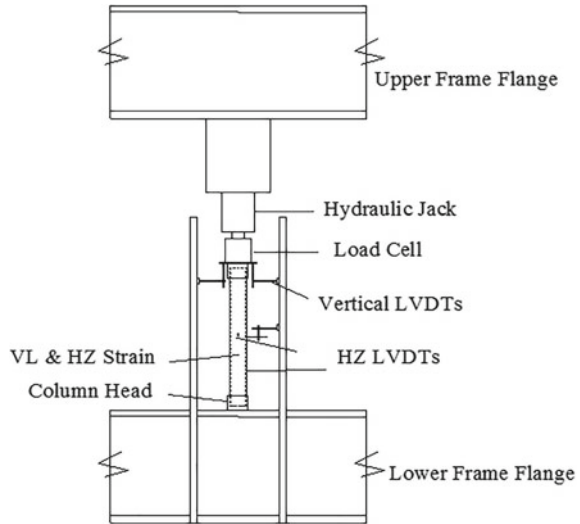
to stop the drop of samples while testing as appeared in Fig. 15.1. Table 15.1 shows the configuration of the six CFST subjected to compression loading.

15.3   Comparisons of Axial Loads of CFST Columns

Tables 15.2, 15.3, 15.4 and 15.5 show the values of ultimate axial loads for both the measured axial strength and that calculated using various design. As the values presented in Tables 15.2, 15.3, 15.4, 15.5 and 15.6, a significant variation between the predicted and test results values are found. At D/t 63.50, the average values of Pn decrease by 14%, 5% and 18% for H/D 3.14, 7.87 and 15.75 respectively compared with the experimental test results. As well as, At D/t 31.75, the average values of Pn decrease by 22%, 14% and 25% for H/D 3.14, 7.87 and 15.75, respectively, with respect to the experimentally measured strength. Generally, the predicted values of the slender steel wall sections (D/t = 63.50) are acceptable than those of the compact sections (D/t = 31.75). This is because confinement of slender steel wall sections is less than that of compact sections. These findings agree with neglecting the confinement in AISC. From the axial strength previous outputs, it can be concluded that, generally EC4 gives good predictions for CFST circular columns. These findings are consistent with that of Leon, where the measured strengths are compatible with the predicted AIJ code values for short columns (H/D < 4) and (4 < H/D < 12). They are non-compatible for long columns (H/D > 12). This is due to the consideration of confinement effect in circular short columns as presented in Tables 15.2, 15.3, 15.4 and 15.5. In case of using AISC and ECP, the predicted values of the slender steel wall sections (D/t = 63.50) are acceptable than those of the compact sections

(D/t = 31.75) due to the confinement consideration. Finally, the confinement has a significant influence for the estimated values of ultimate loads using all codes specifications. So, effect of confinement in AISC and improvement the equations in long CFST columns in AIJ codes should be considered. In case of combined bending moments and axial forces, the AIJ concerns a wide criteria and factors leads to provide accurate predicted values compared with other selected codes.

Table 15.3 Comparisons of ultimate axial loads between measured and calculated using ECP

Sample name	D/t	H/D	Nu (kN)	ECP 205-2007	
				P (kN)	Ratio
C40-2	63.5	3.14	860	768	0.89
C100-2		7.87	743	726	0.98
C200-2		15.75	724	576	0.79
C40-4	31.8	3.14	1260	1002	0.80
C100-4		7.87	1098	954	0.87
C200-4		15.75	1078	783	0.73

Table 15.4 Comparisons of ultimate axial loads between measured and calculated using EC4

Sample name	D/t	H/D	Nu (kN)	EC4	
				P (kN)	Ratio
C40-2	63.5	3.14	860	768	0.90
C100-2		7.87	743	658	0.90
C200-2		15.75	724	655	0.91
C40-4	31.8	3.14	1260	1119	0.89
C100-4		7.87	1098	913	0.85
C200-4		15.75	1078	899	0.85

Table 15.5 Comparisons of ultimate axial loads between measured and calculated using AIJ

Sample name	D/t	H/D	Nu (kN)	AIJ	
				P (kN)	Ratio
C40-2	63.5	3.14	860	851	0.99
C100-2		7.87	743	670	0.90
C200-2		15.75	724	477	0.66
C40-4	31.8	3.14	1260	1159	0.92
C100-4		7.87	1098	970	0.88
C200-4		15.75	1078	698	0.65

Table 15.6 Comparison between design provisions

Item	AISC-LRFD	EC4	AIJ-SRC
Concept	Determine the axial load using a column curve	Determine the axial load using a column curve	Uses the superposed strength method
Confinement effects	Effect of confinement is neglected	Considered only if the following conditions are satisfied: a. Compact circular sections b. The normalized stiffness (λ) ≤ 0.5 c. The eccentricity of loading (e) $\leq$ D/10	Considered for short circular columns

15.4   Discussion

Design provisions and standards of CFST sections under axial and flexural loadings have been analyzed and compared. The comparisons usually include the design assumptions, design capacities, in addition to the experimental and numerical basis for the design formulas. Table 15.6 shows the comparison between design provisions for different codes. This inconsistency has alerted researchers to conduct studies on various issues concerning compression of columns (ECP 205-2007 2007; Khan et al. 2022; Li et al. 2022; Nazar et al. 2022; Shen et al. 2022).

15.5   Conclusions

Six CFST were tested under compression, where the results were compared with the ones calculated using various design codes. it can be concluded that:

- EC4 gives good predictions for CFST circular columns, which is in good agreement with Leon et al. (2007).
- For short column, the strength calculated using the AIJ code is closer to that measured. On the other hand, for long columns, the strength is not accurate with respect to the experimentally measured strength. This is due to the consideration of confinement effect in circular short columns.
- For slender steel wall sections (D/t = 63.50), the strength calculated using AISC and ECP is accurate. In the contrary, for the compact sections (D/t = 31.75), the predicted values are less accurate, which is due to the confinement consideration.

References

AIJ (2008) Recommendations for design and construction of concrete filled steel tubular structures. Architectural Institute of Japan (AIJ), Tokyo, Japan

AISC 360-10 (2010) Specification for structural steel buildings. American Institute of Steel Construction (AISC), Chicago (IL)

Deifalla AF, Fattouh FM, Fawzy MM, Hussein IS (2019) Behavior of stiffened and unstiffened CFT under concentric loading. An Exp Study Steel Compos Struct Int'l J 33(6):793–803. https://doi.org/10.12989/scs.2019.33.6.793

ECP 205-2007 (2007) Design of steel structures. National research center for housing and construction, Cairo, Egypt

Eurocode 4 (2004) Design of composite steel and concrete structures. European Committee for Standardization, Brussels

Khan MA, Aslam F, Javed MF, Alabduljabbar H, Deifalla AF (2022) New prediction models for the compressive strength and dry-thermal conductivity of bio-composites using novel machine learning algorithms. J Clean Prod, 350, art. no. 131364. https://doi.org/10.1016/j.jclepro.2022.131364

Leon RT, Kim DK, Hajjar JF (2007) Limit state response of composite columns and beam-columns Part 1: formulation of design provisions for the 2005 AISC Specifications. J Eng 341–358

Leon RT, Perea T, Hajjar JF, Denavit MD (Oct 2011) Concrete-filled tubes columns and beam-columns: a database for the AISC 2005 and 2010 Specifications. Festschrift Gerhard Hanswille, Germany, pp 203–212

Li Y, Zhang Q, Kamiński P, Deifalla AF, Sufian M, Dyczko A, Kahla NB, Atig M (2022) Compressive strength of steel fiber-reinforced concrete employing supervised machine learning techniques. Materials 15(12), art. no. 4209. https://doi.org/10.3390/ma15124209

Nazar S, Yang J, Ahmad W, Javed MF, Alabduljabbar H, Deifalla AF (2022) Development of the new prediction models for the compressive strength of nanomodified concrete using novel machine learning techniques. Buildings 12(12), art. no. 2160. https://doi.org/10.3390/buildings12122160

Nishiyama I, Morino S, Sakino K, Nakahara H, Fujimoto T, Mukai A, Inai E, Kai M, Tokinoya H, Fukomoto T, Mori K, Yoshioka K, Mori O, Yonezawa K, Uchikoshi M, Hayashi Y (2002) Summary for research on Concrete-Filled structural steel tube column system carried out under the US-Japan cooperative research program on composite and hybrid structures. ISSN 0453-4972, BRI Research Paper No. 147

Potty SN, Ismail A, John VK (2009) High strength concrete filled square and circular steel tubes under axial load. Department of Civil Engineering, University Teknologi Petronas, Bandar Seri Iskandar, 31750 Tronoh, Perak Darul Ridzuan, Malaysia. In: 10th international conference on concrete engineering and technology, CONCET'09, 2–4 March 2009

Roik K, Bergmann R (1989) Report on Eurocode clauses 4.8 and 4.9. Eurocode 4, Bonn, Germany

Roik K, Bergmann R (1990) Design method for composite columns with unsymmetrical cross-sections. J Constr Steel Res 15:153–168

Shaker FMF, Ghanem GM, Deifalla AF, Hussein IS, Fawzy MM (2022) Influence of loading method and stiffening on the behavior of short and long CFST columns. Steel Compos Struct An Int'l J. Accepted

Shen Z, Deifalla AF, Kamiński P, Dyczko A (2022) Compressive strength evaluation of ultra-high-strength concrete by machine learning. Materials 15(10), art. no. 3523. https://doi.org/10.3390/ma15103523

Chapter 16
Evaluation of Early-Age Cracking in Arch Feet of PC Girder-CFST Arch Rib Composite Bridge

Xu Huang, Huaqian Zhong, Shaohua He, Ayman S. Mosallam, and Ashraf Abdelkhalek Agwa

Abstract The prestressed concrete (PC) girder-to-concrete filled steel tubular (CFST) arch composite bridge has increasingly become popular in recently constructed railway bridges. The CFST arch feet connecting the PC girder and CFST arch rib are commonly cracked during bridge construction. This paper performs experimental and numerical studies on CFST arch feet to uncover the reasons behind the early-age cracking of the arch feet' concrete. Firstly, the prototype bridge was briefly introduced, and a finite element (FE) model using beam element was established to determine internal forces at the arch feet. Then, a solid FE model was established for the arch-to-girder joint structure, and the procedure of hydration heat for the CFST core concrete was simulated and presented. The accuracy of the solid model was calibrated using the experimental results obtained from the arch feet of the actual bridge. Critical factors that cause tensile stress in the concrete abutment are determined based on the results. It shows that concrete hydration heat caused significant temperature differences between the CFST core and abutment concrete, triggering large tensile stress in the concrete arch feet. The maximum tensile stress measured at the abutment surface was 2.3 MPa on average, which was beyond the concrete cracking strength. Furthermore, recommendations for lowering the risk of concrete cracking are suggested. The outcome of this study is supposed to provide a reference for optimizing the early-age cracking performance of CFST arch feet (CFSTAF) in PC girder-to-CFST arch composite bridges.

X. Huang · H. Zhong · S. He (✉)
School of Civil & Transportation Engineering, Guangdong University of Technology, Guangzhou, Guangdong, China
e-mail: hesh@gdut.edu.cn

A. S. Mosallam
Department of Civil & Environmental Engineering, University of California, Irvine, CA, USA

A. A. Agwa
Department of Structural Engineering and Construction Management, Future University in Egypt, Cairo, Egypt

Keywords Composite bridge · Arch foot · Concrete-filled steel tube · Cracking performance · Numerical simulation

16.1 Introduction

Prestressed concrete (PC) girder-to-concrete filled steel tubular (CFST) arch composite bridges, using CFST arch ribs to strengthen the main girders, is considered to be a competitive alternative for constructing large-span bridges. The merits of such bridges include the smaller height, larger spans, convenient construction, and economic cost (Zheng and Wang 2018; Chen et al. 2017; He et al. 2022; Nakamura 2000). The steel arch rib and the concrete girder are usually connected with the arch foot, mostly in the structural form of the CFST arch rib that is typically inserted into a concrete abutment. For the construction of the CFST arch feet (CFSTAF), the pre-buried hollow steel tube is usually filled with concrete that is pumped after completely folding the steel tubular arch rib. The pumping pressure and hydration heat cause the steel tubular expansion, which inevitably extrudes the surrounding concrete, resulting in advanced abutment cracks (Zhou and Li 2013; Lin et al. 2014).

Over the past few years, many scholars conducted various studies that focused on assessing the numerically local stress status of the CFSTAF. The unneglectable impact of pumping pressure and hydration heat generated from CFST core concrete on early-age cracking of arch feet has been reported in several publications (e.g., Ma et al. 2011; Cao 2015; Deng 2016; Emborg and Bernander 1994; Liu et al. 2013). Previous studies indicated that early cracking of concrete abutment in CFSTAF may be attributed to the following reasons: (i) expansion of tubular steel subjected to pumping pressure of CFST core concrete that squeezes abutment concrete and generating tensile stresses in arch feet concrete; (ii) heat generated from the hydration of core concrete that causes the temperature difference between the inner and outer concrete, resulting in the tensile stress on abutment surface; and (iii) the different Poisson ratios of steel and concrete causing a different amount of expansion the two materials when subjected to axial compression that leads to an increase of extruding actions in the tubular-concrete interface and tensile stress in abutment concrete. Despite the importance of the numerous numerical studies related to the structural performance of CFSTAF under external loadings, qualitative analysis and experimental tests in assessing the early-age performance of abutment concrete during bridge construction are scarce.

This paper presents a summary of an experimental and numerical investigation that was performed on CFSTAF to identify reasons that contribute to and cause early cracking of abutment concrete. In this study, a long-span continuous PC girder-CFST arch composite bridge, the Liuxi River Bridge located in Guangdong Province, China, is selected as the background project. With the help of Midas Civil software, a finite element (FE) model using beam element was developed for the entire bridge to determine internal forces at the arch feet when the core concrete generated hydration heat. Then, a solid FE model using ANSYS® FE code was established for the

arch feet structure, and the concrete hydration process was simulated and calibrated via experimental results. Furthermore, recommendations for lowering the risk of concrete cracking are provided. The outcome of this study provides a reference for optimizing the anti-cracking performance of CFSTAF in PC girder-to-CFST arch composite bridges in early-age.

16.2   Prototype Bridge Description

The Liuxi River Bridge in Guangdong Province, China, is a continuous PC box girder-CFST arch composite bridge. Figure 16.1 shows the arrangement and main dimensions of the bridge. The PC girder and steel arches are made of C55 normal concrete and Q345 steel, respectively. The cross-section of the PC box girder is in the form of a single box with a double chamber. The CFST arch rib is in a dumbbell shape. The PC box girder connects the CFST arch ribs through two CFSTAF. The span arrangement of the bridge is 90 m + 180 m + 90 m, and the sectional height of the PC box-girder is 4.5 m at the mid-span point and 10.0 m near piers. The embedment depth of the CFST arch rib in concrete abutment ranges from 3.5 to 5.5 m. The arch rib height is 36.0 m, and the rise-span ratio is 1:5. Figure 16.2 shows the sectional form of the arch rib at the arch foot. The following steps are concrete casting sequences in the steel arch rib tubular: (i) filling the upper steel tubular with pumping concrete; (ii) filling the lower steel tubular with pumping concrete; and finally, (iii) filling the patch between the upper and lower steel tubular with pumping concrete.

16.3   Determinations of Internal Forces in CFST Arch Feet

As mentioned earlier, the internal forces of the arch feet were determined using a FE model for the bridge based on the Midas Civil software (Yang 2009). The PC girder, steel arch rib, and transverse brace are simulated using beam elements, while vertical suspenders are modeled using truss elements. Figure 16.3 shows the numerical model of the entire bridge. Numerical simulation results demonstrated that the abutment's concrete experienced the most severe stresses when concrete hydration heat proceeded. The corresponding internal forces are presented in Table 16.1. As can be seen, the arch feet are mainly subjected to the axial loads from CFST arch ribs, and the shear force at the arch feet is minor and insignificant.
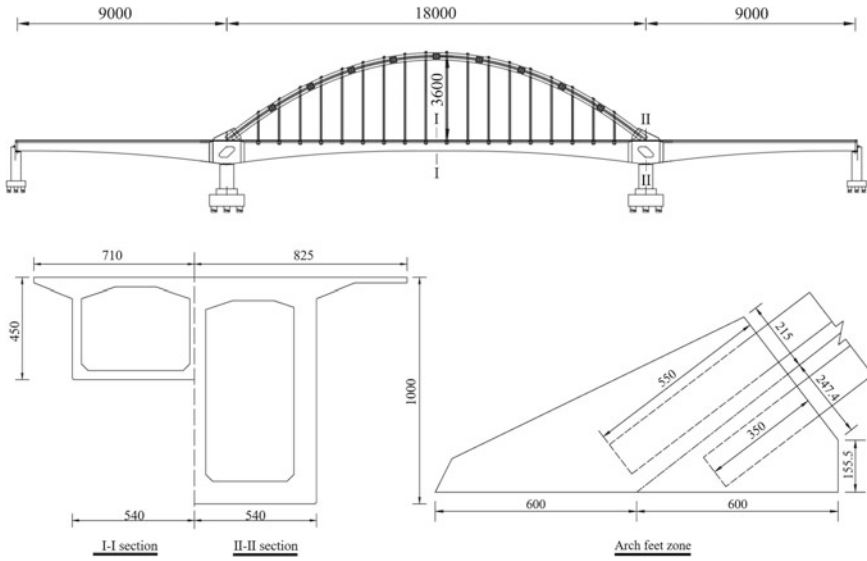
Fig. 16.1 Overview of bridge arrangements (*Unit: cm*)

Fig. 16.2 Dumbbell shaped
CFST arch ribs (*Unit: cm*)

(a) Midas rod structure   (b) Finite element blanking of full bridge
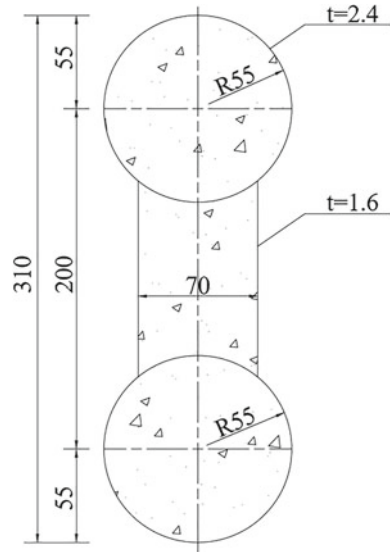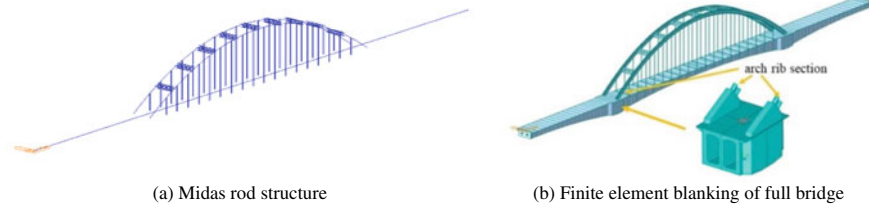
Fig. 16.3 Midas civil model of liuxi river bridge

Table 16.1 Internal force of arch ribs

Axial force (kN)	Shearing force (kN)	Bending moment (kN m)
12,052.0	257.0	4,183.0

16.4 Assessment of Early-Age Cracking Performance of CFST Arch Feet

16.4.1 Simulation of Temperature Field in CFST Arch Field

16.4.1.1 FE Model Establishment

The FE solid model used to calculate the local temperature field of the arch foot under core concrete hydration heat was developed by the thermal analysis module of the ANSYS® software. Using the temperature field analysis model, one can analyze the stresses in the arch feet resulted from the hydration heat of core concrete (Lin et al. 2007, 2009, 2011; Zhang et al. 2009; Du and Liu 1994). In developing the thermal analysis model, Solid 70 thermal analysis solid elements are used for the concrete abutment and CFST core concrete, while Shell 157 thermal analysis shell element is used for modeling the steel tube. Figure 16.4 presents the thermal analysis model and the details of the prestressed reinforcement in the arch feet structure.

The thermal properties of materials are critical for calculating the temperature field at the arch feet zone. For temperature field analysis conducted in this study, the thermal properties of steel and concrete are defined using the thermal conductivity (λ), specific heat (c), and density (ρ) that were specified in specification GB50936-2014 (2014) and reference (Zhu 1999). Table 16.2 provides a summary of the parameters.

Temperature calculations focus on the CFST core concrete's hydration development. The definition of material modulus, thermal expansion coefficient, initial temperature, and hydration heat is indispensable and introduced as follows:

(a) Thermal analysis model   (b) Arrangement of prestressed reinforcements
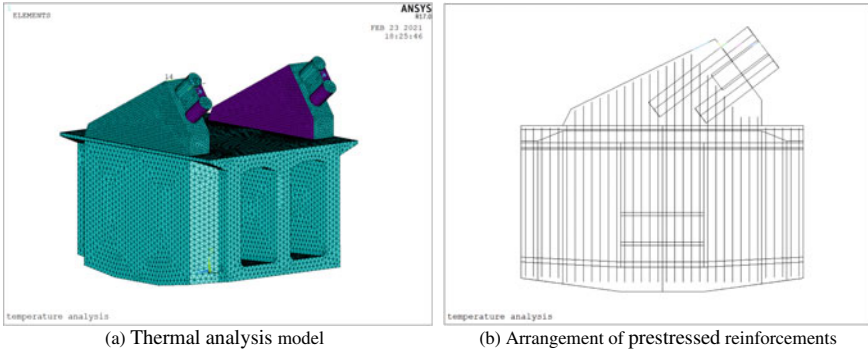
Fig. 16.4 Local FE model of arch foot

Table 16.2 Thermal performance parameters of materials

Material	Density kg/m^3	thermal conductivity J/(h m °C)	Specific heat capacity J/(kg °C)
Concrete	2,400	9,750	480
Steel	8,005	172,800	920

i. *Materials elastic modulus*

The following composite exponential formula expresses the relationship between elastic modulus and curing age in the FE model (Sun and Xie 2019).

$$E(t) = E_0(1 - e^{-at^b}) \qquad (16.4.1)$$

where: t is the concrete age; E_0 is the final elastic modulus of concrete; and a and b are constants. The elastic modulus of steel, E_s, is 2.06×10^5 N/mm^2.

ii. *Thermal expansion coefficients*

The thermal expansion coefficient of concrete, α_c, is $1.0 \times 10^{-5}(0 \le °C \le 100)$ (GB 50010-2010 2010). The thermal expansion coefficient of steel, α_s, is 1.2×10^{-5} (GB 50017-2017 2010).

iii. *Initial temperature*

The initial temperature of the core concrete is calculated according to the following expression:

$$T_p = T_1 + (T_a - T_1)(\phi_1 + \phi_2 + \phi_3 + \cdots + \phi_n) \qquad (16.4.2)$$

where: T_p is concrete pouring temperature; T_1 is concrete mixing temperature; T_a is the environmental temperature during concrete transportation and pouring; and

$\phi_1, \ldots, \phi_n$ are the temperature loss coefficients described in reference (Li and Liu 2009).

iv. *Cement hydration heat*

In this analysis, the double exponential formula is used as the cement hydration heat calculation model (Zhu 2014). The expression of the double exponential calculation model is:

$$Q(t) = Q_0(1 - e^{-at^b}) \tag{16.4.3}$$

where: $Q(t)$ is the hydration heat generated at the age t (kJ/kg); Q_0 is the final hydration heat of cement, unit (kJ/kg); t is curing age (d); and a and b are constants.

Prior to analyzing arch feet members' stresses, the thermal analysis model should be converted into a structural analysis model. In the process of model conversion, the loading conditions of the structural analytical model are defined based on the internal forces listed in Table 16.1, in addition to the temperature force from the transformed thermal analysis model. The elements defined in the structural analysis model are as follows: the PC girder, concrete abutment, and steel tubular are simulated using the transformed Solid 185 structural element. The steel tubular is modeled using the transformed Shell 63 structural plate-shell element. The prestressed tendons, steel reinforcements, and tension rods are simulated using the Link8 structural element. The tendons are prestressed through the temperature reduction method.

16.4.1.2   Temperature Field Results

The key nodes of the arch rib and concrete abutment surface are selected for temperature–time history analysis. The distribution of section nodes is shown in Fig. 16.5, and the temperature–time history curve of each node is shown in Figs. 16.6 and 16.7, respectively. Figure 16.8 presents the temperature nephogram of the arch foot model.

As shown in Fig. 16.6, the cement hydration heated the core concrete rapidly, and the peak temperature of concrete occurred 12 h immediately after casting the concrete in the upper tubular. The upper arch rib's temperatures at points A, B, and C (refer to Fig. 16.5) are 48.7 °C, 43.3 °C, and 45.1 °C, respectively. The peak temperature of core concrete in the lower arch rib occurred 18 h after casting concrete in the lower tubular portion. The development of concrete temperature in the lower arch rib is similar to that of the upper rib. The lower arch rib's temperatures measured at points D, E, and F (refer to Fig. 16.5) are 48.8 °C, 42.9 °C, and 44.9 °C, respectively. One can see from Fig. 16.7 that after reaching the highest temperature, the concrete temperature decreases to the ambient temperature and the drop rate gradually decreases.

Concerning the temperature nephogram of the arch foot, Fig. 16.8 shows that the temperature followed the distribution principle of A > C > B and D > F > E. As shown, the temperature at the core concrete center was high and showed an

Fig. 16.5 Temperature measuring point arrangement

(a) A ~ C curve of the measuring point   (b) D ~ F curve of the measuring point

Fig. 16.6 Time history curve of temperature measuring points A–F of arch rib

obvious temperature gradient from the center to the edges. It is observed that the core concrete's temperature increases after completely pumping the core concrete. Under the temperature gradient, the temperature of arch foot concrete increases and reaches a peak value of 33.1 °C after 44 h of pouring the concrete. One can also see that the temperature of concrete abutment along the upper arch rib axis is high in the middle and low on the edges, while the temperature near the arch rib surface is low due to the large heat dissipation surfaces. Due to lower hydration heat, surface temperature near the main beam is found to be low.

(a) Points G ~ L

(b) Points M ~ P

(c) Points Q ~ U 、 G、 M

Fig. 16.7   Time history curve of G–U temperature at measuring point of arch foot
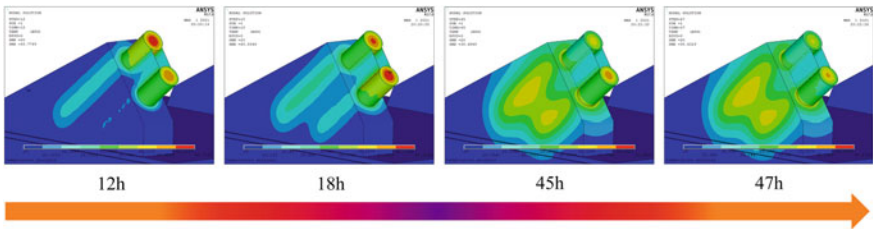
Fig. 16.8   Temperature nephogram of arch foot model in main time

16.4.2   Local Temperature Stress in CFST Arch Foot

As stated earlier, the CFSTAF's thermal stress was obtained from hydration heat by transforming the thermal analysis model into a structural analysis model. To verify the accuracy of the thermal stress analysis, thermal strain in the actual arch feet of the Liuxi River Bridge due to hydration generated heat of core concrete was measured

using *intelligent vibrating wire strain sensors.* The test arrangement of sensors at the bridge construction site is shown in Fig. 16.9. A comparison between numerically-predicted strain–time curves and corresponding experimental results is shown in Fig. 16.10.

Figure 16.10 shows that the predicted strain–time curve correlated well with the measured strain–time curves. The strain–time curves at points G and M are consistent with the measured values, and the relative error of peak strain is below 5%, indicating that the analytical model can simulate the concrete stress development in CFSTAF under hydration heat. Based on the temperature–time curve and thermal stress analysis results, the thermal stress-time curves for points G and M are obtained (see Fig. 16.11). The temperature stress-time curves of the abutment concrete are shown in Fig. 16.12. The main tensile stress nephogram of the abutment concrete is shown in Fig. 16.13.

(a) Pumping pipe concrete construction stage site   (b) Arrangement of steel string strain gages
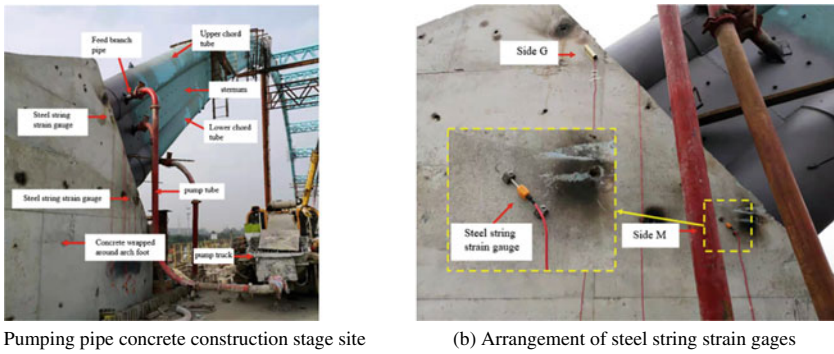
Fig. 16.9 Site construction, instrumentation and testing

Fig. 16.10 Comparison between measured and calculated strain time history curves
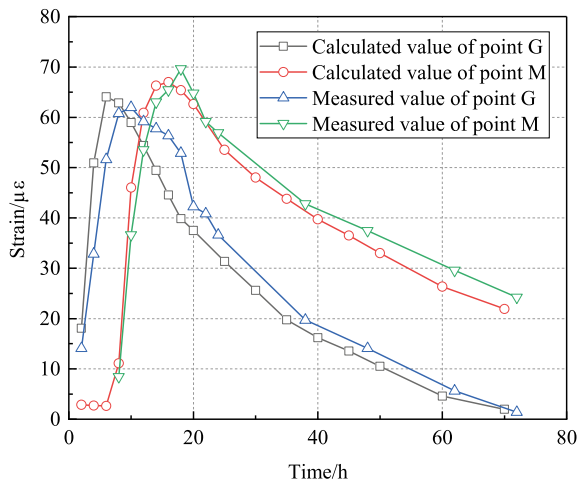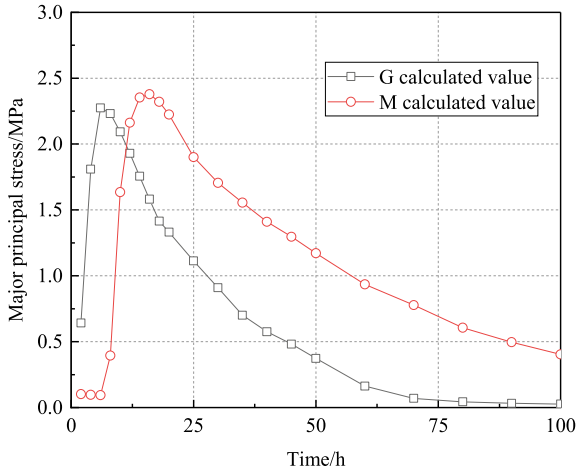
Fig. 16.11   Temperature stress-time curve of points G and M

(a) Points G ~ L

(b) Points M ~ P

(c) Points Q ~ U
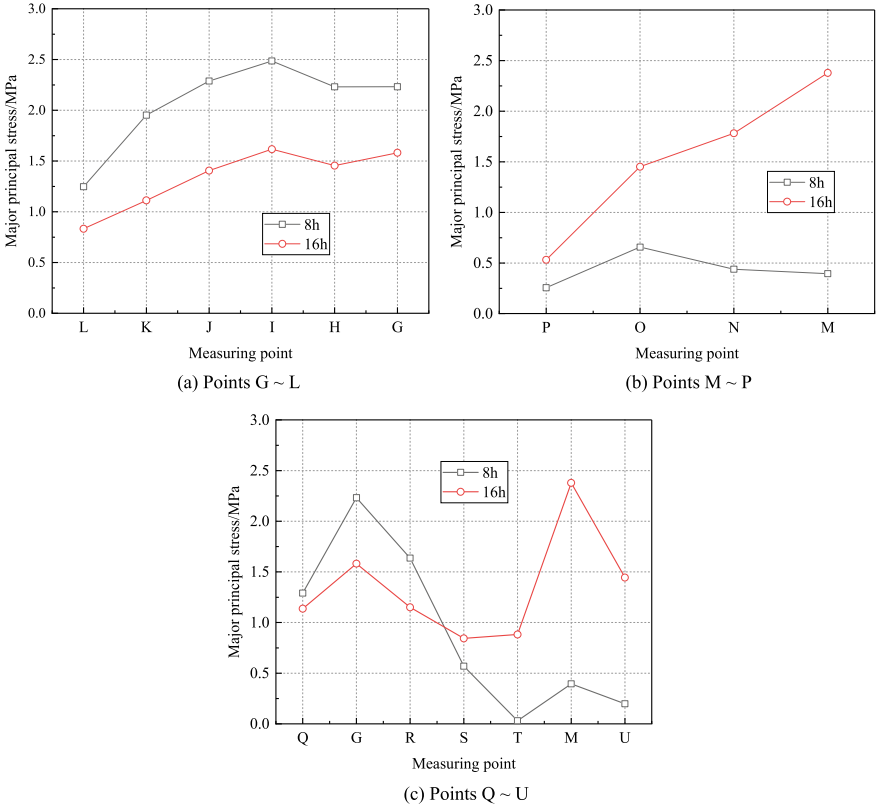
Fig. 16.12   Eight-hour and sixteen-hour S1 stress at each measuring point of the arch foot

(a) 8h main tensile stress   (b) 16h main tensile stress
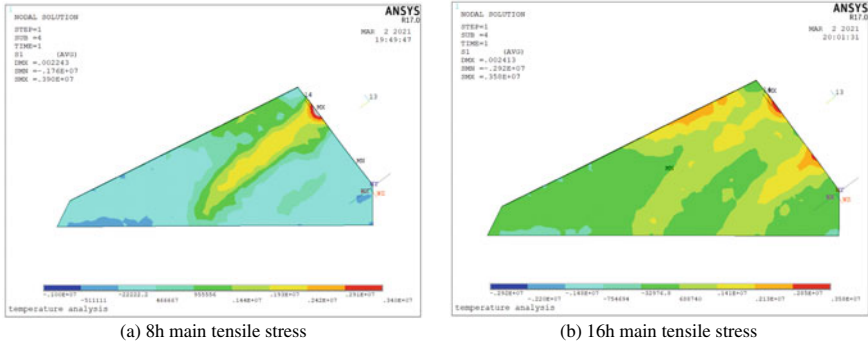
Fig. 16.13 Eight-hour and sixteen-hour S1 stress nephogram of concrete outside arch foot

As shown in Fig. 16.11, the hydration heat caused a significant temperature difference between the inner and outer surfaces of the arch foot. The thermal tensile stresses at points G and M increased with increasing the hydration heat in the upper arch rib processed. The maximum stress at point G was 2.2 MPa after 8 h of pouring the concrete, while the maximum stress at point M reached 2.41 MPa after 16 h of the concrete cast. Figure 16.12 shows that the tensile stress in abutment concrete is higher near the upper rib arch axis and that the tensile stress at point I after 8 h is 2.48 MPa. Also, results showed that the tensile stress at point G near the vault is 67% higher than at point L. In Fig. 16.13, the stress concentration occurs at the arch foot boundary parallel to the arch rib. Similar to the lateral surface, the abutment concrete's upper surface has a large tensile stress area. An explanation is the thermal expansion of the core concrete and the temperature difference. The large tensile stress in concrete abutment would inevitably cause a crack of the arch feet in the early construction stage.

In terms of reducing the risk of cracking in CFSTAF, it is critical to improve the concrete strength and eliminate the steel tubular expansion in early-age. Eliminating tubular expansion at the construction stage may be practical for preventing the cracking of concrete abutments. As the steel tubular expansion was determined by pumping pressure and hydration heat of the lately cast concrete, it is recommended to optimize the structural form of CSFTAF and fabricate core concrete with the surrounding concrete.

16.5 Conclusions

This paper focused on assessing the cracking performance of CFSTAF during the PC bridge construction stage. Midas Civil software was used to determine the internal forces at the CFSTAF, while ANSYS® FE software was employed to develop numerical models to analyze the temperature field and thermal stresses in the arch feet structure. Based on the temperature field and temperature stress analysis, the following conclusions can be drawn:

(1) The hydration heat of tubular core concrete generates a thermal expansion of the CFST arch rib that dominates the early-age cracking of the arch foot. The temperature at the center point A of the upper arch rib increased to 48.7 °C after 12 h, while the center point D at the lower arch rib reached a peak temperature of 48.8 °C after 18 h.
(2) The use of dumbbell-shaped CFST arch rib results in a lower heat dissipation coefficient of the steel tube surface in the region that creates a thermal insulation effect for the steel tube surface.
(3) A good correlation between numerical simulation results and field measured data was achieved with a peak strain error of less than 5%, which confirms the validity and reliability of the arch foot's proposed model.
(4) Hydration heat of the lately cast concrete determined the steel tubular portion expansion of the CFSTAF. Also, optimizing the CFSTAF's structural form and fabricating core concrete with the surrounding concrete is recommended.

References

Cao Z (2015) Construction dumbbell CFST arch bridge construction optimization and stress analysis. Changsha University of Science & Technology (in Chinese)

Chen BC, Wei JG, Zhou J, Liu JP (2017) Application of concrete-filled steel tube arch bridges in China: current status and prospects. Chin Civ Eng J 50(6):50–61. https://doi.org/10.15951/j.tmgcxb.2017.06.006

Deng FT (2016) The research of arch foot crack and control strategy of CFST tied arch bridge. Southeast University (in Chinese)

Du CJ, Liu GT (1994) Numerical procedure for thermal creep stress in mass concrete structures. Commun Numer Methods Eng 10(7):545–554. https://doi.org/10.1002/cnm.1640100706

Emborg M, Bernander S (1994) Assessment of risk of thermal cracking in hardening concrete. J Struct Eng 120(10):2893–2912. https://doi.org/10.1061/(asce)0733-9445(1994)120:10(2893)

GB 50010-2010 (2010) Code for design of concrete structures. (in Chinese)

GB 50017-2017 (2010) Standard for design of steel structures. (in Chinese)

GB50936-2014 (2014) Technical code for concrete-filled steel tube structures. (in Chinese)

He SH, Li QF, Yang G, Zhou X, Mosallam A (2022) Experimental study on flexural performance of HSS-UHPC composite beams with perfobond strip connectors. J Struct Eng (ASCE) 148(6):04022064. https://doi.org/10.1061/(ASCE)ST.1943-541X.0003366

Li, Zhou, Liu (2009) Simulation calculation research of long span CFST arch bridge based on optimization algorithm. In: Second international conference on intelligent computation technology and automation. IEEE Comput Soc

Lin CJ, Zheng JL, Qin R (2007) Finite element analysis of hydration heat temperature distribution of dumbbell shaped concrete filled steel tube section. J China Foreign Highw 04:125–127 (in Chinese)

Lin CJ, Zheng JL, Huang HD (2009) Experimental study on the temperature field by hydration heat of circular CFST arch bridge. Concrete 10:13–15 (in Chinese)

Lin CJ, Chen JH, Gu Z, Fu GE (2014) An investigation of diseases of concrete filled steel tubular arch bridge in Guangxi. Appl Mech Mater 501–504:1233–1237. https://doi.org/10.4028/www.scientific.net/AMM.501-504.1233

Lin CJ, Lin CW, Ou W (2011) Experimental study on hydration heat temperature of new dumbbell-shaped concrete filled steel tubular arch rib during construction. Concrete (08):138–139+143. (in Chinese)

Liu GG, Liu Q, Pan Z, Zhu ZJ, Nie LY (2013) Analysis of the stress characteristics of the arch abutment joint of the rigid tied arch bridge with underpass. Sci Technol Eng 12:3327–3330 (in Chinese)

Ma YL, Mao YN, Liu SZ, Ye D (2011) Spatial stress analysis of arch foot of concrete filled steel tubular arch bridge. Railw Stand Des 11:49–53. https://doi.org/10.13238/j.issn.1004-2954.2011.11.017

Nakamura S (2000) New structural forms for steel/concrete composite bridges. Struct Eng Int 10(1):45–50. https://doi.org/10.2749/101686600780620955

Sun JY, Xie JB (2019) Thermal stress during hardening of concrete in steel tube arch based on equivalent age. J Tongji University (natl Sci) 06:755–763 (in Chinese)

Yang L (2009) Spatial stress analysis for complex-shaped bridges based on FEM. IEEE. https://doi.org/10.1109/ICEC.2009.20

Zhang J, Qi K, Hou DW (2009) Calculation of temperature field of early age concrete based on adiabatic temperature rise test. Eng Mech 08:155–160 (in Chinese)

Zheng JL, Wang JJ (2018) Concrete-filled steel tube arch bridges in China. Engineering 01:143–155 (in Chinese)

Zhou SX, Li W (2013) Analysis on common diseases of concrete filled steel tube arch bridge. J Chongqing Jiaotong University (Natl Sci) (S1):738–741+826. (in Chinese)

Zhu BF (1999) Temperature stress and temperature control of mass concrete. China Electric Power Press. (in Chinese)

Zhu BF (2014) Thermal stresses and temperature control of mass concrete. Tsinghua University Press. (in Chinese)

Chapter 17
Torsion Strength of Concrete Beams with Steel Fibers, Lightweight, or FRP: Data Driven Code Appraisal

Ahmed Awad, Jawad Ahmed, Ahmed F. Deifalla [ID], Maged Tawfik, and Amr El-Said

Abstract Despite extensive research efforts directed toward the shear and torsional behavior of concrete elements, torsion strength remains an unexplored area. Numerous new materials are being used in construction as a result of advances in concrete technology. The use of lightweight concrete, steel-fiber reinforced concrete, and FRP-reinforced concrete are all kinds of advancements. The objective of the current work is to enhance torsion strength prediction for these three aspects. A summary of a series of power equation models for torsion strength based on a massive experimental database of 346 beams tested under torsion is outlined. The model validation is discussed. The developed models are accurate while remaining simple for design purposes.

Keywords Torsion · Lightweight concrete · FRP reinforced concrete · And Steel fibered concrete

A. Awad
Faculty of Engineering, October University for Modern Sciences and Arts, Giza, Egypt
e-mail: Amosad@msa.edu.eg

J. Ahmed
Swedish College of Engineering, Wah Cant, Pakistan
e-mail: Jawadcivil13@scetwah.edu.pk

A. F. Deifalla (✉)
Future University in Egypt, New Cairo, Egypt
e-mail: Ahmed.deifalla@fue.edu.eg

M. Tawfik
Department of Civil Engineering, The Higher Institute of Engineering, El Shrouk, Cairo, Egypt
e-mail: m.nashaat@sha.edu.eg

17.1 Introduction

A reliable design necessitates a thorough understanding of the characteristics of concrete components subjected to torsion (ACI-445 2013). Recently, the ACI examined torsion of all cases, including high-strength concrete (HSC), prestressed concrete (PC), and normal weight concrete (NWC) (ACI-445 2013). However, steel fiber reinforced concrete (SFRC), concrete with Fiber reinforced polymer (FRP), and lightweight concrete (LWC) were not discussed. Researchers all over the world are investigating the design and behavior of elements subjected to shear, torsion, and punching shear (ACI 213R-03 2014; Muttoni 2018; Kuchma et al. 2019; Deifalla et al. 2021; Deifalla 2020a, b, 2022, 2023; Badra and Deifalla 2022; Graybeal 2014; Greene and Graybeal 2013, 2015). Especially, torsion design and analysis of NWC beams require simplified, accurate, and unified approaches (Deifalla and Ghobarah 2014; Chalioris 2008; Chalioris and Karayannis 2009; Deifalla 2015; Deifalla et al. 2014; Deifalla et al. 2015; Hassan and Deifalla 2016; Rahal 2013; Deifalla 2020, 2021; ACI-318-19, ACI Committee 318 2019; prEC2: PT1prEN 1992-1-1/2018-04 2018). Although combined loading is the most common situation, most research studies have focused on pure torsion to distinguish the torsion effect (ACI-445 2013; Deifalla and Ghobarah 2014; Chalioris 2008; Chalioris and Karayannis 2009; Deifalla 2015; Deifalla et al. 2014; Deifalla et al. 2015; Hassan and Deifalla 2016; Rahal 2013; Deifalla 2021; Deifalla 2020c; ACI-318-19, ACI Committee 318 2019; prEC2: PT1prEN 1992-1-1/2018-04 2018). Very little guidance is offered by Design Codes and guides regarding the design of LWC, SFRC, and FRP reinforced beams (ACI 213R-03 2014; MC 2010; CSA 2004; EC2 2004; JSCE 2007; Nawaz et al. 2019; Khaloo and Sharifian 2005a).

For over two millenniums, the popularity of Lightweight concrete (LWC) in construction is growing (ACI 213R-03 2014). It has several advantages over NWC, including better insulation, and lower weight. On contrary, it had more cracking due to lower concrete stiffness. However, the experimentally observed behavior of LWC was found to be like that of the NWC (ACI 213R-03 2014). Recently, LWC is implemented in construction applications as it is considered a good alternative for NWC. These applications are as follows: (1) the walls whether curtain or structural; (2) marine structures or offshore; (3) folded plates and shell roofs; (4) bridge girders and decks; (5) beams and slabs that are precast, pre-tensioned, or post-tensioned; and (6) High-rise buildings elements walls, columns, and floors. LWC is helpful for the optimization of the reinforced concrete (RC) structures' construction process, self-weight, and member sizes (ACI 213R-03 2014). Using the LWC is better than NWC in achieving functional and architectural design (ACI 213R-03 2014). Thus, many extraordinary structures made of LWC are spread all around the world (ACI 213R-03 2014). The ACI Guides do not offer any recommendations for the torsion design of beams for LWC; instead, it directs practitioners to the ACI design codes, which are

primarily developed for NWC (ACI 213R-03 2014). Although LWC design guidelines are generally conservative, the design's consistency and economy are questionable. Since the economic factor governs the world directions towards all life aspects including RC structures.

With the economical aspect of design, thus, reducing safety factors, and improving the accuracy of the design models is the researcher's goal (ACI 213R-03 2014). Worldwide, FRP bars are noncorrosive; thus, used in many projects (ACI-445 2013; Muttoni 2018). The available design codes and guidelines, except the Canadian Standards Association (CSA), include detailed provisions only for shear and bending design of beams. While CSA includes torsion design. Thus, an objective for researchers is to provide practitioners with reliable design methods in torsion (Muttoni 2018). The design codes torsion provisions are lacking due to the following reasons: (1) shear and bending are more frequent compared to torsion; (2) if the applied torque is less than cracking torque, it can be neglected, and (3) Shear and bending are investigated much more than that for torsion. For the economy and safety of RC members. Since the complete comprehension of the torsion design is of the utmost importance, thus, it is still under investigation.

The design of FRP-RC beams under shear is attracting the core of research studies; thus, it is beneficial to examine the torsion behavior versus the shear behavior. Although shear and torsion strength in beams are formed by a set of diagonal and orthogonal internal forces, one of which is in compression and the other in tension, there are several distinctions between the two exist as follows: (1) Parallel pattern propagation for the shear cracks, while spiral pattern propagation for torsion cracks; thus, shear cracks spread in the same direction while torsion cracks spread in two opposite directions; (2) the torque strain varies in the three dimensions and it is non-uniform, while shear force strain varies in the two-dimension plane and it is uniform as well as perpendicular to the plane of applied shear; (3) mostly uniform stresses are developed due to shear forces, while in torsion cause bending on beam sides and thus the stress varies both horizontally and vertically across the cross-section. (4) the equivalent hollow tube thickness, which is resisting the applied torsion. In addition, it varies with the applied load. This is like the compression zone effective thickness in the case of bending moment; and (5) In flanged beams, the web mainly carries the shear forces, while the torque moments are carried by the flange and the web. The addition of steel fibers, which are available in various shapes and cross-sections, to the concrete mix leads to the creation of FRC. The characteristics are enhanced by the addition of steel fiber. Many researchers have extensively studied the behavior of this composite material. This current study aims at improving the torsion strength prediction for these three problems. A summary of a series of power equation models for torsion strength based on a massive experimental database of 346 beams tested under torsion is outlined. The model validation is discussed. Concluding remarks are outlined.

17.2   Model Development

17.2.1   Lightweight Concrete

Based on the existing previous investigations regarding the cracking torque, the following form is proposed as follows:

$$T_{cr} = c_1 \left(\frac{1 + 0.004d}{2} \right)^{c_2} \left(\frac{3\gamma_c}{64} \right)^{c_3} F^{c_4} (f_c')^{c_5} \left(\frac{A_c^2}{P_c} \right)^{c_6} \tag{17.1}$$

Thus, using the multi variable nonlinear regression using the gathered database, the following formula is proposed such that:

$$T_{cr} = 0.38 \left(\frac{1 + 0.004d}{2} \right)^{-0.5} \left(\frac{3\gamma_c}{64} \right)^{1.07} F^{0.034} (f_c')^{0.36} \left(\frac{A_c^2}{P_c} \right)^{1.14} \tag{17.2}$$

where d is the distance between the extreme compression fibers to the centroid of longitudinal tensile reinforcements (mm).

A_c is the total area of the concrete cross-section (mm^2).

p_c is the perimeter of the concrete section (mm).

γ_c is the unit weight of concrete (kN/m^3).

f_c' is the cylinder concrete compressive strength (MPa).

F is the fiber index.

17.2.2   Steel Fibered Concrete

Using multivariable nonlinear regression, the strength predictions of the strength of beams under torsion (T) for SFRC beams, can be such that:

$$T = \begin{cases} 0.19x^2y\sqrt{f_{cu}}(1 + 0.04F) & \text{for rectagular cross section} \\ 0.1D^3\sqrt{f_{cu}}(1 + 0.08F) & \text{for circular cross section} \\ 0.2\sum x^2y\sqrt{f_{cu}}(1 + 0.15F) & \text{for flanged cross section} \end{cases} \tag{17.3}$$

While for SFRC beams, the torsional strength (T) can be such that:

$$T = 0.2 \sum x^2 y \sqrt{f_{cu}} + 0.13F \frac{x_o y_o}{x_o + y_o} xy \sqrt{f_{cu}} + kA_s f_{ty} \frac{x_1 y_1}{s} \tag{17.4}$$

where x is the cross-smaller section's dimension.

x_0 is the smaller center-to-center dimension of the thin wall tube analogy, which is roughly equal to (5/6)x.

x_1 is the smaller dimension of the steel stirrup, which is taken approximately as 0.9 x.

y is the cross-bigger section's dimension.

y_0 is the bigger center-to-center dimension of the thin wall tube analogy, which is roughly equal to (5/6)y.

y_1 is the bigger dimension of the steel stirrup, which is roughly equal to 0.9 y.

A_s is the cross-sectional area of the stirrup.

f_{ty} is the yield strength of transverse reinforcement.

f_{cu} is the cubic compressive strength of the concrete.

F is the fiber index.

17.2.3 FRP Reinforced Concrete Beams

For torsion, Deifalla adapted the power-law equation, which was first proposed by Rahal with respect to the beams with Glass FRP. In addition, experimental investigations by Belarbi and Hsu were implemented. Thus, implementing the multi-variable non-linear regression, a model for the ultimate and cracking torsion was proposed. Thus, to capture nonuniform strain and stress distribution across the stirrups and the cross section (Deifalla 2022; Deifalla et al. 2015; Noshy et al. 2017). For cracking torque, all effective variables were included as follows: the concrete compression stress (f'_c), perimeter of cross section (p_c), area of cross section (A_c), such that:

$$T = \begin{cases} 0.19\left(A_c^2/p_c\right)^{0.9}\left(f'_c\right)^{1.15} \text{ for rectangular cross section} \\ 0.09\left(A_c^2/p_c\right)^{0.9}\left(f'_c\right)^{1.15} \text{ for rectangular cross section} \end{cases} \qquad (17.5)$$

While for ultimate torsional moment, Nonlinear Multi-variable Regression was employed with the inclusion of all effective variables as follows: longitudinal reinforcement forces ($f_{Fu}A_l$), transversal reinforcement ratio $\left(\frac{f_y A_t}{s} + \frac{f_{Fu}A_t}{s}\right)$, cross section perimeter (p_c), the concrete compression stress (f'_c), and area of cross section A_c; such that:

$$T = 0.16(f_{c'})^{0.67}A_c^{1.3}\left(\frac{f_y A_t}{s} + \frac{f_{fu}A_t}{s}\right)^{0.1}\left(f_{fu}A_l\right)^{0.12} \leq 0.34 A_{oh} t_w f'_c \qquad (17.6)$$

where A_{oh} is the enclosed area within the outermost closed stirrup's centerline (mm^2).

A_l is the torsion-resistant longitudinal reinforcement (mm^2).

A_t is the transversal reinforcement area that is bearing the torsion (mm^2).

s is the spacing between stirrups.

f_{fu} is the FRP bar's maximum tensile strength (MPa).

f_y is the yield strength of the longitudinal steel reinforcements (MPa).

t_w is the idealized hollow section's wall thickness, which is supposed to be no larger than the ratio of A_{oh}/ph or two times the minimum c (mm).

17.3   Model Validation

17.3.1   Lightweight

Table 17.1 shows the details and test results for the experimental LWC beams, while Table 17.2 and Fig. 17.1 show the ratio between the experimental torsional strength and that calculated using previous methods as well as the proposed model (PM1). For the cracking torque, the proposed model PM1 performance is more consistent and accurate but simple for design purposes compared to existing design codes. In addition, the coefficient of variation is 29% for the proposed model, while the existing model's coefficient of variation is 33%, 36%, and 29% for the ACI, CSA, and EC2, respectively. Moreover, the average values of the ratio between the measured torsional strength and that calculated using the ACI, the CSA, and the EC2, and the proposed model are 1.47, 1.32, 0.88, and 1.04, respectively. For the ultimate torque, the proposed model performance is more accurate and consistent but simple for design purposes compared to existing design codes. In addition, the proposed model coefficient of variation is 23%, while the existing model's coefficient of variation is 31%, 21%, and 25% for the ACI, CSA, and EC2, respectively. Moreover, the average values of the ratio between the measured strength and that calculated strength using the ACI, the CSA, and the EC2, and the proposed model are 1.30, 0.96, 1.00, and 1.21, respectively.

17.3.2   Steel Fibered Concrete

Table 17.3 shows the details and test results for the experimental steel-fibered concrete beams, while Table 17.4 and Fig. 17.2 show the ratio between the experimental torsional strength and that calculated using Nayraan and Karim model (NKPT) and the proposed models (PM2), and (PM3). The proposed model PM2 based on the Nayraan model is more accurate and consistent than the proposed model PM3 based on the ACI. The proposed model PM2 coefficient of variation is

Table 17.1 Details and test results for the experimental LWC beams database

#	ID	Cross section (mm)	Length (mm)	γc kN/m^3	f_c' MPa	f_c' MPa	T_{cr} kN m	T_u kN m
Nawaz et al. (2019)	LC-1–7	R200 × 100	700	15.45	6.97	1.21	0.71	0.71
	LC-1–14			15.45	7.17	1.21	0.72	0.72
	LC-1–42			15.35	8.18	1.31	0.75	0.75
	LC-1–90			15.27	8.38	1.31	0.77	0.77
	NC-2–7			16.46	12.22	1.62	0.87	0.87
	NC-2–14			16.51	15.25	1.72	0.97	0.97
	NC-2–21			16.36	16.67	1.82	1.00	1.00
	NC-2–42			16.31	18.69	1.92	1.03	1.03
	NC-3–7			15.96	11.62	1.52	0.85	0.85
	NC-3–42			15.66	17.78	1.92	1.02	1.02
	NC-4–21			15.15	14.75	1.72	0.96	0.96
	NC-4–42			15.20	16.67	1.82	0.99	0.99
	HC-5–7			18.18	48.58	3.13	1.65	1.65
	HC-5–14			18.08	50.00	3.23	1.67	1.67
	HC-5–21			18.13	55.95	3.33	1.85	1.85
	HC-5–42			18.08	59.09	3.43	1.79	1.79
	HC-6–14			18.08	57.17	3.43	1.91	1.91
	HC-6–21			18.03	60.60	3.54	1.84	1.84
	HC-6–28			18.08	66.36	3.64	2.09	2.09
	HC-7–3			19.19	27.67	2.42	1.49	1.49
	HC-7–7			19.24	42.52	2.93	1.58	1.58
	HC-7–21			19.19	58.58	3.43	1.92	1.92
	HC-7–42			19.17	66.46	3.74	2.09	2.09
	HC-8–7			17.13	21.21	2.12	1.26	1.26
	HC-8–14			17.07	26.56	2.32	1.28	1.28
	HC-8–42			17.07	36.66	2.73	1.49	1.49
	HC-9–7			20.72	52.82	3.33	1.74	1.74
	HC-9–14			20.63	68.28	3.74	1.92	1.92
	HC-9–28			20.63	78.28	4.04	2.29	2.29
	HC-10–7			20.36	48.58	3.13	1.72	1.72
	HC-10–28			20.30	74.44	3.94	2.16	2.16
	HC-10–42			20.30	82.21	4.14	2.16	2.16
Khaloo and Sharifian (2005a)	LC1	R200 × 100	700	17.85	9.09	1.41	0.73	0.73
	LC1-0.5–32			18.11	9.09	1.41	0.78	0.78
	LC1-1.0–32			18.37	9.09	1.41	0.81	0.81

(continued)

Table 17.1 (continued)

#	ID	Cross section (mm)	Length (mm)	γc kN/m^3	f_c' MPa	f_c' MPa	T_{cr} kN m	T_u kN m
	LC1-1.5–32			18.63	9.09	1.41	0.86	0.86
	LC1-2.0–32			18.90	9.09	1.41	0.92	0.92
	LC1-3.0–32			19.42	9.09	1.41	0.92	0.92
	LC2			19.20	12.12	1.62	0.88	0.88
	LC2-0.5–25			19.38	12.12	1.62	0.87	0.87
	LC2-0.5–32			19.38	12.12	1.62	0.91	0.91
	LC2-1.0–25			19.68	12.12	1.62	0.97	0.97
	LC2-1.0–32			19.68	12.12	1.62	1.01	1.01
	LC2-1.5–25			19.98	12.12	1.62	1.11	1.11
	LC2-1.5–32			19.98	12.12	1.62	1.17	1.17
	LC2-2.0–25			20.27	12.12	1.62	1.22	1.22
	LC2-2.0–32			20.27	12.12	1.62	1.30	1.30
	LC2-3.0–25			20.87	12.12	1.62	1.25	1.25
	LC2-3.0–32			20.87	12.12	1.62	1.33	1.33
	NC			17.60	30.30	2.53	1.44	1.44
	NC-0.5–32			17.77	30.30	2.53	1.48	1.48
Khaloo and Sharifian (2005b)	NC-1.0–32	R200 × 100	700	17.95	30.30	2.53	1.62	1.62
	NC-1.5–32			18.13	30.30	2.53	1.84	1.84
	NC-2.0–32			18.30	30.30	2.53	2.26	2.26
	NC-3.0–32			18.64	30.30	2.53	2.26	2.26
	HC			20.06	61.61	3.54	1.93	1.93
	HC-0.5–25			20.28	61.61	3.54	1.94	1.94
	HC-0.5–32			20.28	61.61	3.54	2.05	2.05
	HC-0.5–50			20.40	61.61	3.54	2.12	2.12
	HC-1.0–25			20.50	61.61	3.54	2.13	2.13
	HC-1.0–32			20.50	61.61	3.54	2.34	2.34
	HC-1.0–50			20.62	61.61	3.54	2.68	2.68
	HC-1.5–25			20.73	61.61	3.54	2.30	2.30
	HC-1.5–32			20.73	61.61	3.54	2.76	2.76
	HC-2.0–25			20.95	61.61	3.54	2.69	2.69
	HC-2.0–32			20.95	61.61	3.54	3.02	3.02
	HC-3.0–25			21.38	61.61	3.54	2.64	2.64
	HC-3.0–32			21.38	61.61	3.54	2.98	2.98
Yap et al. (2016)	OPSC-0	R100 × 100	500	18.48	34.24	3.33	0.00	0.00
	OPSC-25			18.91	39.69	4.34	0.22	0.23

(continued)

Table 17.1 (continued)

#	ID	Cross section (mm)	Length (mm)	γc kN/m³	f'_c MPa	f'_c MPa	T_{cr} kN m	T_u kN m
	OPSC-50			19.33	41.61	5.45	0.25	0.26
	OPSC-75			19.78	46.36	6.77	0.29	0.30
	OPSC-100			20.22	47.77	8.28	0.29	0.31
	OPSC-0	R200 × 150	1500	19.90	33.13	2.83	5.54	5.56
	OPSFRC-55			20.89	34.74	3.64	7.35	7.43
	OPSFRC-65			20.61	35.86	3.94	7.85	7.96
	OPSFRC-80			20.91	37.37	3.94	8.67	8.69
Yap et al. (2015)	LR1	R300 × 150	2000	18.69	26.77	2.32	3.27	8.30
	LR2			18.69	29.29	2.42	4.36	9.27
	LR3			18.69	31.31	2.53	5.98	11.79
	LT1	T300 × 400/150 × 100		18.69	29.80	2.42	5.25	14.62
	LT2			18.69	30.81	2.53	8.36	18.82

Table 17.2 Model validation with respect to Lightweight concrete beams

	Statistical measure	ACI 19	CSA	EC2	PM1
Cracking torsion moment	Mean	1.47	1.32	0.88	1.04
	C.O.V (%)	33	36	29	29
Ultimate torsion moment	Mean	1.30	0.96	1.00	1.21
	C.O.V (%)	31	21	25	23

17%, while the existing model NKPT and the proposed model PM3 coefficient of variation are 22 and 19%. The average values of the ratio between the experimental torsional strength and that calculated strength using the existing NKPT model, and the proposed models PM2, and PM3 are 1.21, 1.01, and 1.02 respectively.

17.3.3   FRP Reinforced Concrete Beams

Table 17.5 shows the details and test results for the experimental FRP reinforced concrete beams, while Table 17.6 and Fig. 17.3 show the ratio between the experimental torsional strength and that calculated using the previous Hasan and Deifalla model (HD), the CSA, and the proposed model (PM4). For the cracking torque, the proposed model performance is more consistent and accurate but simple for design purposes compared to existing models. In addition, the coefficient of variation is 24% for the proposed model, while the existing model's coefficient of variation is
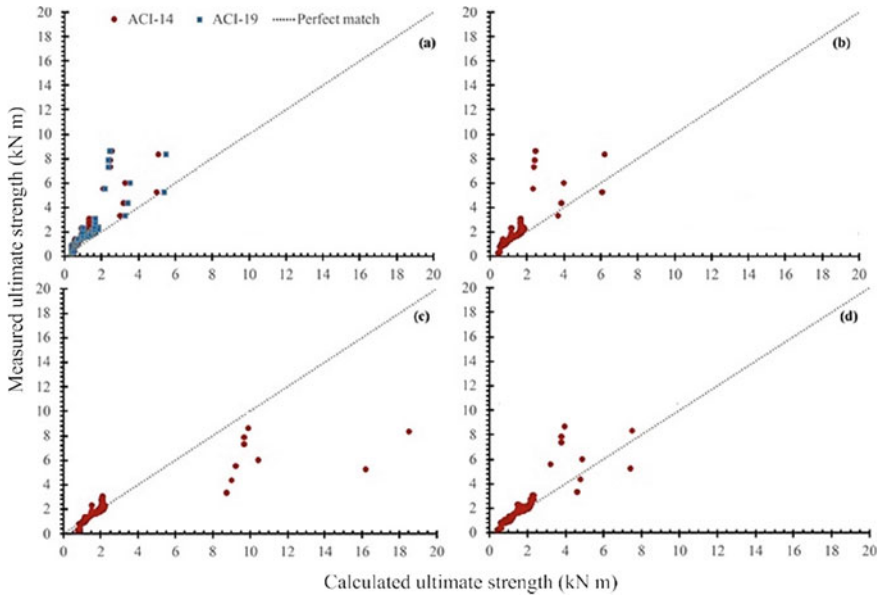
Fig. 17.1 The relation between experimental versus calculated ultimate torsional strength using: **a** the ACI, **b** CSA, **c** EC2, **d** PM1

63% and 37% for the CSA, and HD, respectively. Moreover, the average values of the ratio between the measured torsional strength and that calculated using the CSA, the HD model, and the proposed model PM4 are 1.33, 1.2, and 0.95, respectively. For the ultimate torque, the proposed model PM4 performance is more accurate and consistent but simple for design purposes compared to existing design codes. In addition, the proposed model coefficient of variation is 36%, while the existing model's coefficient of variation is 63% and 47% for the CSA, and HD, respectively. Moreover, the average values of the ratio between the measured torsional ultimate strength and that calculated using the CSA, the HD model, and the proposed model PM4 are 1.33, 1.65, and 1.24, respectively.

17.4   Conclusions

Three massive experimental databases of a total of 346 beams were tested under torsional moments. Four models were proposed for predicting the torsional strength of lightweight concrete beams, steel fiber reinforced concrete beams, and beams with FPR reinforcements, which is based on the database and using Multi-linear regression. The present work can reasonably lead to the following conclusions:

Table 17.3 Details and test results for the experimental steel-fibered concrete beams database

References	Cross section (mm)	ρ_f (%)	f_{cu} (MPa)	f_{ly} (MPa)	ρ_l (%)	f_{ty} (MPa)	ρ_t (%)	Tu (kNm)
Noshy et al. (2017)	R100 × 155	0.75	20.5	390	0.73	–	–	1.3
	R100 × 155	0.75	20.5	390	0.73	371	1.14	1.75
	R100 × 155	1.25	21.4	375	0.73	–	–	1.32
	R100 × 155	1.25	21.4	390	0.73	–	–	1.37
	R100 × 155	1.25	21.4	450	1.3	–	–	1.38
	R100 × 155	1.25	21.4	390	0.73	371	0.82	1.91
	R100 × 155	1.25	21.4	390	0.73	371	1.07	2.03
	R100 × 155	1.75	21.6	390	0.73	–	–	1.43
	R100 × 155	1.75	21.6	390	0.73	371	1.14	2.27
Sharma (1989)	R152 × 310	0.5	40.2	350	1.26	400	1.1	13.95
	R152 × 310	1	40.2	350	1.26	400	1.1	15.67
Kaushik and Sasturkar (1989)	R125 × 300	0.5	24.2	400	1.1	400	2.34	7.5
	R125 × 300	1	26.6	400	1.1	400	2.34	9
	R125 × 300	1.5	25.5	400	1.1	400	2.34	8.5
Al-Ausi et al. (1989)	R85 × 178	1.34	43.1	314	1.35	–	–	2.65
	R85 × 178	1.91	42.3	310	0.77	–	–	2.63
	R85 × 178	0.9	42.3	314	1.35	368	0.45	2.8
	R85 × 178	1.34	41.8	314	1.35	–	–	2.43
	R85 × 178	1.86	41.4	368	0.25	–	–	2.31
	R85 × 178	0.59	51.3	310	0.77	310	0.77	2.74
	R85 × 178	0.82	49.1	310	0.77	310	0.54	2.56
	R85 × 178	1.09	46.1	310	0.77	368	0.25	2.6
	R85 × 178	1.16	48.6	310	0.77	368	0.18	2.76
	R85 × 178	0.52	48.6	368	0.25	310	1.34	2.18
	R85 × 178	1.11	46.1	368	0.25	310	0.77	2.18
	R85 × 178	1.42	44.9	368	0.25	368	0.45	2.67
	R85 × 178	1.61	47.5	368	0.25	368	0.25	2.63
	R85 × 178	0.84	49.1	339	0.48	310	1.34	2.74
	R85 × 178	1.59	48.4	339	0.48	–	–	2.46
	R85 × 178	0.95	48.2	310	1.15	–	–	2.76
	R85 × 85	1.06	48.2	310	1.61	–	–	1.02
	R85 × 145	1.42	44.9	310	0.94	–	–	1.83
	R300 × 300	0.5	25.8	380	0.7	380	0.79	27.34
	R300 × 300	1	21.4	380	0.7	380	0.79	29.01

Table 17.3 (continued)

References	Cross section (mm)	ρ_f (%)	f_{cu} (MPa)	f_{ly} (MPa)	ρ_l (%)	f_{ty} (MPa)	ρ_t (%)	Tu (kNm)
Narayanan and Kareem-Palanjian (1986)	R300 × 300	1.5	28	380	0.7	380	0.79	34.67
	R300 × 300	1	21.4	380	1.05	380	1.18	36.46
	R300 × 300	1	21.4	380	1.4	380	1.57	40.86
Mansur et al. (1989)	R100 × 200	0.6	31.2	250	1.57	250	0	1.41
	R100 × 200	1.2	40.1	250	1.57	250	0	1.74
	R100 × 200	0.6	38.9	250	1.57	250	0.35	2.29
	R100 × 200	1.2	35.6	250	1.57	250	0.35	2.84
	R100 × 200	0.3	40.1	500	1.01	500	1.68	5.56
El-Niema (1993)	R100 × 200	0.6	41.1	500	1.01	500	1.68	5.69
	R100 × 200	0.9	42	500	1.01	500	1.68	5.73
	R100 × 200	1.2	43.3	500	1.01	500	1.68	5.82
	R100 × 200	0.3	41.3	500	1.57	500	0.85	4.11
	R100 × 200	0.6	42.2	500	1.57	500	0.85	4.19
	R100 × 200	0.9	43.4	500	1.57	500	0.85	4.23
	R100 × 200	1.2	44.1	500	1.57	500	0.85	4.23
	R100 × 200	0.3	41.5	500	0.57	500	1.51	3.85
	R100 × 200	0.6	42.8	500	0.57	500	1.51	3.93
	R100 × 200	0.9	43.1	500	0.57	500	1.51	3.98
	R100 × 200	1.2	43.9	500	0.57	500	1.51	4.02
	R100 × 200	0.3	35.2	500	1.57	500	0.02	2.01
Rao and Rama Seshu (2005)	R100 × 200	0.6	37	500	1.57	500	0.02	2.27
	R100 × 200	0.9	37.7	500	1.57	500	0.02	2.61
	R100 × 200	1.2	38.4	500	1.57	500	0.02	2.82
	R100 × 200	0.3	33.9	500	0.14	500	2.51	1.75
	R100 × 200	0.6	34.4	500	0.14	500	2.51	2.31
	R100 × 200	0.9	35	500	0.14	500	2.51	2.57
	R100 × 200	1.2	35.3	500	0.14	500	2.51	2.69
Rao and Seshu (2006)	R100 × 200	1	17	415	1.57	–	–	2.41
	R100 × 200	3	16.4	415	1.57	–	–	2.73
	R100 × 200	1	19	415	1.57	344	0.75	2.73

Table 17.3 (continued)

References	Cross section (mm)	ρ_f (%)	f_{cu} (MPa)	f_{ly} (MPa)	ρ_l (%)	f_{ty} (MPa)	ρ_t (%)	T_u (kNm)
	R100 × 200	3	16.9	415	1.57	344	0.75	3.15
Chalioris and Karayannis (2009b)	R100 × 200	0.3	51	432	1.57	432	1.51	6.67
	R100 × 200	0.6	51.8	432	1.57	432	1.51	6.76
	R100 × 200	0.9	52.5	432	1.57	432	1.51	6.84
	R100 × 200	1.2	53.9	432	1.57	432	1.51	6.93
	R100 × 200	0.3	51.1	432	1.57	432	0.8	5.22
	R100 × 200	0.6	52.1	432	1.57	432	0.8	5.3
	R100 × 200	0.9	53.4	432	1.57	432	0.8	5.39
	R100 × 200	1.2	54.1	432	1.57	432	0.8	5.47
	R100 × 200	0.3	52.6	432	0.57	432	1.51	5.77
	R100 × 200	0.6	53.2	432	0.57	432	1.51	5.82
	R100 × 200	0.9	54.1	432	0.57	432	1.51	5.9
	R100 × 200	1.2	55.5	432	0.57	432	1.51	5.99
Rao et al. (2010)	R150 × 200	0.3	33.4	460	0.67	460	0.55	4.58
	R150 × 200	0.6	31.3	460	0.67	460	0.55	5.68
	R150 × 200	0.3	31	460	0.67	460	0.55	4.94
	R150 × 200	0.6	30.9	460	0.67	460	0.55	5.87
	R150 × 200	0.3	32.7	460	0.67	460	0.55	4.92
	R150 × 200	0.6	29.5	460	0.67	460	0.55	5.88
	R150 × 200	0.3	31.9	460	0.67	460	0.55	4.85
	R150 × 200	0.6	30	460	0.67	460	0.55	5.49
	R150 × 200	0.3	31.7	460	1.51	460	0.55	6.01
	R150 × 200	0.3	31.6	460	1.51	460	0.55	6.25

Where ρ_f is the volume ratio of fibers
ρ_l is the longitudinal steel reinforcement ratio
ρ_t is the transversal steel reinforcement ratio
f_{ly} is The yield strength of longitudinal steel reinforcing bars
f_{ty} is The yield strength of transversal steel reinforcement

Table 17.4 Model validation with respect to steel fibered concrete beams

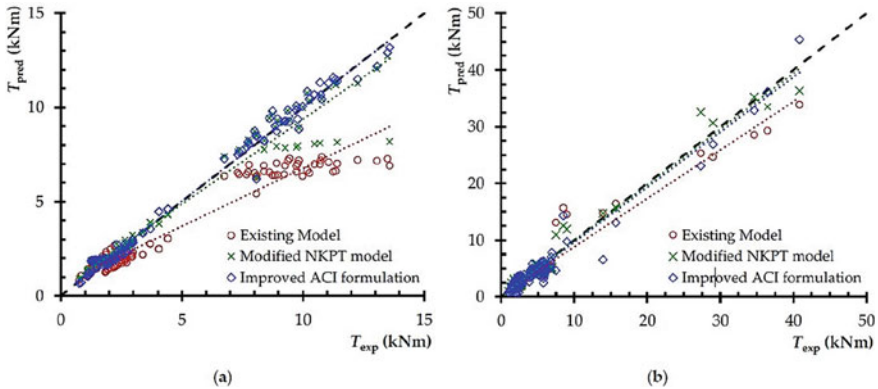|	Statistical measure	Existing model (NKPT)	PM2	PM3
Ultimate torsion moment	Mean	1.21	1.01	1.02
	C.O.V (%)	22	17	19

Fig. 17.2 Comparison of calculated and experimental ultimate torsion strengths for **a** L and T-beams and **b** R-beams

1. There is an absence of consensus among code provisions about many concepts, such as lightweight concrete, shear contribution for concrete, cracking torsional moment, size effect, angle of inclination of the strut, maximum nominal shear stress, and interaction between the torsion, shear, and moment.
2. The proposed model PM2 based on the NKPT model proved notably high efficiency in predicting torsional strength for steel fibered concrete beams and a lower coefficient of variation when compared to the NKPT model and the proposed model PM3 which is based on the ACI provisions.
3. The proposed model PM4 outperformed the previous Hasan and Deifalla model HD and the CSA provisions in predicting ultimate and cracking torsional strength for FRP-reinforced concrete beams.
4. The coefficient of variation and the average of the ratios between the experimentally measured torsional strength and that calculated showed that all the proposed models PM1, PM2, PM3, and PM4 are simple, consistent, and accurate, which are suitable for the purpose of design. These models could be the base for future design code developments.

Table 17.5 Details and test results for the experimental FRP beams database

References	Beam	f'_c MPa	f_{ftu} MPa	Dimensions (mm)	Conc. type	Long. Rfts	Trans. Rfts	T_{cr} (kN m)	T_u (kN m)
Okay and Engin (2012)	B5	25	400	R200 × 100	NC	Steel (3φ10) and GFRP (2φ10)	Steel 8 @ 200 mm	1.8	2.7
	B6	25	400		NC	Steel (3φ10)	Steel 8 @ 200 mm and GFRP 8 @ 200 mm	1.1	1.7
	B7	25	400		NC	Steel (3φ10) and GFRP (2 φ10)	Steel 8 @ 200 mm and GFRP 8 @ 200 mm	1.58	2.2
	B8	25	400		NC	GFRP (3φ10)	GFRP 8 @ 200 mm	0.86	1.2
	B9	25	400		NC	GFRP (3φ10)	GFRP 8 @ 200 mm	1.09	1.5
	B10	25	400		NC	GFRP (3φ10)	GFRP 8 @ 100 mm	0.58	1.1
	B11	25	400		NC	GFRP (2φ10)	GFRP 8 @ 100 mm	0.96	1.3
	B12	25	400		NC	GFRP (3φ10)	GFRP 8 @ 200 mm	1.14	1.6
	B13	25	400		NC	GFRP (3φ10)	GFRP 8 @ 200 mm	1.02	1.3
	B14	25	400		NC	GFRP (3φ10)	GFRP 8 @ 200 mm	1.31	1.8
	B15	25	400		NC	GFRP (3φ10)	GFRP 8 @ 200 mm	1.0	1.4
	B16	25	400		NC	GFRP (2φ10)	Steel 8 @ 100 mm	1.33	1.9
	B17	25	1500		NC	CFRP (3φ10)	Steel 8 @ 200 mm	1.91	1.9
	B18	25	1500		NC	CFRP (2φ10)	Steel 8 @ 200 mm	1.28	1.9

(continued)

Table 17.5 (continued)

References	Beam	f'_c MPa	f_{fu} MPa	Dimensions (mm)	Conc. type	Long. Rfts	Trans. Rfts	T_{cr} (kN m)	T_u (kN m)
Shehab et al. (2009)	B1	30	360	R200 × 100	SCC	GFRP (4φ10)	GFRP 8 @ 100 mm	1.4	2.3
	B2	45	360		SCC	GFRP (4φ10)	GFRP 8 @ 100 mm	2.4	3.4
	B3	90	360		HSCC	GFRP (4φ10)	GFRP 8 @ 100 mm	3.0	4.5
	B4	45	360		SCSFC (0.75%)	GFRP (4φ10)	GFRP 8 @ 100 mm	3.0	3.8
	B5	90	360		HSCSFC (0.75%) HSCSFC (1.5%)	GFRP (4φ10)	GFRP 8 @ 100 mm	3.0	5.0
	B6	90	360			GFRP (4φ10)	GFRP 8 @ 100 mm	4.0	5.1
Ragab and Eisa (2013)	BC120	38.5	1562	R600 × 250	NC	CFRP (8φ13)	CFRP 9.5 @ 120 mm	30.45	62.9
	BC180	38.5	1562		NC	CFRP (8φ13)	CFRP 9.5 @ 180 mm	29.87	49.4
	BC240	38.5	1562		NC	CFRP (8φ13)	CFRP 9.5 @ 240 mm	27.35	39.4
	BC300	38.5	1562		NC	CFRP (8φ13)	CFRP 9.5 @ 300 mm	28.65	35.7
Mohamed et al. (2015)	LB2	25	360	L350 × 150/150 × 400	NC	GFRP (2φ12)	Steel 6 @ 143 mm	2.1	8.4
	LB3	25	400		NC	GFRP (2φ12)	GFRP 6 @ 143 mm	2.1	10.0
	LB4	25	400		NC	GFRP (2φ12)	GFRP 8 @ 143 mm	2.1	14.0
	LB5	25	400		NC	GFRP (2φ12)	GFRP 10 @ 143 mm	2.1	20.0
Mohamed and Benmokrane (2015)	BG120	41.47	948	R600 × 250	NC	CFRP (7φ19)	GFRP 9.5 @ 120 mm	27.46	52.7
	BG180	41.47	948		NC	CFRP (7φ19)	GFRP 9.5 @ 180 mm	26.19	41.8

(continued)

Table 17.5 (continued)

References	Beam	f'_c MPa	ffu MPa	Dimensions (mm)	Conc. type	Long. Rfts	Trans. Rfts	T_{cr} (kN m)	T_u (kN m)
	BG240	38.5	948		NC	CFRP (7φ19)	GFRP 9.5 @ 240 mm	26.14	34.2
	BG300	41.47	948		NC	CFRP (7φ19)	GFRP 9.5 @ 300 mm	25.98	29.9
Mohamed and Benmokrane (2016)	BG-W	41.47	948	R600 × 250	NC	CFRP (8φ13)	–	23.11	25.0
	BG-120	41.47	948		NC	CFRP (8φ13)	GFRP 9.5 @ 120 mm	27.46	52.7
	BG-60	39.25	948		NC	CFRP (8φ13)	GFRP 9.5 @ 60 mm	27.76	56.9
	BC-W	38.5	1562		NC	CFRP (8φ13)	–	28.62	34.1
	BC120	38.5	1562		NC	CFRP (8φ13)	CFRP 9.5 @ 120 mm	30.45	62.9
	BC60	39.25	1562		NC	CFRP (8φ13)	CFRP 9.5 @ 60 mm	30.14	69.3
Zhou et al. (2017)	S-1	42.5	700	R150 × 200	PFC	GFRP (4φ14)	GFRP 8 @ 50 mm	2.88	5.5
	S-2	42.5	700		PFC	GFRP (8φ14)	GFRP 8 @ 50 mm	2.78	5.8
	F-1	40.2	700		PFC	GFRP (4φ14)	GFRP 8 @ 50 mm	2.88	6.7
	F-2	40.2	700		PFC	GFRP (8φ14)	GFRP 8 @ 50 mm	3.02	7.0
	F-3	40.2	700		CMC	GFRP (4φ14)	GFRP 8 @ 50 mm	2.78	5.7
	F-4	40.2	700		CMC	GFRP (8φ14)	GFRP 8 @ 50 mm	2.55	6.4
	E-1	32.8	700		CMC	GFRP (4φ14)	GFRP 8 @ 50 mm	2.28	8.2
	E-2	32.8	700		CMC	GFRP (8φ14)	GFRP 8 @ 50 mm	2.2	8.7

Table 17.6 Model validation with respect to FRP-reinforced concrete beams

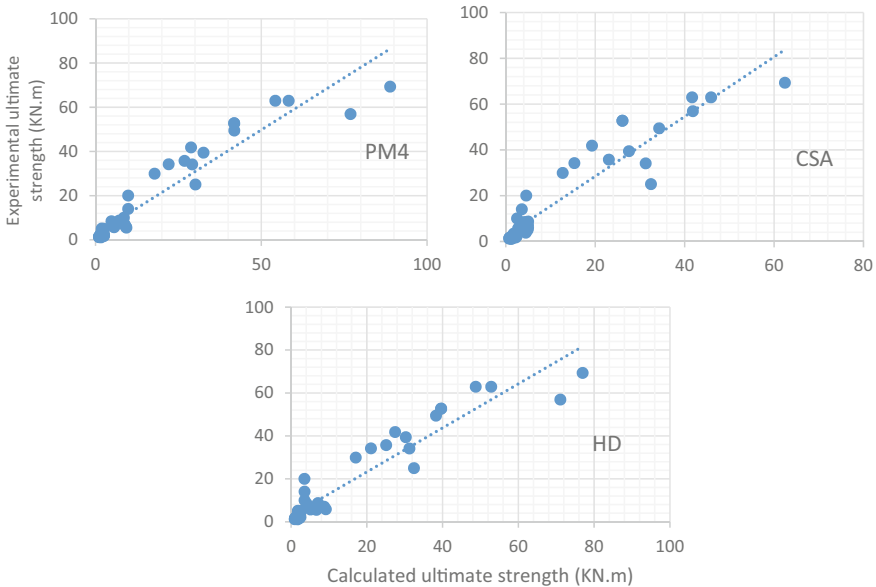|	Statistical measure	CSA	HD	PM4
Cracking torsion moment	Mean	1.33	1.20	0.95
	C.O.V (%)	63	37	24
Ultimate torsion moment	Mean	1.33	1.65	1.24
	C.O.V (%)	63	47	36

Fig. 17.3 The relation between experimental versus calculated ultimate torsional strength using PM4, CSA, and HD

References

ACI 213R-03 (2014) Guide for structural lightweight-aggregate concrete. ACI Committee 213. American Concrete Institute, Farmington Hills, Michigan, USA

ACI-318-19, ACI Committee 318 (2019) Building Code Requirements for Structural Concrete (ACI 318-19) and Commentary on Building Code Requirements (ACI 318-19). Farmington Hills (MI): American Concrete Institute

ACI-445 (2013) Report on torsion in structural concrete. Reported by Joint ACI-ASCE Committee 445. ACI 445.1R-12, ASCE-ACI Committee 445 on shear and torsion, April 2013, ISBN-13: 978-0-87031-810-8, ISBN: 0-87031-810-1, 80 pp

Al-Ausi MA, Abdul-Whab HMS, Khidair RM (1989) Effect of fibres on the strength of reinforced concrete beams under combined loading. In: Proceedings of the international conference held at the University of Wales, College of Cardiff, School of Engineering, Cardiff, UK, 18–20 September 1989; Elsevier Applied Science Publishers Limited; Elsevier Science Publishers: Essex, UK, pp 664–675

Badra N, Deifalla A (2022) Design reinforced concrete slabs with FRP reinforcements. In: Proceedings of the 7th international conference on civil structural and transportation engineering (ICCSTE'22) Niagara Falls, Canada–June 05–07, 2022, Paper No. 154. https://doi.org/10.11159/iccste22.154. Reliability-based evaluation of two-way shear.

Chalioris CE (2008) Torsional strengthening of rectangular and flanged beams using carbon fibre-reinforced-polymers-experimental study. Constr Build Mater 22(1):21–29

Chalioris CE, Karayannis CG (2009) Effectiveness of the use of steel fibers on the torsional behaviour of flanged concrete beams. Cem Concr Compos 31(5):331–341

CSA (2004) Design of concrete structures for buildings. Canadian Standards Association, Rexdale, Ontario, Canada

Deifalla A, Ghobarah A (2014) Behavior and analysis of inverted T-shaped RC beams under shear and torsion. Eng Struct 62:776–786

Deifalla A (2015) Torsional behavior of rectangular and flanged concrete beams with FRP reinforcements. J Struct Eng ASCE 04015068

Deifalla A (2020a) Design of lightweight concrete slabs under two-way shear without shear reinforcements: a comparative study and a new formula. Eng Struct Eng Struct 222:111076. https://doi.org/10.1016/j.engstruct.2020.111076

Deifalla A (2020b) Strength and ductility of lightweight reinforced concrete slabs under punching shear. Structures 27:2329–2345. https://doi.org/10.1016/j.is-truc.2020.08.002

Deifalla A (2020c) Torsion Design of lightweight concrete beams without or with fibers: a comparative study and a refined cracking torque formula. Structures 28:786–802. https://doi.org/10.1016/j.istruc.2020.09.004

Deifalla AF, Zapris AG, Chalioris CE (2021) Multivariable regression strength model for steel fiber-reinforced concrete beams under torsion. Materials 14:3889. https://doi.org/10.3390/ma14143889

Deifalla A (2021) Refining the torsion design of fibered concrete beams reinforced with FRP using multi-variable non-linear regression analysis for experimental results. Eng Struct 224

Deifalla A (2022) Data driven appraisal for one-way and two-way shear design of lightweight concrete and FRP-reinforced concrete elements. In: Proceedings of the 7th international conference on civil structural and transportation engineering (ICCSTE'22) Niagara Falls, Canada–June 05–07, 2022. Paper No. 203. https://doi.org/10.11159/iccste22.203.

Deifalla A (2023) Extended critical shear crack theory for punching shear of lightweight, FRP-reinforced, or prestressed concrete. In: Casini M (ed) Proceedings of the 2nd international civil engineering and architecture conference. CEAC 2022. Lecture notes in civil engineering, vol 279. Springer, Singapore. https://doi.org/10.1007/978-981-19-4293-8_37

Deifalla A, Hamed M, Saleh A, Ali T (2014) Exploring GFRP bars as reinforcement for rectangular and L-shaped beams subjected to significant torsion: an experimental study. Eng Struct 59:776–86

Deifalla A, Khalil MS, Abdelrahman A (2015) Simplified model for the torsional strength of concrete beams with GFRP stirrups. Compos Constr ASCE 19(1)

EC2 (2004) Eurocode 2: design of concrete structures–Part 1-1: general rules and rules for buildings. Incl. Corrigendum 1: EN 1992-1-1:2004/AC:2008, incl. Corrigendum 2: EN 1992-1-1:2004/AC:2010, incl. Amendment 1: EN 1992-1-1:2004/A1.: EN 1992-1-1:2004, 2014

El-Niema EI (1993) Fiber reinforced concrete beams under torsion. ACI Struct J 90.

Graybeal B (2014) Lightweight concrete: development of mild steel in tension. Technical Brief No. FHWA- HRT-14-030, Federal Highway Administration, Washington, DC

Greene G, Graybeal B (2013) Lightweight concrete: mechanical properties. Report No. FHWA-HRT-13-062, Federal Highway Administration, Washington, DC, 12 pp

Greene G, Graybeal B (2015) Lightweight concrete: shear performance," Report No. FHWA-HRT-15-022, Federal Highway Administration, Washington, DC, 20 pp

Hassan MM, Deifalla A (2016) Evaluating the new CAN/CSA-S806-12 torsion provisions for concrete beams with FRP reinforcements. Mater Struct. https://doi.org/10.1617/s11527-015-0680-9

JSCE (2007) Subcommittee on English version of standard specifications for concrete structures-2007 Japan Society of Civil Engineers (JSCE), December 2010, JSCE 2010 Concrete Committee, ISBN 978-4-8106-0752-9

Kaushik S, Sasturkar P (1989) Simply supported steel fibre reinforced concrete beams under combined torsion, bending and shear. In: Proceedings of the international conference held at the University of Wales, College of Cardiff, School of Engineering, Cardiff, UK, 18–20 September 1989; Elsevier Applied Science Publishers Limited; Elsevier Science Publishers: Essex, UK, pp 687–698

Khaloo AR, Sharifian M (Sep 2005a) Behavior of low to high-strength lightweight concrete under torsion. Int J Civ Eng 3(3&4):182–191

Khaloo AR, Sharifian M (2005b) Experimental investigation of low to high-strength steel fiber reinforced lightweight concrete under pure torsion. Asian J Civil Eng (Build Hous) 6(6)

Kuchma D, Wei S, Sanders D, Belarbi A, Novak L (Jul 2019) The development of the one-way shear design provisions of ACI 318-19. ACI Struct J 116(4). https://doi.org/10.14359/51716739

Mansur MA, Nagataki S, Lee SH, Oosumimoto Y (1989) Torsional response of reinforced fibrous concrete beams. ACI Struct J 86

MC (2010) Fédération internationale du béton. fib Model Code for Concrete Structures 2010. Lausanne; 2013

Mohamed HM, Benmokrane B (2016) Reinforced concrete beams with and without FRP Web reinforcement under pure torsion. J Bridge Eng 21(3):04015070. https://doi.org/10.1061/(ASCE)BE.1943-5592.0000839

Mohamed HM, Chaallal O, Benmokrane B (2015) Torsional moment capacity and failure mode mechanisms of concrete beams reinforced with carbon FRP bars and stirrups. J Compos Constr 19(2):04014049. https://doi.org/10.1061/(ASCE)CC.1943-5614.0000515

Mohamed HM, Benmokrane B (2015) Torsion behavior of concrete beams reinforced with GFRP bars and stirrups. ACI Struct J 112(5):543–552. https://doi.org/10.14359/51687824

Muttoni A (2018) Shear design and assessment: the coming steps forward for fib Model Code 2020. Struct Concr 19:3–4. https://doi.org/10.1002/suco.201870012

Narayanan R, Kareem-Palanjian AS (1986) Torsion in beams reinforced with bars and fibers. J Struct Eng 112:53–66

Nawaz W, Abdalla JA, Hawileh RA, Alajmani HS, Abuzayed IH, Ataya H et al (2019) Experimental study on the shear strength of reinforced concrete beams cast with Lava lightweight aggregates. Arch Civil Mech Eng 2019(19):981–996

Noshy A, Elwan S, Said H, Khalil A (Jan 2017) Torsional behavior of light weight concrete beams. Al-Azhar Univ Civ Eng Res Mag (CERM) 39(1)

Okay F, Engin S (2012) Torsional behavior of steel fiber reinforced concrete beams. Constr Build Mater 28:269–275

prEC2: PT1prEN 1992-1-1/2018-04 (2018) Eurocode 2: Design of Concrete Structures-Part 1-1: General rules for buildings, bridges and civil engineering structures. Third and final Draft by the Project Team SC2.T1

Ragab KS, Eisa AS (2013) Torsion behavior of steel fibered high strength self compacting concrete beams reinforced by GFRB bars. World Acad Sci Eng Technol Int J Civ Archit Sci Eng 7(9):331–341

Rahal K (2013) Torsional strength of normal and high strength reinforced concrete beams. Eng Struct 56:2206–2216

Rao TDG, Seshu DR (2006) Torsional response of fibrous reinforced concrete members: effect of single type of reinforcement. Constr Build Mater 20:187–192

Rao G, Seshu D, Warnitchai P (2010) Effect of steel fibers on the behavior of over-reinforced beams subjected to pure torsion. Civ Eng Dimens 12:44–51

Rao TDG, Rama Seshu D (2005) Analytical model for the torsional response of steel fiber reinforced concrete members under pure torsion. Cem Concr Compos 27:493–501

Sharma A (1989) Analysis of fiber reinforced concrete beams under combined loadings. Transp Res Rec 1226:94–104

Shehab HKHS, El-Awady M, Husain M, Mandour S (2009) Behavior of concrete beams reinforced by FRP bars under torsion. In: Proceedings of the 13th ICSGE, Cairo, Egypt, 6 pp

Yap SP, Khaw KR, Alengaram UJ, Jumaat MZ (2015) Effect of fibre aspect ratio on the torsional behavior of steel fiber-reinforced normal weight concrete and lightweight concrete. Eng Struct 2015(101):24–33

Yap SP, Alengaram UJ, Jumaat MZ, Khaw KR (2016) Torsional and cracking characteristics of steel fiber-reinforced oil palm shell lightweight concrete. J Compos Mater 50(1). https://doi.org/10.1177/0021998315571431

Zhou J, Shen W, Wang S (2017) Experimental study on torsional behavior of FRC and ECC beams reinforced with GFRP bars. Constr Build Mater 152:74–81

Chapter 18
Use of Recycled Waste Additives to Reduce Moisture Damage in Asphalt Mixes

Ashraf Rahim, Anthony Boyes, and Shadi Saadeh

Abstract It is evident that transportation has an enormous impact on the U.S. economy, and on the lives of its residents. Pavement conditions deteriorate over time because of the combined effects of traffic and climate. Exposure to moisture often causes premature failure of asphalt pavements as it reduces the stiffness of the asphalt and enable stripping of the asphalt from the aggregate. A laboratory study to evaluate the use of recycled waste additives in reducing moisture damage in Hot Mix Asphalt (HMA) was conducted. Two recycled waste additives (Fly Ash and Cement Kiln Dust) along with Hydrated Lime were investigated. These additives were added to the mix in three different application methods; namely Saturated Surface Dry (SSD), slurry and dry methods. The SuperPave mix design was adopted and moisture susceptibility was tested by employing Modified Lottman Test (AASHTO T 283). For all the modified mix combinations tested in this study the standard Tensile Strength Ratio (TSR) ratio exceeded the 80% threshold. However, when TSR was calculated as a ratio of the Indirect Tensile Strength (ITS) of the unmodified/unconditioned mix, several mixes failed to pass the 80% TSR threshold. Peak amount of additives for both recycled waste additives and hydrated lime were observed in this study. In terms of TSR, mixes modified using the SSD application method performed the best, followed by mixes modified using the slurry application and dry application method, respectively. Cement Kiln Dust and Hydrated Lime proved to be cost effective as compared with Fly Ash additives investigated in this study.

A. Rahim (✉)
California Polytechnic State University, San Louis Obispo, CA, USA
e-mail: arahim@calpoly.edu

A. Boyes
Dewberry Engineers, Inc., Rancho Cordova, CA, USA
e-mail: aboyes@drakehaglan.com

S. Saadeh
California State University, Long Beach, CA, USA
e-mail: Shadi.saadeh@csulb.edu

18.1 Background

Moisture damage in asphalt pavements, also known as stripping or moisture suscep-
tibility, can simply be defined as the breaking of the aggregate-binder bond by the
intrusion of water. As water is exposed to asphalt pavements, it seeps through tiny
cracks in the asphalt surface. Asphalt pavements that are exposed to water infiltra-
tion often begin losing aggregates, mainly due to the chemical attractiveness aggre-
gates have towards water, leading to the weakening of bond between asphalt binder
and aggregates (Kringos and Scarpas 2008). With the continued action of moisture-
induced weakening and cyclic traffic loading, progressive dislodgement of aggregates
becomes the dominant mode of failure in asphalt pavement which appears in the form
of distresses such as rutting, shoving, raveling, or cracking (Esarwi et al. 2008).

In a survey conducted by the National Cooperative Highway Research Project
(NCHRP), seventy percent of state and province departments of transportation in
North America that responded to the survey experienced moisture damage-related
problems in their pavements (Hicks 1991).

Adhesion is the attraction force that occurs between the interface of the bituminous
film and aggregate surface. Loss of adhesion is the primary mechanism of moisture
damage. Other mechanisms of moisture damage include loss of cohesion, when
water weakens the intermolecular attraction between molecules; hydraulic scouring,
when water rubs against pavement through cyclic pressure; and rupture of the bitu-
minous film surrounding the aggregates, when pore water pressure increases internal
stresses; failure of the bond between the aggregate and the binder; and degradation
of individual aggregate particles. For aggregates that have affinity for water absorp-
tion (hydrophilic aggregate), the binder is stripped off the aggregate surface. This
eventually leads to potholes and a failure of the under-layers (Terrel and AL-Swailmi
1994).

Aggregate ranges from basic (limestone) to acidic (quartzite) in pH while asphalt
binder has neutral to acidic tendencies (Santucci 2010). Therefore, the binder would
most likely form a stronger bond with limestone. Also, the cleanliness of the aggregate
is as aggregates coated with dust or fines create a barrier to the bonding between the
asphalt binder and the aggregate.

The result of pavement exposure to moisture is premature failure through stripping
of the pavement. Stripping typically begins at the bottom layer of the hot mix asphalt
(HMA) and progresses upward over time, though it can be difficult to detect since
stripping can also cause cracking, rutting, and corrugations. Stripping that begins at
the surface and progresses downward over time is known as raveling (Kennedy et al.
1983; Roberts et al. 1996; Chakravarty and Sinha 2020).

Various liquid antistripping and solid additives have been historically used to
improve adhesion between the binder and aggregate. The effects of commercially

available anti-stripping additives on the physical properties of the binder were reviewed through experimental studies (Anerson et al. 1982). A variety of liquid antistripping have been used to mitigate moisture sensitivity of hot-mix asphalt. These chemicals are added directly to the binder either at the refinery or binder terminal, or at the contractor's facility during production of the mix (Tunnicliff and Root 1984).

Solid additives have been used to provide resistance to moisture in hot-mix asphalt mixtures. Examples of these solid additives include, including hydrated lime, Portland cement, fly ash, flue dust, and polymers. These additives are typically added to the aggregate and mixed before mixing with the binder in the hot-mix asphalt production process. However, hydrated lime or Portland cement has been added in the drum mixing operation at the point of entry of the binder to the heated aggregate (Epps et al. 2003).

Huang et al. investigated the impact of adding fly ash Class F on mitigating moisture damage in HMA (Huang et al. 2010). It was reported that 1.0% concentration of class F fly ash resulted in a resilient modulus similar to that for the control mixture, but slightly lower than that for HMA treated with hydrated lime. In the same study, the TSR for mixes treated with fly ash class F showed a 15% higher ratio over the control mixture, although hydrated lime increased the TSR by 25% over that for the control mix (Huang et al. 2010).

The asphalt binder requirements can be significantly reduced by mixing CKD with asphalt binder before it is introduced to the aggregate. It also has the potential to replace hydrated lime and reduce moisture damage in pavements due to its high lime content (Siddique 2008). Huang et al. verified this in their study testing various mineral fillers. Adding 1.0% CKD to the asphalt mix produced a TSR within a few percent of the hydrated lime variations and nearly 25% higher than the untreated control mixture (Siddique 2008).

Also, nanomaterials, have been recently investigated in the literature for better improvements in moisture resistance and the preliminary results showed somewhat improvement in resistance to moisture damage (Ameri et al. 2016; Yang et al. 2018).

The objective of this research was to investigate the use of Fly Ash (FA), Cement Kiln Dust (CKD) and hydrated lime in mitigating moisture related damage in HMA. Three different methods of adding additives to the mix were investigated. An economical evaluation of the three agents used in this study was conducted to evaluate their cost-effectiveness.

Table 18.1 Specific gravity of coarse and fine aggregates

Aggregate type	Bulk specific gravity	Bulk specific gravity (SSD)	Apparent specific gravity	Absorption, %
Coarse	2.52	2.54	2.60	1.40
Fine	2.47	2.53	2.58	2.50

18.2 Materials

18.2.1 Aggregates

Crushed stone aggregate commonly used on the Central Coast of California was used and Table 18.1 presents results for specific gravities and water absorption. The aggregate used in this study had a Sand Equivalent (SE) value of 85% and loss in Los Angeles abrasion test of 40%.

18.2.2 Binder

Binder Performance Grade 64-16 (PG 64-16) with 1.03 specific gravity was used in this study. The virgin binder was tested in the Dynamic Shear Rheometer (DSR) before and after being aged in Rolling Thin Film Oven (RTFO). The binder was heated and additives were thoroughly mixed into the asphalt binder before being poured into silicone specimen molds to be tested in DSR. Results for the DSR test for unaged and aged binder with antistripping additives at different percentages are presented in Table 18.2.

The rutting parameter ($G^*/\sin\delta$) values for the binder under different aging conditions and additive types/contents are presented in Figs. 18.1 and 18.2. As noticed in the figures, the rutting parameter ($G^*/\sin\delta$) increases by adding additives which means more resistance to rutting deformation. From among the three recycled waste additives CKD resulted in the highest increase in $G^*/\sin\delta$. Also, at the same additive content $G^*/\sin\delta$ for lime treated binder was higher than that for binder treated with recycled waste additive.

18.2.3 Hot Mix Asphalt

The design of HMA was conducted in accordance with the SuperPave mix design procedure. The design procedure began with aggregate selection, followed by binder content selection. Three aggregate gradations (presented in Table 18.3) were considered for the study and Caltrans gradation requirements for 12.5-mm (0.50-inch)

Table 18.2 Dynamic shear rheometer test results

Treatment	Additive content, %	Complex modulus, kPa	Phase angle, °	Shear stress, kPa
Virgin binder				
Control	0.0	1.40	88.3	0.17
Class C FA[a]	1.00	2.45	87.0	0.30
	3.00	2.35	88.2	0.28
	5.00	4.50	87.8	0.57
	7.00	8.30	87.2	0.90
Class F FA[a]	1.00	1.94	87.7	0.23
	3.00	3.12	87.9	0.39
	5.00	4.05	87.8	0.54
	7.00	9.67	87.2	0.11
CKD[a]	1.00	2.08	87.6	0.25
	3.00	5.90	87.4	0.72
	5.00	6.62	87.4	0.80
	7.00	9.50	87.1	0.12
Lime[a]	1.00	3.12	88.1	0.48
	1.50	4.84	87.0	0.61
	2.00	6.66	86.9	0.80
RTFO aged binder				
Control	0.0	3.15	85.4	0.37
Class C FA[a]	1.00	5.85	83.2	0.68
	3.00	8.25	84.5	0.98
	5.00	13.8	84.2	1.70
	7.00	19.5	84.6	2.30
Class F FA[a]	1.00	4.74	83.9	0.57
	3.00	9.30	83.5	1.15
	5.00	12.85	84.4	1.55
	7.00	20.40	84.0	2.51
CKD[a]	1.00	5.30	83.9	0.62
	3.00	11.45	83.1	1.36
	5.00	16.55	84.4	2.03
	7.00	25.30	84.1	3.10
Lime[a]	1.00	3.12	85.2	0.48
	1.50	11.85	83.7	1.47
	2.00	13.70	84.2	1.68

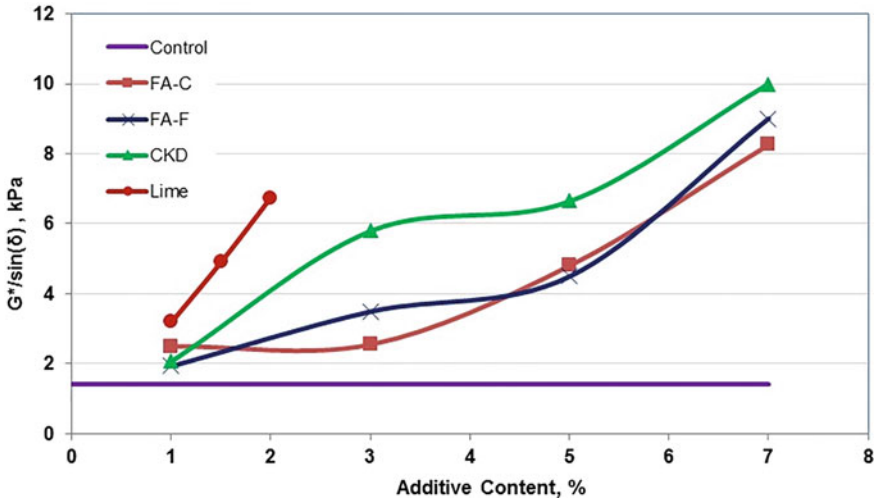[a] Percentage per aggregate weight

Fig. 18.1 $G^*/\sin(\delta)$ for unaged binder mixed with different antistripping additives
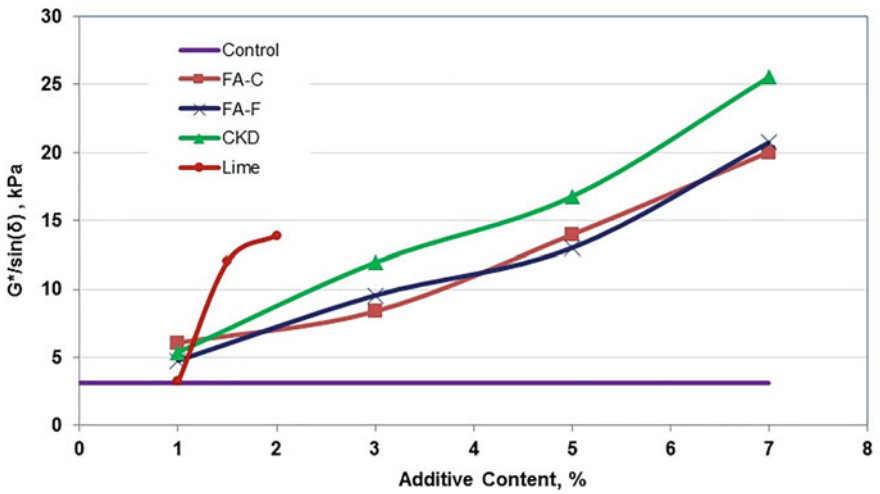

Fig. 18.2 $G^*/\sin(\delta)$ for RTFO-aged binder mixed with different antistripping additives

HMA, as shown in Table 18.3, were adopted. The SuperPave mix design resulted in an optimum binder content of 6.0% with blend 3 as the design blend.

Table 18.3 Grain size distribution for different aggregate blends

Sieve size, mm	19	12.5	9.5	4.75	2.38	0.60	0.075
Caltrans specification range, % passing	100	95–99	75–95	55–66	38–49	15–27	2–8
Blend #1	100	95	76	57	41	17	3
Blend #2	100	96	82	60	43	18	5
Blend #3	100	97	88	62	45	22	6

18.3   HMA Testing and Results

Four different additives, including Hydrated Lime normally used in California, were investigated in this study. The percentages at which additives were added to the mix are presented in Table 18.2. Additives were introduced to the asphalt mix by three different methods. In the first method, additives were added to the Saturated Surface Dry (SSD) aggregate. In the second method, additives were added in a slurry form according to Caltrans standard procedure in which one part of the additive was mixed with two parts of water forming a slurry. The slurry was then added to SSD aggregate and then the mix was left to marinate for 24-h period before being dried in oven before mixing with asphalt binder. The third introduction method investigated in this study was by adding additives directly to the asphalt binder. This was done by adding the correct amount of additive to heated asphalt binder and thoroughly mixing before being added to the aggregate and mixed. Note that the slurry and dry application methods were performed only for the optimum additive percentage determined based on the ITS for SSD prepared specimens. Table 18.4 presents the additive percentages used in the three different application approaches.

Six specimens were prepared per each treatment combination and specimens were split into two sets; one set was sealed and placed in a water bath at 25 °C (77 °F) for two hours and the other set was conditioned in accordance with AASHTO T 283. The tensile strengths for the conditioned specimens were then determined and the Tensile Strength Ratios (TSR) were calculated. Note that TSR was calculated by two different methods. In the first method the TSR was calculated as the ratio of ITS of the conditioned specimen to the ITS of the unconditioned specimen from the

Table 18.4 Additive percentages tested for different application approaches

Application approach	Additive content, %			
SSD	FA-C	FA-F	CKD	Hydrated lime
	1	1	1	1
	3	3	3	1.5
	5	5	5	2
	7	7	7	
Slurry	3	5	3	2
Dry	3	5	3	2

same additive combination and is referred to as $TSR_{standarad}$. In the second method the TSR is calculated as the ratio of the ITS of conditioned specimens to the ITS of unconditioned unmodified (control) specimen/mix and is referred to as $TSR_{unmodified}$ throughout this paper.

18.3.1 Tensile Strength Ratio (TSR)

SSD Application Method. Tensile Strength Ratio (TSR) is used to present the results of the AASHTO T 283 test for HMA specimens after and before conditioning. TSR is normally calculated as the ratio of the ITS of conditioned specimens and that for unconditioned specimens and the minimum acceptable value is 80%. It can be seen in Fig. 18.3 that all mixes treated with recycled additives have exceeded the minimum $TSR_{standarad}$ value of 80%. In Fig. 18.3 and for the range of additives content evaluated, it is noticed that HMA treated with Hydrated Lime produced the best TSR values. HMA modified with Fly Ash (FA) Class C and Class F resulted in TSR values that are comparable to that for HMA treated with Hydrated Lime. However, these TSRs were achieved at higher additives content (3–5% for FA-C and 5–7% for FA-F).

The ITS of conditioned modified specimens were compared to the ITS of unconditioned unmodified/control specimens to determine $TSR_{unmodified}$. In this approach all ITS would be compared to the same reference ITS making the comparison more rational. It can be seen in Fig. 18.4 that at the lowest additive content (1%) investigated in this study all mixes treated with antistripping, with the exception of lime treated HMA, had $TSR_{unmodified}$ that were at or slightly below the 80% threshold. However, at 3% additive content HMA treated with FA-C produced the highest $TSR_{unmodified}$
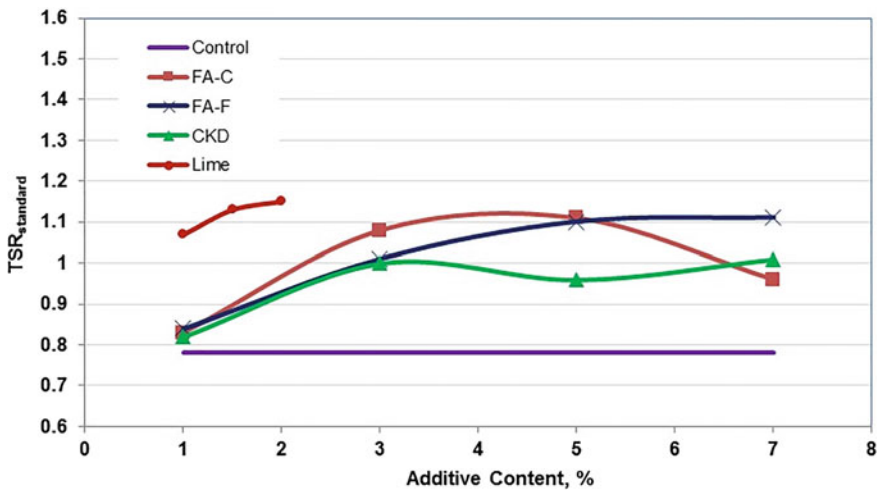

Fig. 18.3 TSR for HMA treated with different antistripping additives
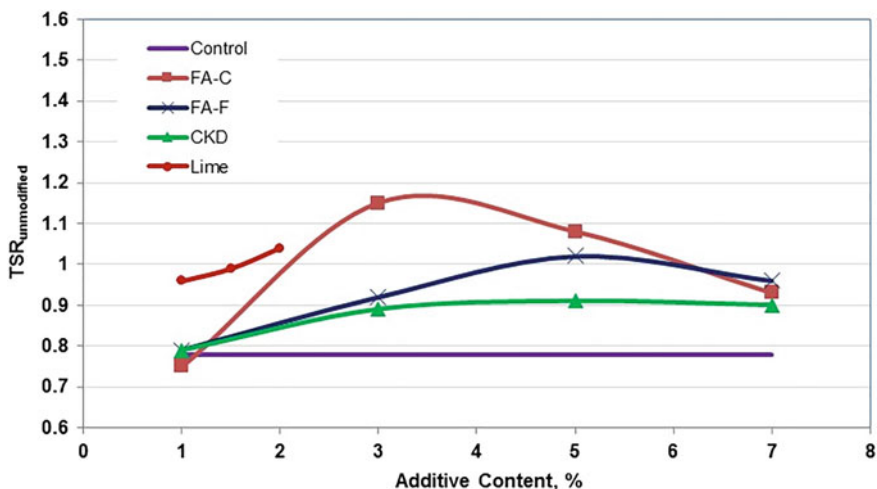
Fig. 18.4 $TSR_{unmodified}$ for conditioned HMA treated with different antistripping additives

as compared with all other mixes with different additive contents. Also, it is noticed that TSRs calculated following this approach differed from TSR values calculated following the standard approach.

Slurry Application Method. The TSR values for HMA mixes modified using the slurry application method are presented in Table 18.4. Note that optimum additive content from Fig. 18.4 was used in the slurry and dry application method. In general, the $TSR_{standarad}$ for mixes modified using the slurry application method were less than those for mixes modified using the SSD preparation method. However, $TSR_{standarad}$ were significantly higher than the 0.80 threshold. Also, $TSR_{unmodified}$ for mixes modified using the slurry application methods were at or below the 0.80 threshold.

Dry Application Method. The TSR values for HMA mixes modified using the dry application method are presented in Table 18.5. In general, the $TSR_{standarad}$ for mixes modified using the dry application method were higher than the 0.80 threshold. However, $TSR_{standarad}$ for dry application specimens were slightly less than those for mixes modified using the SSD preparation method and almost comparable to $TSR_{standarad}$ for slurry application specimens. Also, $TSR_{unmodified}$ for mixes modified using the dry application methods were all below the 0.80 threshold.

Table 18.5 ITS for specimens with different preparation methods

Additive type/ content	Preparation method					
	SSD		Slurry		Dry	
	TSR$_{standarad}$	TSR$_{unmodified}$	TSR$_{standarad}$	TSR$_{unmodified}$	TSR$_{standarad}$	TSR$_{umodified}$
Control	0.78	0.78	0.78	0.78	0.78	0.78
FA C/ 3%	1.08	1.15	0.96	0.75	0.96	0.71
FA F/ 5%	1.10	1.02	0.94	0.80	0.97	0.68
CKD/ 3%	0.96	0.91	0.95	0.79	0.93	0.67
Lime/ 2%	1.11	1.04	1.00	0.81	0.94	0.72

18.4 Cost Analysis

A brief cost analysis was conducted in this study. According to CalPortland Construction, the unit cost of hydrated lime was estimated at $45 per ton. At an optimum lime content of 2.0%, the material cost of lime would be $0.68 per ton of HMA mix. Also, CalPortland Construction suggested an $4.00 per ton of HMA to account for stockpiling, handling and mixing. This brings the final cost of adding lime to $4.68 per ton of HMA, approximately. Headwaters Resources quoted a unit cost of $72 per ton for Fly Ash Class C. At an optimum Fly Ash Class C of 3.0%, the material cost for the additive would be $2.16 per ton of HMA. After considering the stockpiling, handling and mixing, the total cost added is assumed to be $7.60 per ton of HMA. Fly Ash Class F was quoted at $62 per ton, per Headwaters Resources, which results in an increase of $7.10, approximately, per ton of HMA containing 5% Fly Ash Class F. Note that Fly Ash is not produced locally in California at great quantities making it more expensive than other additives investigated in this study.

CalPortland Construction priced CKD at around $20 per ton. Assuming 3% CKD concentration, the material cost is calculated to be $0.60 per ton of HMA. Considering material stockpiling, handling and mixing, the total increase in the cost is estimated at $4.6 per ton of HMA.

According to this preliminary cost analysis and for the type of aggregate and binder tested in this study, it appears that CKD has the least cost of all additives investigated in this study.

18.5 Conclusion

The study evaluated the moisture sensitivity performance of HMA treated with three different waste recycled additives and hydrated lime. The following conclusions are drawn from the data collected and analyzed in this study:

- All additives had a stiffening effect on the asphalt binder according to results from DSR tests with the highest increase in the rutting parameter ($G^*/\sin\delta$) for hydrated lime additive.
- Of the three waste recycled additives, CKD resulted in the highest increase in the rutting parameter ($G^*/\sin\delta$).
- Tensile Strength Ratio (TSR) for all mixes treated with all four additives were higher than that for the untreated (control) mix. Waste recycled additives resulted in TSR as high as that for hydrated lime treated mixes.
- Mixes in which additives were added following the SSD application method produced TSRs that were higher than those for mixes treated following the slurry application method.
- TSRs calculated as the ratio of ITS of conditioned specimens to the ITS of unconditioned unmodified (control) mixes were different from those calculated following the approach that is normally used to calculate TSR.
- Mixes modified using the SSD application method outperformed those modified using the slurry and dry application methods.
- The authors recommend using the $TSR_{unmodified}$ approach since it compares the ITS for all mixes to the same reference value; namely ITS for unmodified (control) unconditioned mix.
- Based on the preliminary cost analyses conducted in this study recycled waste additives proved to be cost effective. However, more data is needed to draw a robust conclusion especially in areas where recycled waste additives, for example Fly Ash, are locally produced.

References

Ameri M, Nobakht S, Bemana K, Vamegh M, Rooholamini H (2016) Effects of nanoclay on hot mix asphalt performance. Pet Sci Technol 34(8):747–753
Anerson D, Dukatz E (1982) The effect of antistrip additives on the properties of asphalt cement. Assoc Asph Paving Technol 51:298–317

Chakravarty H, Sinha S (2020) Moisture damage of bituminous pavements and application of nanotechnology in its prevention. J Mater Civil Eng 32(8)

Epps J, Berger E, Anagnos JN (2003) Treatments–moisture sensitivity of asphalt pavements. National Seminar, San Diego, CA

Esarwi MA, Hainin MR, Chik AA (2008) Stripping resistance of Malaysian hot mix asphalt mixture using hydrated lime as filler. Universiti Teknologi Malaysia

Hicks RG (1991) Moisture damage in asphalt concrete. NCHRP Synthesis of Highway Practice 175, Transportation Research Board, Washington, D.C.

Huang B, Shu X, Dong Q, Shen J (2010) Laboratory evaluation of moisture susceptibility of hot-mix asphalt containing cementitious fillers. J Mater Civil Eng 667–673

Kennedy T, Roberts F, Lee K (1983) Evaluation of moisture effects on asphalt concrete mixtures. Transp Res Rec 911. Transportation Research Board of the National Academies, Washington D.C.

Kringos N, Scarpas A (2008) Physical and mechanical moisture susceptibility of asphaltic mixtures. Int J Solids Struct 2671–2685

Roberts F, Kandhal P, Brown E, Lee D, Kennedy T (1996) Hot mix asphalt materials, mixture design, and construction, 2nd ed. NAPA Education Foundation, Lanham, Maryland

Santucci L (2010) Minimizing moisture damage in asphalt concrete. UC Berkeley Institute of Transportation Studies, Berkeley

Siddique R (2008) Waste materials and by-products in concrete, 2008 ed. Springer, Berlin

Terrel RL, AL-Swailmi S (1994) Water sensitivity of asphalt-aggregate mixes: test selection. SHRP-A-403, National Research Council, Washington, D.C.

Tunnicliff D, Root R (1984) Use of antistripping additives in asphaltic concrete mixtures. NCHRP Report No. 274. Transportation Research Board of the National Academy, Washington D.C.

Yang Z, Zhang Y, Shi X (2018) Impact of nanoclay and carbon microfiber in combating the deterioration of asphalt concrete by non-chloride deicers. Constr Build Mater 160:514–525